

# UC Berkeley

## UC Berkeley Electronic Theses and Dissertations

### Title

Development, Durability Studies and Application of High Performance Green Hybrid Fiber-Reinforced Concrete (HP-G-HyFRC) for Sustainable Infrastructure and Energy Efficient Buildings

### Permalink

<https://escholarship.org/uc/item/9gj5w1km>

### Author

Hay, Rotana

### Publication Date

2015

Peer reviewed|Thesis/dissertation

Development, Durability Studies and Application of High Performance Green Hybrid Fiber-Reinforced Concrete (HP-G-HyFRC) for Sustainable Infrastructure and Energy Efficient Buildings

By  
Rotana Hay

A dissertation submitted in partial satisfaction of the

requirements for the degree of

Doctor of Philosophy

in

Engineering – Civil and Environmental Engineering

in the

Graduate Division

of the

University of California, Berkeley

Committee in charge:

Professor Claudia P. Ostertag, Chair

Professor Paulo Monteiro

Professor Thomas Devine

Spring 2015



## Abstract

# Development, Durability Studies and Application of High Performance Green Hybrid Fiber-Reinforced Concrete (HP-G-HyFRC) for Sustainable Infrastructure and Energy Efficient Buildings

by

Rotana Hay

Doctor of Philosophy in Civil and Environmental Engineering

University of California, Berkeley

Professor Claudia Ostertag, Chair

Concrete-related construction industry consumes considerable amount of energy, resulting in large CO<sub>2</sub> release into the atmosphere. Cement which is used as the main binder in concrete is energy intensive to produce and contributes about 7% to total global anthropogenic carbon emission. Infrastructure across the globe suffers from durability problems and requires frequent repair and maintenance. This brings about high direct cost for rehabilitation and unaccounted indirect cost resulted from loss of productive time, traffic congestion and diversion, and in the process more CO<sub>2</sub> emission. In the meantime, buildings which are part of the overall civil infrastructure system require extensive amount of energy to keep the internal environment comfortable to users. The sector accounts for about 40% of global primary energy consumption. With increasing population and demand, actions from various building disciplines are needed to build a more sustainable industry. This research addresses these issues through the development of a new high performance fiber-reinforced concrete, its durability studies and its application to reduce operational energy in buildings. Durability is critical for infrastructure systems whose frequent maintenance and rehabilitation pose adverse impacts to the environment and add considerable costs to the economy. By accounting for sustainability aspects from materials conception to usage and disposal, this study encompasses the concept of sustainability through life cycle consideration. This represents a deviation from conventional sustainable approach where a focus is usually spent on reducing embodied energy of concrete composites.

The first area of focus was on the development of a new concrete composite called high performance green hybrid fiber-reinforced concrete (HP-G-HyFRC) reinforced with polyvinyl alcohol (PVA) micro- and hooked-end steel macrofibers. For easy construction and durability, the design criteria were defined to cover high workability, high strength and deflection hardening which is defined as an ability of the composite to carry increasing load after the first crack is formed. It was demonstrated that theoretical analysis could be used to limit the number of trials in determining the critical fiber volume fractions for the deflection hardening behavior in the composite. As compared to conventional self-consolidating concrete (SCC), fine aggregate over coarse aggregate ratio had to be increased in FRC for enhanced workability. Addition of supplementary cementitious materials (SCMs) in concrete especially fly ash helped to improve the composite's workability. This is attributed to fly ash's favorable fineness, size distribution and



spherical shape which resulted in ball-bearing action provided to other concrete constituents. PVA microfibers controlled propagation of micro cracks inherent in concrete or formed during loading. They also provided toughening around steel fibers and ensured a gradual pullout of steel fibers. The synergy of PVA micro- and steel macrofibers led to a smooth deflection hardening behavior of the composite under flexure at a relatively low fiber volume fractions of 1.5% steel fibers and 0.15% PVA fibers.

A study on corrosion performance of HP-G-HyFRC with accelerated corrosion test with an impressed current was then conducted. It was found that wide cracks ranging from 1.1 to 2 mm were observed in high performance concrete (HPC) without fibers. The presence of hybrid fibers in HP-G-HyFRC, on the other hand, reduced corrosion rates by half, attributable to crack bridging of fibers and the resulting formation of distributed cracks of small sizes. Also, under no applied current, all embedded steel rebars in HP-G-HyFRC were in the inactive corrosion zone even with the presence of 4% NaCl in the mixing water. Microscopic observation at steel-concrete interface showed a densification of corrosion products, which is postulated to limit iron dissolution and subsequently to reduce corrosion rates of the embedded bars. HP-G-HyFRC corrosion samples were also able to retain most of its strength after the accelerated corrosion tests.

As corrosion resistance of HP-G-HyFRC was considered at a composite level, the effects of individual mix component such as slag and fibers on corrosion were yet unknown. The next area of focus was on the influence of high-volume slag as cement replacement, hybrid fibers and steel-concrete interface on corrosion of steel in concrete. The studies elaborated various phenomena observed in the corrosion study of HP-G-HyFRC and also provided a fundamental understanding of different concrete parameters on corrosion.

It was found that due to shrinkage-induced cracking and possibly poor quality passive film due to the presence of reducing agents in concrete pore solutions, samples with 60% slag replacement and with no fiber reinforcement showed an early corrosion initiation and higher mass loss induced by the impressed current. Microstructural imaging showed that the samples with slag, despite having a higher gas permeability, showed a denser matrix but more continuous distributed microcracking in the matrix. This led to its poor ability to accommodate corrosion products at the interface and as a result the concrete experienced an early onset of cracking. Under the same regime of applied current, samples made of slag concrete also experienced higher gravimetric mass losses. This is attributed to a less stable passive film and more intense acidification at the interface due to a reduction in calcium hydroxide (CH) in the matrix. Also, an inclusion of hybrid fibers in concrete slightly increased concrete permeability although this did not adversely affect corrosion initiation performance of concrete. However, under propagation stage achieved by an induced current, hybrid fibers in concrete significantly reduced corrosion rates through confinement and densification of corrosion products at steel-concrete interface. The influence of interface qualities on corrosion of steel in concrete showed conflicting performance in corrosion initiation and propagation stages. It was found that higher porosity at the steel-concrete interface initiated an early corrosion. However, the porous interface could accommodate more corrosion products. This led to a smaller pressure buildup from the corrosion products and less damage to the surrounding concrete. As a result, smaller corrosion rates were observed in the samples with more porous interfaces after impressed current regimes. The finding helps to explain the more extensive damage in high performance concrete (HPC) as compared to normal strength concrete. This warrants the inclusion of fibers in HPC to extend the service life of structures constructed with the composite.

The study ended with a proposed application of HP-G-HyFRC in an innovative double skin façade (DSF) system in place of a conventional solid façade system to enhance operational energy performance of buildings. It was found that although the DSF is more energy intensive and more costly to construct, it allowed for a full recovery of the additional embodied energy within the first year of operation and cost recovery within the first 6 years of operation. The overall study exemplifies a life-cycle consideration adopted for materials design, durability investigation and application to ensure more sustainable infrastructure and buildings for our society.

# Table of Contents

|   |      |
|---|------|
| ABSTRACT .....  | 1    |
| Table of Contents .....   | i    |
| DEDICATION .....  | VI   |
| List of Figures .....   | vii  |
| List of Tables .....  | xii  |
| List of Symbols and Abbreviations .....   | xiii |
| ACKNOWLEDGEMENT .....   | XV   |
| 1 INTRODUCTION .....  | 1    |
| 1.1 Concrete structures and environmental impact .....  | 1    |
| 1.2 A new design paradigm and framework .....   | 2    |
| 1.3 Required materials and engineering properties .....   | 2    |
| 1.4 Objectives .....  | 5    |
| 1.5 Structure of the report .....   | 5    |
| 2 PERFORMANCE-BASED DESIGN OF HIGH PERFORMANCE GREEN HYBRID FIBER-REINFORCED<br>CONCRETE (HP-G-HYFRC) ..... | 8    |
| Summary .....   | 8    |
| 2.1 Introduction .....  | 8    |
| 2.2 Materials and methods .....   | 9    |
| 2.2.1 Materials .....   | 9    |
| 2.2.2 Concrete mixing and slump flow test .....   | 10   |
| 2.2.3 Specimens .....   | 11   |
| 2.2.4 Flexural test setup .....   | 11   |
| 2.2.5 Gas permeability test .....   | 12   |
| 2.2.6 Chloride migration test .....   | 13   |
| 2.3 Analytical procedure .....  | 15   |
| 2.3.1 Design criteria .....   | 15   |
| 2.3.2 Workability of fresh concrete .....   | 15   |
| 2.3.3 Mechanical properties of hardened concrete .....  | 15   |
| 2.3.3.1 Critical fiber volume .....   | 15   |
| 2.3.3.2 Checking criteria for deflection hardening .....  | 18   |
| 2.4 Results .....   | 18   |
| 2.4.1 Mix designs .....   | 18   |
| 2.4.2 Fresh concrete properties .....   | 19   |
| 2.4.3 Compression test results .....  | 21   |
| 2.4.4 Flexural test results .....   | 21   |
| 2.4.5 Compressive property development of the final mix .....   | 23   |
| 2.4.6 Coefficients of gas permeability .....  | 24   |
| 2.4.7 Coefficients of chloride migration .....  | 26   |
| 2.5 Discussion .....  | 27   |
| 2.5.1 Effects of PVA fibers and compressive strength on flexural response .....                             | 27   |
| 2.5.2 Interaction of macro and microfibers beyond hook region .....   | 29   |

|   |    |
|---|----|
| 2.5.3 Workability effects on concrete flexural response.....  | 30 |
| 2.6 Further research .....  | 31 |
| 2.7 Conclusions.....  | 31 |
| 3 CORROSION RESISTANCE OF HIGH PERFORMANCE GREEN HYBRID FIBER-REINFORCED CONCRETE (HP-G-HyFRC) .....  | 33 |
| Summary .....   | 33 |
| 3.1 Introduction.....   | 33 |
| 3.2 Materials and methods .....   | 34 |
| 3.2.1 Accelerated corrosion test.....   | 34 |
| 3.2.2 Materials .....   | 37 |
| 3.2.3 Concrete mix designs.....   | 37 |
| 3.2.4 Specimen preparation and corrosion testing procedure .....                                      | 38 |
| 3.2.5 Microscopic analysis.....   | 40 |
| 3.2.6 Gravimetric mass loss analysis .....  | 40 |
| 3.2.7 Pore press and inductively coupled plasma (ICP) .....   | 40 |
| 3.3 Results.....  | 42 |
| 3.3.1 Mechanical properties of concrete mixes .....   | 42 |
| 3.3.2 Corrosion initiation of samples with no applied current.....                                    | 43 |
| 3.3.3 Corrosion results of samples with applied current.....  | 45 |
| 3.3.4 Gravimetric mass loss results.....  | 48 |
| 3.3.5 Flatbed digital imaging and optical microscopy .....  | 51 |
| 3.3.6 BSE & EDX element mapping .....   | 54 |
| 3.3.7 ICP results .....   | 57 |
| 3.4 Discussion.....   | 58 |
| 3.4.1 Time to cracking under accelerated corrosion test .....   | 58 |
| 3.4.2 Cell voltage and IR compensation .....  | 59 |
| 3.4.3 Corrosion cracking process and damage mitigation due to fibers .....                            | 60 |
| 3.4.4 Influence of fibers in corrosion propagation stage .....  | 61 |
| 3.4.5 Residual strength after applied current .....   | 62 |
| 3.5 Conclusions.....  | 65 |
| 4 EFFECTS OF SLAG ON CORROSION OF REINFORCING BARS IN CONCRETE UNDER ACCELERATED CORROSION TEST ..... | 68 |
| Summary .....   | 68 |
| 4.1 Introduction.....   | 68 |
| 4.2 Literature review .....   | 70 |
| 4.2.1 Chloride permeability .....   | 70 |
| 4.2.2 Pore solution pH and steel passivity .....  | 71 |
| 4.2.3 Corrosion resistance of steel in concrete with slag.....  | 72 |
| 4.3 Materials and methods .....   | 74 |
| 4.3.1 Materials .....   | 74 |
| 4.3.2 Concrete mix designs.....   | 74 |
| 4.3.3 Specimen preparation and corrosion testing procedure .....                                      | 74 |
| 4.3.4 Microscopic analysis.....   | 76 |
| 4.3.5 Gravimetric mass loss analysis .....  | 76 |
| 4.3.6 Thermal gravimetric analysis (TGA).....   | 76 |
| 4.3.7 Pore solution analysis .....  | 78 |

|   |     |
|---|-----|
| 4.3.8 Gas permeability test.....  | 78  |
| 4.4 Results.....  | 78  |
| 4.4.1 Mechanical properties of concrete mixes .....   | 78  |
| 4.4.2 Corrosion initiation .....  | 79  |
| 4.4.3 Corrosion results with applied current.....   | 81  |
| 4.4.4 Gravimetric mass loss results.....  | 83  |
| 4.4.5 Flatbed digital imaging and optical microscopy.....   | 84  |
| 4.4.6 Pore solution analysis results.....   | 87  |
| 4.4.7 Gas permeability test results .....   | 89  |
| 4.4.8 TGA results.....  | 90  |
| 4.5 Discussion.....   | 91  |
| 4.5.1 Early corrosion initiation for C-60S .....  | 91  |
| 4.5.2 Crack initiation.....   | 94  |
| 4.5.3 Gravimetric mass loss and water oxidation .....   | 96  |
| 4.5.4 Gravimetric mass loss and interfacial acidification .....   | 97  |
| 4.6 Conclusions.....  | 98  |
| 5 EFFECTS OF HYBRID FIBERS AND CURRENT INTENSITIES ON CORROSION OF REINFORCING BARS IN CONCRETE WITH HIGH-VOLUME SLAG ADDITION..... | 100 |
| Summary.....  | 100 |
| 5.1 Introduction.....   | 100 |
| 5.2 Materials and methods .....   | 101 |
| 5.2.1 Materials .....   | 101 |
| 5.2.2 Concrete mix designs.....   | 102 |
| 5.2.3 Specimen preparation and corrosion testing procedure.....   | 103 |
| 5.2.4 Microscopic analysis.....   | 103 |
| 5.2.5 Gravimetric mass loss analysis.....   | 103 |
| 5.3 Results.....  | 104 |
| 5.3.1 Mechanical properties.....  | 104 |
| 5.3.2 Corrosion initiation in HyFRC.....  | 104 |
| 5.3.3 Corrosion results for HyFRC with applied current.....   | 107 |
| 5.3.4 Corrosion results for plain concrete with slow applied current .....  | 109 |
| 5.3.5 Corrosion rates for HyFRC and plain concrete.....   | 111 |
| 5.3.6 Gravimetric mass loss results.....  | 112 |
| 5.3.7 Flatbed digital imaging and optical microscopy.....   | 116 |
| 5.3.8 Backscattered electron imaging (BSE) & EDX element mapping .....  | 118 |
| 5.4 Discussion.....   | 120 |
| 5.4.1 Passive confinement of fibers on corrosion rates .....  | 120 |
| 5.4.2 Corrosion of steel fibers in accelerated corrosion test.....  | 121 |
| 5.4.3 Corrosion of fibers with no applied current and its effect on corrosion of anodic rebar .....                                 | 124 |
| 5.4.4 Chloride penetration of plain concrete under slow applied current.....  | 125 |
| 5.4.5 Porosity and gravimetric mass losses .....  | 126 |
| 5.4.6 Hybrid fibers and porosity .....  | 126 |
| 5.5 Conclusions.....  | 127 |
| 6 INFLUENCE OF INTERFACE QUALITIES ON CORROSION OF REINFORCING BARS IN CONCRETE ...   | 129 |
| Summary.....  | 129 |

|   |     |
|---|-----|
| 6.1 Introduction.....   | 129 |
| 6.2 Literature review .....   | 130 |
| 6.2.1 SCI inherent defects and steel corrosion.....   | 130 |
| 6.2.2 SCI disturbance due to loading and steel corrosion.....   | 132 |
| 6.3 Materials and methods .....   | 133 |
| 6.3.1 Materials .....   | 133 |
| 6.3.2 Concrete mix designs.....   | 133 |
| 6.3.3 Specimen preparation and corrosion testing procedure.....   | 134 |
| 6.3.4 Microscopic analysis.....   | 135 |
| 6.3.5 Gravimetric mass loss analysis .....  | 135 |
| 6.4 Results.....  | 135 |
| 6.4.1 Mechanical properties.....  | 135 |
| 6.4.2 Corrosion initiation in samples with different interface qualities.....   | 136 |
| 6.4.3 Corrosion results for concrete with applied current.....  | 137 |
| 6.4.4 Gravimetric mass loss results.....  | 142 |
| 6.4.5 Flatbed digital imaging and optical microscopy .....  | 144 |
| 6.4.6 Backscattered electron imaging (BSE) & EDX element mapping .....  | 146 |
| 6.5 Discussion.....   | 148 |
| 6.5.1 Corrosion of reinforcement in FRM .....   | 148 |
| 6.5.2 Influence of steel-concrete interface on corrosion.....   | 151 |
| 6.5.3 Gravimetric and theoretical mass losses .....   | 152 |
| 6.5.4 Potential problems with accelerated corrosion test.....   | 154 |
| 6.6 Conclusions.....  | 155 |
| 7 INNOVATIVE DOUBLE SKIN FAÇADE (DSF) WITH HP-G-HyFRC FOR SUSTAINABLE AND ENERGY EFFICIENT BUILDINGS IN THE TROPICS ..... | 157 |
| Summary .....   | 157 |
| 7.1 Introduction.....   | 157 |
| 7.2 Double skin façade (DSF) system.....  | 159 |
| 7.2.1 The façade system.....  | 159 |
| 7.2.2 Heat transfer.....  | 160 |
| 7.2.3 Benefits .....  | 161 |
| 7.2.4 Construction.....   | 161 |
| 7.3 Materials, methods and modelling.....   | 162 |
| 7.3.1 Concrete composites and reinforcement.....  | 162 |
| 7.3.2 Flexural test setup .....   | 163 |
| 7.3.3 Functional unit .....   | 164 |
| 7.3.4 Embodied energy of concrete constituents .....  | 165 |
| 7.3.5 Embodied energy of rebars, fibers and EP.....   | 167 |
| 7.3.6 Operational energy modelling.....   | 168 |
| 7.4 Results.....  | 170 |
| 7.4.1 Mechanical properties of façade systems .....   | 170 |
| 7.4.2 Embodied energy of concrete constituents and concrete mixes .....   | 172 |
| 7.4.3 Operational energy modeling results .....   | 173 |
| 7.4.4 Life cycle cost analysis .....  | 174 |
| 7.4.5 Uncertainties in data .....   | 176 |
| 7.5 Discussion.....   | 176 |

|  |     |
|--|-----|
| 7.5.1 Environmental impact of DSF system ..... | 176 |
| 7.5.2 Accuracy of COMFEN5 .....                | 177 |
| 7.5.3 Durability of GFRP .....                 | 177 |
| 7.5.4 Constructability of DSF .....            | 177 |
| 7.5.5 Size effects .....                       | 178 |
| 7.6 Conclusions .....                          | 179 |
| 8 CONCLUDING REMARKS .....                     | 180 |
| 8.1 Summary .....                              | 180 |
| 8.2 Concluding statements .....                | 181 |
| 8.3 Limitations of the current study .....     | 183 |
| 8.4 Recommendations for future studies .....   | 183 |
| REFERENCES .....                               | 186 |

# Dedication

I humbly dedicate this dissertation to my parents, sisters and brothers. My parents, along with other Cambodian fellows, lost their loved ones, good health due to extreme labor and right to ownership during the Khmer Rouge. Raising up kids from their bare hands, literally, with little external support would be an extreme challenge that makes them deserve a respect as a parent. Although they never finished secondary school, they always encourage me to pursue higher education, and they have made a lot of sacrifices for that to happen. Also, the encouragement, sympathy and support from my sisters and brothers cannot be underestimated in helping me to cling onto the PhD program and to work hard to achieve it. I am very fortunate and happy to be their kid and sibling. And with a PhD, I hope to make positive contributions to the society and to make my family proud.



# List of Figures

|  |    |
|--|----|
| Figure 1.1: Proposed framework for design consideration of concrete composite for sustainable and energy efficient buildings.....  | 2  |
| Figure 1.2: Typical stress-strain response of FRC in tension: (a) strain-softening behavior, (b) strain-hardening behavior (Naaman, 2007) .....  | 4  |
| Figure 2.1: Fibers used in the study: (a) 30 mm hooked-end steel fibers, and (b) PVA microfibers .....   | 10 |
| Figure 2.2: Flexural test setup.....   | 12 |
| Figure 2.3: Permeater cell (Rilem, 1999).....  | 13 |
| Figure 2.4: Schematic diagram for gas permeability test setup (Celik et al., 2014).....  | 13 |
| Figure 2.5: Test setup for non-steady state Cl <sup>-</sup> migration test .....   | 14 |
| Figure 2.6: Typical pullout curves for straight and hooked-end fibers (Markovich et al., 2001; Naaman & Najm, 1991).....   | 17 |
| Figure 2.7: Effects of concrete constituents on workability: (a) fine-coarse aggregate ratio, (b) steel fiber volume fractions, (c) PVA fiber volume fractions, and (d) SCMs .....                     | 19 |
| Figure 2.8: Slump flow shapes for different trial mixes .....  | 20 |
| Figure 2.9: 28-day compressive strengths of selected mixes.....  | 21 |
| Figure 2.10: Load-deflection curves for selected trial mixes with variable fiber volume fractions .....  | 22 |
| Figure 2.11: Load-deflection curves for selected trial mixes with different SCM replacement levels at 28 days .....  | 23 |
| Figure 2.12: Compression strength development for HP-G-HyFRC.....  | 24 |
| Figure 2.13: Elastic modulus development for HP-G-HyFRC.....   | 24 |
| Figure 2.14: Coefficients of gas permeability.....   | 25 |
| Figure 2.15: Distribution of air voids in: (a) HPC-60R, and (b) HP-G-HyFRC .....   | 25 |
| Figure 2.16: Coefficients of chloride migration .....  | 27 |
| Figure 2.17: Portion of pulled-out hooked fiber in compact tension specimen: (a) separation on one side of the fiber, and (b) crushing and microcracking on the other side (Bentur et al., 1985) ..... | 28 |
| Figure 2.18: Load deflection curve for FRC mixes with W/B of 0.33 and 0.25 .....   | 28 |
| Figure 2.19: Crack distribution developed on the tensile face of flexure specimen for: (a) PF-0b, and (b) HP-G-HyFRC .....   | 29 |
| Figure 2.20: Interaction of macro and microfibers close to crack plane .....   | 30 |
| Figure 2.21: 28-day elastic modulus for selected mixes.....  | 31 |
| Figure 3.1: Schematic representations: (a) corrosion process with electrochemical reactions, and (b) simplified electrical circuit model.....  | 35 |
| Figure 3.2: Charge transfer and formation of corrosion products in accelerated corrosion test.....   | 36 |
| Figure 3.3: Bar preparation for accelerated corrosion test: (a) sandblasting, (b) bars ready for casting, (c) bar hung by cross rod, and (d) first lift of concrete.....                               | 38 |
| Figure 3.4: Accelerated corrosion test setup.....  | 39 |
| Figure 3.5: Pore press configuration.....  | 41 |
| Figure 3.6: Compressive strengths of HPC-0R, HPC-60R and HP-G-HyFRC at 28 days and 56 days .....   | 42 |
| Figure 3.7: Corrosion potentials for samples without applied current.....  | 43 |

|   |    |
|---|----|
| Figure 3.8: Corrosion rates for samples without applied current.....  | 44 |
| Figure 3.9: Reduction in corrosion potential with cathodic control .....  | 44 |
| Figure 3.10: Corrosion potentials for HPC and HP-G-HyFRC samples with applied current of:<br>(a) 24 hours, and (b) 48 hours.....  | 45 |
| Figure 3.11: Corrosion rates for HPC samples with applied current of: (a) 24 hours, and (b) 48<br>hours.....  | 47 |
| Figure 3.12: Cracking on surfaces of samples with different regimes of applied current, with $\delta_{cr}$<br>representing maximum observed crack width .....   | 48 |
| Figure 3.13: Corrosion rates and time integration for theoretical mass loss measurement .....   | 49 |
| Figure 3.14: Corrosion spots on HP-G-HyFRC-0H after 98 days in NaCl solution .....  | 50 |
| Figure 3.15: Bar surfaces showing no corrosion for samples with no applied current and uniform<br>corrosion for samples with 24 and 48 hours of applied current.....  | 51 |
| Figure 3.16: Scanned images of sections for corrosion samples .....   | 52 |
| Figure 3.17: Optical microscopic results for steel-concrete interfaces.....   | 53 |
| Figure 3.18: BSE images and corresponding EDX element mapping for: (a) HPC-0R-0H, (b)<br>HPC-60R-0H, (c) HP-G-HyFRC-0H, (d) HP-G-HyFRC-24H and , (e) HP-G-HyFRC-<br>48H.....  | 55 |
| Figure 3.19: Circumferential and radial cracking due to drying shrinkage: (a) Four-sandstone<br>disc model (Hsu, 1963), and (b) cracking schematic of an isolated aggregate in the<br>matrix (Hearn, 1999).....                             | 56 |
| Figure 3.20: Chemical concentrations in pore solution of pastes at 1 month.....   | 57 |
| Figure 3.21: Cell voltage (presumably compensated) with time for HPC-0/60R and HP-G-<br>HyFRC to generate 1 mA/cm <sup>2</sup> applied current .....  | 59 |
| Figure 3.22: Cell voltage (uncompensated) with time for HPC-0/60R and HP-G-HyFRC to<br>generate 1 mA/cm <sup>2</sup> applied current.....   | 59 |
| Figure 3.23: Crack propagation process in (a) HPC and (b) HP-G-HyFRC under applied current<br>.....   | 60 |
| Figure 3.24: (a) Steel fiber bridging corrosion-induced crack, and (b) steel fiber not bridging<br>corrosion-induced crack.....   | 62 |
| Figure 3.25: Tensile splitting results of corrosion samples .....   | 63 |
| Figure 3.26: Proposed structural service life models for HPC and HP-G-HyFRC .....   | 65 |
| Figure 4.1: SEM and X-ray map at steel-paste interface: (a) OPC specimen, and (b) slag-OPC<br>specimen (Macphee, 1993).....   | 72 |
| Figure 4.2: Corrosion rate of steel as a function of percent cement replaced by slag in concrete<br>after 90 days of NaCl solution exposure (Dehghanian, 1999).....   | 73 |
| Figure 4.3: Bar preparation for accelerated corrosion test: (a) sandblasting, (b) bars before and<br>after sand blasting with epoxy coating, (c) heat shrink tubing, and (d) bar with heat<br>shrink tube and wiring ready for casting..... | 75 |
| Figure 4.4: Accelerated corrosion test setup.....   | 76 |
| Figure 4.5: Example illustrating the calculation of A and B in the TG curve (Girao, 2007) ....  | 77 |
| Figure 4.6: Compressive strengths of concrete at 28 days and 56 days .....  | 79 |
| Figure 4.7: Corrosion potentials for samples without applied current.....   | 80 |
| Figure 4.8: Corrosion rates for samples without applied current.....  | 81 |
| Figure 4.9: Corrosion potentials for samples with applied current of: (a) 24 hours, and (b) 48<br>hours.....  | 82 |

|   |     |
|---|-----|
| Figure 4.10: Corrosion rates for samples with applied current of: (a) 24 hours, and (b) 48 hours  | 83  |
| Figure 4.11: Scanned images of sections from plain concrete corrosion samples   | 85  |
| Figure 4.12: Optical microscopic results for steel-concrete interfaces  | 86  |
| Figure 4.13: Non-uniformity of corrosion on steel surfaces  | 87  |
| Figure 4.14: Pore solution pH values  | 88  |
| Figure 4.15: Measured concentrations of Al, Ca, K, Na, S and Si in pore solutions   | 89  |
| Figure 4.16: Coefficient of gas permeability  | 90  |
| Figure 4.17: Weight percentage of CH in pastes with and without slag replacement  | 91  |
| Figure 4.18: Elastic modulus of concrete at 28 and 56 days  | 92  |
| Figure 4.19: Cl <sup>-</sup> penetration with AgNO <sub>3</sub> spray   | 93  |
| Figure 4.20: Shrinkage cracking in C-60S before immersion in 3.5% NaCl solution   | 94  |
| Figure 4.21: SEM micrographs of interfaces for: (a) C-0S-0H, (b) C-45S-0H, and C-60S-0H   | 95  |
| Figure 4.22: SEM micrographs and corresponding EDX results for Fe, O, Ca and Si at interfaces of: (a) C-0S-48H, and (b) C-45S-48H   | 96  |
| Figure 5.1: Fibers used in the study: (a) 30 mm and 60 mm hooked-end steel fibers, and (b) PVA microfibers  | 102 |
| Figure 5.2: Compressive strengths of HyFRC at 28 days and 56 days   | 104 |
| Figure 5.3: Corrosion potentials for samples without applied current  | 105 |
| Figure 5.4: Corrosion potentials for samples without applied current  | 106 |
| Figure 5.5: Corrosion rates for samples without applied current   | 106 |
| Figure 5.6: Corrosion potentials for HyFRC samples with applied current of: (a) 24 hours, and (b) 48 hours  | 107 |
| Figure 5.7: Corrosion rates for HyFRC samples with applied current of: (a) 24 hours, and (b) 48 hours   | 109 |
| Figure 5.8: Corrosion potentials for plain concrete samples with 0.2 mA/cm <sup>2</sup> applied current for 240 hours   | 110 |
| Figure 5.9: Corrosion rates for plain concrete samples with 0.2 mA/cm <sup>2</sup> applied current for 240 hours and with 1 mA/cm <sup>2</sup> applied current for 48 hours | 110 |
| Figure 5.10: Corrosion-induced cracks for plain concrete with slow applied current  | 111 |
| Figure 5.11: Corrosion rates for plain concrete samples with 0.2 mA/cm <sup>2</sup> applied current for 240 hours   | 112 |
| Figure 5.12: Corrosion on bar surfaces showing patches of corrosion on bars with no applied current   | 114 |
| Figure 5.13: Fiber corrosion on surfaces of HyFRC-45S   | 115 |
| Figure 5.14: Corrosion product natures for C'-60S-240H and C'-60S-48H   | 116 |
| Figure 5.15: Scanned images of sections for HyFRC corrosion samples   | 117 |
| Figure 5.16: Optical microscopic results for steel-concrete interfaces  | 118 |
| Figure 5.17: BSE images and corresponding EDX element mapping for: (a) HyFRC-0S-48H, (b) HyFRC-45S-48H, and (c) HyFRC-60S-48H   | 120 |
| Figure 5.18: Corrosion rates of HyFRC-60S-48H and C-60H-0/24/48H  | 120 |
| Figure 5.19: Equivalent electrical half circuit for accelerated corrosion test  | 121 |
| Figure 5.20: Mechanism of steel fiber corrosion under applied current   | 122 |
| Figure 5.21: 30 mm steel fiber retrieved from C-0S-48H: (a) fiber more parallel to anodic steel rebar, and (b) fiber more perpendicular to anodic steel rebar               | 123 |

|  |     |
|--|-----|
| Figure 5.22: Corrosion of #2 rebar embedded near the surface of the sample: (a) stain on the surface, and (b) extent of corrosion .....  | 123 |
| Figure 5.23: Split HyFRC-0S-48H showing no corrosion of fibers in the bulk concrete .....  | 124 |
| Figure 5.24: Cl <sup>-</sup> penetration with AgNO <sub>3</sub> spray on concrete samples with slow applied current .....  | 125 |
| Figure 5.25: Microscopic pictures of steel-concrete interface.....   | 126 |
| Figure 5.26: Microscopic pictures at steel-concrete interface of: (a) C-45S-24H, and (b) HyFRC-45S-24H .....   | 127 |
| Figure 6.1: Corrosion potentials: (a) steel wrapped with filter paper in mortar (NaCl in both mixing water and immersion solution), and (b) steel directly immersed in CH solution (Yonezawa et al., 1988) .....     | 131 |
| Figure 6.2: Microcell current density for various steel elements (H for Horizontal, V for Vertical, first T/B that follows for top/bottom bars, and second T/B for top/bottom elements) (Mohammed et al., 1999)..... | 132 |
| Figure 6.3: Bars with different interfaces: (a) plain rebar, (b) rebar coated with FRM, and (c) rebar covered with filter paper .....  | 134 |
| Figure 6.4: Compressive strengths of plain concrete and FRM (E) .....  | 136 |
| Figure 6.5: Corrosion potentials for samples without applied current.....  | 136 |
| Figure 6.6: Corrosion rates for samples without applied current.....   | 137 |
| Figure 6.7: Corrosion potentials for samples with applied current of: (a) 24 hours, and (b) 48 hours.....  | 138 |
| Figure 6.8: Corrosion rates for plain concrete with 4% NaCl with applied current of: (a) 24 hours, and (b) 48 hours .....  | 140 |
| Figure 6.9: Cracking on surfaces of samples with different regimes of applied current .....  | 141 |
| Figure 6.10: Corrosion stain at C-F-48H top surface where corrosion products leached out .   | 142 |
| Figure 6.11: Cell voltage with time for C-E samples .....  | 143 |
| Figure 6.12: Corrosion on bar surfaces showing patches of corrosion on C-D-0H/C-E-0H and uniform corrosion for all other samples.....  | 144 |
| Figure 6.13: Scanned images of sections for corrosion samples with different interfaces.....   | 145 |
| Figure 6.14: Optical microscopic results at steel-concrete interfaces with different corrosion regimes.....  | 146 |
| Figure 6.15: BSE images and corresponding EDX element mapping for: (a) C-D-48H, (b) C-E-48H, and (c) C-F-48H.....  | 148 |
| Figure 6.16: Corrosion rates of rebar in FRM and plain concrete with 48 hours of applied current .....   | 149 |
| Figure 6.17: (a) Crack pattern on a cut section of FRM sample, and (b) BSE micrograph showing crack and penetration of corrosion products into the matrix .....  | 149 |
| Figure 6.18: Difference in accelerated corrosion mechanism in: (a) E sample and (b) C-E sample .....   | 150 |
| Figure 6.19: Flexural responses of FRM at 56 days .....  | 151 |
| Figure 6.20: Crack distribution of flexural FRM samples .....  | 151 |
| Figure 6.21: Theoretical against gravimetric mass losses .....   | 153 |
| Figure 6.22: Corrosion equilibrium under accelerated corrosion test.....   | 154 |
| Figure 6.23: Total cell voltage drops between the anode and cathode .....  | 155 |
| Figure 7.1: Side and cross-section views of: (a) SW, and (b) DSF with HP-G-HyFRC skins   | 160 |
| Figure 7.2: Radiation heat transfer in concrete DSF.....   | 161 |

|   |     |
|---|-----|
| Figure 7.3: Casting procedure for DSF .....   | 162 |
| Figure 7.4: Flexural test set up for DSF element .....  | 164 |
| Figure 7.5: Plan view of functional unit .....  | 165 |
| Figure 7.6: Analysis scenarios for energy modelling .....   | 169 |
| Figure 7.7: Annual temperatures.....  | 169 |
| Figure 7.8: Flexural test results for solid façade, and HP-G-HyFRC DSF.....                           | 170 |
| Figure 7.9: Failure modes of DSF: (a) GHP-G-HyFRC tensile failure, and (b) crushing of GFRP bar ..... | 171 |
| Figure 7.10: Multiple cracks on the bottom face of DSF .....  | 171 |
| Figure 7.11: Energy and CO <sub>2</sub> emission for different scenarios .....                        | 174 |
| Figure 7.12: Size effects of flexural responses of HP-G-HyFRC elements .....                          | 178 |

# List of Tables

|  |     |
|--|-----|
| Table 2.1: Compositions of cement, slag and fly ash .....  | 10  |
| Table 2.2: Fiber properties .....  | 10  |
| Table 2.3: Critical fiber volume estimation .....  | 17  |
| Table 2.4: Mix proportions of trial mixes kg/m <sup>3</sup> .....  | 19  |
| Table 2.5: Classification of concrete quality based on gas permeability coefficients (Torrent, 1999) .....                                       | 26  |
| Table 3.1: Rebar chemical compositions (%) .....   | 37  |
| Table 3.2: Mix designs for accelerated corrosion test (kg/m <sup>3</sup> ) .....   | 37  |
| Table 3.3: Gravimetric and theoretical mass losses .....   | 50  |
| Table 3.4: Estimated gravimetric mass loss during the applied current period .....   | 64  |
| Table 4.1: Concrete mix designs for accelerated corrosion study kg/m <sup>3</sup> .....  | 74  |
| Table 4.2: Gravimetric and theoretical mass losses .....   | 84  |
| Table 5.1: Fiber properties .....  | 102 |
| Table 5.2: Mix designs for concrete mixes used in accelerated corrosion study (kg/m <sup>3</sup> ) .....   | 103 |
| Table 5.3: Gravimetric and theoretical mass losses .....   | 113 |
| Table 6.1: Compositions of FRM powder .....  | 133 |
| Table 6.2: Mix designs for accelerated corrosion test (kg/m <sup>3</sup> ) .....   | 134 |
| Table 6.3: Gravimetric and theoretical mass losses .....   | 142 |
| Table 7.1: Concrete mix design (kg/m <sup>3</sup> ) .....  | 163 |
| Table 7.2: Rebar properties .....  | 163 |
| Table 7.3: Technologies adopted in processes of cement production .....  | 166 |
| Table 7.4: Average contributions of energy source (%) by countries .....   | 167 |
| Table 7.5: Transportation inputs .....   | 167 |
| Table 7.6: Occupancy level for COMFEN analysis in residential buildings .....  | 168 |
| Table 7.7: Embodied energy and carbon emission of concrete constituents, rebar, EP (per 1000 kg), and concrete mixes (per m <sup>3</sup> ) ..... | 172 |
| Table 7.8: Materials, embodied energy and carbon emission for SW, DSF, and DSF+EP .....  | 173 |
| Table 7.9: U-factors for wall components (w/m <sup>2</sup> k) .....  | 173 |
| Table 7.10: Unit costs of concrete constituents .....  | 175 |
| Table 7.11: Comparative results of functional unit with different wall types .....   | 175 |

# List of Symbols and Abbreviations

|               |  |
|---------------|--|
| $\delta$      | : Mid-span deformation, mm   |
| $\phi$        | : Mid-span curvature at steel-yield point  |
| $\eta$        | : Dynamic viscosity of fluid, N s m <sup>-2</sup>  |
| $\sigma$      | : Stress, MPa  |
| $\sigma_{mu}$ | : Matrix tensile strength or modulus of rupture, MPa   |
| $\Omega$      | : A constant accounting for bond mobilization, expected pullout length ratio, group reduction factor of fibers and stress distribution |
| $\tau$        | : Average fiber-matrix bond strength, MPa  |
| $\nu$         | : Poisson's ratio  |
| $A$           | : Specimen cross-sectional area or surface area, mm <sup>2</sup> or cm <sup>2</sup>  |
| $A_w$         | : Atomic weight of iron, g   |
| $b$           | : Specimen width, mm   |
| $B$           | : Stern-Geary constant, mV   |
| $c_0$         | : Chloride concentration in catholyte solution, N  |
| $c_d$         | : Chloride concentration at which color changes, N (0.07 N for OPC concrete)   |
| $C_a$         | : Anodic capacitance, F  |
| $C_c$         | : Cathodic capacitance, F  |
| $d$           | : Specimen depth, mm   |
| $d_f$         | : Fiber diameter, mm   |
| $D_{nssm}$    | : Non-steady-state migration coefficient, m <sup>2</sup> /s  |
| $erf^{-1}$    | : Inverse of error function  |
| $f'_c$        | : Concrete compressive strength, MPa   |
| $F$           | : Faraday's constant, coulombs/equivalent mass or J/V.mol  |
| $h$           | : Section thickness or height, mm or m   |
| $i_{corr}$    | : Corrosion rate intensity, mA/cm <sup>2</sup>   |
| $I_{corr}$    | : Corrosion rate, mA   |
| $k$           | : Shear coefficient  |
| $K$           | : Coefficient of gas permeability, m <sup>2</sup>  |
| $M$           | : Corrosion mass loss, g   |
| $L$           | : Specimen clear span, mm  |
| $L_f$         | : Fiber length, mm   |
| $n$           | : Valency  |
| $P$           | : Applied load, kN   |
| $p$           | : Absolute inlet pressure, Pa  |
| $p_a$         | : Atmospheric pressure, Pa   |
| $Q$           | : Volume flow rate of nitrogen, m <sup>3</sup> /s  |
| $R$           | : Gas constant (8.314 J/K.mol)   |
| $R_a$         | : Anodic polarization resistance, $\Omega$   |
| $R_c$         | : Cathodic polarization resistance, $\Omega$   |

$R_e$  : Concrete or electrolyte resistance,  $\Omega$   
 $R_p$  : Polarization resistance,  $\Omega$   
 $R_{st}$  : Steel resistance,  $\Omega$   
 $T$  : Average value of the initial and final temperatures in the anolyte solution, K  
 $U$  : Absolute value of the applied voltage, V  
 $U_e$  : Cell voltage, V  
 $V_f$  : Fiber volume fraction, %  
 $W$  : Warburg impedance,  $\Omega$   
 $x_d$  : Average value of the penetration depths, m

CH : Calcium hydroxide  $\text{Ca(OH)}_2$   
 DSF : Double-skin façade  
 ECC : Engineered cementitious composite  
 FA : Fly ash  
 FRM : Fiber reinforced mortar  
 GFRP : Glass fiber-reinforced polymer  
 HPC : High performance concrete  
 HPRCC : High performance fiber-reinforced cementitious composite  
 HP-G-HyFRC : High-performance green hybrid fiber-reinforced concrete  
 HyFRC : Hybrid fiber-reinforced concrete  
 ICP : Inductively coupled plasma  
 ITZ : Interfacial transitional zone  
 LCA : Life cycle assessment  
 NSC : Normal strength concrete  
 PVA : Polyvinyl alcohol  
 SCC : Self-consolidating concrete  
 SC-HyFRC : Self-consolidating hybrid fiber-reinforced concrete  
 SEM : Scanning electron microscopy  
 SP : Superplasticizer  
 SF : Silica fume  
 TGA : Thermal gravimetric analysis  
 VMA : Viscosity modifying admixture



# Acknowledgement

Many people deserve recognition and gratitude for their support and contribution to the research. First and foremost, I would like to thank my research advisor, Prof. Claudia Ostertag, for providing financial support during my studies. Her expertise and enthusiasm in the field of fiber reinforced concrete, concrete durability and sustainability have been instrumental in defining the scope and progress of the research. Her care, understanding and motherly concern about our general welfare enabled us to have frank and productive discussions about both research, academic life and professional goals. I cannot imagine how difficult the PhD life would have been without her wise and articulate guidance.

I also owe greatly to Prof. Paulo Monteiro, Prof. Arpad Horvath, Prof. Thomas Devine and Prof. Gail Brager who served as the committee in charge of the preliminary exam. Their advice and valuable comments help to orientate and streamline the focus of the research. Prof. Paulo Monteiro and Prof. Thomas Devine also served in the dissertation committee. Their feedback and comments are critical in shaping the report.

I would also like to thank my colleague Mr. Gabe Jen for constructive advice, discussion on many aspects of my research, guidance and help with sample preparations and experimental setups. Many thanks to technicians/engineers Lev Stepanov, Timothy Teague, Andrew Yang, Paul D. Brooks, Cruz Carlos, Matt Cataleta, Jeff Higginbotham, Phil Wong, Mick Franssen and Jesse Lopez for their kind and relentless assistance with laboratory work and testing. Additional thanks also go to Mr. Will Trono, Mr. Will Nguyen, Mr. Alexandra Lin, Mr. Ishihara Yosuke and Mr. Kevin Kim for their help with concrete mixing and sample preparation; Mr. Kevin Ahn for his assistance with TGA/DTA; and Ms. Petek Gursel for sharing the Greenconcrete LCA Web Tool. They either have graduated or are currently undergraduate and graduate students at UC Berkeley. I am also thankful to many other Cambodian, international and local friends for the good times we have together. I cannot imagine how tough and stressful my PhD life would be without them.

# 1 Introduction

## 1.1 Concrete structures and environmental impact

Construction and building industries consumes energy and emits a tremendous amount of CO<sub>2</sub> into the atmosphere. Cement used as the main binder in concrete is energy-intensive to produce and as a result contributes significantly to global greenhouse gas emission. One tonne of cement produces approximately 900 kg of CO<sub>2</sub> (Mahasenan et al., 2003). With global cement production (blended and unblended) of 3.6 billion tonnes in 2011 (van Oss, 2013) and with an assumed clinker proportion of 75%, cement industry represents about 2.4 billion tonnes or 7% of the 34.5 billion-tonne total anthropogenic CO<sub>2</sub> emission from fossil fuel use and cement production (Olivier et al., 2013). The number will be more significant if we look at concrete industry as a whole. Typical concrete contains 12% cement, 8% mixing water and 80% aggregate by mass (Mehta, 2002). This means that in addition to cement, concrete industry also consumes 2 billion tonnes of mixing water and 20 billion tonnes of aggregates annually, leading to more CO<sub>2</sub> emission into the atmosphere. This makes concrete industry one of the world's largest consumers of natural resources.

During construction, additional energy will also be required. The energy mainly arises from production, transportation and placement of concrete. When the construction of civil infrastructure is completed, the system will also require more energy to operate and to maintain. The distribution of the energy will depend on the nature and function of the system. For instance, in buildings most of the energy is consumed during operation. The building sector globally accounts for 30% of annual greenhouse gas emissions and 40% of total primary energy use (UNEP Sustainable Buildings & Climate Initiative, 2009). In the US, buildings account for about 40% of the total primary energy use of which about 50% is spent on heating and cooling (US Department of Energy). The sector's contribution to the country's carbon dioxide emissions increased from 33% in 1980 to 40% in 2011. On the other hand, more energy and resources are consumed during the maintenance phase for infrastructure, which is also translated to addition environmental impact and cost. According to a recent assessment study by the American Society of Civil Engineers (ASCE), America's infrastructure was classified as in poor condition and was given a D+ grade, meaning that it is mostly below standard with many elements approaching the end of their service life (America Society of Civil Engineers (ASCE), 2013). It was also estimated that a total of \$930 billion will be needed in the next 5 years to bring the nation's bridges and roads up to a good condition (America Society of Civil Engineers (ASCE), March, 2009). This represents about 5.5% of gross domestic product (GDP) recently estimated to be about \$16,768 billion (The World Bank, 2014).

From concrete materials engineering standpoint, a holistic approach is needed to deal with the issues of energy consumption, CO<sub>2</sub> emission and high cost related to construction industry. The approach needs a multidisciplinary consideration to address the three distinguished yet reinforcing dimensions of sustainability: society, economy and the environment (United Nations, 1987). These three factors are inherently attached to the different stages of concrete structure's life cycle. For infrastructure, a reduction in cement use in concrete will lower the environmental impact of the material. At the same time, a more durable concrete will require less maintenance during the usage stage. This leads to less disruption to the daily activities of people, resulting in direct cost saving

and indirect benefits attributed to saving in time from traffic congestion and diversion. Citizens will have more time for family and leisure and this will improve their welfare.

## 1.2 A new design paradigm and framework

In construction, after the design stage, materials are produced to construct structures. The structures are then operated, maintained and demolished at the end of their life cycles. As such, sustainability design can no longer focus on only a single aspect of the process. This calls for a new paradigm shift which considers sustainability as part of the whole life cycle of structures encompassing materials development, production, construction, operation, maintenance and demolition. With regard to concrete for the building sector which is one of the focuses of this study, industrial wastes may be used to replace cement to reduce concrete's embodied energy. To save labor and reduce energy during concrete placement, a composite that can flow into place or need little vibration to consolidate is desired. The composite should also allow for flexibility and versatility for application in both structural and non-structural elements so that more efficient and economical systems can be achieved. At the same time, to reduce frequency of repair and maintenance, the composite should be able to resist both load-induced cracking and chemical attacks. With a system that may outlast the functionality of the building, the system may be constructed with modular units so that they can be individually recovered for reuse at the end of the building life. For sustainable concrete composite design, a sustainability framework based on building life cycle phases and their attributes is proposed and is illustrated in **Fig. 1.1**.

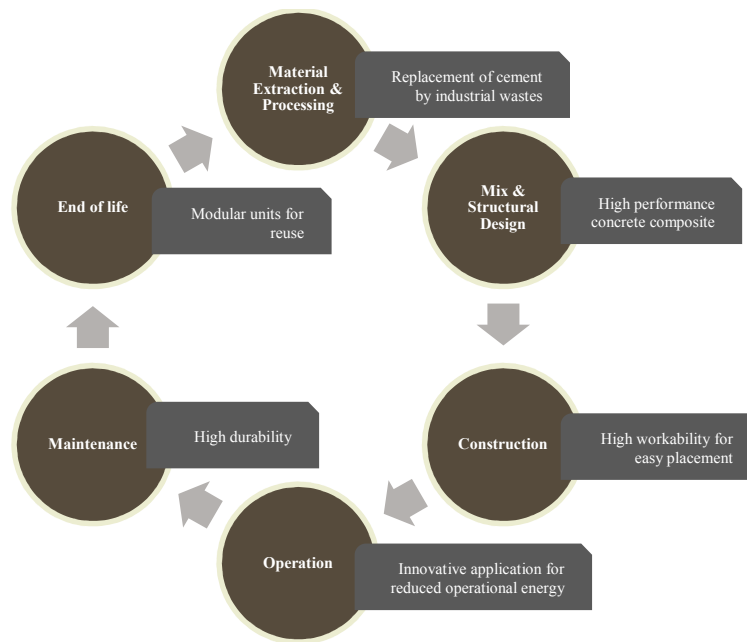


**Figure 1.1: Proposed framework for design consideration of concrete composite for sustainable and energy efficient buildings**

## 1.3 Required materials and engineering properties

As cement replacement, ground granulated blast furnace slag (GGBS or slag) and fly ash (FA) are the most widely used industrial waste products due to their availability, cost and ability to enhance concrete properties. Slag is a waste product from metallurgical processes where iron ore, limestone and coke are heated up to 1500 °C (Satish, 1997). The molten mixture consists of iron layer and

slag layer on top as a result of its lower density. The molten slag comprises mainly silicates, alumina and calcium oxide or lime (Siddique, 2008). The mixture may be rapidly quenched through high-pressure water jet to form slag granulates which will be later dried and ground to form ground granulated blast furnace slag (GGBS). Fly ash, on the other hand, is a residue derived from the combustion of pulverized coal in thermal power plants (Satish, 1997). It is generally collected through electrostatic precipitation method from exhaust gases. The physical and chemical characteristics of fly ash vary depending on the combustion operation system and original compositions of coal. Fly ash particles are mostly spherical and some are hollow due to an enclosing of air pockets during the liquid-to-solid formation.

During construction, fresh concrete needs to be pumped, vibrated and levelled off. The process is generally labor and equipment-intensive, leading to additional cost and energy consumption. A type of concrete called self-consolidating concrete (SCC) is a good candidate to remedy this problem. It is defined as a highly workable concrete that can spread and consolidate into place under its own weight without vibration and defects arising from segregation and bleeding (Khayat, 1999). The use of SCC provides various benefits including faster rate of placement, improved finishing, improved concrete consolidation and filling in congested regions, labor savings, faster construction speed (National Ready Mixed Concrete Association (NRMCA), 2004), prevention of noise pollution, and body strain to workers (De Schutter et al., 2008). If an SCC also exhibits high strength, high durability and dimensional stability, it can be classified as high performance concrete (HPC) (Mehta & Aitcin, 1990). The high strength property is useful for precasting and tall building applications (Mehta & Monteiro, 2006).

However, one problem with high strength concrete is its reduced effective fracture process zone and high brittleness (Gettu et al., 1990). This means that high strength concrete is susceptible to crack propagation under loading. Addition of steel fibers into the matrix helps to improve concrete compressive strength, splitting tensile strength, modulus of rupture and index of toughness (Song & Hwang, 2004). A relatively new type of fiber-reinforced concrete (FRC) called high performance fiber reinforced cementitious composites (HPFRCC) exhibits either strain or deflection hardening after the first crack formation (Naaman, 2003). Strain hardening is defined as an increase in stress with increasing strain accompanied by multiple cracking of members in direct tension (Naaman, 2007). The difference between strain softening and hardening is depicted in **Fig. 1.2**. As observed, stress suddenly dropped in strain softening composite after the onset of the first crack. This coincides with strain localization and single crack formation before failure. On the other hand, stress continues to increase in HPFRCC with strain hardening. Increasing load carrying capacity of HPFRCC after the first crack formation enhances its crack distribution, fracture toughness and impact resistance. The crack resistance and multiple cracking formation ensure that the embedded steel rebars or fibers themselves are protected from corrosive environment and this has an important implication for durability of the composite. Hence, HPFRCC or other concrete composites with similar properties contribute to both easy construction, superior mechanical and durability properties.

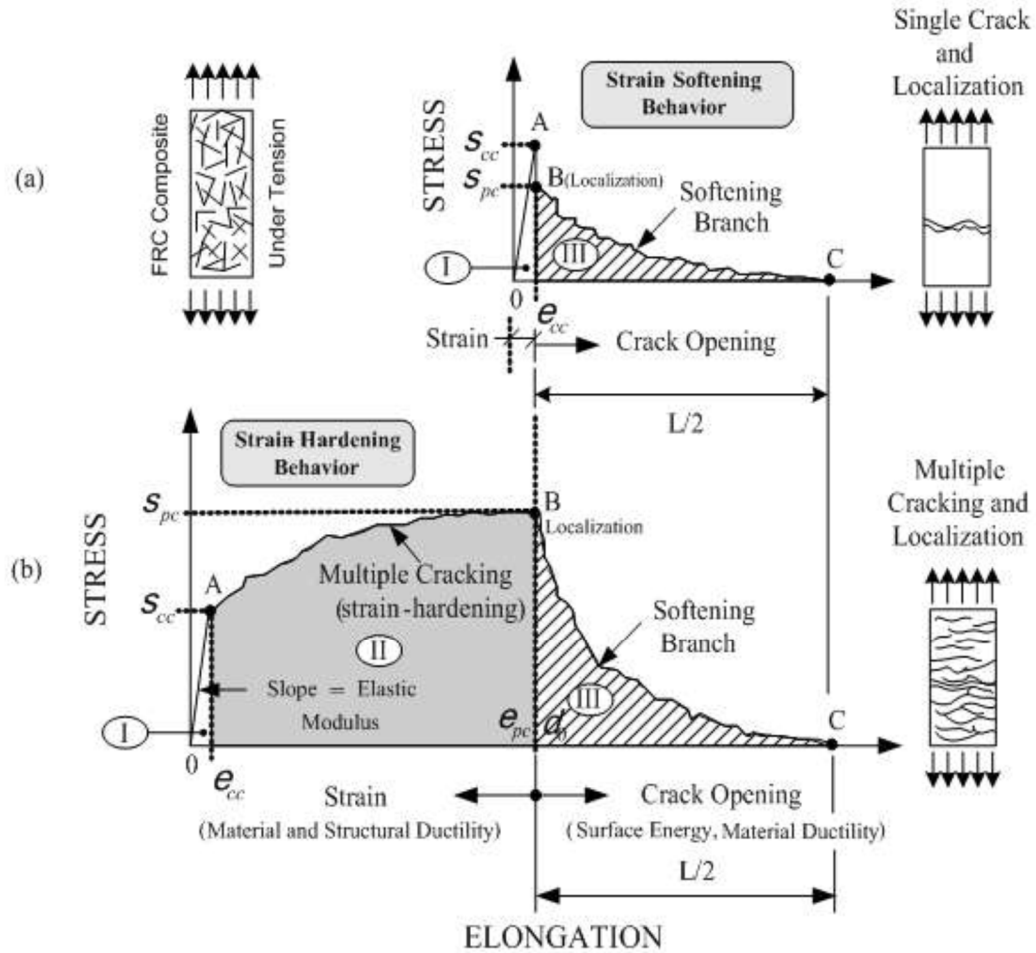


**Figure 1.2: Typical stress-strain response of FRC in tension: (a) strain-softening behavior, (b) strain-hardening behavior (Naaman, 2007)**

Replacement of cement by supplementary cementitious materials (SCMs) such as slag and fly ash at low volume fractions have been known to improve concrete mechanical and durability properties. However, their benefits at high volume fractions are still debatable and were found to depend on various parameters such as the chemical and physical properties of the SCMs, water-binder ratio and curing regimes. In an earlier study where concrete mixes were designed to match 28-day compressive strengths, comparable performance with regards to modulus of elasticity, drying shrinkage, creep, and freeze-thaw durability was found for concrete with and without integration of high-volume fly ash (Langley et al., 1989). For pastes with water-binder ratio of 0.55 and fly ash replacement levels of up to 67%, enhanced chloride binding ability was observed due to increased formation of Friedel's salt (Dhir et al., 1997; Dhir & Jones, 1999). However, other researchers found seemingly contradictory results. Total porosity in paste of cement blended with ordinary fly ash was found to be higher than that in OPC paste (Chindaprasirt et al., 2005). For 7-day moist curing, the total chloride content and total charge passed were found to be higher in concrete with 50% fly ash replacement level as compared to the values found in concrete with plain OPC (Kayali & Sharfuddin Ahmed, 2012). High volume slag replacement was found to increase autogenous shrinkage in concrete mixes with maintained or similar volume of binder (Lee et al., 2006; Lim & Wee, 2000) and to reduce deicer-salt scaling resistance (Talbot et al., 2000).

More detailed discussion on the effects of slag on concrete durability will be given in **Chapter 4**. The use of fibers in concrete is expected to counteract many of the possible disadvantages of supplementary cementitious materials at high volume fractions. However, the high cost of fibers with respect to other concrete constituents, the difficulty with placement of FRC and the huge variability in performance prevent a wide adoption of the composite for applications. To reverse the trend, there is a need to prove that FRC can be more cost efficient and more environmentally friendly during the structure's useful lifespan. For infrastructure case, it is required that the concrete composite be more durable against most commonly occurring deterioration problems such as corrosion and alkali-silica reaction, leading to less maintenance, repair and replacement. Also, for buildings where disruption from maintenance is not as significant, a composite with a high versatility should be used in area that can help to reduce the operational energy. These targeted uses and the resulting benefits can help to offset the initial high cost and high embodied energy of FRC.

## **1.4 Objectives**

The objective of the study is to develop a new high performance fiber reinforced cementitious composite (HPFRCC) that is green and of high performance for applications in infrastructure and buildings for sustainability. To achieve the goal, the following approaches were adopted:

- To develop an HPFRCC to meet a number of design criteria including high workability for easy placement and incorporation of slag and fly ash for reduction in the composite's embodied energy. The composite is to exhibit high compressive strength at all ages and deflection hardening after 28 days when mechanical loads are generally applied. High early strength is beneficial to construction as it allows for early formwork removal and precasting possibilities. Meanwhile, the hardening behavior is a prerequisite for multiple crack formation in concrete under flexure. The distribution of cracks limits the ingress of moisture and aggressive ions into the composite to ensure its high durability.
- To study the corrosion resistance of the new HPFRCC. Corrosion is one of the most commonly occurring durability problems in concrete structures. Hence, the study constitutes the sustainability assessment of the composite for infrastructure application.
- To understand the fundamentals and mechanisms behind the corrosion behavior of steel in concrete with supplementary cementitious materials and fibers. As such, the influence of supplementary cementitious materials, fibers, and interface qualities which are closely linked to concrete strength and consolidation on corrosion of steel in concrete will be studied.
- To propose an innovative application for buildings to reduce their operational energy by utilizing the high performance and versatility of the new HPFRCC. Life cycle assessment of the new system in comparison to the existing system will be conducted to assess their sustainability performances. This constitutes the sustainability assessment of the composite for building application.

## **1.5 Structure of the report**

The dissertation report is divided into 8 chapters. The chapters address different aspects of the topic and their short descriptions are given below.

- **Chapter 1** is this chapter and covers the motivations and defines the objectives of the study.
- **Chapter 2** covers the development process of a new HPFRCC termed high performance green hybrid fiber-reinforced concrete (HP-G-HyFRC) to meet a set of predefined fresh and hardened properties. Concepts used in the design, fresh and hardened properties of the composite will be detailed. Special characteristics of HP-G-HyFRC include the use of conventional materials—unlike other HPC whose materials usually need special processing—high workability, high strength, deflection hardening and corresponding distributed microcracks before the peak load is reached under flexure.
- **Chapter 3** outlines the durability assessment of HP-G-HyFRC with respect to its counterparts without fiber inclusion. Accelerated corrosion test was adopted and 4% NaCl of binder weight was used in the mixing water to destabilize steel passivity in concrete. In accelerated corrosion, current is applied on steel rebar in concrete to induce different levels of corrosion in a short period of time, imitating damages in propagation stage of natural corrosion. It was found that under no applied current, HP-G-HyFRC maintained the corrosion rates to within an inactive region throughout the measurement period of 98 days. Also, under applied current regimes, HPC without fibers were more susceptible to cracking under rebar corrosion due to their dense interface and poor ability to accommodate corrosion products. HP-G-HyFRC, on the other hand, exhibited multiple microcracking and managed to reduce corrosion rates by half as a result of passive confinement provided by fibers.
- Studies in **Chapters 4, 5 and 6** were implemented to further elucidate crucial phenomena observed in **Chapter 3** and to isolate the effects of slag, fibers and interface qualities on corrosion performance of steel in concrete. **Chapter 4** outlines the corrosion performance of medium-strength (32-45 MPa at 28 days) concrete with slag as cement replacement at 0%, 45% and 60% levels by mass. Accelerated corrosion method was adopted. Pore solutions of corresponding pastes and microstructural study of steel-concrete interfaces were also conducted. It was found that while there was little change to pH values, 60% slag as cement replacement initiated an early corrosion activity. Also, a higher corrosion mass loss and a denser matrix, possibly attributed to better particle packing, of concrete with slag caused an early cracking and more extensive damage.
- **Chapter 5** details the combined effects of fibers and slag on corrosion resistance of steel rebar in concrete. Replacement levels of cement by slag were 0%, 45% and 60% by mass. Fiber reinforcement was a hybridization of 1.3% steel macrofibers and 0.2% micro polyvinyl alcohol (PVA) fibers. Despite a higher gas permeability coefficients, hybrid fibers in concrete were found not to adversely affect corrosion initiation in concrete but significantly reduced corrosion rates during propagation stage. As compared to slag, fibers in the hybrid fiber reinforced concrete (HyFRC) were found to be a more dominant parameter in controlling corrosion behavior (rate and damage) of concrete in corrosion propagation stage.
- **Chapter 6** outlines the effects of interface qualities on corrosion initiation and propagation. Corrosion samples with three different steel-concrete interfaces: direct contact, a separation by a propriety polymer fiber-reinforced mortar (FRM), and a separation by filter paper, were constructed and their corrosion behaviors were examined under accelerated corrosion

tests. It was found that the more porous interface created by the FRM and the filter paper led to a higher corrosion activity in samples with no impressed current. However, an ability to accommodate more corrosion products and the resulting interfacial densification minimized damage to the concrete and reduced the subsequent corrosion rates. With regard to HP-G-HyFRC, this confirmed that a denser interface caused an early cracking to the surrounding matrix when fibers were not present. The confinement provided by fibers and the resulting densification of the interface led a slower corrosion activity.

- **Chapter 7** proposes an innovative application of HP-G-HyFRC for use in buildings to reduce operation energy. Double skin façade (DSF) made of 45 mm HP-G-HyFRC skins connected by glass fiber reinforced polymer (GFRP) is suggested for use in place of a conventional solid façade system used in Singapore. Singapore was adopted because of its typical tropical climate and hence would provide a conservative assessment of the benefits of the façade system. Life cycle assessment showed that the DSF with HP-G-HyFRC is more energy intensive and more costly to produce. However, the additional embodied energy can be recovered within the first year of operation while the additional cost can be paid back within 6 years of operation.
- **Chapter 8** provides concluding remarks and recommendations for future studies.



# **2 Performance-based design of high performance green hybrid fiber-reinforced concrete (HP-G-HyFRC)**

## **Summary**

A theoretical analysis and experimental investigation were conducted in the development of a new concrete composite termed high performance green hybrid fiber-reinforced concrete (HP-G-HyFRC) to meet a set of predefined fresh and hardened properties. Materials for conventional concrete were used as constituents of the new composite. Polyvinyl alcohol (PVA) micro and steel macrofibers were used as discontinuous reinforcement of the concrete composite. With water-binder ratio of 0.25, careful proportioning of the mix compositions produced a highly workable concrete composite. Hybridization of 1.5% steel fibers and 0.15% PVA fibers led to a smooth deflection hardening and formation of distributed microcracks up to yield strain of reinforcing steel bar. In addition to reducing the embodied energy of the composite, slag and fly ash used as cement replacement in the composite were shown to improve concrete workability, consolidation and deflection hardening behavior. The composite, however, showed a slight increase in permeability as compared to a similar mix without fiber inclusion although its effect on concrete durability performance was expected to be minimal.

## **2.1 Introduction**

High performance concrete (HPC) is defined as a composite with high strength, high dimensional stability (low creep and shrinkage), impermeability and high workability; all contributing to its high durability (Mehta & Aitcin, 1990). The composite has been widely used in bridge structures, offshore oil-drilling platforms (Mehta & Monteiro, 2006) and tall buildings (Breitenbücher, 1998). However, the enhanced strength makes the concrete more brittle and less resistant to crack growth under loadings. Cracks allow for ingress of moisture and aggressive ions into the composite and pose durability and serviceability problems during the lifetime of the structures. The addition of discontinuous fibers in concrete was found to improve its splitting tensile strength, modulus of rupture and toughness index (Song & Hwang, 2004; Wafa & Ashour, 1992; Yi & Ostertag, 2001). The uniform three-dimensional distribution of fibers makes them effective in load distribution. Also, either through crack arresting mechanism or mechanical confinement, the presence of fibers in concrete also enhances concrete resistance to two commonly occurring durability problems: reinforcement corrosion and alkali-silica reaction (Grubb et al., 2007; Jen & Ostertag, 2012; Ostertag et al., 2007; Turanli et al., 2001; Yi & Ostertag, 2005).

Studies have shown that a combined use of micro- and macrofibers allows for an enhanced mechanical performance of the concrete composite as compared to single fiber reinforcement (Banthia & Sappakittipakorn, 2007; Blunt & Ostertag, 2009; Walton & Majumdar, 1975; Yao et al., 2003). Microfibers act as micro reinforcement to control propagation and coalescence of microcracks which are inherent in concrete or formed during loading. As the cracks grow,

macrofibers such as steel fibers bridge the cracks to provide toughening mechanism. The synergy of the fibers allows for multi-level crack arresting mechanism and an improved composite performance at a relatively low fiber volume fraction as compared to other high-performance concretes reinforced with single type of fibers only. It was shown that the use of 1.3% steel macrofibers and 0.2% polyvinyl alcohol (PVA) microfibers in concrete allows for a deflection hardening response beyond the yield strain of steel (Blunt & Ostertag, 2009). Deflection hardening which is defined as an ability of the composite to carry increasing load after the first crack is formed coincides with the formation of distributed microcracks. Microcracks prevent the ingress of moisture and aggressive ions into concrete and hence improve concrete durability. Also, microcrack formation enhances the composite's serviceability by sustaining its stiffness (Ostertag & Blunt, 2008).

High performance fiber-reinforced concrete combines the benefits of both high strength concrete and fiber-reinforced concrete. However, fibers greatly reduce concrete workability (Hughes & Fattuhi, 1976). Dhonde et al. (Dhonde et al., 2007) showed that slump flow, passing ability and filling ability of fiber reinforced concrete generally decrease with increasing fiber factor which is defined as the product of the fiber's aspect ratio and its volume fraction. This is disadvantageous for a concrete composite containing microfibers as their aspect ratios can be several magnitudes greater than those for macrofibers. This study will address the issue by synthesizing empirical and analytical results from past research to optimally develop a new concrete composite to achieve high workability, high strength and deflection hardening. Hybrid polyvinyl alcohol (PVA) and hooked-end steel fibers were used as discontinuous reinforcement of the composite. Fibers were optimized for both workability and deflection hardening characteristic through iterative trials. Conventional coarse aggregates were used along with fine aggregates to limit shrinkage and creep, and to maintain the composite's modulus of elasticity. Greening of the composite was achieved through high-volume replacement of cement by slag and fly ash, leading the authors to call the composite high performance green hybrid fiber-reinforced concrete (HP-G-HyFRC). Gas permeability and chloride migration coefficients were also found as a preliminary indicator of the composite's durability.

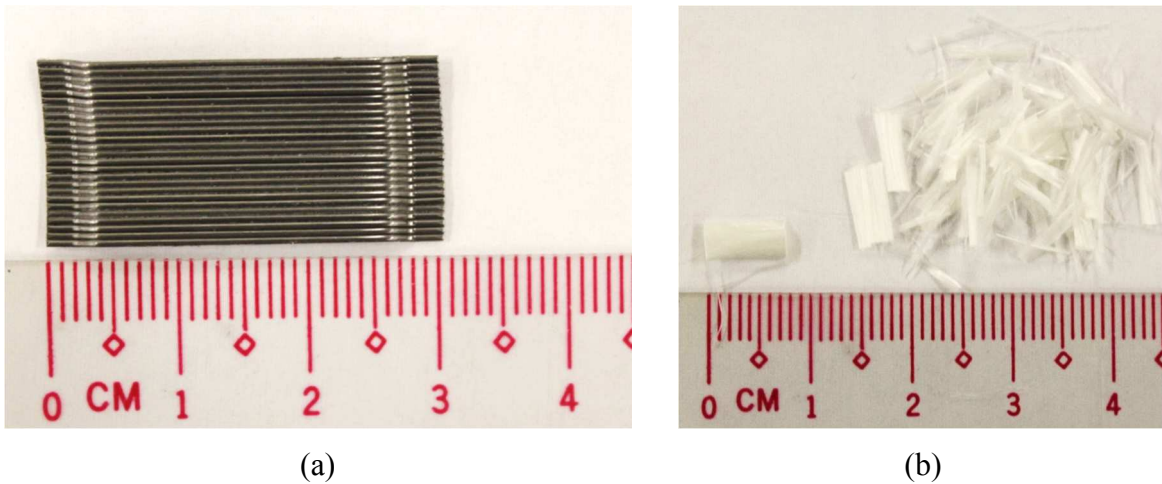
## 2.2 Materials and methods

### 2.2.1 Materials

ASTM Type II cement was used as the main binder. Slag and fly ash were also used as cement replacement. Their chemical compositions based on X-ray fluorescence (XRF) analysis and normalized to 100% are given in **Table 2.1**. Sulfur trioxide (SO<sub>3</sub>) was not listed in the table as it could not be accurately quantified in the XRF analysis due to its volatility during high temperature fusions implemented in sample preparation. Aggregates were composed of pea gravel with a maximum size of 10 mm and fine sand with a measured fineness modulus of 3.2. The hybrid fiber mixture contains a combination of 30 mm steel macrofibers and 8 mm PVA microfibers (**Fig. 2.1**). As compared to the cheaper polypropylene and polyethylene fibers, PVA fibers have a number of advantages including higher strength and stiffness (ACI Committee 544, 2010), and good chemical bond with the surrounding matrix because of its hydrophilic nature (Li et al., 2001). Properties of the fibers are summarized in **Table 2.2**.

**Table 2.1: Compositions of cement, slag and fly ash**

|                                | Cement (%) | Slag (%) | Fly ash (%) |
|--------------------------------|------------|----------|-------------|
| SiO <sub>2</sub>               | 21.80      | 33.47    | 62.43       |
| TiO <sub>2</sub>               | 0.24       | 1.33     | 1.002       |
| Al <sub>2</sub> O <sub>3</sub> | 3.91       | 15.07    | 17.36       |
| FeO                            | 3.30       | 0.37     | 4.41        |
| MnO                            | 0.06       | 0.24     | 0.046       |
| MgO                            | 4.43       | 9.06     | 2.27        |
| CaO                            | 65.37      | 39.45    | 7.31        |
| Na <sub>2</sub> O              | 0.23       | 0.38     | 3.45        |
| K <sub>2</sub> O               | 0.57       | 0.61     | 1.27        |
| P <sub>2</sub> O <sub>5</sub>  | 0.09       | 0.01     | 0.462       |
| SO <sub>3</sub>                | -          | -        | -           |

**Figure 2.1: Fibers used in the study: (a) 30 mm hooked-end steel fibers, and (b) PVA microfibers****Table 2.2: Fiber properties**

| Fiber designation | Fiber material | Fiber length (mm) | Fiber diameter (mm) | Fiber tensile strength (MPa) | Young modulus (GPa) |
|-------------------|----------------|-------------------|---------------------|------------------------------|---------------------|
| PVA fiber         | PVA            | 8                 | 0.038               | 1600                         | 40                  |
| 30 mm steel fiber | Steel          | 30                | 0.55                | 1350                         | 210                 |

### 2.2.2 Concrete mixing and slump flow test

In the mixing process, fine aggregates and binders were first mixed together. Coarse aggregates were then added. This was followed by addition of water premixed with SP and VMA. When the mixture became homogenous, steel fibers were added. The mixing continued until all the steel fibers became well dispersed. PVA fibers were then slowly added into the mix. The dispersion of PVA fibers can be preliminarily checked by extracting a small quantity of mortar from the mix and looking at it under fluorescent light. A mortar lump with fibrous boundary can be observed if

the PVA fibers are well dispersed. Slump flow was used to characterize the workability of the fresh trial mixes. The slump flow measurement was based on a procedure outlined in ASTM C1611 (American Society for Testing and Materials (ASTM), 2010c). The fresh concrete mix was placed in one lift into a frustum of a cone with base 200 mm in diameter, top 100 mm in diameter, and height 300 mm. The concrete was struck off at the level of the mold which was then raised to allow for the fresh concrete to spread. After spreading ceased, the maximum diameter and the diameter in its orthogonal direction were measured and their average value was taken as the slump flow. The slump's maximum height was also recorded to quantify its levelness and homogeneity. The spreads were also observed for signs of segregation and bleeding.

### 2.2.3 Specimens

Three 75 x 75 x 280 mm beams and three 100 x 200 mm cylinders were prepared for each trial mix. The samples were cured in moist room at 24 °C for 28 days before tested for their mechanical properties. Additional 15 cylinders were cast and moist-cured for the final mix to study their strength development at 3, 7, 14, 28 and 56 days. Cylinders of size 100 x 200 mm were also prepared to study the influence of fibers and supplementary cementitious materials (SCMs) on gas permeability coefficients which were used as an indication of durability. For gas permeability test, three different mixes were studied: final mix design for HP-G-HyFRC, corresponding high performance concrete without fibers but with 45% slag and 15% fly ash as cement replacement (HPC-60R), and HPC without fibers and SCMs (HPC-0R). A total of three 100 x 200 mm cylinders were produced for each mix. During the casting, to eliminate entrapped macro voids, the samples were consolidated by lightly hitting the sides of the molds with rubberized hammer. The samples were cured at 24 °C under 100% RH for 28, 56 and 90 days. After curing and left to dry in air for at least 28 days, the samples were sliced into 50 mm segments and oven dried at 110 °C until constant weights were achieved. The slices were cooled in vacuum to room temperature for 24 hours before the gas permeability test was conducted. Some of the selected samples were also used in chloride migration test.

### 2.2.4 Flexural test setup

ASTM C469 (American Society for Testing and Materials (ASTM), 2010a) was followed to find the elastic modulus of the cylindrical samples. The samples were capped with capping compound to ensure levelness of the top and bottom surfaces before testing. They were then loaded and unloaded twice up to 40% of their expected ultimate strength before loaded to failure during the third loading. The modulus of elasticity is the average of the slope values of the linear portions from the last two load-deformation curves. Four point loading method of simple beams following ASTM C1609 (American Society for Testing and Materials (ASTM), 2010b) was used to find flexural characteristics of the beam specimens. The flexural test apparatus consisted of a four-point bending jig with pin and roller-type supports at 225 mm spacing. The test setup is depicted in **Fig. 2.2**. The maximum stress experienced by the beam was calculated based on the following relationship

$$\sigma = PL / bd^2 \quad (2.1)$$

where  $\sigma$  is stress,  $P$  is applied load,  $L$  is span length,  $b$  is average specimen width, and  $d$  is average specimen height.



**Figure 2.2: Flexural test setup**

### **2.2.5 Gas permeability test**

Gas permeability test was conducted based on recommendations by Kollek (1989). Nitrogen gas with dynamic viscosity of  $1.75 \times 10^{-5}$  N-s/m<sup>2</sup> was used as the permeating medium. As the permeator cell was built for 200 mm diameter samples, polyurethane rubber collar was used as a fitting between the sample and a rubber tube which was pressured to 0.82 MPa. The diagram of the permeator cell with the fitting collar is shown in **Fig. 2.3** and the setup of the gas permeability test is elaborated in **Fig. 2.4**. Three absolute pressure stages of 0.15 MPa, 0.2 MPa and 0.3 MPa were applied. The gas flow volumes were adjusted such that the flow times were greater than 20 seconds. The flow times at each pressure level were recorded and were assumed to be at steady state when two successive readings at least 3 minutes apart were different by less than 3%. The coefficient of gas permeability  $K$  (m<sup>2</sup>) at each pressure level was calculated based on **Eq. 2.2** (Kollek, 1989; Rilem, 1999). The overall coefficient was taken as the mean of the values at the three pressure levels.

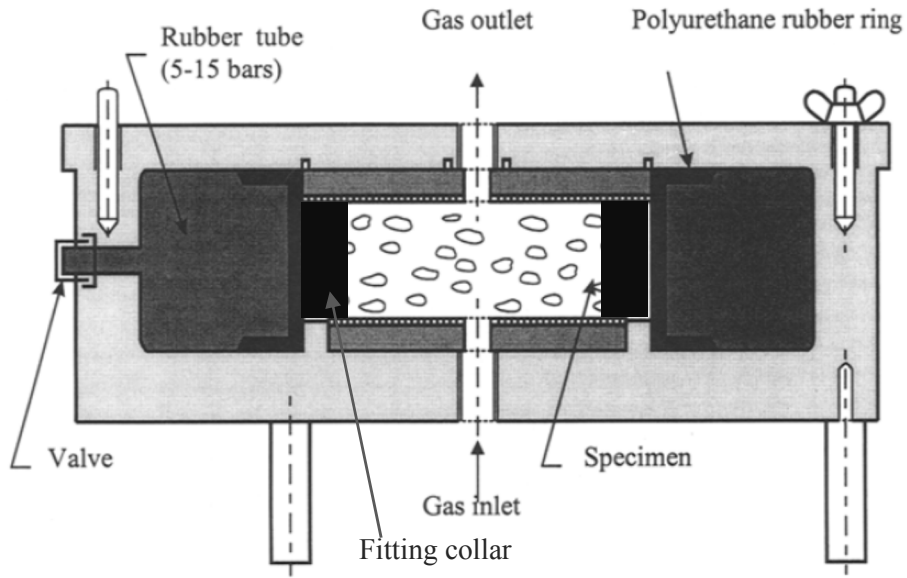


**Figure 2.3: Permeator cell (Rilem, 1999)**

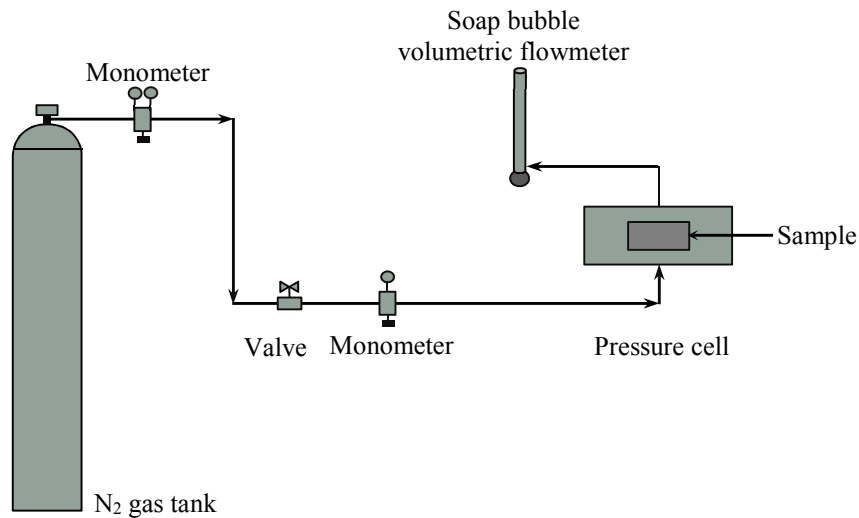


**Figure 2.4: Schematic diagram for gas permeability test setup (Celik et al., 2014)**

$$K = \frac{2Qp_0d\eta}{A(p^2 - p_a^2)} \quad (2.2)$$

where  $Q$  is volume flow rate of nitrogen gas ( $\text{m}^3/\text{s}$ ),  $A$  is cross-sectional area of the specimen ( $\text{m}^2$ ),  $d$  is thickness of the specimen in the flow direction (m),  $\eta$  is dynamic viscosity of the fluid at test temperature ( $\text{N s m}^{-2}$ ),  $p$  is absolute inlet pressure (Pa), and  $p_a$  is atmospheric pressure (Pa).

### 2.2.6 Chloride migration test

The middle samples prepared for air permeability test were also used for non-steady state chloride ( $\text{Cl}^-$ ) migration test according to Nordtest method (NORDTEST NT BUILD 492, 1999). The same specimens were selected to see if there is a relationship between air permeability and  $\text{Cl}^-$  migration

coefficients. In preparation for the test, the middle 50 mm-thick concrete elements were vacuumed for three hours in a desiccator before saturated  $\text{Ca}(\text{OH})_2$  solution was poured in and the vacuum was maintained for another hour. The air was then allowed to re-enter and the specimens were kept in the solution for additional  $18 \pm 2$  hours. The samples were dapped surface-dry and clamped in between two compartment cells, one filled with 0.3 N NaOH solution and the other with 10% NaCl solution ( $\text{Cl}^-$  concentration of about 2 N). The test setup is depicted in **Fig. 2.5**. Two electrical wirings were connected from the cells to a feedback system so that a recommended voltage between the two cells could be applied. Thermocouple was also connected to the NaCl cell to record temperature variation.

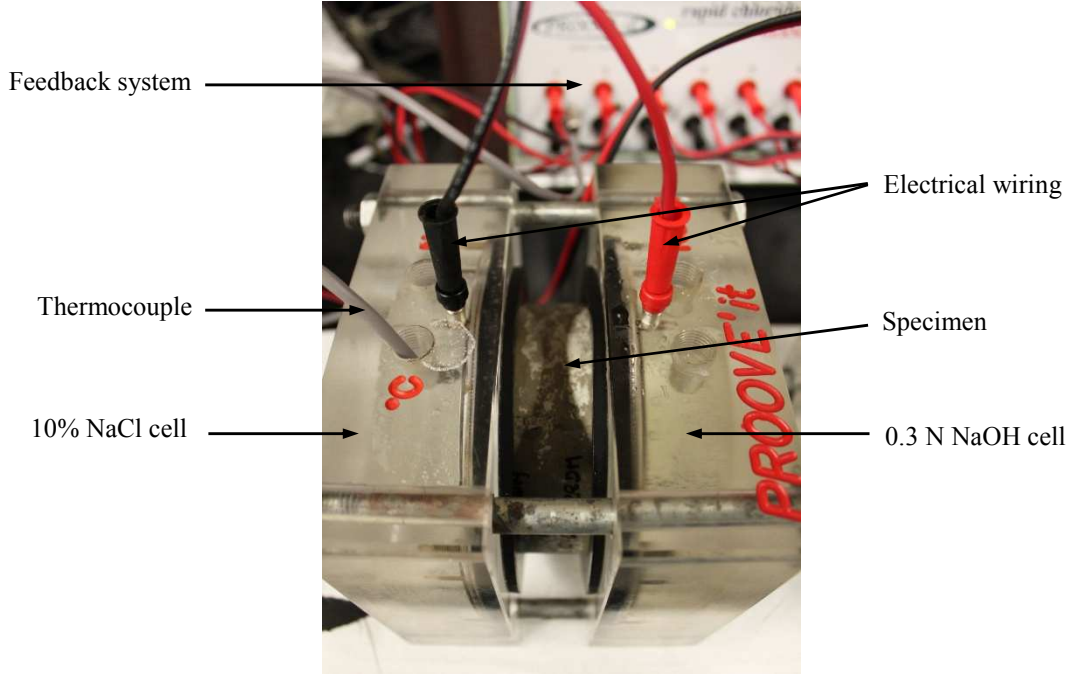


**Figure 2.5: Test setup for non-steady state  $\text{Cl}^-$  migration test**

After an appropriate test duration, the specimens were disassembled and split axially into two pieces. Silver nitrate solution of 0.1 M was sprayed onto one of the freshly split sections for measurement of  $\text{Cl}^-$  penetration depth. From the test results,  $\text{Cl}^-$  migration coefficients which are a measure of concrete resistance to  $\text{Cl}^-$  penetration could be determined according to **Eq. 2.3**.

$$D_{nssm} = \frac{RTh}{nF(U-2)} \cdot \frac{x_d - 2\sqrt{\frac{RTh}{nF(U-2)}x_d} \cdot \text{erf}^{-1}\left(1 - \frac{2c_d}{c_0}\right)}{t} \quad (2.3)$$

where  $D_{nssm}$  is non-steady-state migration coefficient ( $\text{m}^2/\text{s}$ );  $n$  is absolute value of ion valence, for chloride ( $z = 1$ ),  $F$  is Faraday's constant ( $9.648 \times 10^4 \text{ J/V}\cdot\text{mol}$ ),  $U$  is absolute value of the applied voltage (V),  $R$  is gas constant ( $8.314 \text{ J/K}\cdot\text{mol}$ ),  $T$  is average value of the initial and final temperatures in the anolyte solution (K),  $h$  is thickness/height of the specimen (m),  $x_d$  is average value of the penetration depths (m),  $t$  is test duration (seconds),  $\text{erf}^{-1}$  is inverse of error function,  $c_d$  is chloride concentration at which the color changes (0.07 N for OPC concrete), and  $c_0$  is

chloride concentration in the catholyte solution. The mechanism of how  $\text{AgNO}_3$  can be used as color indicator of  $\text{Cl}^-$  penetration into concrete will be elaborated in the next chapter.

## **2.3 Analytical procedure**

### **2.3.1 Design criteria**

A performance-based design criterion was adopted and focused on both fresh and hardened concrete properties. For fresh concrete, the goal was to obtain a minimum required slump flow of 500 mm in diameter. This is the lower slump limit that distinguishes self-consolidating concrete (SCC) from non-SCC (National Ready Mixed Concrete Association (NRMCA), 2004). For hardened concrete, a 28-day cylindrical compression strength greater than 70 MPa and a smooth deflection hardening characteristic were desired. The high strength is intended for a broad application of the composite such as structural elements in infrastructure systems and tall buildings or high-performance façade elements. The high 28-day strength target also means early strength development. This opens up the possibility of using the composite in precasting where a fast turnover is required. It is also required that deflection hardening continues beyond the yield strain  $\epsilon_y$  of 0.2% for conventional reinforcing bar to ensure microcrack formation up to the design capacities of the structural elements which are usually determined at the rebar yield strength.

### **2.3.2 Workability of fresh concrete**

In determining the proportions of the mix compositions for self-consolidation, a procedure recommended by Okamura (2003) is based upon: (i) the coarse aggregate volume is fixed to 50% of solid volume, (ii) sand content is fixed to 40% of mortar volume, (iii) water-powder ratio by volume is chosen between 0.9 and 1, and (iv) SP dosage and final water are determined to ensure self-compactibility. With this, the paste volume is approximated to be 43% of the total concrete volume. A paste volume between 43 to 46% was used in the trial mixes. Due to the presence of fibers, it is expected that the fine aggregate-coarse aggregate (FA/CA) ratio will have to be increased as studies have shown that increasing the amount of fine aggregate helps to improve the workability of fiber-reinforced concrete (Liao et al., 2007; Sahmaran et al., 2005). Also, where applicable, 15% of cement was replaced by fly ash because of its benefit in improving concrete workability through its lubricant effect (Peris Mora et al., 1993). The replacement level was limited to 15% to prevent a great reduction in the composite's compressive strength.

### **2.3.3 Mechanical properties of hardened concrete**

#### **2.3.3.1 Critical fiber volume**

Although concrete becomes more brittle with increasing compressive strength (Gettu et al., 1990), its fracture toughness tends to increase (Einsfeld & Velasco, 2006; Gettu et al., 1990). For a steady-state crack propagation in fiber-reinforced concrete (FRC), the matrix toughness must be less than the complementary energy which is proportional to the peak stress and corresponding deformation at the peak stress (Li et al., 2002). Hence, for a high-strength concrete composite with an increased fracture toughness, it is expected that the amount of fibers required for deflection hardening will be more as compared to that for a lower strength concrete composite. However, besides the matrix properties, fiber characteristic and interface phases also affect crack propagation and toughness of FRC. The fiber is characterized in terms of volume fraction  $V_f$ , fiber length  $L_f$ , diameter  $d_f$ ,



elastic modulus  $E_f$ , and tensile strength  $\sigma_{fu}$  (Li et al., 2001). The interface characteristic depends on physical and chemical adhesion between the fiber and the matrix, the mechanical component of bond arising from fiber geometry, fiber-to-fiber interlock or entanglement, and friction (Naaman & Najm, 1991). To achieve deflection hardening and to account for the interactions of these parameters, a formulation developed by Naaman (2003) using composite mechanics was adopted in our study. It is required that the flexural post-crack strength is at least equal or greater than the composite first cracking strength and the critical fiber volume is given by **Eq. 2.4** which was simplified from the original form through an introduction of a lumped parameter  $\Omega$ .

$$(V_f)_{critical-flexure} = \frac{1}{1 + \frac{\tau L_f}{\sigma_{mu} d_f} \Omega} \quad (2.4)$$

where  $\sigma_{mu}$  is tensile strength or modulus of rupture of the matrix under flexure as defined by **Eq. 2.5** (ACI Committee 363, 1997),  $\tau$  is average fiber-matrix bond strength within the composite,  $\Omega$  is a lumped constant that accounts for bond mobilization, expected pullout length ratio, group reduction factor of fibers and stress distribution.

$$\sigma_{mu} = 0.94\sqrt{f'_c} \quad (2.5)$$

The critical fiber volume fraction was found by back-calculating mix proportioning for a self-consolidating hybrid fiber reinforced concrete (SC-HyFRC) developed at UC Berkeley. The mix has a water-binder ratio of 0.45 and a total fiber volume fraction of 1.5% consisting of 1.3% of hooked-end steel macrofibers and 0.2% of PVA microfibers (Jen & Ostertag, 2012). The composite has an average 28-day cylindrical compressive strength of 42 MPa and exhibits a smooth load deflection curve under four-point bending. A number of assumptions were made. First, PVA fibers were assumed not to contribute to the composite modulus of rupture due to their relatively low volume fraction and their relatively low modulus of elasticity. Also, the modulus of rupture of concrete was found by **Eq. 2.5**. With these assumptions, the theoretical modulus of rupture of the HP-G-HyFRC matrix was approximated to increase by a factor of 1.3 as compared to that for SC-HyFRC matrix. This is due to an increase in compressive strength of HP-G-HyFRC from 42 MPa to the target 70 MPa.

The next main parameter to be used in **Eq. 2.4** is the average fiber-matrix bond  $\tau$ . Immediately at the onset of the matrix's first crack, the slip of the bridging fibers is small and at this stage the bridging capacity is expected to be provided by only the adhesion bond of the steel fibers with the matrix. The adhesion bond comprises physical and chemical bond and hence the bond is higher for hooked-end steel fibers due to their enhanced physical bond. Typical bond-slip curves for straight and hooked-end fibers are given in **Fig. 2.6**. For a single-fiber pullout, the adhesion strength coincides with the start of the descending branch of a bond-slip curve for straight fibers or the decrease in slope for hooked-end fibers. The reduction in slope is attributed to a partial straightening of the hooked ends (Naaman & Najm, 1991). Markovich et al. (2001) more accurately attributed this portion of the pull-out curve to plastic deformations at the two kinks of the hooked-end fiber. The rebending of the second kink to follow the channel profile led to the formation of the second peak. A direct observation of hooked-end fibers embedded in epoxy resin conducted by Weiler & Grosse (1996) confirmed the mechanism.

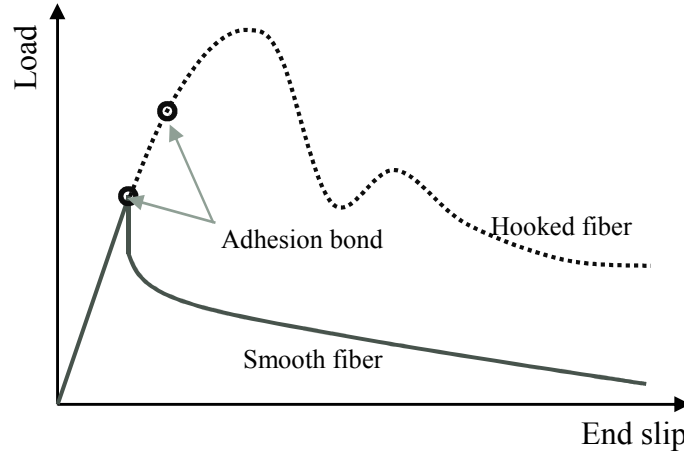


**Figure 2.6: Typical pullout curves for straight and hooked-end fibers (Markovich et al., 2001; Naaman & Najm, 1991)**

**Table 2.3: Critical fiber volume estimation**

| Inclination angle (degrees) | Fiber distribution (%) | Adhesion bond strength increase factor | SC-HyFRC  | HP-G-HyFRC  |
|-----------------------------|------------------------|--|---|---|
| 0                           | 0.8                    | 1                                      | $V_f = 1.3\%$<br>$\frac{\tau}{\sigma_{mu}} \frac{L_f}{d_f} \Omega = 75.9$ | $\frac{\tau}{\sigma_{mu}} \frac{L_f}{d_f} \Omega = 70.6$<br>$V_f = 1.4\%$ |
| 15                          | 4.5                    | 1                                      |   |   |
| 30                          | 15.3                   | 1                                      |   |   |
| 45                          | 28.2                   | 1.3                                    |   |   |
| 60                          | 28.8                   | 1.3                                    |   |   |
| 75                          | 16.5                   | 1.3                                    |   |   |
| 90                          | 5                      | 1.3                                    |   |   |
| Average                     |                        | 1.2                                    |   |   |

For micro-cracking formation in FRC, it is expected that only adhesion bond is mobilized before the formation of new cracks and it is this bond strength that should be utilized in the **Eq. 2.4**. A study conducted by Bantia and Trottier (1994) showed that for moderately deformed fibers such as hooked steel fibers, there is no influence of the matrix strength on the load at the breakage of the elastic or adhesion fiber-matrix bond due to a small bearing component of concrete. However, as the inclination angles of fibers increase, the bond-slip curves of fibers are generally controlled by spalling of concrete wedges at the fiber exits (Li et al., 1990). For this study, it is assumed that for fibers oriented greater than 30°, the adhesion bond is increased proportionally by the square root of compressive strength. With fiber distribution as outlined in a study by Laranjeira (2011) and with an orientation number of 0.7, the average bond strength was estimated to increase by a factor of 1.2, giving a critical fiber volume fraction of 1.4% for HP-G-HyFRC to meet **Eq. 2.4**. The analysis results is summarized in **Table 2.3**. Steel fiber volume fractions of 1.3%, 1.45%, 1.5% and 1.55% were adopted to study the validity of the assumptions and the effects of PVA fibers on concrete mechanical properties. The small variation in steel fiber volume fractions was to ensure that the fibers were optimized because of their high cost as a concrete constituent.

Although PVA fibers were not taken into consideration in the formulation, their effects on fresh and hardened concrete properties will be discussed in the results.

### 2.3.3.2 Checking criteria for deflection hardening

The steel yielding criterion was calculated based on a method outlined in a study by Blunt & Ostertag (2009). In the analysis of this paper, the average concrete elastic modulus  $E$  of 35 GPa based on compression results of trial mixes was adopted. As no direct tensile test was conducted on the trial mixes to assess their tensile strengths, an average matrix tensile strength value was assumed to be 7% of the average compressive strength (ACI Committee 224, 1997; Price, 1951). With coefficient of variation of 10% under good field control (Price, 1951), the tensile strength range for 99% confidence interval was estimated to be between 3.58 MPa and 6.06 MPa. Steel yield strain of 0.2% was used and the corresponding load range was calculate to be between 17.15 kN and 27.43 kN for beams with a cross section of 75 x 75 mm and clear span of 225 mm under third point loading. For a tri-linear curvature, the mid-span deflection attributed to flexure and shear was found by **Eq. 2.6** (Nguyen et al., 2013), giving the corresponding upper and lower deflection limits of 0.29 mm and 0.27 mm.

$$\delta_{midspan} = \frac{23\phi L^2}{216} \left[ 1 + \frac{36(1+\nu)}{23k} \left( \frac{d}{L} \right)^2 \right] \quad (2.6)$$

where  $\phi$  is mid-span curvature at steel-yield point,  $\nu$  is the Poisson's ratio ( $\nu = 0.2$ ),  $k$  is shear coefficient  $\left( k = \frac{10(1+\nu)}{12+11\nu} \right)$ ,  $L$  is clear span and  $d$  is section height.

## 2.4 Results

### 2.4.1 Mix designs

A summary of selected trial mixes are given in **Table 2.4**. Water-binder (W/B) ratio of 0.25 was maintained for all mixes. A parametric study was conducted to study the effects of coarse to fine aggregate ratio, volume fractions of fibers, and supplementary cementitious materials (SCMs) as cement replacement on concrete workability. In the naming convention, A is for aggregate, SF is for steel fibers, PF is for PVA fibers, S is for slag and F is for fly ash. The numbers following the group names for fibers and SCMs represent the volume fractions and mass replacement levels, respectively. For example, SF1.5 is a trial mix with steel fiber volume fraction of 1.5% while S45F15 is a trial mix with 45% slag and 15% fly ash as cement replacement by mass. In the first set of trial mixes (A), the contents of binder, admixtures and fibers were kept constant. The mass ratios of fine over coarse aggregates were 1.1 for A1 and 1.7 for A2. In the second group (SF), the adopted volume fractions of steel fibers were 1.45%, 1.5% and 1.55%. The group has PVA fibers of 0.15% by volume fraction. The third group (PF) contains PVA fiber volume fractions of 0% (PF0-a or PF0-b) and 0.25% (PF0.25). PF0-a and PF0-b were implemented to see if SP could be reduced without significantly affecting the fresh concrete workability. In the fourth group (SCMs), cement was replaced by either slag (45% by mass), fly ash (15% by mass), or a combination of both. A total binder of 762 kg/m<sup>3</sup> was used for S0F0 and 713 kg/m<sup>3</sup> for the rest of the trial mixes in the SCM group. The amount of cement was increased for S0F0 to ensure similar paste volume

as compared to other mixes in the SCM group. Paste volumes between 43% and 46% were applied to all mixes.

**Table 2.4: Mix proportions of trial mixes kg/m<sup>3</sup>**

| Mix Annotations   | Aggregate |      | Steel fibers |       |        | PVA fibers |       |        | SCMs |       |       |        |
|-------------------|-----------|------|--------------|-------|--------|------------|-------|--------|------|-------|-------|--------|
|                   | A1        | A2   | SF1.45       | SF1.5 | SF1.55 | PF0-a      | PF0-b | PF0.25 | S0F0 | S0F15 | S45F0 | S45F15 |
| W/B               | 0.25      | 0.25 | 0.25         | 0.25  | 0.25   | 0.25       | 0.25  | 0.25   | 0.25 | 0.25  | 0.25  | 0.25   |
| Water             | 153       | 153  | 162          | 162   | 162    | 162        | 165   | 162    | 175  | 163   | 163   | 163    |
| Cement            | 267       | 267  | 285          | 285   | 285    | 285        | 285   | 285    | 762  | 606   | 392   | 285    |
| Slag              | 301       | 301  | 321          | 321   | 321    | 321        | 321   | 321    | 0    | 0     | 321   | 321    |
| Fly ash           | 100       | 100  | 107          | 107   | 107    | 107        | 107   | 107    | 0    | 107   | 0     | 107    |
| Sand (FA)         | 751       | 916  | 868          | 868   | 868    | 868        | 868   | 868    | 868  | 894   | 888   | 868    |
| Gravel (CA)       | 683       | 528  | 505          | 505   | 505    | 505        | 505   | 505    | 505  | 520   | 516   | 505    |
| 30mm steel fibers | 103       | 103  | 113          | 117   | 122    | 117        | 117   | 117    | 117  | 117   | 117   | 117    |
| 8mm PVA           | 2.4       | 2.4  | 1.9          | 1.9   | 1.9    | 0          | 0     | 3.3    | 1.9  | 1.9   | 1.9   | 1.9    |
| SP <sup>†</sup>   | 10.5      | 10.5 | 11.8         | 11.8  | 12.3   | 11.8       | 8.5   | 11.8   | 11.2 | 11.1  | 10.5  | 10.5   |
| VMA <sup>‡</sup>  | 5.9       | 5.9  | 6.5          | 6.5   | 6.5    | 6.5        | 6.5   | 6.5    | 7    | 6.5   | 6.5   | 6.5    |

<sup>†</sup>L/m<sup>3</sup>

## 2.4.2 Fresh concrete properties

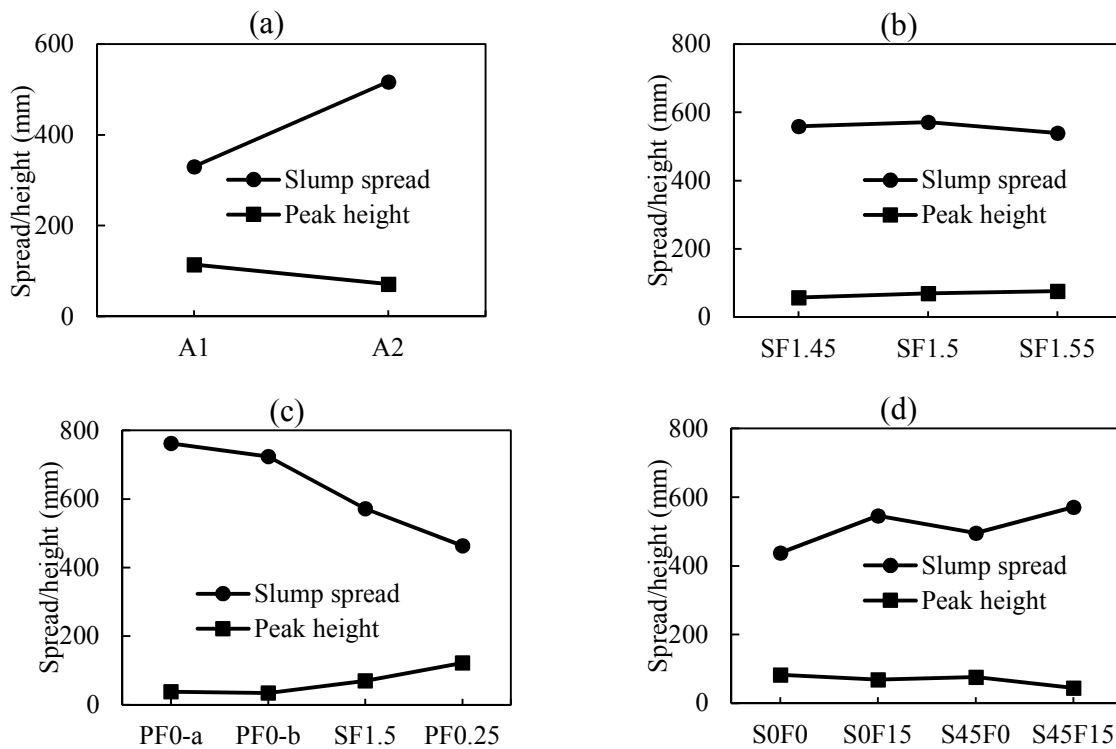


**Figure 2.7: Effects of concrete constituents on workability: (a) fine-coarse aggregate ratio, (b) steel fiber volume fractions, (c) PVA fiber volume fractions, and (d) SCMs**

The effects of aggregate ratios, fiber volume fractions and the presence of SCMs on concrete workability are summarized in Fig. 2.7. A1 with fine to coarse aggregate ratio close to the recommended value for conventional SCC as suggested by Okamura (2003) had very low spread diameter and failed to meet the SCC spread requirement. By increasing the amount of fine aggregate while maintaining the amount of SP, VMA and paste volume in A2, the spread diameter

greatly increased and a more uniform and cohesive mix with low peak height was achieved. Although A2 can be considered as SCC, the composite had steel fiber volume fraction of only 1.3% and did not meet the deflection hardening criteria. This will be discussed later. As a result, the volume fractions of steel fibers were increased in subsequent trial mixes.

The mix design was further optimized in SF group with fresh concrete property results as given in **Fig. 2.7 (b)**. It is observed that varying steel fiber volume fractions from 1.45% to 1.55% did not significantly affect the workability of the fresh concrete. The amount of SP for SF1.55 was slightly higher than that in SF1.45/1.5 although the small variation is not expected to change the workability significantly. The effects of PVA fibers on workability is shown in **Fig. 2.7 (c)**. SF1.5 with PVA fiber volume fraction of 0.15% is also shown in the plot. It is observed that as compared to steel fibers, change in PVA fiber volume fractions had a much greater effect on concrete workability and this is attributed to the higher aspect ratio of PVA fibers. Also, without PVA fibers, it is possible to maintain good workability with a lower SP amount as reflected in PF0-b trial mix.

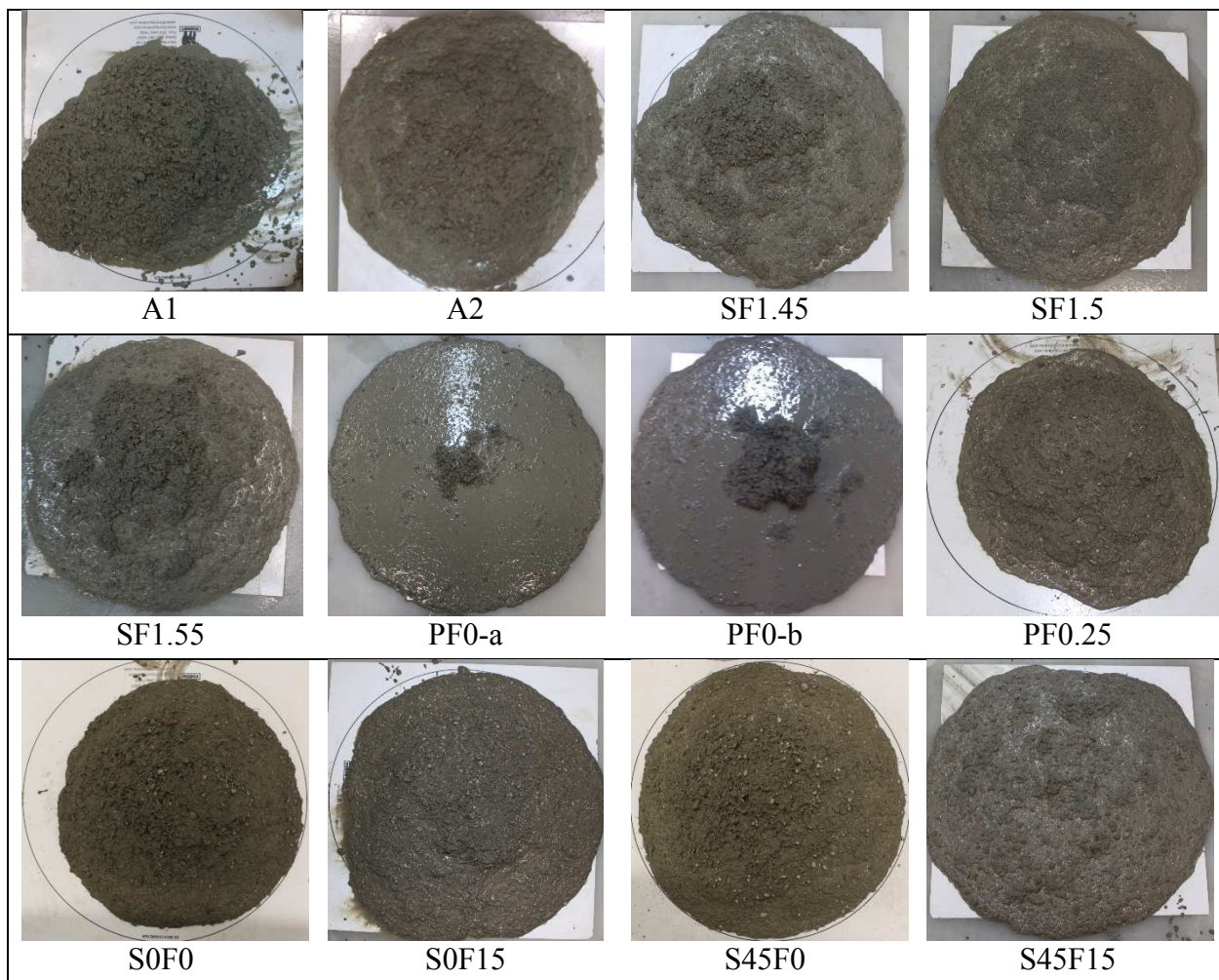


**Figure 2.8: Slump flow shapes for different trial mixes**

The effects of SCMs on workability were studied in SCMs set whose results are given in **Fig. 2.7 (d)**. It is observed that as compared to S0F0, replacing cement by 15% fly ash (S0F15) helped to improve concrete workability and uniformity even with similar levels SP, VMA and paste volume

as compared to other mixes. Replacement of cement by 45% slag slightly increased concrete workability. Also, the combined use of slag and fly ash in S45F15 further enhanced the fresh properties of the composite. This may be attributed to the lubrication effect of fly ash, improved particle packing and a smaller water absorption of slag on its surface. Although the size and shape distribution of fly ash was not quantified in this study, the fly ash was expected to have favorable fineness, size distribution and shape which are known factors to influence concrete workability (Peris Mora et al., 1993). This level of workability would not be achievable with cement only as binder as proven in S0F0. The shapes of slump spreads for all the trial mixes are given in **Fig. 2.8**. The uniformity of the spread correlated well with the slump flow values.

### 2.4.3 Compression test results

The 28-day average compressive strengths of selected trial mixes are shown in **Fig. 2.9**. It is observed that for the same W/B ratio and SCM replacement levels, slight variation in fiber volume fractions as in SF1.45, SF1.5 and SF1.55 did not affect the compressive strength results. Also, without the 45% slag replacement, S0F15 exhibited a 15% increase in compression strengths as compared to the average strength of other mixes with 45% slag and 15% fly ash as cement replacement. S0F0 without cement replacement by SCMs exhibited the highest compressive strength. This is attributable to the higher reactivity of cement as compared to slag and fly ash.

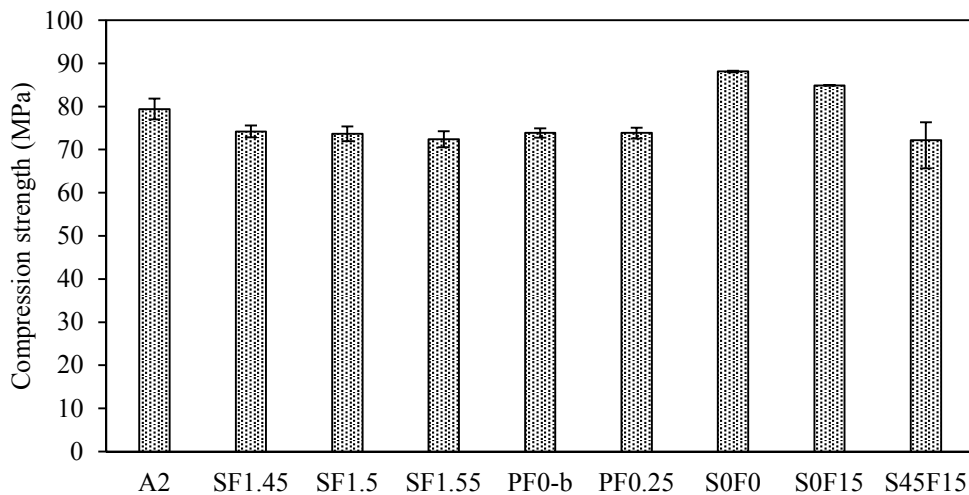


**Figure 2.9: 28-day compressive strengths of selected mixes**

### 2.4.4 Flexural test results

Flexural responses of the selected specimens from A (aggregate), SF (steel fibers) and PF (PVA fibers) groups are given in **Fig. 2.10**. Upper and lower limits for deflection hardening criteria from analytical analysis were also marked on the graph. It is required that the beam peak loads be greater than the upper load limit and that the hardening behavior extends beyond the maximum deflection limit found in the analytical section of the paper. Also, there should not be a sudden dip in load or sudden change in deformation up to the peak load to ensure that crack instability or formation of macrocrack is prevented. The results show that all presented trial mixes exhibited deflection hardening responses. However, A2 mix with 1.3% of steel fibers and 0.2% of PVA fibers did not

reach the upper load limit. Mix A2 also exhibited a crack instability after the first crack was formed. Mixes SF1.45 and SF1.5 with 1.45% and 1.5% of steel fibers, respectively, and 0.15% of PVA fibers met the upper limits for both load and deflection. It is also observed that the small variation in volume fractions of steel fibers did not significantly influence the flexural responses of the beams. The results confirm that the simplified analytical solution can be used to find the critical fiber volume fraction to ensure a smooth deflection hardening in beams under flexure. Interestingly, Mix PF0-b with 1.5% of steel fibers but no PVA fibers had a higher cracking and peak load as compared to other mixes with PVA fibers. This may be attributed to a better consolidation of the fresh PF0-b. It is noted that during concrete placement, all beams were compacted through external agitation with a rubberized hammer for 10 times on each face to release some entrapped macro air voids. Nevertheless, mix PF0-b shows instances of crack instability (sudden increase in deformation or decrease in load) along the hardening portion of its load-deflection curve. The drops were associated with an increase in crack opening due to an absence of PVA fibers in the mix. The results reflect the benefits of PVA fibers in bridging microcracks and in preventing unstable macrocrack formation before the peak load is reached. For a balance of both workability and superior softening-hardening behavior, a hybridization of 1.5% steel fibers and 0.15% PVA fibers was chosen for further study.

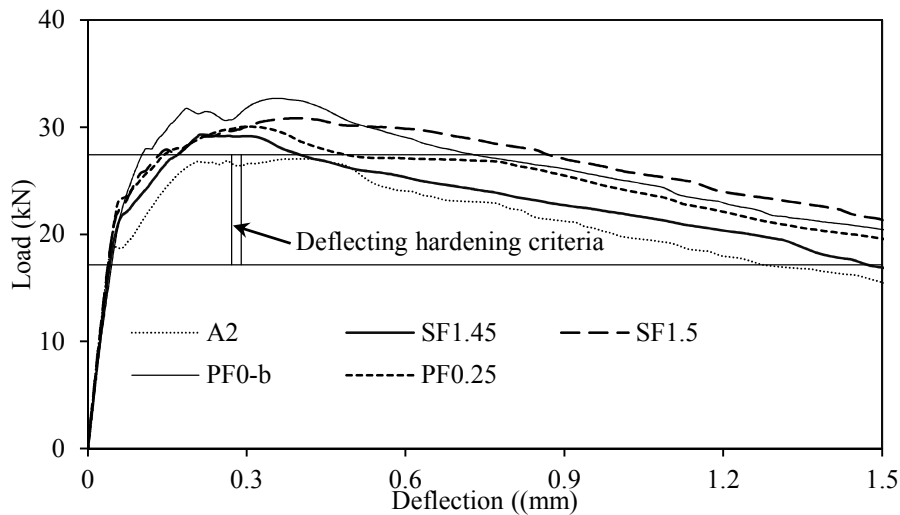


**Figure 2.10: Load-deflection curves for selected trial mixes with variable fiber volume fractions**

The beneficial effects of SCMs on the composite mechanical properties can be observed from flexural test results of S0F0, S0F15, S45F0 and S45S15 samples as given in **Fig. 2.11**. Two sets of data were given for each mix. Although with the same volume fractions of hybrid fibers, S0F0 and S45F0 did not meet the upper limit for deflection hardening criteria. This may be attributed to the poor workability and the resulting poor consolidation of concrete around fibers. Slump flow test results showed that S0F0 and S45F0 had spread diameters of 440 mm and 495 mm, respectively, as compared to 550 mm for S0F15 and 570 mm for S45F15. Under flexural test, as the matrix cracks, the bridging steel macrofibers will be subjected to pullout stress. The poor consolidation and the subsequent poor bond between the fibers and the matrix led to a smaller fiber pullout resistance and a reduced peak load. Hence, the presence of 15% fly ash as cement

replacement is necessary to ensure good workability and good compaction of the composite. The benefits of both slag and fly ash on mechanical properties can also be observed from a higher residual flexural strength after the peak load for mixes with SCMs as compared to mix S0F0 with no slag or fly ash. Mix S45F15 with 45% slag and 15% fly ash as cement replacement was adopted as the final mix for HP-G-HyFRC.

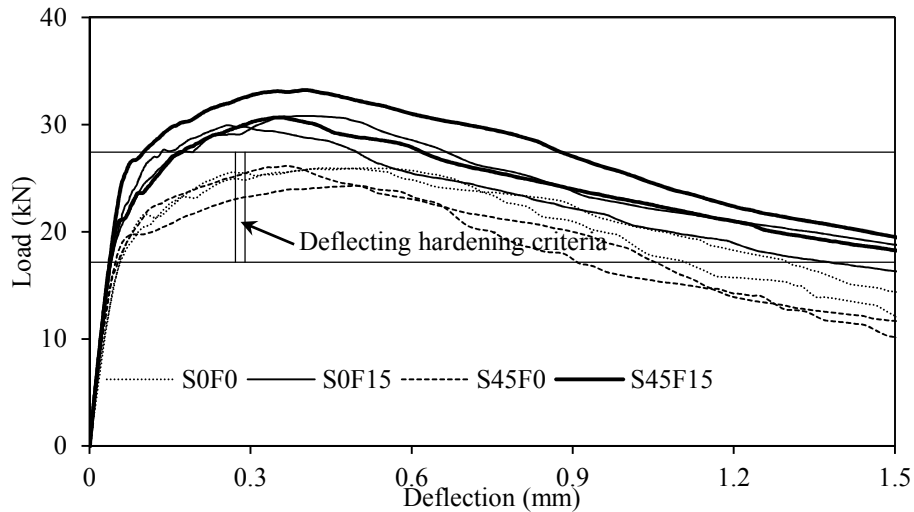


**Figure 2.11: Load-deflection curves for selected trial mixes with different SCM replacement levels at 28 days**

### 2.4.5 Compressive property development of the final mix

**Fig. 2.12** provides compression strength development for HP-G-HyFRC. All samples were moist-cured until testing. It is observed that strength kept on increasing up to 28 days, after which it stabilized. This may be attributed to the low W/B ratio and the cease of hydration after 28 days. Although the samples were moist-cured, it is believed that limited moisture could permeate into the matrix due to pore discontinuity. The results for elastic modulus are given in **Fig. 2.13** and a similar trend to compressive strength development was observed. The average value of 28-day elastic modulus was found to be 32.4 GPa, slightly lower than the assumed 35 GPa used the theoretical analysis. Modification to the deflection hardening formulations with the new elastic modulus value did not significantly affect the deflection hardening envelope.



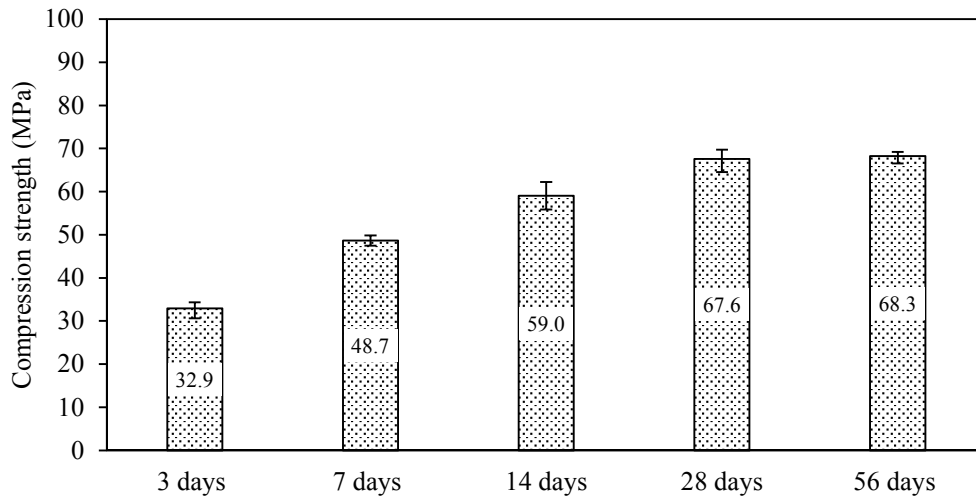


**Figure 2.12: Compression strength development for HP-G-HyFRC**

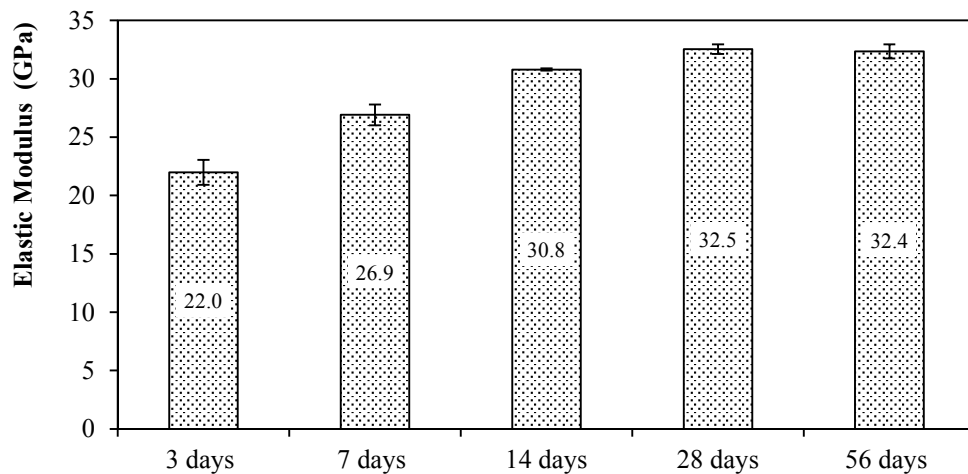


**Figure 2.13: Elastic modulus development for HP-G-HyFRC**

#### 2.4.6 Coefficients of gas permeability

The results for coefficients of gas permeability depicted as bar charts along with error bars are given in **Fig. 2.14**. It is observed that the permeability coefficients within a mix changed insignificantly for different durations of curing. This may be because the low water-binder (W/B) ratio used in the mixes limited a continuing hydration after 28-day of curing. The observation is consistent with strength development results for HP-G-HyFRC as given in **Fig. 2.12** where strengths stabilized after 28 days of curing. Replacement of cement by 45% slag and 15% fly ash helped to reduce concrete permeability. This is attributed to an enhanced workability and formation of discontinuous pores in the matrix from pozzolanic reaction of fly ash and slag. Permeability of concrete has been shown to be reduced with increasing consolidation and

workability (Boel et al., 2007; Leemann et al., 2006; Valcuende et al., 2012; Zhu & Bartos, 2003). As compared to HPC-60R, HP-G-HyFRC with hybrid fibers showed higher permeability. The poorer consolidation of the mix due to the presence of PVA and steel fibers may explain this phenomenon.

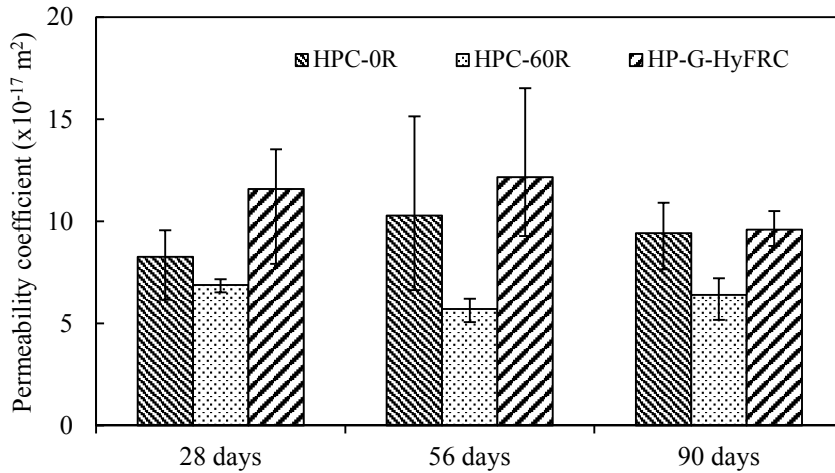
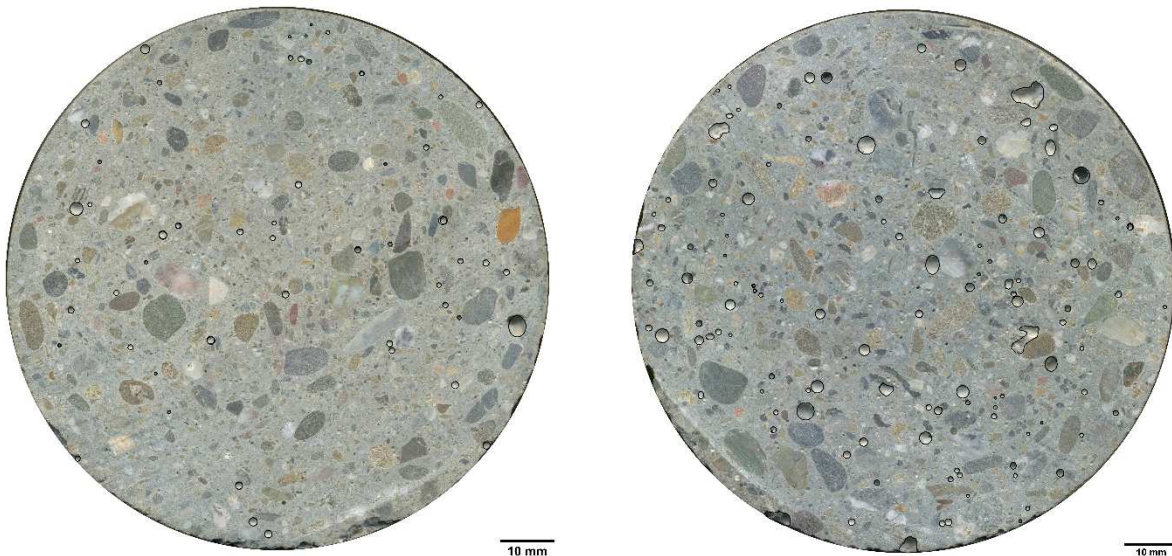


**Figure 2.14: Coefficients of gas permeability**



(a) HPC-60R

(a) HP-G-HyFRC

**Figure 2.15: Distribution of air voids in: (a) HPC-60R, and (b) HP-G-HyFRC**

High resolution scanning of sections at the same height of the cylinders used in the air permeability test (Fig. 2.15) showed that HP-G-HyFRC contained more entrapped air voids. In the pictures, air voids of size greater than or equal to 1 mm were highlighted with black circles or polygons. With

the same mix compositions, except for the inclusion of hybrid fibers in HP-G-HyFRC, an increase in entrapped air volume means higher porosity and possibly increased pore connectivity in HP-G-HyFRC mix and this results in its observed higher gas permeability coefficients.

Gas permeability results can provide us an indication of relative durability performance of concrete. A study conducted by Sugiyama et al. (1996) showed that there existed a relationship between chloride diffusion coefficient of saturated concrete and gas permeability of concrete subjected to air drying for less than 90 days or for oven drying for less than 7 days, which was the drying procedure adopted in our study. Longer drying periods, however, could cause formation of microcracks in the concrete and make the correlation less visible. Hence, it is postulated that HP-G-HyFRC could be less resistant to chloride infiltration as compared to HPC-60R which had the same level of cement replacements by slag and fly ash.

Nevertheless, the gas permeability coefficients of HP-G-HyFRC were about 1/7 of dry normal strength concrete permeability coefficient of about  $80 \times 10^{-17} \text{ m}^2$  after adjusting to  $\text{N}_2$  as a permeating medium (Abbas et al., 2000). Torrent (1999) provided a classification of concrete quality based on gas permeability coefficients as shown in **Table 2.5**. The gas permeability coefficients of HPC-0R, HPC-60R and HP-G-HyFRC were all in the upper “Medium” classification and hence permeability characteristic of the three composites is expected to have a similar effect on their corrosion performance. However, the crack bridging and toughness enhancement of HP-G-HyFRC would help to control corrosion-induced loads and this could be beneficial in extending the overall service life of structures. A more detailed study of corrosion resistance of HP-G-HyFRC will be conducted in **Chapter 3**.

**Table 2.5: Classification of concrete quality based on gas permeability coefficients (Torrent, 1999)**

| Ranking | $K_{\text{N}_2} (10^{-17} \text{ m}^2)$ | Quality   |
|---------|---|-----------|
| 1       | <0.9                                    | Excellent |
| 2       | 0.9-4.4                                 | Very good |
| 3       | 4.4-21.9                                | Medium    |
| 4       | 21.9-109.4                              | Poor      |
| 5       | 109.4                                   | Very poor |

### 2.4.7 Coefficients of chloride migration

Chloride migration coefficients of the middle elements used for air permeability test are given in **Fig. 2.16**. It is noted that in between the two tests, the samples were left in the laboratory air and as a result some moisture would have been reabsorbed into the matrix. However, the level of relative humidity in laboratory air of about 60% (Parrott, 1991) was not expected to induce further hydration in the matrix. Moist curing between 28 and 56 days showed little gain in strength. It is observed that the  $\text{Cl}^-$  migration coefficients reduced with the presence of 60% slag and fly ash as cement replacement. This may be attributed to refinement of pore structure of the matrix due to pozzolanic reaction. Except for HP-G-HyFRC at 90 days, the results show an insignificant variation in migration coefficients of samples with different curing durations. However, there is no clear relationship between the air permeability and  $\text{Cl}^-$  migration coefficients. For instance, although HP-G-HyFRC exhibited the greatest gas permeability coefficients, the mix showed the least  $\text{Cl}^-$  migration coefficients. As the same samples were used in the two tests, the discrepancy is attributed to the polarization of steel fibers in HP-G-HyFRC. The reduction of oxygen by

electrons from the polarized steel fibers would lead to the formation  $\text{OH}^-$  which is postulated to offset migration of  $\text{Cl}^-$  toward the anode side (cell with 0.3 N NaOH solution). Also,  $\text{Cl}^-$  may also be bound by  $\text{Fe}^{2+}$  to form corrosion products. Iron chloride hydroxide and chlorinated iron oxides were found as part of corrosion products on surface of steel embedded in concrete (Neff et al., 2011; Takaya et al., 2013). From the observation,  $\text{Cl}^-$  migration coefficients should be treated with caution especially in steel fiber-reinforced concrete or other types of concrete with traces of virgin metals in the matrix. Also, as the  $\text{Cl}^-$  migration test was conducted on oven-dry concrete and represented a deviation from the standard procedure, the results bear little indication of the true performance of the composites as compared to air permeability coefficients.

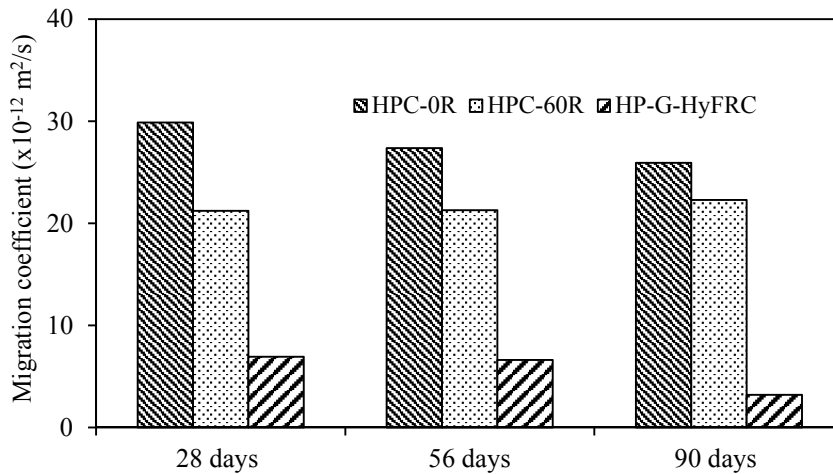


**Figure 2.16: Coefficients of chloride migration**

## 2.5 Discussion

### 2.5.1 Effects of PVA fibers and compressive strength on flexural response

The synergy of macro- and microfibers in providing deflection hardening can be understood through an examination of fiber-matrix interaction. In a study by Bentur et al. (1985), it was shown that when hooked-end fibers were subjected to pullout, considerable asymmetrical cracking developed in the matrix around the fibers. Under compact tension test to mimic composite action under flexure, the fibers experienced both pullout and bending behavior which resulted in local crushing of the matrix and debonding at the fiber-matrix interface. The local damage to concrete surrounding a hooked-end steel fiber during pullout is depicted in **Fig. 2.17**. It is observed that crushing of concrete and microcracking occurred on one side of the hook. Hence, the presence of PVA fibers and their micro size will be effective in controlling the propagation of microcracks around the steel macrofibers. They ensure a gradual macrofiber pullout and stable crack propagation which leads to new crack formation. Also, a higher strength matrix will also provide more resistance to pullout with higher crushing strength of the matrix around the kink zones of the hooked-end fibers. Load-deflection curves for two different FRC mixes with W/B of 0.33 and 0.25 are given in **Fig. 2.18**. Although the two mixes have similar mix composition and the same volume fractions of fibers, the mix with W/B = 0.25 showed a higher peak load and higher load increase from the first crack to peak. It is noted that the two mixes had similar paste volumes of about 44%.

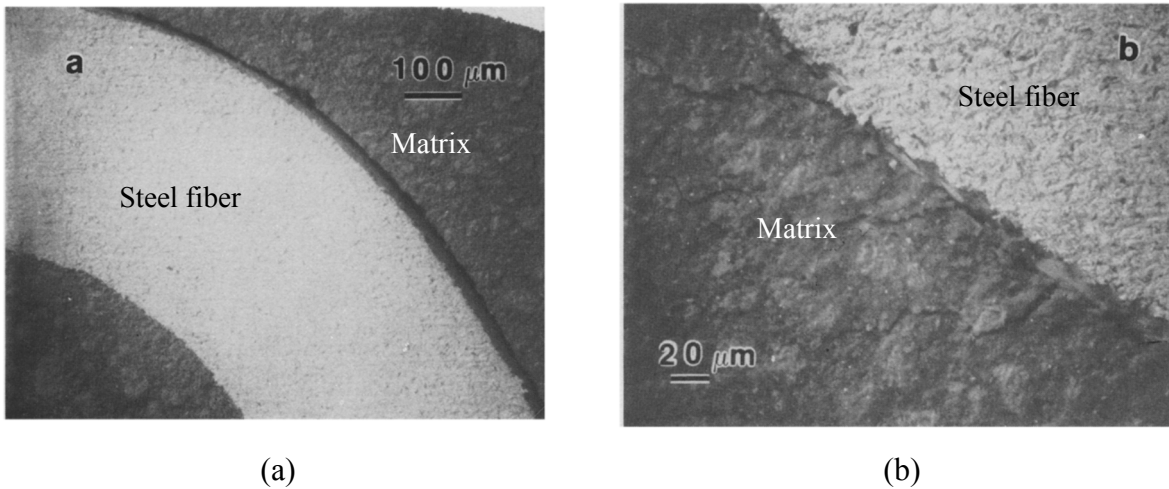


**Figure 2.17: Portion of pulled-out hooked fiber in compact tension specimen: (a) separation on one side of the fiber, and (b) crushing and microcracking on the other side (Bentur et al., 1985)**

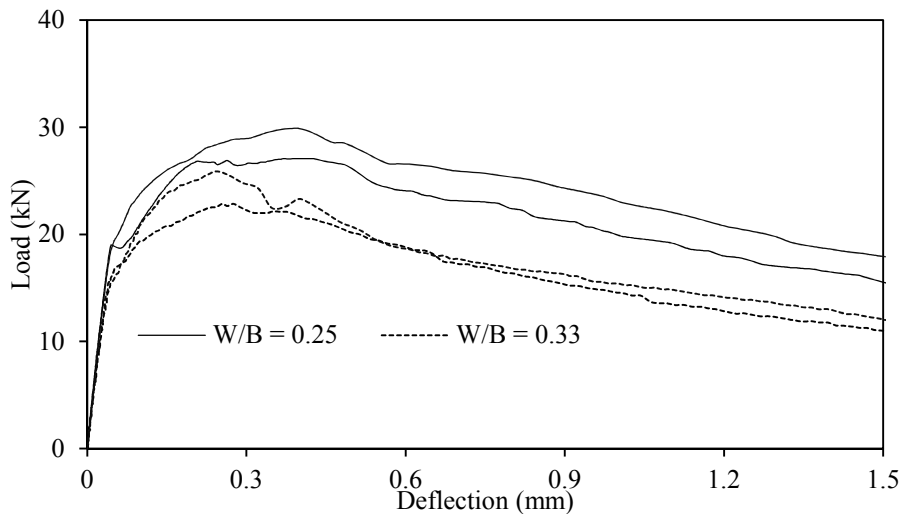


**Figure 2.18: Load deflection curve for FRC mixes with W/B of 0.33 and 0.25**

Typical central regions of tensile faces of tested flexure beams for PF-0b and HP-G-HyFRC (final mix design for HP-G-HyFRC) are shown in **Fig. 2.19**. As observed, there were multiple microcracks distributed over the middle one third region of the tensile face of HP-G-HyFRC. These cracks were in the form of very fine hairline cracks that were almost invisible to the naked eyes. This kind of cracks is beneficial to concrete durability as they limit the ingress of moisture and aggressive ions into concrete. Permeability of water which is a medium of ion transport was shown to decrease in hybrid fiber-reinforced concrete due to distribution and tortuosity of cracks (Lawler et al., 2002). This is critical as in cracked concrete, many researchers have shown that corrosion activity of steel increased with increasing crack widths (Okada & Miyagawa, 1980; Otieno et al., 2010; Ramm & Biscopig, 1998; Schiessl & Raupach, 1997). During loading, it was observed that the ultimate crack started to open up only after the peak load was reached. Hence,

deflection hardening observed in the final mix for HP-G-HyFRC coincides with the formation of multiple microcracks as argued. The beneficial effect of PVA fibers in crack distribution is also observed in **Fig. 2.19**. PF-0b with 1.5% steel fibers but without PVA fibers showed only a few bands of microcracks on its tensile face. This confirms the benefits of PVA fibers in controlling crack propagation and inducing distributed microcracks.

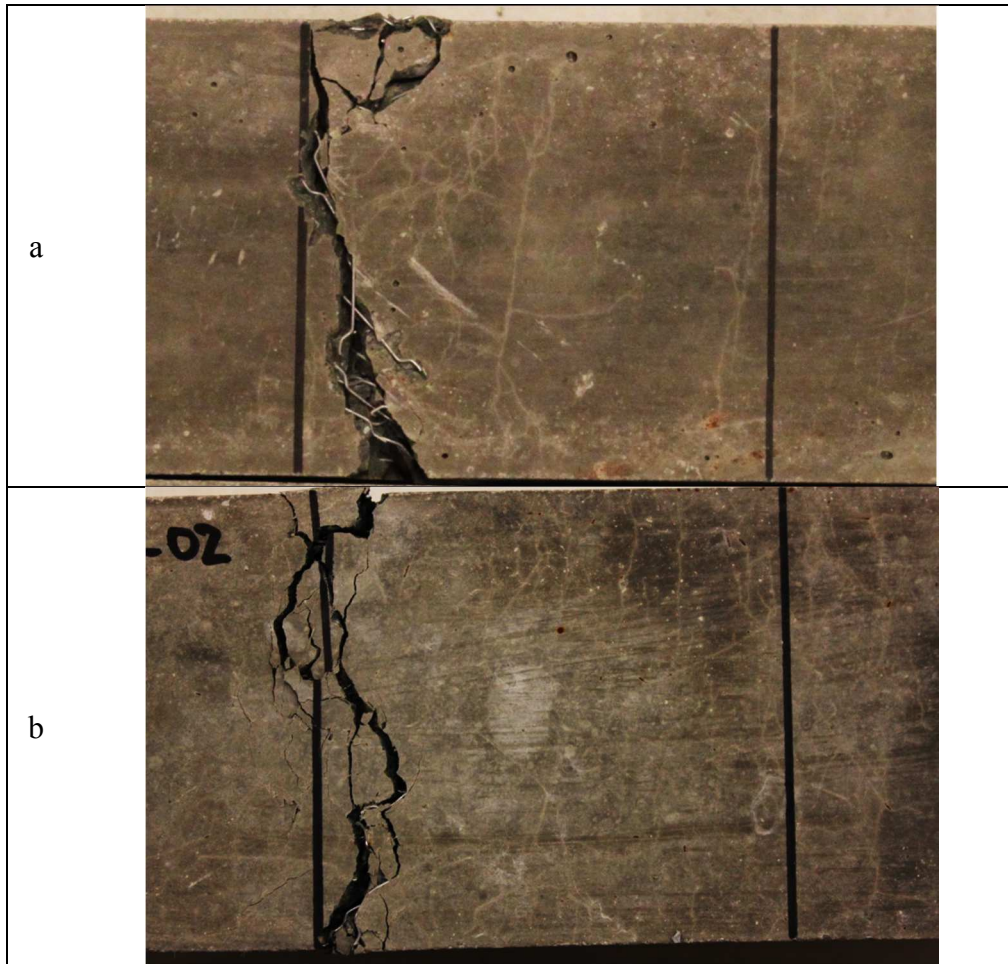


**Figure 2.19: Crack distribution developed on the tensile face of flexure specimen for: (a) PF-0b, and (b) HP-G-HyFRC**

### **2.5.2 Interaction of macro and microfibers beyond hook region**

The toughening mechanism provided by PVA microfibers may be extended beyond the hook region. In the case of steel macrofibers bridging a flexural crack, as the fibers are being pulled out, a tension force is created in the matrix due to frictional force transfer. If the tensile strength of the matrix is less than the induced tensile stress, cracks transverse to the direction of the bridging macrofibers would be formed. The presence of PVA microfibers in the matrix would help to prevent the opening of these cracks, leading to increased pullout resistance of the macrofibers. This phenomenon is observed in **Fig. 2.20**. It represents optical microscopic image which was obtained from a concrete element sliced from the bottom one-third of the flexural beam perpendicular to the macrocrack direction. Epoxy with blue dye was used to improve the



visualization of cracks. It is apparent that the cracks radiating from the steel fiber were bridged by PVA microfibers. This is inferred from the deviation of the crack propagation direction. The occurrence of this kind of crack is expected to be more prevalent in flexural samples as compared to compact tension specimens where only a single fiber is subjected to pull-out. This is because as there are more fibers bridging cracks in the flexural specimens, more prominent tensile stress field and cracking would be formed.

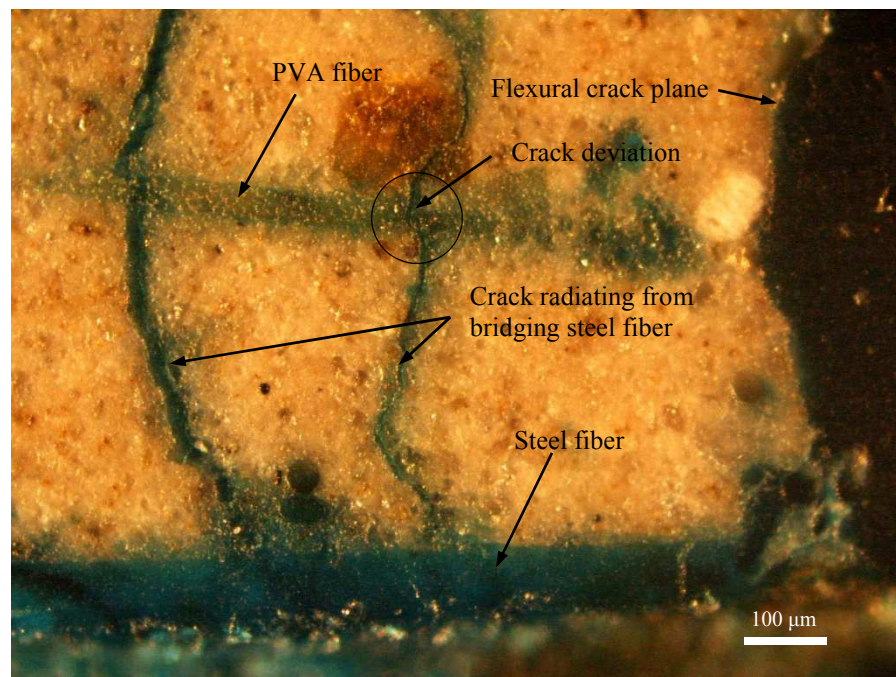


**Figure 2.20: Interaction of macro and microfibers close to crack plane**

### 2.5.3 Workability effects on concrete flexural response

Through microstructural analysis of self-compacting concrete (SCC) mixture and two conventionally vibrated concrete (CVC) mixtures, Leemann et al. (2006) showed that compaction has a significant influence on the porosity and width of the interfacial transition zone (ITZ) of concrete. Lower compressive strength, higher oxygen permeability and higher water conductivity were observed for conventionally vibrated concrete. With regard to HP-G-HyFRC, more porous steel fiber-matrix ITZ under the presence of PVA fibers would reduce steel fiber-matrix bond. This may explain the higher peak load observed for PF0-b as compared to the peak loads for other trial mixes with PVA fibers as shown in **Fig. 2.10**. The beneficial effects of SCMs can be similarly inferred. From **Fig. 2.11**, S0F15 and S45F15 with higher workability and cohesiveness showed smooth deflection hardening responses with enhanced peak loads as compared to S0F0 and S45F0. In this study, the consolidation level was quantified against the elastic modulus of the composites. The elastic modulus values for selected mixes after 28-day moist curing are given in **Fig. 2.21**. As the results were obtained from only one cylindrical sample of each respective mix, no errors bars were provided. In view of the small standard deviation of the elastic modulus values in concrete (as shown in **Fig. 2.13**), the results can be assumed to be representative of the average values. It is observed that PF0-b, S0F15 and S45F15 had about 10% increase in elastic modulus as compared to other trial mixes. This means the mixes had a better consolidation and this resulted in their enhanced peak flexural loads and smoother hardening curves.

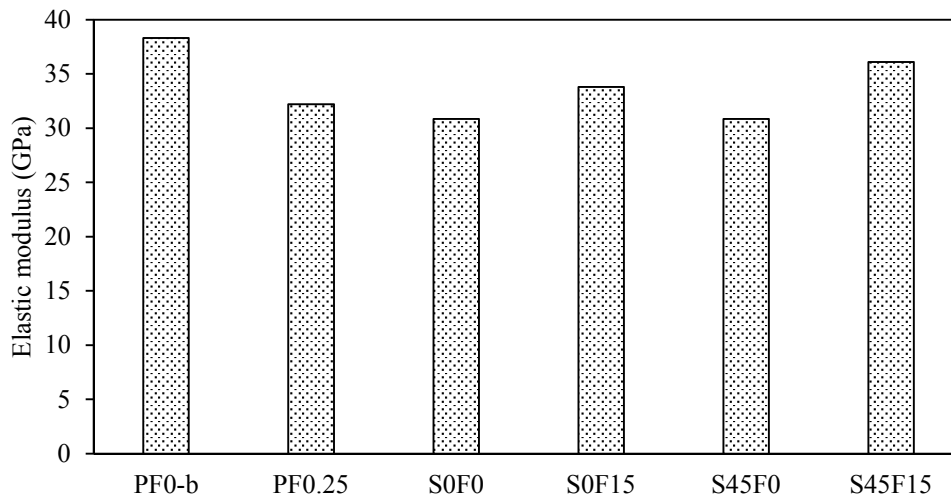


**Figure 2.21: 28-day elastic modulus for selected mixes**

## 2.6 Further research

HPC-0R, HPC-60R and HP-G-HyFRC were all just classified as good quality based on their gas permeability coefficient values. Hence, it is desirable to investigate the performance of HP-G-HyFRC against some of the most commonly occurring durability problems such as steel rebar corrosion or alkali silica reaction (ASR). Also, the benefits of enhanced deflection provided by hybridization of fibers on durability performance will have to be verified. For structural applications, the size effect on the performance of HP-G-HyFRC should also be investigated. Fracture mechanics theory showed that nominal strength of concrete structural element reduced with increasing size (Bazant, 1984). In this study, only relatively small-size specimens, cylinders of size 100 x 200 mm and beams of size 75 x 75 x 280 mm were used for mechanical property study. Although 60% of cement was replaced by slag and fly ash, the presence of fibers and the high amount of binder mean that the composite still has a higher embodied energy as compared to conventional concrete. For building application, to offset this, innovative application of the composite to reduce operational energy should be investigated. The issues will be discussed in the next chapters.

## 2.7 Conclusions

Based on the results of this analytical and experimental work, the following conclusions are drawn:

- Theoretical analysis was used to determine the critical fiber volume fraction for deflection hardening. The required volume fraction was found to be about 1.4% for a concrete composite with  $W/B = 0.25$ .
- For high workability, fine aggregate over coarse aggregate ratio will have to be increased in FRC as compared to conventional SCC mixes.
- Experimental results showed that deflection hardening was achieved even at steel fiber volume fraction of 1.3%, less than the value estimated by the analytical results. This may be attributed to an underestimation of adhesion bond between steel and concrete, or an unaccountability for the beneficial effects of PVA fibers. However, the mix with 1.3% steel



fibers did not meet the upper limit for steel yield point criteria and showed deformation instability after the first crack was formed.

- The presence of SCMs especially fly ash greatly improves workability of hybrid fiber-reinforced concrete.
- Even when up to 60% of cement was replaced by slag and fly ash, the composite was still able to achieve a high 28-day compressive strength. This is even with aggregates of sand and gravel as commonly used for making conventional concrete.
- High workability improves concrete consolidation and enhances mechanical behavior and permeability properties of the composite.
- PVA fibers control microcrack propagation within the matrix. The crack control by PVA fibers around steel fiber-concrete interface helps to ensure a gradual pullout of steel macrofibers and that induces multiple microcrack distribution.
- With a hybridization of 1.5% steel fibers and 0.15% PVA fibers as reinforcement, a high strength concrete composite with  $W/B = 0.25$  exhibits a smooth deflection hardening with multiple microcracks beyond the steel yield point.
- The effects of enhanced deflection hardening on durability properties, especially corrosion, in HP-G-HyFRC will have to be investigated.

The next chapter will cover corrosion performance study of HP-G-HyFRC.

# 3 Corrosion resistance of high performance green hybrid fiber-reinforced concrete (HP-G-HyFRC)

## Summary

A new concrete composite called high performance green hybrid fiber-reinforced concrete (HP-G-HyFRC) was developed. The composite has high compressive strength and exhibits deflection hardening behavior which leads to the formation of distributed microcracking under mechanical loading. However, the beneficial effects of hybrid fibers and the resulting deflection and distributed microcracking on corrosion resistance of the composite were unknown and need to be characterized. Accelerated corrosion test method was adopted and 4% NaCl as binder weight was added into the mixing water. The results showed that under no applied current to induced corrosion, HP-G-HyFRC was able to maintain the corrosion rates to within an inactive corrosion region even with the added NaCl in the mixing water. Also, high strength concretes were found to be susceptible to cracking from rebar corrosion due to their dense interface and less ability to accommodate corrosion products as compared to lower strength and more porous concretes. Hybrid fibers at the fiber volume fractions adopted in HP-G-HyFRC ensured multiple crack formation and reduced subsequent corrosion rates under accelerated corrosion test. The results conclude the superior mechanical and durability performance of HP-G-HyFRC.

## 3.1 Introduction

A new concrete composite termed high performance green hybrid fiber-reinforced concrete (HP-G-HyFRC) was developed. The development process and mechanical properties was given in details in **Chapter 2**. The composite exhibits a high workability and a high compressive strength greater than 70 MPa after 28 days of moist curing. Hybridization of 1.5% steel macrofibers and 0.15% polyvinyl alcohol (PVA) microfibers also allows for a deflection hardening behavior and distributed microcracking up to the peak load under flexural test. The composite is made of conventional materials used for normal strength concrete allowing for easy onsite or factory production. The greening of the composite was achieved by replacing cement with 45% slag and 15% fly ash by mass. In a preliminary investigation of its transport properties as presented in **Chapter 2**, the composite showed slightly higher gas permeability coefficients as compared to plain concrete counterparts HPC-0R and HPC-60R. With the same matrix compositions (except for fibers in HP-G-HyFRC), the higher permeability of HP-G-HyFRC was attributed to a poorer consolidation and the resulting increased porosity in the composite. Cracking due to autogenous and drying shrinkage was phased out due to the presence of fibers and their ability to restrict cracking (Chen & Chung, 1996; Grzybowski & Shah, 1990; Swamy & Stavrides, 1979). Provided no prior cracks are present, the higher gas permeability may lead to an enhanced ingress of oxygen, aggressive ions and moisture into the composite and that can compromise its durability, especially with regard to chloride-induced corrosion. It was argued that concrete permeability is an excellent

measure for the resistance against the ingress of aggressive media and hence a measure of its durability (Torrent, 1999).

During corrosion propagation stage, high strength composite can experience higher corrosion-induced pressure. This is because the refined microstructure of the interface in high strength composite will not be able to accommodate as much corrosion products at the interface as lower and more porous concrete. This phenomenon was explained in a propagation cracking model as proposed by Weyers (1998). It was proposed that before a pressure is created to the surrounding concrete, the corrosion products would have to fill up the accommodation region at steel-concrete interface. Through image analysis of corrosion product penetration in concrete under non-accelerated corrosion, it was suggested that the region comprises air voids, capillary pores, pores inherent in concrete or created by dissolution of the hydrates (Wong et al., 2010). Hence, well-consolidated high strength concrete, aggravated by its high brittleness, would experience more detrimental damage for the same volume of corrosion product formed during corrosion propagation stage. This is critical in view that the service life of structures under corrosion is a combination of corrosion initiation and propagation periods. One mitigation approach is the inclusion of fibers into the composite to enhance its durability performance. Fibers in normal strength concrete were shown to reduce corrosion activity and damage in the propagation stage (Grubb et al., 2007; Jen & Ostertag, 2012). However, the influence of fibers on corrosion performance of concrete at a high strength level has not yet been investigated.

The objective of the study is to examine the corrosion behavior of HP-G-HyFRC and the confinement benefits of hybrid fibers in the composite. The effects of supplementary cementitious materials (SCMs) on corrosion of high strength concrete were also investigated and isolated, by a comparative study of plain concretes with and without cement replacement by slag and fly ash. To study corrosion initiation, corrosion potentials and corrosion rates of non-accelerated corrosion samples were measured up to 98 days. In propagation stage study, accelerated corrosion test with a constant  $1 \text{ mA/cm}^2$  applied current to induce different levels of corrosion cracking was implemented. To eliminate the effect of steel passivity on the effectiveness of the induced current, 4% NaCl by weight of the total binder was added into the mixing water to make concrete. At the end of the electrochemical measurements, the samples were prepared for microstructural analysis at steel-concrete interface with scanning electron microscopy (SEM). The results gave an insight into the effects of concrete strength, fibers and interfacial porosity on corrosion initiation and propagation of steel in concrete.

## **3.2 Materials and methods**

### **3.2.1 Accelerated corrosion test**

Steel corrosion in concrete takes place in two sub-processes (Raupach, 1996). At the anode, iron is oxidized to form iron ions leaving behind electrons which travel to the cathode region. At the cathode, electrons, water and oxygen are converted into  $\text{OH}^-$  which subsequently reacts with iron ions near the anode to form corrosion products. A simplified electrical circuit can be used to model this anode-cathode reaction. Schematic representations of the corrosion process with electrochemical reactions and corresponding simplified circuit are shown in **Fig. 3.1**. The equivalent circuit model consists of cell voltage  $U_e$ , concrete or electrolyte resistance  $R_e$ , resistance of steel  $R_{st}$  whose value is negligible, anodic polarization resistance  $R_a$ , cathodic polarization resistance  $R_c$  and electrical current between the anode and cathode  $I_e$ . Capacitances  $C_a$  and  $C_c$  in

parallel to the anodic and cathodic resistances, respectively, were also added to represent double layer resulting from absorbed ions and water molecules (Hladky et al., 1980). Warburg impedance  $W$  at the cathode was also included to describe diffusion of oxygen in the corrosion process.

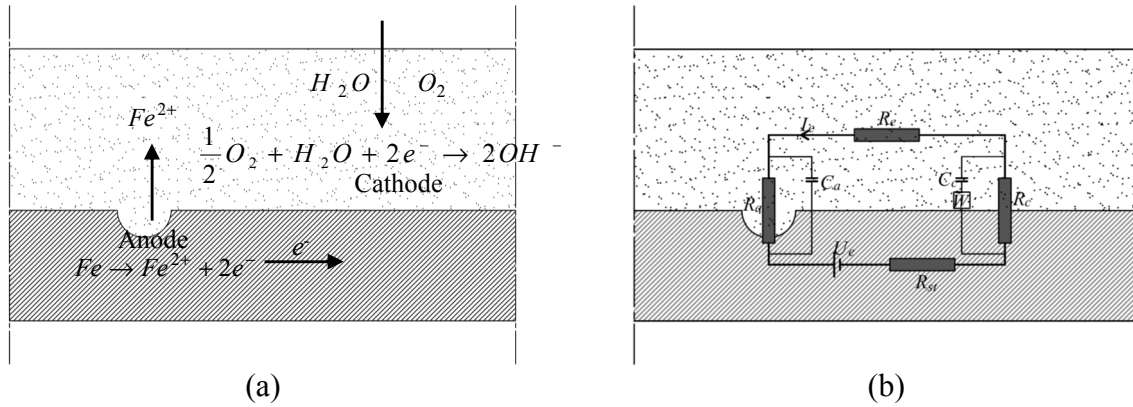


**Figure 3.1: Schematic representations: (a) corrosion process with electrochemical reactions, and (b) simplified electrical circuit model**

In accelerated or impressed corrosion technique, corrosion is induced by applying an electrochemical potential between the reinforcing steel (anode) and the cathode (El Maaddawy & Soudki, 2003). The driving potential can be kept constant or varied so as to achieve a constant current density. With the direct current (DC), the capacitances and impedance presented in equivalent circuit in **Fig. 3.1** will have no influence on the dissolution of ion. Under an ideal condition, the amount of metal loss or level of corrosion can be estimated by Faraday's Law as given in **Eq. 3.1**. With respect to service life of structures, accelerated corrosion test effectively eliminates the corrosion initiation period and allows us to observe the propagation and damage induced by the predefined corrosion magnitude or metal mass loss.

$$M = \frac{A_w}{nF} \int I(t) dt \quad (3.1)$$

where  $A_w$  is atomic weight of iron (55.85g),  $n$  is valency (2) and  $F$  is Faraday's constant (96,500 coulombs/equivalent mass). It is noted that different types of corrosion products with different iron valences are expected to form during the applied current depending on conditions such as pH of the pore solution, oxygen supply and moisture content (Liu & Weyers, 1998). However, a valency of 2 was shown to have a good agreement between the theoretical and gravimetric mass loss calculations under accelerated corrosion (El Maaddawy & Soudki, 2003). Also, based on dissolution of pure iron sheet in chlorinated solution at high pH, it was found that the initial iron ion concentration was dominated by that of  $Fe^{2+}$  (Sagoe-Crentsil & Glasser, 1993). Hence, it is assumed in this study that polarized Fe contributes only 2 electrons to the system and the Faraday's law given in **Eq. 3.1** with valency of 2 is still valid.

The diagram in **Fig. 3.2** elaborates how charges are transported and how corrosion products are formed in an accelerated corrosion test with a cylindrical sample immersed in NaCl solution. The cathode may be made of stainless steel mesh and can be wrapped around the sample. The diagram shows only half of a cut section of the system. Under a cell voltage to generate the desired current intensity, iron of the rebar is polarized to  $Fe^{2+}$  and  $2e^-$ . The electrons are then transported in the circuit to the external cathode. A reduction reaction with water, dissolved oxygen ( $O_2$ ) and the

electrons to form  $\text{OH}^-$  takes place at the cathode (2). Meanwhile, as the surface of the embedded steel is now polarized, a potential difference is created between the anode and the cathode. The positively charged surface of the anode draws  $\text{OH}^-$  and  $\text{Cl}^-$  from the immersion solution into the concrete (3). When  $\text{OH}^-$  and  $\text{Fe}^{2+}$  meet, they bind to form corrosion products (4). It is noted that under the presence of  $\text{Cl}^-$ , intermediate or final corrosion products are oxide, hydroxide and oxy-hydroxide amalgamation of  $\text{Fe}^{2+}$  and  $\text{Fe}^{3+}$  with or without  $\text{Cl}^-$  as impurity (Misawa et al., 1974; Refait & Génin, 1993; Sagoe-Crentsil & Glasser, 1993). However, for simplicity in the discussion, only  $\text{Fe}^{2+}$  is presented in the diagram. The presence of  $\text{Cl}^-$  near the steel surface ensures a continual pitting and depassivation of the steel rebar, and subsequently supply of electrons from the anode under the cell voltage. From the diagram, it is observed that a dense concrete would limit the movement of  $\text{Cl}^-$ ,  $\text{OH}^-$  and  $\text{H}_2\text{O}$  toward the polarized anode surface. This may help to limit corrosion-induced damage in concrete as an ample supply of  $\text{H}_2\text{O}$  is critical for expansion.  $\text{H}_2\text{O}$  is absorbed by the corrosion products to form a product phase of higher volume. It was found that highly expansive hydrated corrosion product  $\text{Fe}(\text{OH})_3 \cdot n\text{H}_2\text{O}$  formed only with high availability  $\text{O}_2$  and moisture (cross referenced from (Marcotte, 2001)). Also, the presence of dissolved  $\text{O}_2$  at the interface also contributes to phase transitioning of the corrosion products (Misawa et al., 1974).

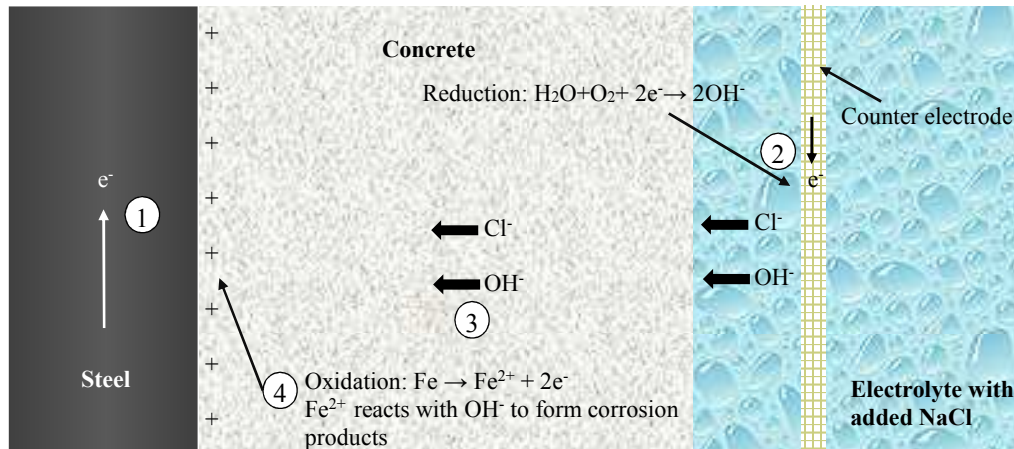


**Figure 3.2: Charge transfer and formation of corrosion products in accelerated corrosion test**

It is important to note that the mass loss obtained from Faraday's law is not always consistent with the gravimetric or measured mass loss due to other competing reactions against oxidation of steel (Ballim & Reid, 2003). Under accelerated corrosion with high cell voltage, one of the processes is water oxidation (Caré & Raharinaivo, 2007). The phenomenon may be attributed to the passive state of steel in concrete, which prevents steel from being oxidized under the cell voltage. Adding salt in mixing water destabilizes the passive film on steel surface and this ensures that dissolution of steel is the main anodic process in accelerated corrosion test. It was shown that although there is no general relationship between sample expansion and electrical charge in chloride-free solution, expansion was proportional to applied charged in samples soaked in chlorinated solution (Caré & Raharinaivo, 2007). In another study, 5% NaCl by weight of cement was added into the mix and a good agreement between the measured and predicted mass losses was observed (El Maaddawy & Soudki, 2003). In the study to be presented in this chapter, NaCl was added into the mixing water. The amount of NaCl to be added will be discussed.

### 3.2.2 Materials

ASTM Type II cement was used as the main binder. Slag and fly ash were also used as cement replacement. Their chemical compositions based on X-ray fluorescence (XRF) analysis were given in **Table 2.1** of **Chapter 2**. Aggregates were composed of pea gravel with a maximum size of 10 mm and fine sand with a measured fineness modulus of 3.2. The hybrid fiber mixture used in HP-G-HyFRC contains a combination of 30 mm steel macrofibers and 8 mm PVA microfibers (**Fig. 2.1**). Properties of the fibers were summarized in **Table 2.2**. Structural steel reinforcement with a yield strength of 420 MPa was used as the anode. Its chemical compositions are given in **Table 3.1**. It is noted that the presence of cerium (Ce) is to de-hydrogenate hydrogen and hence to eliminate defects which may serve as fracture initiation point (Keis & Komissarov, 1963).

**Table 3.1: Rebar chemical compositions (%)**

| Fe    | C     | Mn    | P     | S     | Si    | Ni    | Cr    | Mo    | Cu    | V     | Cb    | Ce    |
|-------|-------|-------|-------|-------|-------|-------|-------|-------|-------|-------|-------|-------|
| 97.06 | 0.400 | 1.110 | 0.018 | 0.046 | 0.130 | 0.100 | 0.130 | 0.020 | 0.370 | 0.003 | 0.001 | 0.610 |

### 3.2.3 Concrete mix designs

**Table 3.2: Mix designs for accelerated corrosion test (kg/m<sup>3</sup>)**

|                   | HPC-0R | HPC-60R | HP-G-HyFRC |
|-------------------|--------|---------|------------|
| W/B               | 0.25   | 0.25    | 0.25       |
| Water             | 162.9  | 162.9   | 162.9      |
| Cement            | 715.6  | 285.0   | 285.0      |
| Slag              | -      | 320.7   | 320.7      |
| Fly ash           | -      | 106.9   | 106.9      |
| Fine aggregate    | 942.0  | 894.3   | 868.0      |
| Coarse aggregate  | 547.8  | 520.0   | 504.7      |
| 30mm Steel fibers | -      | -       | 117.0      |
| 8mm PVA           | -      | -       | 1.9        |
| SP <sup>†</sup>   | 11.0   | 11.0    | 11.0       |
| VMA <sup>†</sup>  | 6.6    | 6.6     | 6.6        |

<sup>†</sup> L/m<sup>3</sup>

Concrete mixes with water-binder (W/B) ratio of 0.25 were used in study. A total of three mix variations were adopted: high performance concrete (HPC), HPC with cement replaced by 45% slag and 15% fly ash by mass, and HPC with 45% slag, 15% fly ash reinforced with 1.5% 30 mm steel fibers and 0.15% PVA fibers. The third mix is the final mix design of HP-G-HyFRC as presented in **Chapter 3**. The mix designs are summarized in **Table 3.2**. In the sample annotations, HPC-0R is HPC with no cement replacement, HPC-60R is HPC with 45% slag and 15% fly ash as cement replacement, and HP-G-HyFRC is for high performance green hybrid fiber-reinforced concrete. In **Table 3.2**, SP is for superplasticizer, and VMA is for viscosity modifying agent.

Also, to break down the passive film in concrete and to prevent its reformation, NaCl was added into the mixing water at 4% by mass of the binder. The critical chloride content to initiate corrosion of reinforcing steel in concrete depends on a number of parameters. These include pH of pore solution, electrochemical potential of steel in which the presence of chloride modifies the anodic polarization curve, steel-concrete interface quality, binder type, surface condition of steel, moisture

and oxygen content of concrete, presence of mineral admixtures, W/B ratio, degree of hydration, electrical resistance of concrete, chemical composition of steel, temperature, type of chloride salt and chloride source (Angst et al., 2009). For mixed-in chloride, the high limit for critical total chloride content was found to be about 2% (Lambert et al., 1991; Manera et al., 2008; Treadaway et al., 1989). This is translated to 3.3% in terms of NaCl. For the study of this chapter, destabilize steel passivity, NaCl of 4% by mass of the binder was added into the mixing water.

### 3.2.4 Specimen preparation and corrosion testing procedure

Cylinders of size 100 x 200 mm embedded with 137.5 mm long #8 or 25 mm-diameter bars in the center were procured for the accelerated corrosion test. The bars were cut to the desired length and their surfaces were sandblasted to remove the mill scale. The top end of the bar was tapped to accommodate a 6-32 x 3/8 screw for wiring. To confine the corrosion area to the cylindrical surface of the bar, their end surfaces were coated by electrical protective coating in two layers which were allowed to cure for 24 hours before the casting. The protective coating effectively prevented these portions of the bar from corroding and was confirmed after the accelerated corrosion test. During casting, the wired rebars were hung at 31.25 mm from a temporary cross steel rod which were placed on top of plastic cylindrical molds. Concrete placement was made in two equal lifts. For each lift, the sides of the cylindrical molds were lightly agitated by rubberized hammer to consolidate the fresh concrete. The steps for bar preparation and casting are depicted in **Fig. 3.3**. The specimens were cast and moist cured for at least 28 days. Accelerated corrosion tests were implemented when the samples were at least 28 days old. Six additional cylinders cured under the same regime were also produced to find compressive strengths of each mix design at 28 and 56 days.

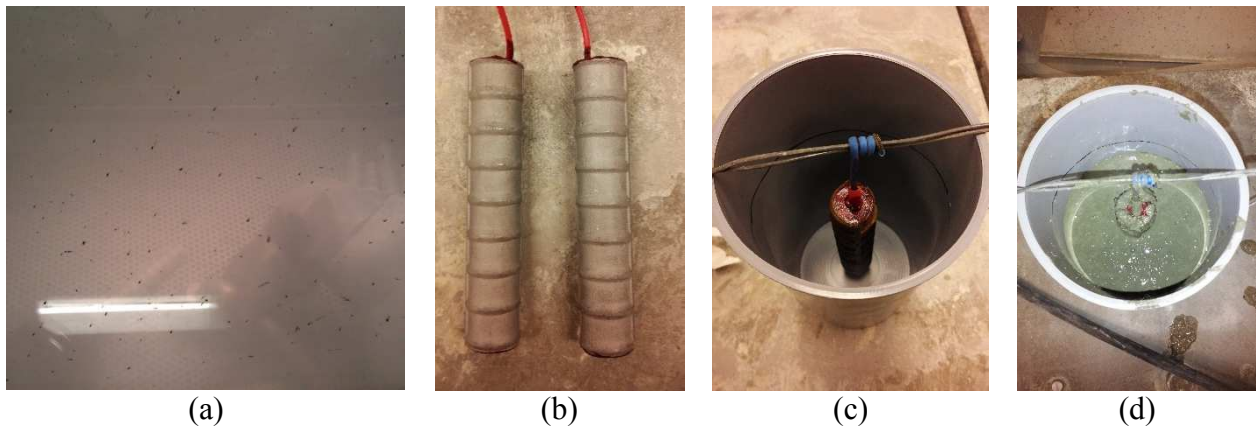


**Figure 3.3: Bar preparation for accelerated corrosion test: (a) sandblasting, (b) bars ready for casting, (c) bar hung by cross rod, and (d) first lift of concrete**

The setup of accelerated corrosion test and electrochemical measurement is shown in **Fig. 3.4**. As the working electrodes were totally embedded in concrete, they could not be seen in the figure. The corrosion cycles were performed with a Gamry G750 Potentiostat, using the DC105 software package. The rebar or the working electrode was connected to the electrometer through a screw terminal and insulating wire. A closed circuit was formed through a counter electrode connected to stainless steel mesh encircling the concrete cylinder. A saturated calomel electrode (SCE) was used as a reference electrode. The samples were immersed in 17.5% NaCl solution by weight up to a height roughly 12.5 mm from the top of the concrete cylinder. The salt concentrations of the



immersion solution were equivalent to the concentration used in the mixing water. After immersing the samples in the NaCl solution for 24 hours, the accelerated corrosion tests were initiated. A continuous current of 111.5 mA ( $1 \text{ mA/cm}^2$ ) was applied for either 24 or 48 hours on the accelerated corrosion samples at room temperature. Afterward, the samples were allowed to come to a steady state in their respective NaCl solutions. Following the applied current regimes, the electrochemical tests including linear polarization resistance and Tafel tests were then performed at 1, 3, 7 and 14 days. For non-accelerated samples, electrochemical measurements were made up to 98 days after immersion into NaCl. Linear polarization resistance measurements were conducted by sweeping potential  $\pm 10 \text{ mV}$  from the corrosion potential at a rate of  $0.1 \text{ mV/s}$ . For Tafel scan measurements, a potential sweep of  $\pm 75 \text{ mV}$  was conducted on samples undergoing the same exposure condition. A corresponding set of samples without any applied current was also procured and electrochemical behavior was monitored up to 98 days. It is noted that during the application of current, the counter electrode was used as reference. That is the reference electrode sensor was connected to the counter electrode and no SCE reference electrode was used.

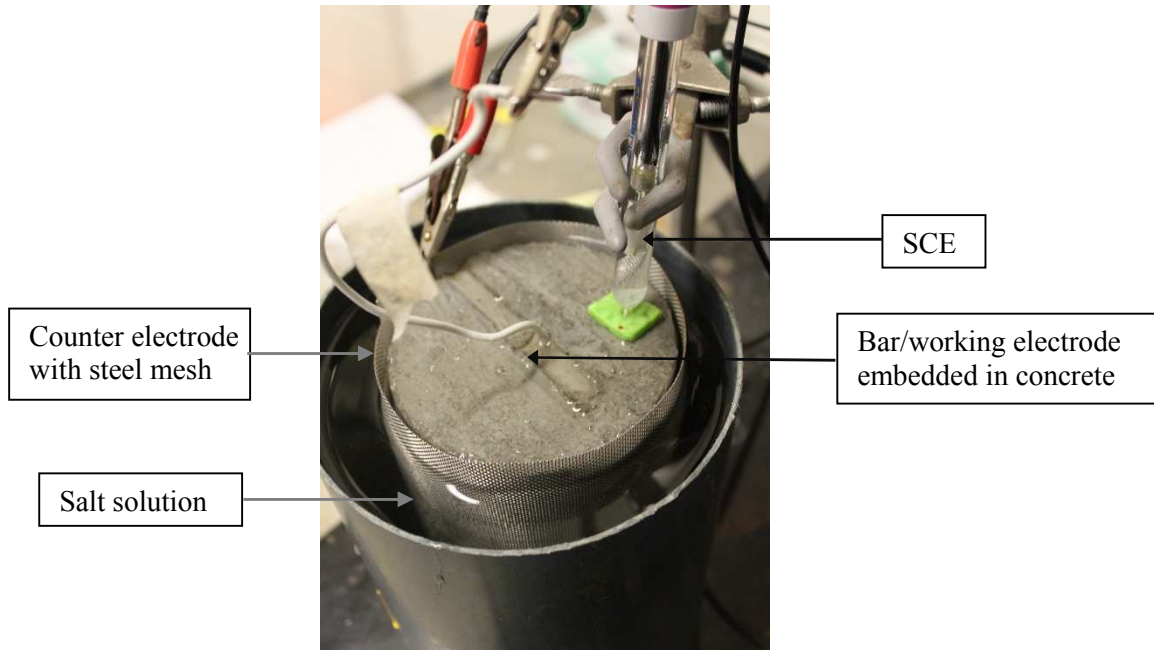


**Figure 3.4: Accelerated corrosion test setup**

Two samples were prepared for each current regime, one for linear polarization and one for Tafel testing. This was to prevent possible errors that may be caused by irreversible polarization under Tafel test where the potential sweep of  $\pm 75 \text{ mV}$  from the corrosion potential was applied. Corrosion rates were determined using **Eq. 3.2**, in which  $R_p$  is polarization resistance ( $\Omega$ ),  $B$  is Stern-Geary constant (mV), and  $I_{corr}$  is corrosion rate (mA). Corrosion rate intensity ( $i_{corr}$ ) was found by dividing corrosion rates with an exposed surface area of  $111 \text{ cm}^2$ .  $R_p$  and  $B$  can be found from linear polarization and Tafel curves, respectively, as outlined in ASTM G102-89 (American Society for Testing and Materials (ASTM), 2010d). Additional annotations were added to the sample naming convention with 0H, 24H and 48H for no applied current, 24 hours and 48 hours of  $1 \text{ mA/cm}^2$  applied current, respectively. For example, HPC-0R-48H refers to high performance concrete with no cement replacement and with 48 hours of applied current.



$$I_{corr} = \frac{B}{R_p} \quad (3.2)$$

### 3.2.5 Microscopic analysis

Following the accelerated corrosion, the samples from the linear polarization group were sliced in the middle region to obtain disc elements of thickness 21.5 mm. The slicing was done with an abrasive cutter at a very low feed rate with water as lubricant. Other researchers (Wong et al., 2010) also used water as lubricant and no leaching of corrosion products were observed. The leaching may be prevented by the burring the steel rebar from abrasion with the saw. The elements were then oven dried at 110 °C overnight. Oven drying removed moisture from the concrete and hence effectively stopped corrosion. The slices were coated with epoxy under vacuum to avoid air bubbles and promote good penetration. The epoxy filled all voids on the sample surfaces up to a penetration depth of approximately 1 to 2 mm. After the epoxy was allowed to cure in air for three days, the slices were further trimmed on their sides with diamond-blade saw and water as lubricant to form the final samples of rectangular shape approximately 35 × 25 mm with rebars in the center. After trimming, the samples were immediately dried with paper towel and compressed air to prevent reintroduction of water into the matrix. The samples were then ground and polished sequentially with 9 micron grit, 3 micron grit, 3 micron paste, and finished with 1/4 micron paste. The polishing removed the surface layer of epoxy and exposed the steel, aggregate, and cement paste, leaving only epoxy in the voids. From this onward, the samples were stored in a vacuum desiccator with silica beads as water absorber until optical and SEM microscopic analyses were conducted.

After the optical microscopy, the samples were coated with 25 nm thick carbon layer in vacuum with polished titanium plate as a color indicator. To prevent over-charging of the samples during scanning electron microscopy (SEM), a brass conduction strip was attached to one side of the samples to enable electrons to flow from the sample top surface to a conductor located at the supporting platform. Back scattered electron (BSE) imaging and energy dispersive X-ray (EDX) microanalyses were conducted with Zeiss Evo MA10. Images was captured at 20 kV and with probe current maintained at 1 nA. Qualitative element mapping in EDX was carried out at 256 x 208 pixel resolution with beam dwell time of 200 μs and with 128 frames.

### 3.2.6 Gravimetric mass loss analysis

The samples from the Tafel group were also dried in oven at 110 °C for 24 hours and were subsequently subjected to splitting tensile test for rebar removal. The wiring was removed and the coating at both ends was then cleaned off with a stripper solution. To remove corrosion products without significantly removing the base metal, the rebars were then immersed in a solution made of 500 mL hydrochloric acid (HCl, sp gr 1.19) and 3.5 g hexamethylene tetramine per 1 L solution for at least 10 minutes as recommended by ASTM G1-03 (American Society for Testing and Materials (ASTM), 2011). During the immersion, the rebars were intermittently removed from the cleaning solution for light brushing. Until satisfaction, the samples were rinsed with water and ethanol before their masses got recorded to ±0.1 g accuracy.

### 3.2.7 Pore press and inductively coupled plasma (ICP)

Pastes with no added NaCl corresponding to HPC-0R and HPC-60R were also prepared and moist-cured for pore solution extraction with a pore press equipment similar to that described by

Barneyback & Diamond (Barneyback Jr & Diamond, 1981). The pore press consists of 5 main parts: Piston, Part A, Positioning Ring, Part B and Base as shown in **Fig. 3.5**. Part A contains a 57 mm-diameter sample compartment. In test setup, Part A is placed onto Part B with the aluminum positioning ring to hold them in place. Part B consists of two channels, one to direct the extracted pore solution through a hole into the pore solution collection compartment of the base, the other is to accommodate a greased O-ring so that the extracted solution will be contained. A vial is to be placed in the collection compartment of the base so that the dripping pore solution can be captured. In extraction preparation, the surface of Part B where the sample would be resting, the wall of the sample compartment of Part A and the wall of the piston were lubricated with dry Teflon-based lubricant spray. Cement paste was crushed with a hammer in a heavy duty plastic bag to particles less than 10 mm in size. About 250 g of the crushed sample was placed into the sample cavity in three layers, each layer compacted lightly with a pestle. A Teflon disc 57 mm in diameter and 5 mm in thickness was leveled on top of the compacted sample before the piston was placed on top of it. Pressure was then applied in two steps. A load of about 25 kN was first applied and released to level the plunger and the bearing plate. After ensuring that the piston turned freely inside the cavity, the load was reapplied at a rate of 150 kN/min until it reached 1200 kN and was held at that level for 2 minutes. The load was then slowly released and the pore solution vial was removed. Part A, now with the pressed sample and the piston, was placed on two equal-sized wooden blocks and a small load was applied to remove the pressed sample. After the internal surfaces and channels of the pore press were cleaned with sand paper and ethyl/isopropyl alcohol, the process was repeated for other samples.

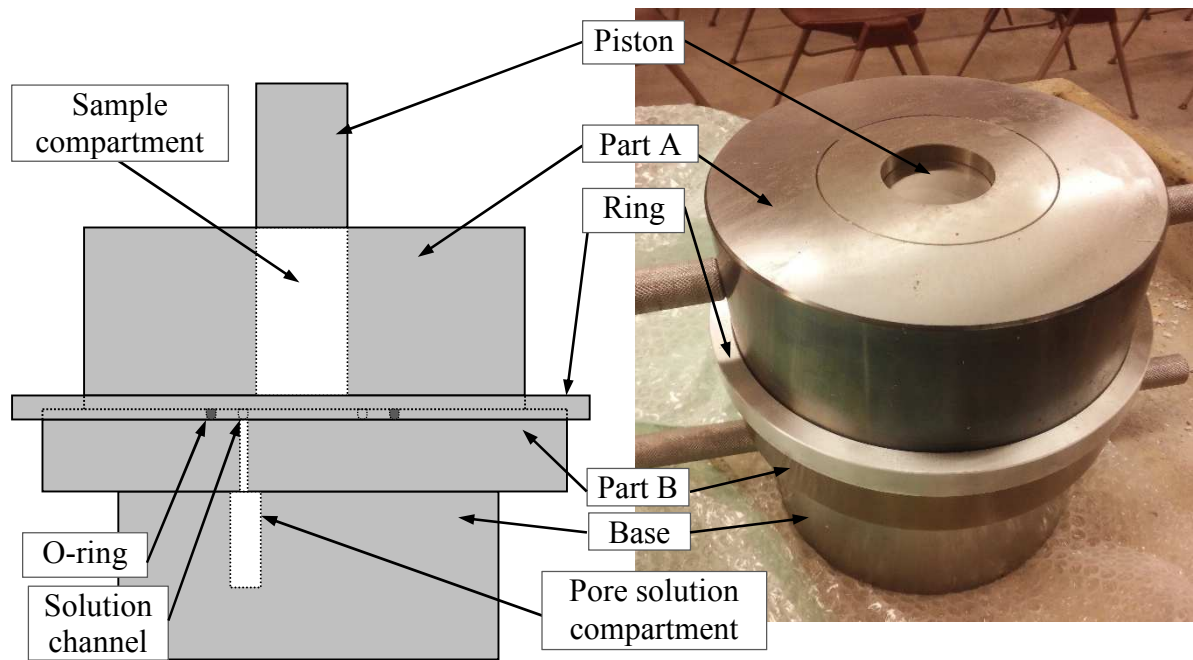


**Figure 3.5: Pore press configuration**

To prevent sample contamination and water evaporation, the extracted solutions in the plastic vials were immediately sealed and later divided into two parts, one for pH measurement and the other

one for inductively coupled plasma (ICP) spectroscopy. ICP analysis was performed with Perkin Elmer 5300 DV optical emission ICP. In sample preparation process, the sealed solutions were filtered with 5  $\mu\text{m}$  nylon syringe filters, diluted 3 times with 6.5%  $\text{HNO}_3$  solution and 6 times with 5%  $\text{HNO}_3$  solution. Dilution by acid solution is necessary to prevent ion oversaturation and precipitation. From ICP analysis results, concentrations of Ca, K and Na were found by comparing the peak intensities against standard solutions. Pore solution analysis of the samples was to investigate if high-volume replacement of cement by slag and fly ash changes pore solution chemistry which might have an implication on corrosion resistance of the corresponding concrete composites.

### 3.3 Results

#### 3.3.1 Mechanical properties of concrete mixes

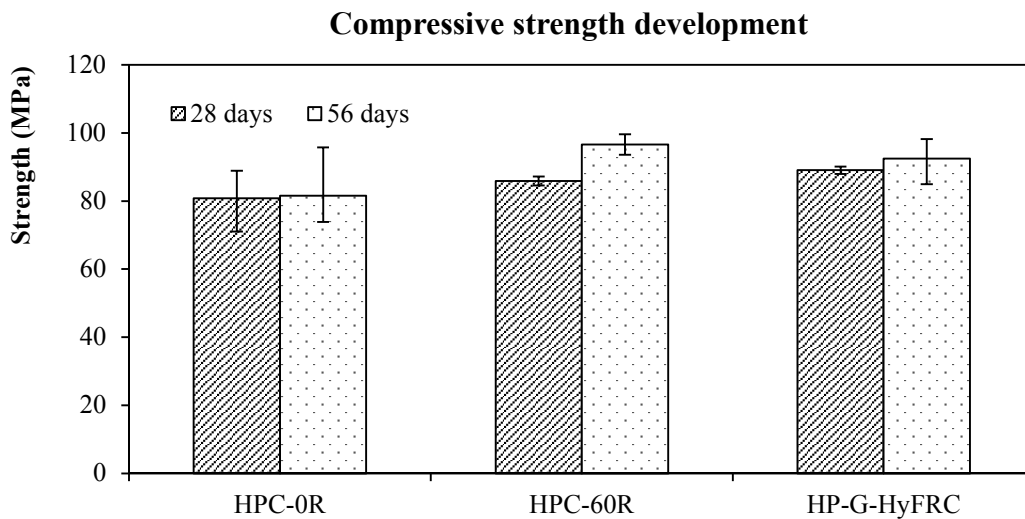


**Figure 3.6: Compressive strengths of HPC-0R, HPC-60R and HP-G-HyFRC at 28 days and 56 days**

The compression test results with error bars for mixes used for the corrosion study are given in **Fig. 3.6**. It is observed that compressive strengths for HPC-0R were slightly lower than those found for HPC-60R and HG-G-HyFRC at all ages. The presence of supplementary cementitious materials in HPC-60R and HP-G-HyFRC led to pozzolanic reaction, refinement of microstructure and the resulting strength increase. NaCl in the mixing water also enhanced concrete strength. As compared to samples without NaCl as presented in the previous chapter, HP-G-HyFRC with 4% NaCl showed about 25% increase in 28-day compressive strength. NaCl or seawater was shown to increase compressive strengths of concrete due to its acceleration property (Taylor & Kuwairi, 1978). For HPC-60R and HP-G-HyFRC where 60% of cement was replaced by slag and fly ash, fibers in concrete did not significantly influence concrete compressive strength. There was also an insignificant strength increase from 28 to 56 days. This may be attributed to two factors: cessation of hydration and pozzolanic reactions after 28 days, and enhanced hydration under the presence of  $\text{Cl}^-$  within the first 28 days of moist curing. Compression results of HP-G-HyFRC presented in the previous chapter also consistently showed a stabilization of strength development after 28 days.

### 3.3.2 Corrosion initiation of samples with no applied current

The results for corrosion potentials of samples without applied current are given in **Fig. 3.7**. According to ASTM C876-09 (American Society for Testing and Materials (ASTM), 2009), there is a greater than 90 % probability that reinforcing steel bar is actively corroding in an area at a given time when the half-cell corrosion potentials are more negative than -350 mV against copper-copper sulfate reference electrode (CSE) or -277 mV versus saturated calomel electrode (SCE). The limits of corrosion potentials were based on empirical relationship between half-cell corrosion potential results and corrosion states of steel in concrete (Stratfull, 1973). Half-cell corrosion potential as a corrosion detection technique was first used by Stratfull for bridges in California (1957). It is observed that all samples had corrosion potentials more negative than -277 mV from the first day of measurement. Hence, it is highly probable that all samples experienced active corrosion. It is also noted that HP-G-HyFRC had similar negative corrosion potential as compared to HPC-60R. This confirmed that the slightly higher gas permeability coefficients as presented in **Chapter 2** did not influence the corrosion initiation characteristic of the two mixes. On the other hand, up to 28 days, HPC-0R exhibited less negative corrosion potentials as compared to HPC-60R and HP-G-HyFRC. It is postulated that the higher alkalinity of the pore solution in HPC-0R helped to reduce the pitting activity of the rebar. This will be confirmed in the pore solution analysis results to be presented in the next section of this chapter.

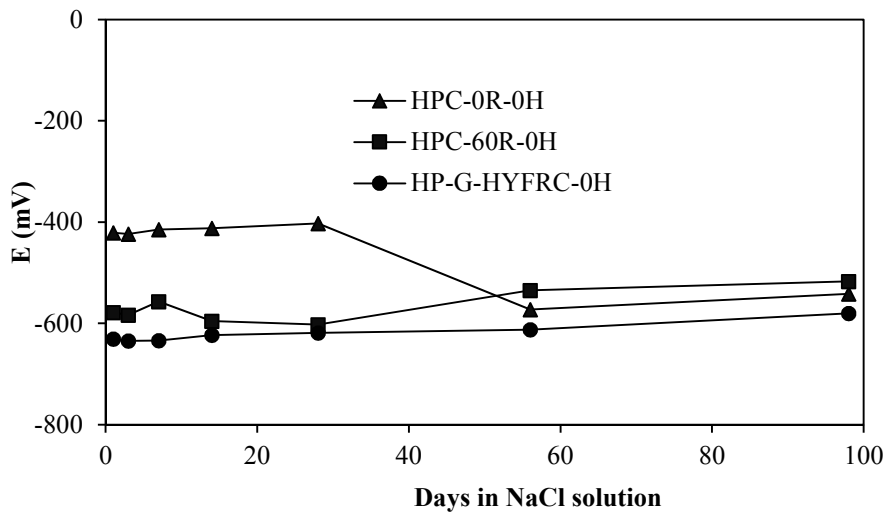


**Figure 3.7: Corrosion potentials for samples without applied current**

The corresponding corrosion rates are given in **Fig. 3.8**. For laboratory measurements, corrosion rates greater than  $0.2 \mu\text{A}/\text{cm}^2$  indicates an active corrosion while a frontier between  $0.1$  and  $0.2 \mu\text{A}/\text{cm}^2$  is within an uncertain activity (Andrade & Alonso, 1996). In this study,  $0.1 \mu\text{A}/\text{cm}^2$  was taken as the lower limit for active corrosion. It is observed that corrosion rate values were around  $0.1 \mu\text{A}/\text{cm}^2$ , indicating inactive or negligible corrosion activity. The results are contradictory to the inference given by the corrosion potentials in which all samples were expected to undergo active corrosion. As steel passivity was compromised from the day of casting with the added NaCl in the mixing water, it is expected a limited availability of  $\text{O}_2$  at the interface caused corrosion potentials to appear very negative without increasing corrosion rates. This phenomenon is called cathodic control of corrosion and its influence on corrosion potential are depicted in **Fig. 3.9**. With

low  $O_2$  concentration in the electrolyte, the cathodic curve plateaus at low potential values. This leads to more negative potential yet a reduced corrosion density corresponding to the intersection of the polarization curves. Hence, concrete permeability which determines the ingress of moisture and dissolved oxygen into embedded steel surface plays a crucial role in controlling both the corrosion activity and the apparent corrosion potentials of steel in concrete.

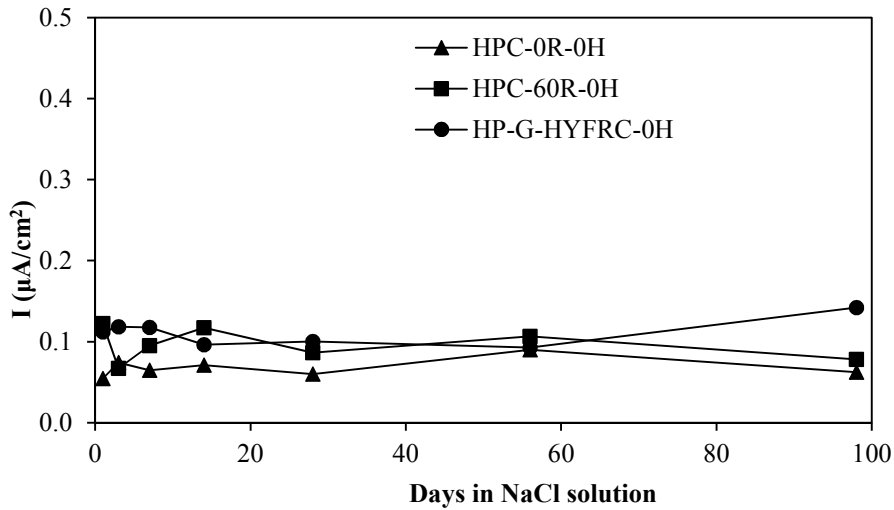


**Figure 3.8: Corrosion rates for samples without applied current**

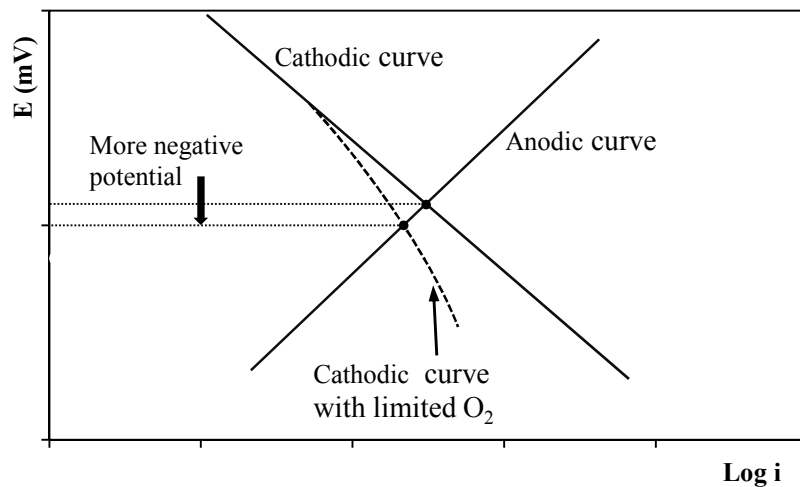


**Figure 3.9: Reduction in corrosion potential with cathodic control**

The findings imply that corrosion potential values can only be used to indicate corrosion probability of steel in concrete but not the extent of corrosion activity. Corrosion potentials measured at the surface of concrete were shown to be dependent on various parameters including electrolyte resistivity, oxygen availability which is discussed in this study, anode-to-cathode area ratio, cover thickness, type of corrosion process (uniform versus pitting corrosion), water and chloride content in concrete (Elsener, 2002; Pour-Ghaz et al., 2009; Schiegg et al., 2009).

### 3.3.3 Corrosion results of samples with applied current

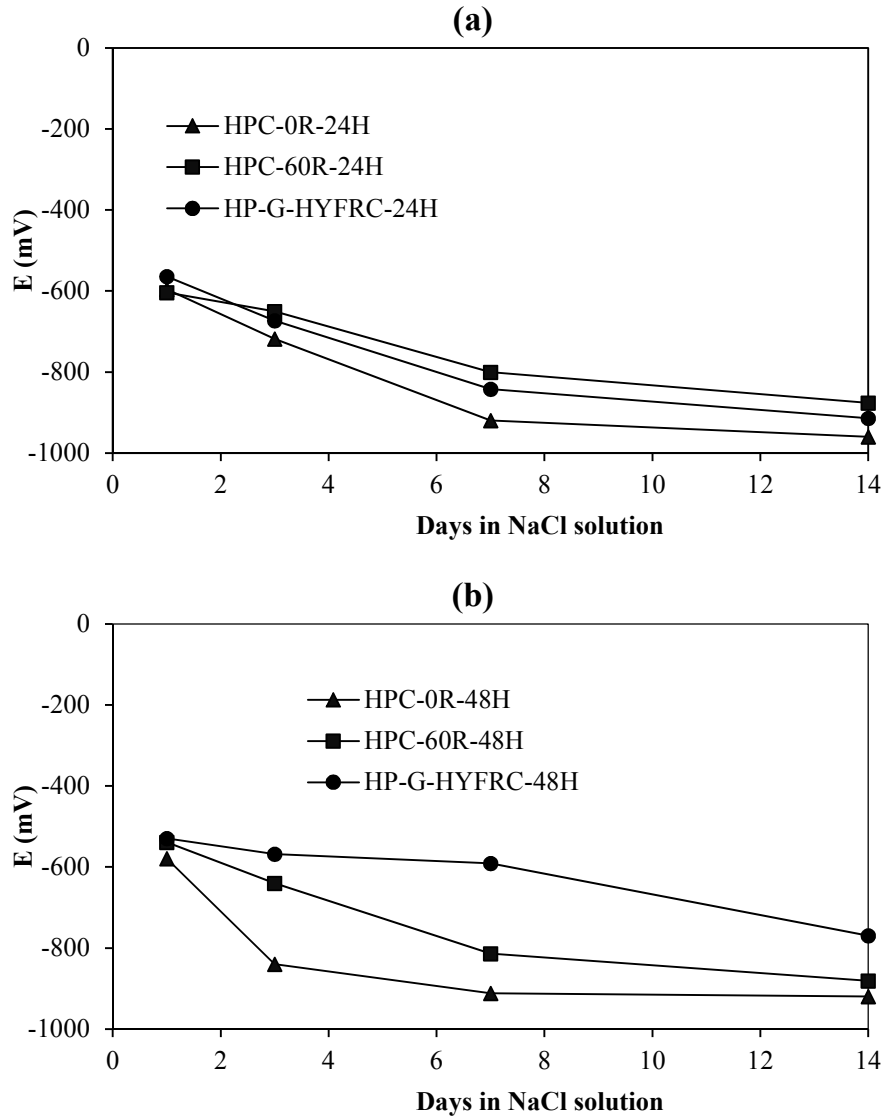


**Figure 3.10: Corrosion potentials for HPC and HP-G-HyFRC samples with applied current of: (a) 24 hours, and (b) 48 hours**

Corrosion potentials of the concrete samples with 24 and 48 hours of applied current are given in **Fig. 3.10**. It is observed that corrosion potential values for all samples were more negative than -277 mV, indicating that all samples were potentially in an active corrosion region. There is no distinguishable difference in corrosion potentials among the samples with 24-hour applied current regime. However, as the duration of applied current increased from 24 to 48 hours, HP-G-HyFRC-48H showed the least negative corrosion potentials as compared to HPC-0R and HPC-60R. As cracks occurred due to the pressure induced by corrosion products, fibers were engaged, providing confinement to the corroding rebar. The confinement of the accumulating corrosion products made the interface denser and reduced the movement of ions, oxygen and moisture in and out of the anodic site. This led to a reduced corrosion activity and less negative corrosion potentials. From

the corrosion potential results, it is also observed that the role of fibers became more apparent with longer induced current period. This is attributed to an increase in confinement when more corrosion products are formed. This resulted in a less negative potential of HP-G-HyFRC-48H as compared to those in HP-G-HyFRC-24H.

It is recognized that with the given corrosion potential values, compositions of corrosion products or passive film may be inferred. Based on Pourbaix diagram for steel at pH of about 13, corrosion potential of -600 mV vs SCE or -359 mV vs standard hydrogen electrode suggests that corrosion products would be of  $\text{Fe}^{3+}$ . However, to be discussed later, interfacial solution pH can be locally depressed under the impressed current due to acidification. At lower pH of about 10, the combination of pH and corrosion potential would give rise to the formation of corrosion products of  $\text{Fe}^{2+}$ . At even lower pH value, aqueous  $\text{Fe}^{2+}$  would be formed. The dissolved iron ion may leach out through cracks and transform into solid corrosion products when exposed to alkaline environment. With this, it is postulated that corrosion products contained a mixture of iron with valencies 2 and 3. The time dependence of the corrosion potentials and the interface pH values due to dilution or leaching may also imply the phase transformation of corrosion products.

The corrosion rates of corresponding samples after the applied current regimes are given in **Fig. 3.11**. For both 24 and 48 hours of applied current, corrosion rates for HPC-0R and HPC-60R were of similar magnitude. This is attributed to the nature of crack formation in the samples under accelerated corrosion tests. As corrosion products were formed and expansive pressure was built up, cracks were initiated at various locations in the samples. At the weakest point, crack would propagate to the surface and increase in size to accommodate additional strain induced by the accumulating corrosion products at the steel-concrete interface. The through macrocracks led to a more direct exposure of the rebar to the electrolyte. Hence, with similar crack patterns and amount of corrosion products, HPC-0R and HPC-60R with through macrocracks would have similar corrosion activity.

Interestingly, the corrosion rates in HPC samples were much smaller as compared to those observed in cracked plain concrete with added NaCl to be presented later in **Chapter 6**. For instance, with 48 hours of applied current, HPC-0R showed corrosion rates that is about 1/10 of that in plain concrete samples. This may be attributed to the wide cracking opening of high strength matrix and a reduced dissolution of  $\text{O}_2$  due to high concentration of NaCl in the immersion solution of this study. The phenomenon will be further explained in the discussion portion of the chapter. The beneficial effects of hybrid fibers were observed with the reduced corrosion rates in HP-G-HyFRC-24/48H. The presence of hybrid fibers in the composite reduced corrosion rates by about 2 times as compared to those found in plain HPC-0/60R. Fibers enhanced crack distribution of the composite under the expansive pressure induced by corrosion products. This helped to confine and densify corrosion products, leading to lower corrosion activity.

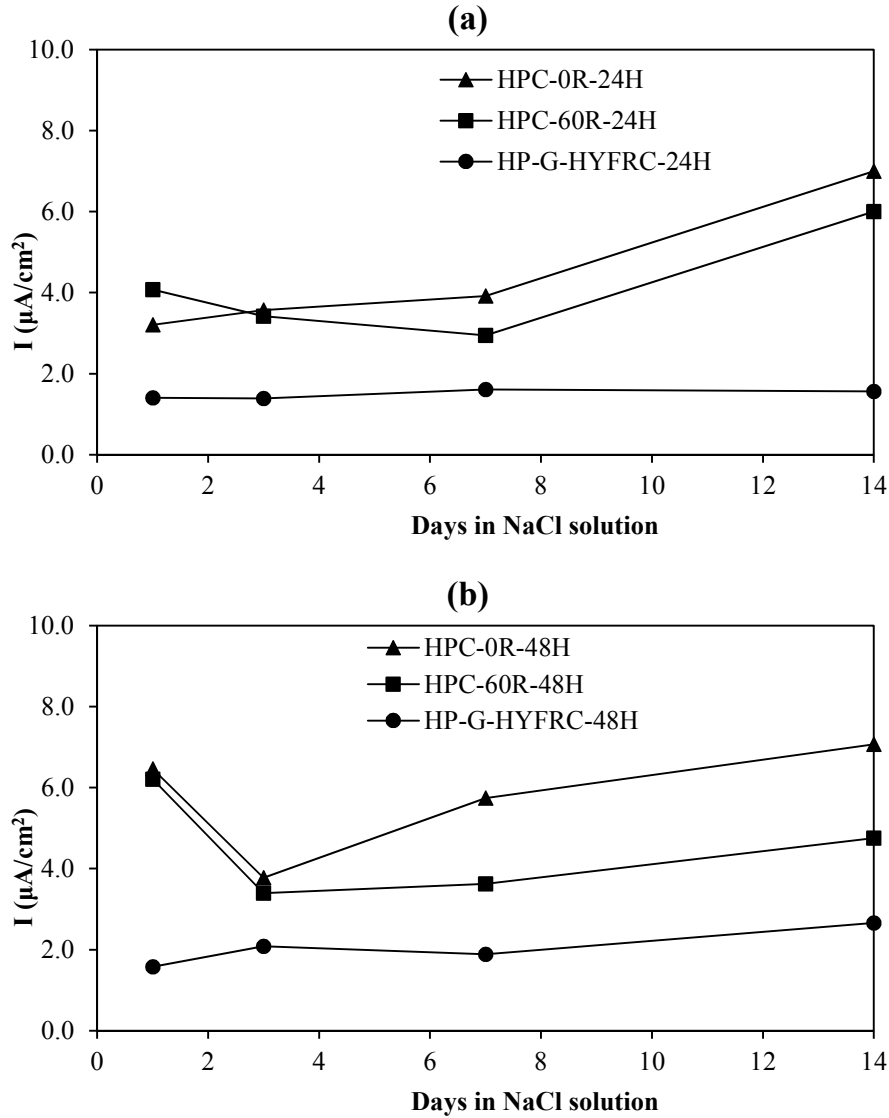


**Figure 3.11: Corrosion rates for HPC samples with applied current of: (a) 24 hours, and (b) 48 hours**

The exteriors of the samples were examined after the applied current. Pictures of the side and bottom faces of the samples with different applied current regime along with the maximum crack widths on the surfaces are given in **Fig. 3.12**. Macrocracks ranging from 1 to 2 mm in width were observed in HPC-0R/60R. Only a single macrocrack propagated to the surface of HPC-0R/60R with the applied current. The bottom surfaces showed that several non-through cracks developed around the rebar. The macrocracks, as discussed, loosened the steel-concrete interface and exposed the rebars to the electrolyte, leading to higher corrosion activity of the reinforcing steel as compared to uncracked concrete. Also, crack widths increased with the duration of the applied current. As more corrosion products are formed, the surrounding concrete experienced more prying action which led to wider crack opening. In contrast, HP-G-HyFRC showed distributed multiple cracks on their surfaces with the two induced current regimes. The deflection hardening



behavior of the composite led to the observed crack distribution under expansive pressure caused by corrosion products accumulated at steel concrete interface.

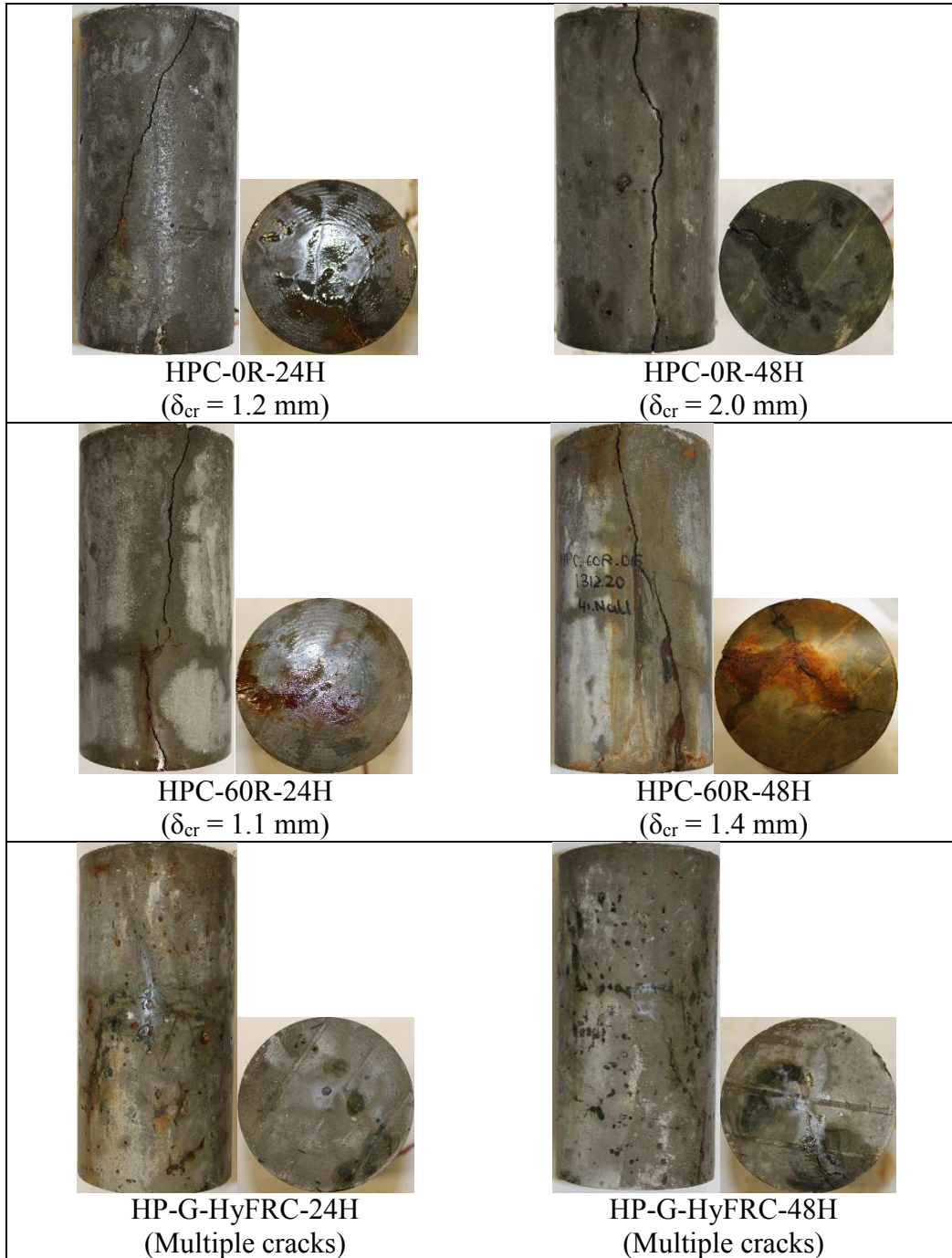


**Figure 3.12: Cracking on surfaces of samples with different regimes of applied current, with  $\delta_{cr}$  representing maximum observed crack width**

### 3.3.4 Gravimetric mass loss results

The corrosion samples were subjected to splitting tensile test to retrieve the embedded rebars. The gravimetric mass losses measured by cleaning the rebars and theoretical mass losses were

compared to study the effectiveness of the applied current. The theoretical mass loss is the sum of mass loss during the applied current and during 14-day period of the subsequent electrochemical measurements or just during the 98-day period of electrochemical measurements for samples with no induced current. The theoretical mass losses after the applied corrosion regime was based on time integration of the measured corrosion rates which were presented earlier. Corrosion rates were assumed to be negligible during the curing period. **Fig. 3.13** showed typical corrosion history experienced by a rebar in concrete under accelerated corrosion test. Between  $t_0$  and  $t_1$  (durations of 0, 24 or 48 hours), a current of  $1 \text{ mA/cm}^2$  was applied and the theoretical mass loss  $m_1$  corresponding to that period was found with Faraday's Law. After the applied current, the rebar still underwent corrosion activity although at a much lower intensity. Trapezoidal rule combined with Faraday's law was used to calculate mass loss between the electrochemical measurements. The total theoretical mass loss was the sum of the two mass losses.

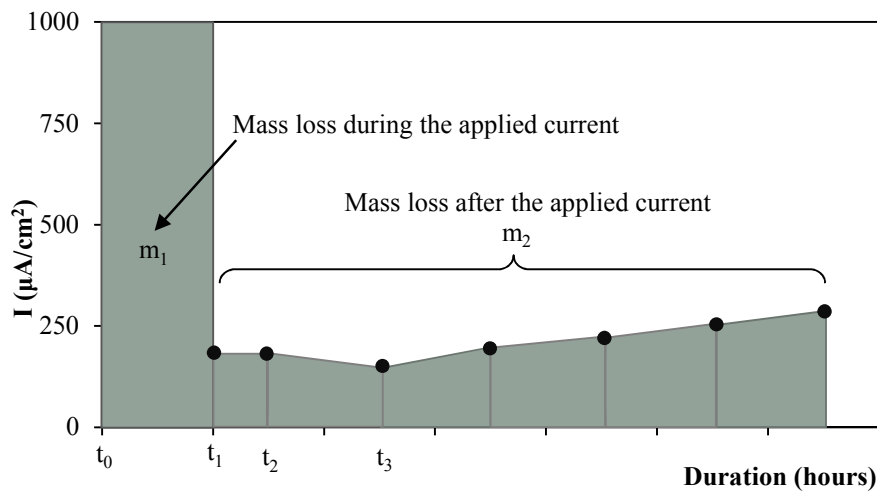


**Figure 3.13: Corrosion rates and time integration for theoretical mass loss measurement**

The results of gravimetric, theoretical mass losses and normalized mass losses (to the bar total weight) are summarized in **Table 3.3**. It is observed that for samples without any applied current, the gravimetric mass losses are always greater than the theoretical mass losses. This may be attributed to the etching of part of the base metal by the cleaning solution. For 24 and 48 hours of applied current, the gravimetric mass losses for HPC-0R and HPC-60R were greater than the theoretical mass losses. This may be attributed to acidification at the interfaces under high cell voltage. Acidification led to autocatalytic dissolution of steel. The acidic environment was induced by the hydrolysis of water by iron ions. This will be discussed in more details in **Chapter 4**. Nevertheless, for HP-G-HyFRC, the gravimetric mass losses were similar to the values based on theoretical analysis. The confinement effects of fibers densified corrosion products at the steel-concrete interface and this would make it more difficult to further oxidize the anode (embedded steel rebar). A higher cell voltage would have to be applied in HP-G-HyFRC to generate the required  $1 \text{ mA/cm}^2$  induced current, leading to breaking down of water and a net contribution to electron flow in the circuit and a subsequent reduced oxidation of the rebar. It is also observed that the mass loss values are not proportional to the corrosion rates obtained from electrochemical measurement. For instance, HP-G-HyFRC-24H had a corrosion rates that were about half of those

in HPC-60R-24H although its gravimetric mass loss was just 22% less. This is because a large proportion of the mass losses occurred during the applied current regime but it is the densification of the corrosion products at steel-concrete interface that played a critical role in determining the electrochemical corrosion rates.

**Table 3.3: Gravimetric and theoretical mass losses**

|                | Current 1mA/cm <sup>2</sup> | Gravimetric |       | Theoretical |
|----------------|-----------------------------|-------------|-------|-------------|
|                | Hours                       | ΔM (g)      | % M   | ΔM (g)      |
| HPC-0R-0H      | 0                           | 0.6         | 0.11% | 0.02        |
| HPC-0R-24H     | 24                          | 5.7         | 1.06% | 2.95        |
| HPC-0R-48H     | 48                          | 7           | 1.30% | 5.88        |
| HPC-60R-0H     | 0                           | 0.6         | 0.11% | 0.03        |
| HPC-60R-24H    | 24                          | 4.1         | 0.76% | 2.93        |
| HPC-60R-48H    | 48                          | 7           | 1.30% | 5.71        |
| HP-G-HyFRC-0H  | 0                           | 0.4         | 0.07% | 0.03        |
| HP-G-HyFRC-24H | 24                          | 3.2         | 0.59% | 2.83        |
| HP-G-HyFRC-48H | 48                          | 5.1         | 0.95% | 5.63        |

The higher cell voltages applied across the anode and cathode in HP-G-HyFRC to keep the induced current of 1 mA/cm<sup>2</sup> led to fiber corrosion and this was confirmed with corrosion spots on the surfaces of HP-G-HyFRC with 24 and 40 hours of applied current as shown in **Fig. 3.12**. In comparison, HP-G-HyFRC-0H surface showed little sign of corrosion spots. Surface of HP-G-HyFRC-0H after 98 days in NaCl solution is shown in **Fig. 3.14**. A smaller number of corrosion spots were observed even though the sample was immersed in the NaCl solution for much longer period of time (98 days). Further discussion on steel fiber corrosion and its effect on accelerated corrosion test will be provided in **Chapter 5**.

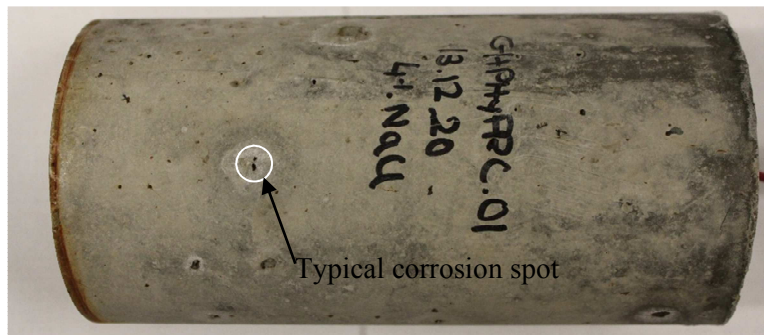


**Figure 3.14: Corrosion spots on HP-G-HyFRC-0H after 98 days in NaCl solution**

Bars before cleaning off corrosion products are shown in **Fig. 3.15**. No sign of corrosion was observed for all samples with no applied current. Corrosion occurred over the entire bars' areas for samples with induced current. 4% NaCl in the mixing water is effective in destabilizing the passive film and in causing a more uniform corrosion on the bar surfaces in concrete. The ability to accommodate corrosion products were minimal for all the samples due to their high strength and low interfacial porosity. As a result, corrosion-induced cracks were formed early, leading to direct exposure to the electrolyte of a portion of steel underneath the crack mouth. This portion of the rebar will experience higher dissolution under the applied current due to a lack of physical protection from concrete. Grooves were hence observed along the crack lines. The results implied

that for concrete with corrosion-induced crack, post-cracking corrosion may be concentrated to areas under the crack mouths and that may be detrimental to structures due to localized rebar diameter loss as compared to a case with more distributed corrosion. Also, due to a lack of confinement and densification, it is observed that the corrosion products on HPC-0R/60R were less intact as compared to those found in HP-G-HyFRC samples. Slightly longer immersion time in the cleaning solution and more brushing were required to clean corrosion products off rebars retrieved from HP-G-HyFRC samples.



**Figure 3.15: Bar surfaces showing no corrosion for samples with no applied current and uniform corrosion for samples with 24 and 48 hours of applied current**

### 3.3.5 Flatbed digital imaging and optical microscopy

The flatbed scanned images of corrosion sample sections are shown in **Fig. 3.16**. Marks for visible cracks were also drawn on the surfaces. With 24 and 48 hours of applied current, as compared to HP-G-HyFRC more extensive cracks occurred for HPC-0R/60R. Single major crack with a few secondary cracks were observed in these set of samples. As the samples disintegrated during the cutting process, the cracks observed in the graphs were not indicative of the real crack widths. On the other hand, cracks in HP-G-HyFRC samples were distributed throughout the surface. As cracks formed, the bridging fibers got stressed. When the crack width grew, the pullout resistance of the bridging fibers also increased as a result of the deflection hardening behavior of the composite. The enhanced resistance to pullout led to new crack formation. The distribution of cracks and subsequent reduced crack opening prevented the egress of corrosion products. The corrosion products would fill up the microcracks and lead to crack plugging and interfacial densification. The limited access of oxygen, moisture and movement of ions in and out of the anodic area led to lower corrosion activity as observed in the corrosion rate results.



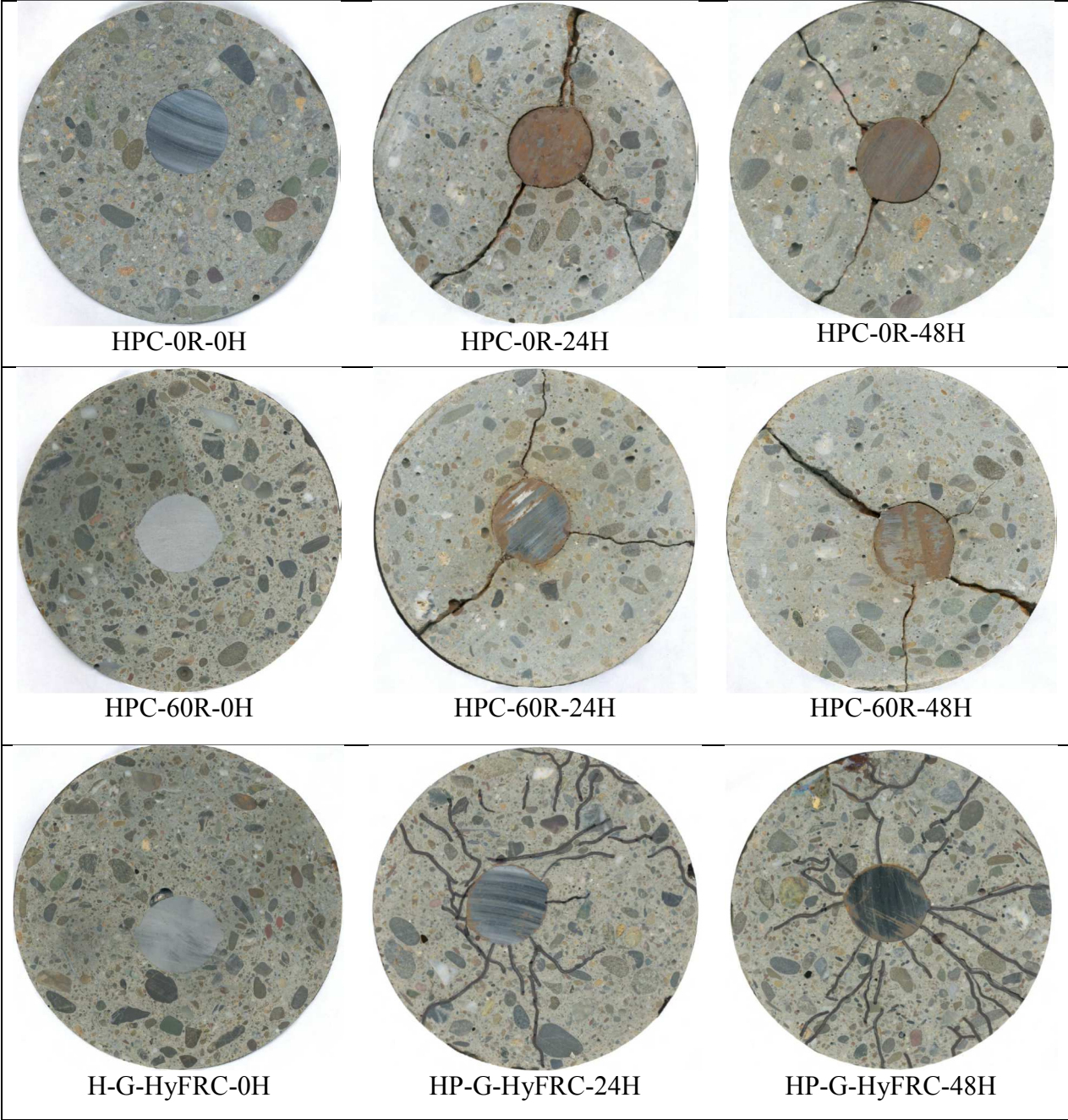


**Figure 3.16: Scanned images of sections for corrosion samples**

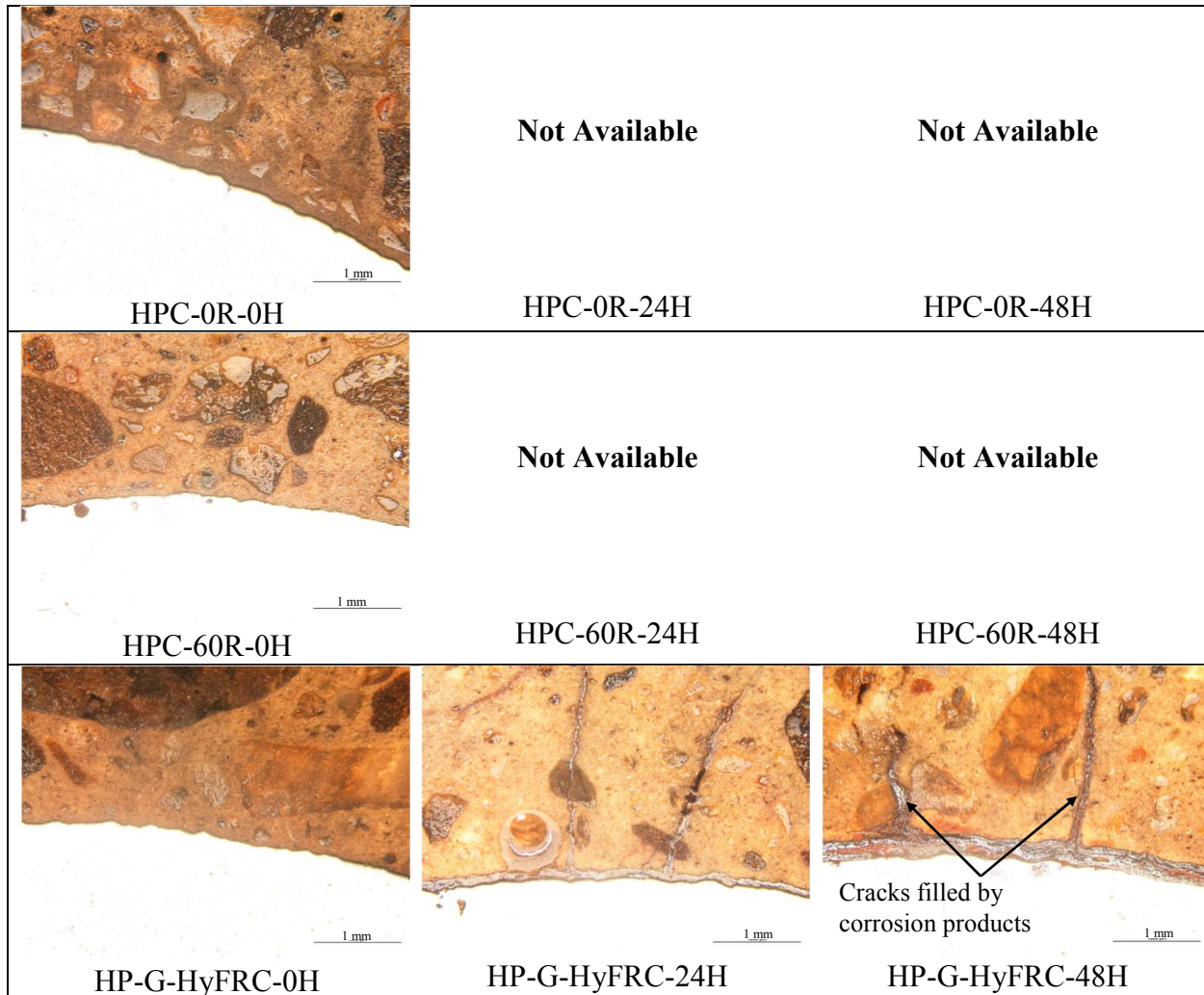
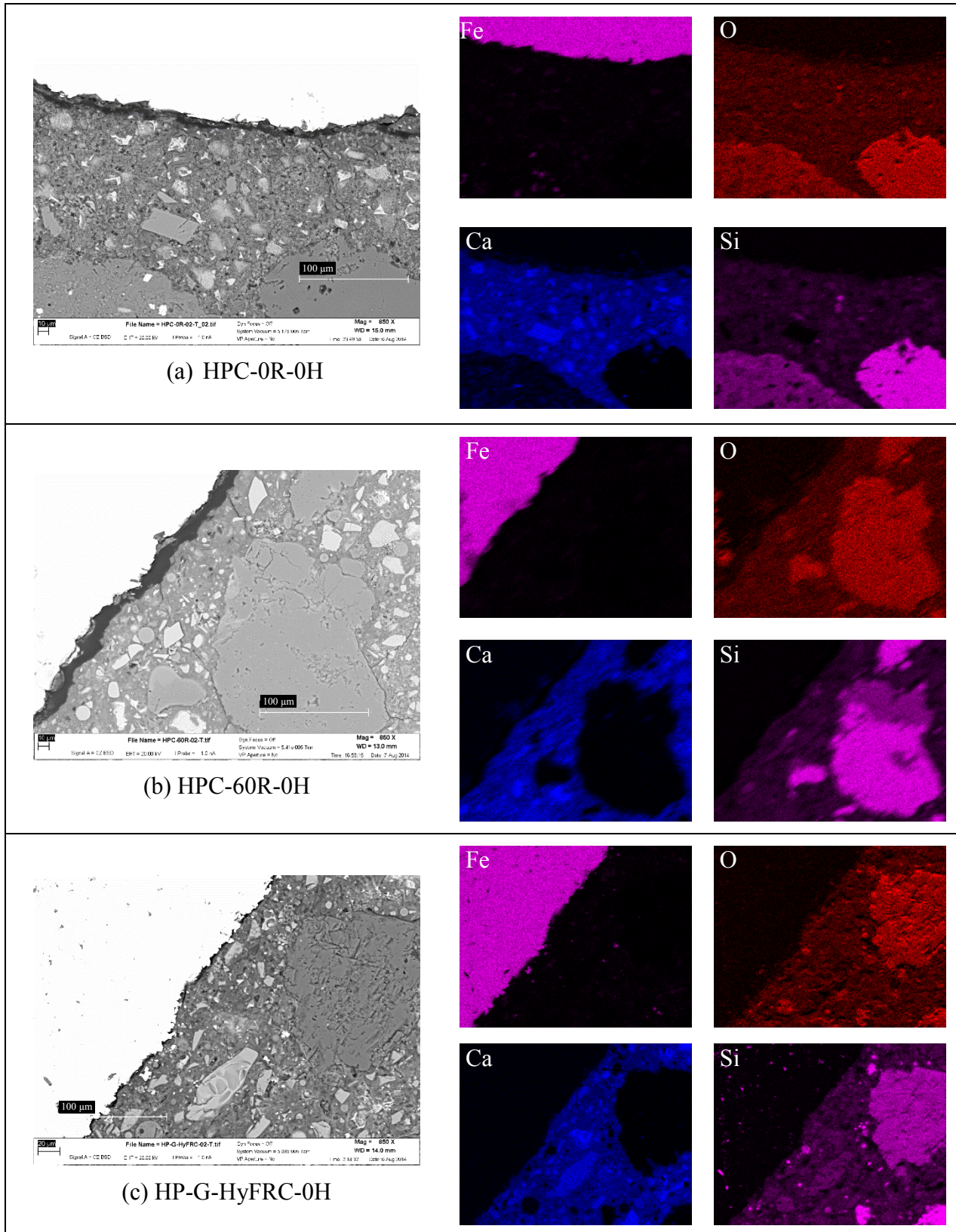


**Figure 3.17: Optical microscopic results for steel-concrete interfaces**

The optical microscopy results at steel-concrete interfaces for corresponding samples are shown in **Fig. 3.17**. No optical microscopy results could be obtained for HPC-0R/60R-24H and HPC-0R/60R-48H samples as they broke apart during cutting. In the micrographs, the dark areas represent corrosion products. It is observed that no corrosion products formed for HPC-0R/60R-0H and HP-G-HyFRC-0H. This substantiates the corrosion inactivity of these samples as presented in the corrosion rate results. With applied current, corrosion products accumulated at the interface and cracks in HP-G-HyFRC samples. The corrosion products were dense as oven drying did not cause extensive cracking to the corrosion layer. To be presented in the next chapters, extensive cracking of corrosion layers after oven drying were observed for samples made with lower strength concrete. Also, wedge-shaped cracks were observed in the HP-G-HyFRC samples as a result of the crack bridging by the hybrid fibers. These cracks were filled up with corrosion products, leading to densification and contributing to a reduction in corrosion activity.



### 3.3.6 BSE & EDX element mapping



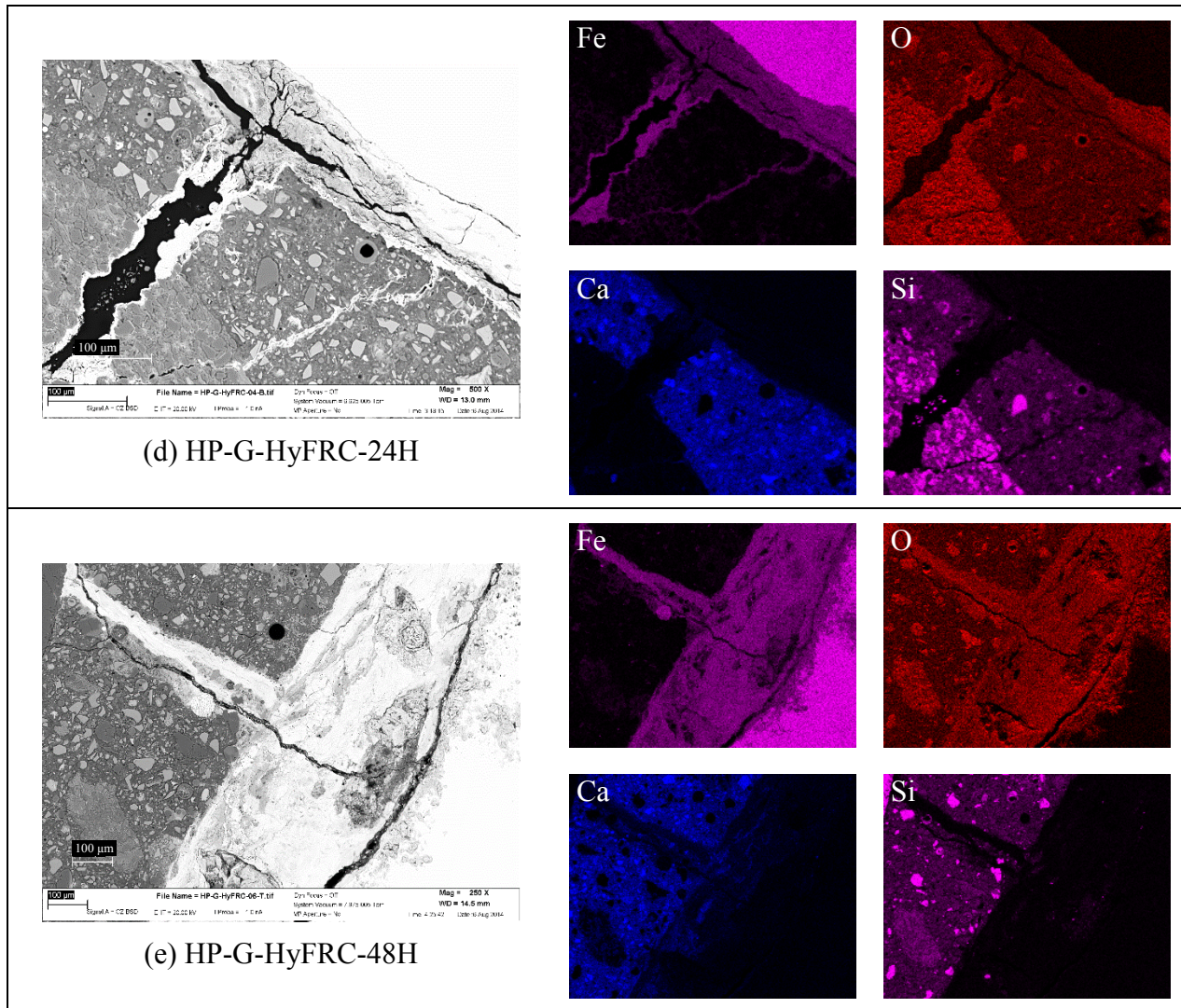


**Figure 3.18: BSE images and corresponding EDX element mapping for: (a) HPC-0R-0H, (b) HPC-60R-0H, (c) HP-G-HyFRC-0H, (d) HP-G-HyFRC-24H and , (e) HP-G-HyFRC-48H**

The backscattered electron (BSE) images and corresponding EDX element mapping of the corrosion samples with different regimes of applied current are shown in **Fig. 3.18**. It is observed that although the matrix around the steel was dense, a gap occurred between steel and concrete in HPC-0/60R. This is attributed to oven-drying and the resulting drying shrinkage in the specimens. Hsu et al. (1963) observed that microcracking between aggregates and mortar exists before any loading due to drying. Contrary to general belief, a mathematical model conducted by Hsu (1963) confirmed that high tensile stress can exist at aggregate-mortar interface and within the matrix depending on the clear distance between aggregates. Using photo-elastic analysis, it was shown that due to a restraint from adjacent aggregates, tensile stresses in the paste and at the aggregate-cement paste interface were created by drying shrinkage (Theocaris & Koufopoulos, 1969). This resulted in circumferential and radial cracking on all levels of the fractal scale in concrete (Hearn, 1999) as depicted in **Fig. 3.19**. Cracks between aggregates and cement paste in dried mortar were also observed by Bisschop & van Mier (1999) using environmental scanning electron microscopy.



In parallel to this, as HPC-0R matrix shrank during oven drying, the matrix would be restrained by the dispersed fine and coarse aggregates. As the bond between the steel rebar and the matrix was weaker due to its larger size and the resulting more interfacial defect, the bond crack would be concentrated at steel-concrete interface. This resulted in rebar separation from the matrix as observed in the SEM images. Also, it is observed that the presence of slag and fly ash increased the separation of steel and concrete, attributed to an increase in drying of the matrix.

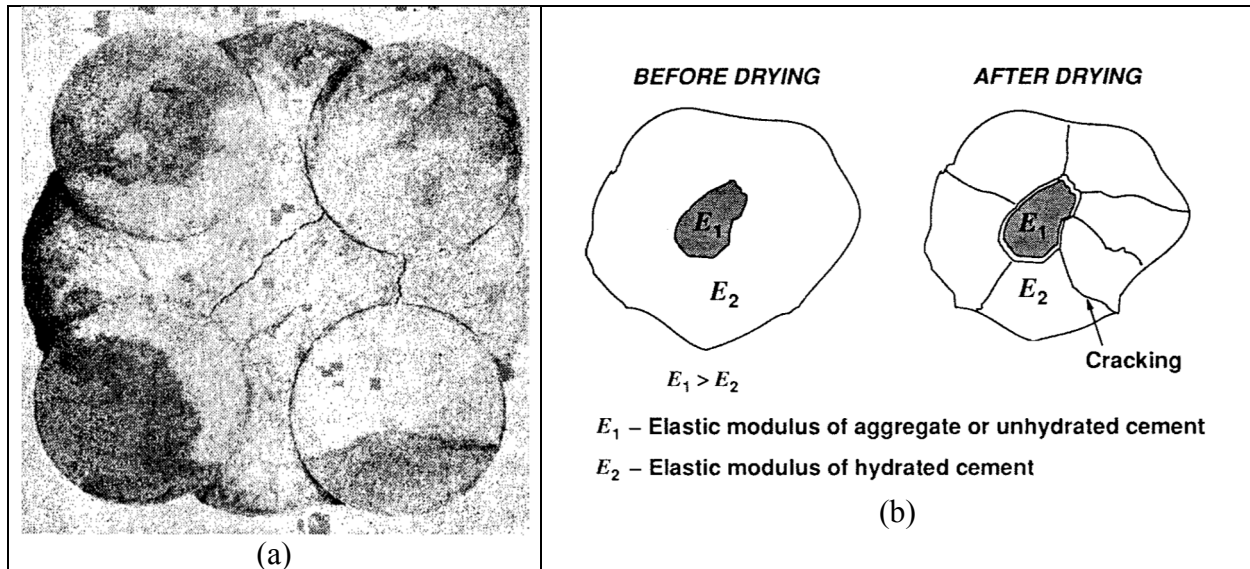


**Figure 3.19: Circumferential and radial cracking due to drying shrinkage: (a) Four-sandstone disc model (Hsu, 1963), and (b) cracking schematic of an isolated aggregate in the matrix (Hearn, 1999)**

In contrast, steel and the matrix were in intimate contact in HP-G-HyFRC-0H. The presence of hybrid fibers helped to restrict shrinkage in the samples. The bond between the aggregate and steel rebar may also be increased with the presence of fibers. Kim & Robertson (1998) showed that inclusion of a small amount of PVA in concrete matrix caused cohesive failures of the cement paste and limestone aggregate, arising from reduction in thickness of interfacial transitional zone due to hydrophilic nature of PVA fibers. Hence, in addition to the confinement effects during the propagation stage, hybrid fibers in concrete also led to a more intimate contact between steel and concrete and this provided a physical protection against corrosion initiation in concrete. Consistent with optical microscopy results, the corrosion layers were dense in HP-G-HyFRC as evident by the minimal cracking they experienced after oven-drying. A clear boundary between the matrix and corrosion layer was also observed, meaning that corrosion products were not able to penetrate into the matrix of HP-G-HyFRC beyond the crack lines. This led to an early onset of cracking and wider crack width at the end of the induced current regimes for plain HPC. This will be more evident when corrosion resistance of lower-strength concrete are presented in the next chapters.

A similar densification of corrosion product layers in strain hardening cementitious composite (SHCC) were observed with BSE element mapping and nano indentation by Šavija et al. (2014). Precipitation of iron oxides was not observed in the material matrix around the reinforcement and the elastic modulus values for the confined corrosion product in SHCC were found to be between 49.4 and 67.9 GPa. In control samples with no fibers, the corrosion product layer showed signs of

cohesion loss, possibly attributed to a lack of confinement or partial leaching of corrosion products. This resulted in lower elastic modulus values of corrosion product layer in the control samples. As corrosion products are more thermodynamically stable than steel, their densification at steel-concrete interface due to fiber confinement will protect the steel substrate in a similar manner to steel protection by the passive film. The dense corrosion product layer will limit the movement of O<sub>2</sub>, moisture and ions between the steel substrate and the electrolyte, resulting in a reduction in electrochemical activity of the steel substrate. This explains the low corrosion rates of HP-G-HyFRC in which the bridging fibers confined and densified the accumulated corrosion products at steel-concrete interface.

### 3.3.7 ICP results

Pore solution chemistry can affect the quality of the passive film and the passivity of steel. The concentration of Ca, Na and K of pore solutions extracted from pastes corresponding to HPC-0R and HPC-60R are given in Fig. 3.20. It is observed that Ca concentration is much lower as compared to that of Na and K. This means that the alkalinity of the pore solutions were mainly controlled by Na and K. The replacement of cement by slag and fly ash in paste reduced the total alkalinity (Na + K) in the pore solution. However, pH values were not greatly reduced to detrimentally affect the steel passivity in concrete. Pore solution pH values were calculated based on the total alkalinity and were found to be 13.5 for HPC-0R and 12.9 for HPC-60R. The pore solution pH values were greater than 10.5 which is the level that the protective mechanism of passivity on steel can be maintained (Roy et al., 1999). Hence, the replacement of cement by 45% slag and 15% fly ash will not compromise the initial passivity of steel in concrete although its effects on Cl<sup>-</sup>-induced pitting may be adverse due to a reduction in total alkalinity in the pore solution.

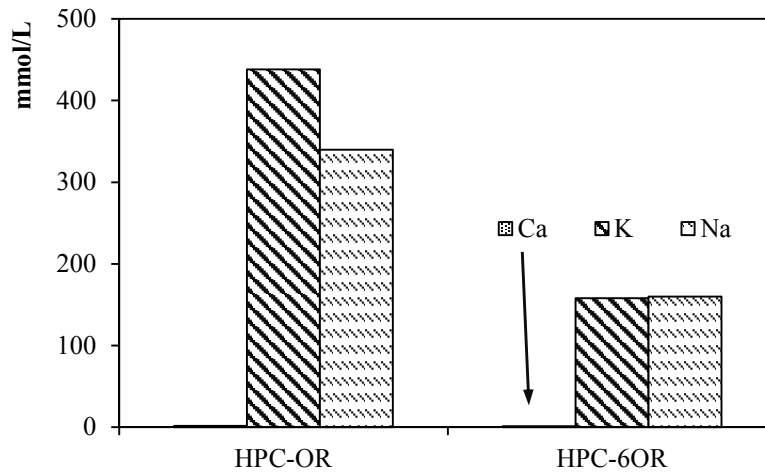


**Figure 3.20: Chemical concentrations in pore solution of pastes at 1 month**

## 3.4 Discussion

### 3.4.1 Time to cracking under accelerated corrosion test

Typical graphs for cell voltage to generate a current of  $1 \text{ mA/cm}^2$  against time up to 80000 seconds for the three concrete mixes are shown in **Fig. 3.21**. With reference electrode sense connected to the counter electrode and with assumed negligible resistance of the cable and connection junctures, the cell voltage can be regarded as a voltage between the cathode and the anode. The voltage values were presumably compensated for the voltage drop across concrete and the electrolyte although, to be discussed in the next part of the report, this may not be the case. Duration of 80000 seconds (22 hours) was adopted for consistency as the application of the current regime for some of the samples had to be put on hold for a short period of time to allow for electrochemical measurements of other samples at designated dates. The vertical axis represented the required voltage measured against the counter electrode to maintain a flowing current of  $1 \text{ mA/cm}^2$ . As concrete cracked, the interfacial resistance was reduced and steel was more exposed to the environment, leading to a drop in the cell voltage value. It is observed that the first crack usually occurred between 10000 seconds to 20000 seconds after the start of the applied current. With 20000 seconds, the corresponding theoretical mass loss was estimated to be 0.65 g. This is equivalent to a radius loss of  $7.5 \text{ }\mu\text{m}$  for the bar size used in the corrosion study. This is much less than the suggested radius loss values of  $15\text{-}50 \text{ }\mu\text{m}$  to cause the first visible crack in normal strength concrete (Alonso et al., 1998). In their experiment, 3%  $\text{CaCl}_2$  by cement weight was added into the mix and accelerated corrosion test with applied constant current of  $0.1 \text{ mA/cm}^2$  was also implemented. The accelerated nature of the experiment makes a direct comparison of the magnitude of radius loss on concrete cracking. An even higher radius loss value in the range of  $100\text{-}200 \text{ }\mu\text{m}$  was suggested by other researchers in natural corrosion (Browne, 1980; Wong et al., 2010). Although natural corrosion allows for more corrosion products to penetrate into the matrix, the much smaller observed radius loss of steel prior to crack in HPC is attributed its dense interface. Hence, high-strength concrete is susceptible to an early onset of cracking under corrosion as compared to the more porous normal strength concrete counterpart. It is also noted that the cell voltage stabilized after the first drop in HPC-0/60R. In contrast, the cell voltage values fluctuated in HP-G-HyFRC. As the cell voltage dropped when the first crack was formed, more corrosion products formed and accumulated between steel and concrete interface. They were subsequently confined by the fibers. The confinement densified the steel-concrete interface, leading to higher cell voltages to induce the  $1 \text{ mA/cm}^2$  current. The cell voltage dropped again when new cracks were formed. The many fluctuations of the cell voltage values (highlighted in the diagram) corresponded to crack formations and subsequent densification at steel-concrete interface. The confinement effect of fibers were also evident from the higher cell voltages to generate  $1 \text{ mA/cm}^2$  current in HP-G-HyFRC as compared to the level applied in HPC-0/60R after crack formation.

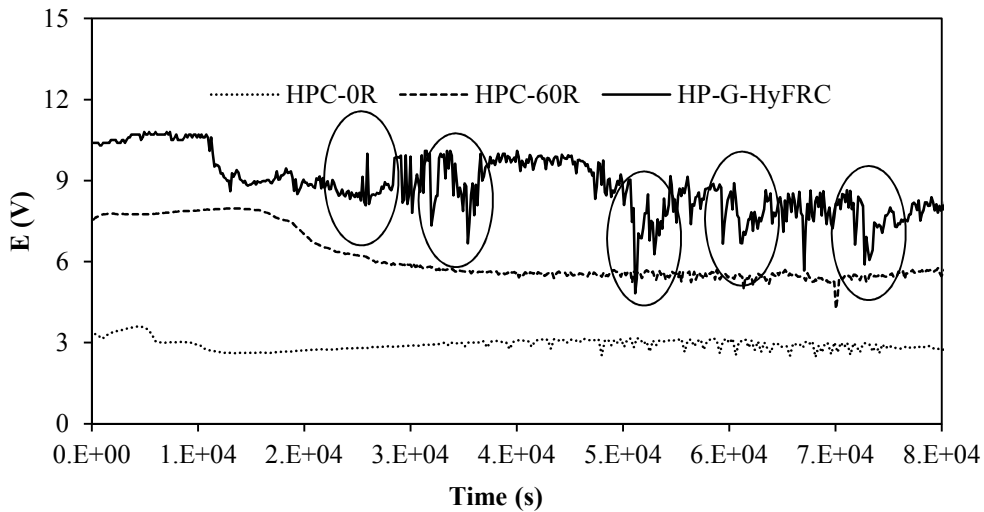


**Figure 3.21: Cell voltage (presumably compensated) with time for HPC-0/60R and HP-G-HyFRC to generate 1 mA/cm<sup>2</sup> applied current**

### 3.4.2 Cell voltage and IR compensation

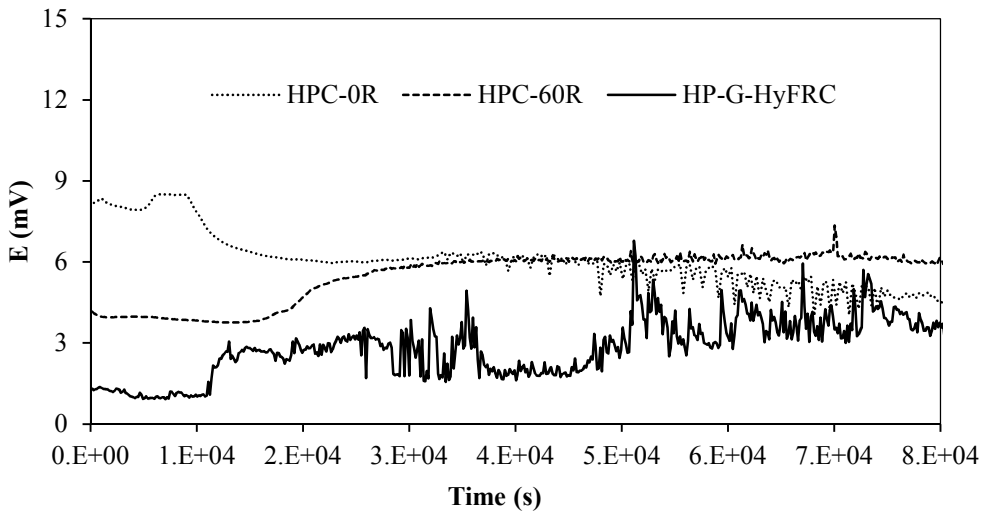


**Figure 3.22: Cell voltage (uncompensated) with time for HPC-0/60R and HP-G-HyFRC to generate 1 mA/cm<sup>2</sup> applied current**

As IR compensative option was activated during the tests, the cell voltage values shown in **Fig. 3.21** were presumably compensated for a voltage or IR drop caused by concrete and the electrolyte. However, it seems that the Potentiostat was not able to accurately capture the IR drop in the experiment. Graphs for uncompensated cell voltage against time for the same samples in **Fig. 3.21** are shown in **Fig. 3.22**. It is observed that although the uncompensated cell voltage increased as expected in HPC-60R, the values decreased in HPC-0R (early stage of the applied current) and HP-G-HyFRC samples. Although exact reasoning has yet to be further investigated, the current

interrupt method employed in the Potentiostat (Gamry Instruments, 2011) did not seem to work in concrete with SCM replacement and steel fibers as reinforcement. Nevertheless, the fluctuation of the cell voltages follows the trend in Fig. 3.21.

### 3.4.3 Corrosion cracking process and damage mitigation due to fibers

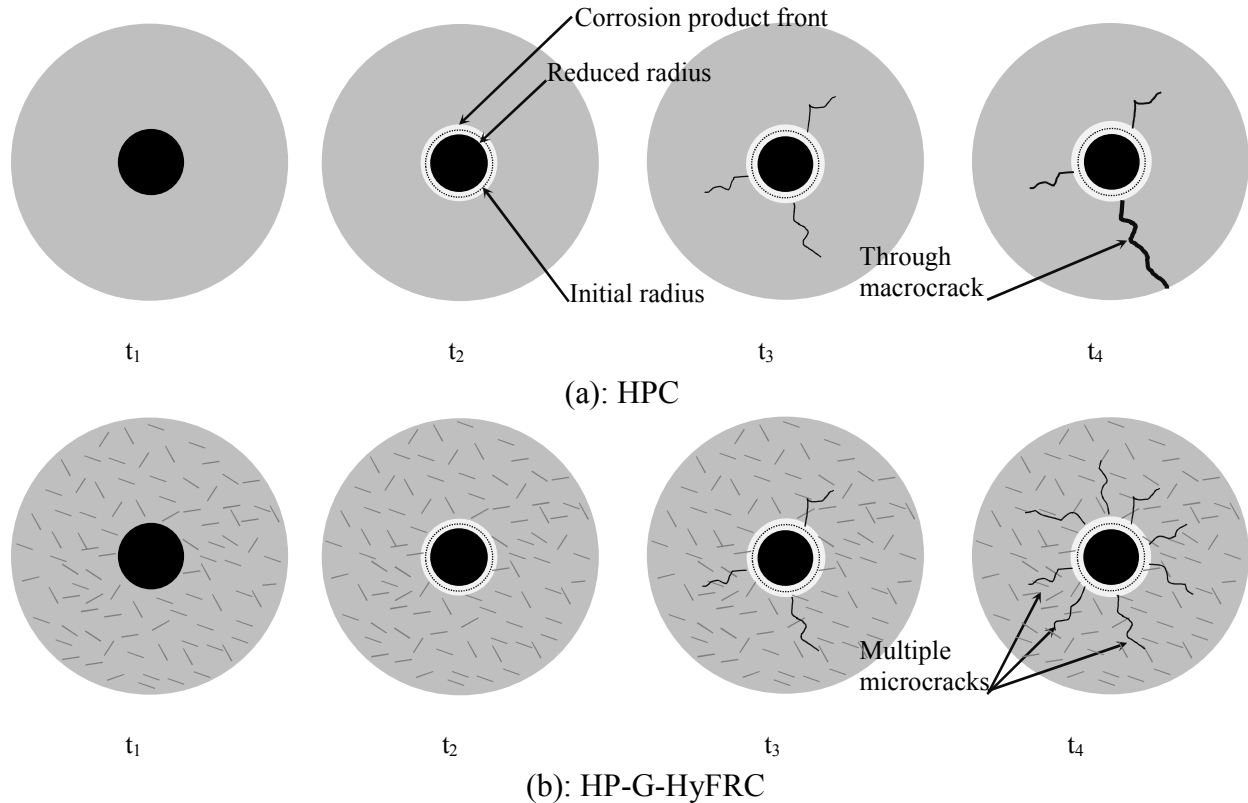


**Figure 3.23: Crack propagation process in (a) HPC and (b) HP-G-HyFRC under applied current**

To better understand the role of fibers in restricting cracking and limiting damage caused by corrosion products, a model for cracking process is proposed for HPC and HP-G-HyFRC and is shown in Fig. 3.23. It is based on a thick-walled cylinder idealization to model concrete cover damage from reinforcement bar corrosion as adopted by many authors (Balafas & Burgoyne, 2010a; Balafas & Burgoyne, 2010b; Pantazopoulou & Papoulia, 2001; Weyers, 1998). The schematic is applicable from the time of the current application to the time that macrocrack forms in HPC. The current is assumed to be applied at time  $t_1$ . At time  $t_2$ , corrosion products are formed but no pressure is exerted on the surrounding matrix as corrosion product is accommodated by the voids at the steel-concrete interface. At time  $t_3$  when more corrosion products are formed and exceed the critical quantity that can be accommodated by the space at steel-concrete interface, pressure is exerted on the surrounding matrix. The higher hoop stress near the rebar means that cracks will be initiated from the steel-concrete interface outward when the tensile stress of the matrix is exceeded. At time  $t_4$ , more corrosion products are formed and higher strain will be experienced by the matrix. Ultimately, crack will propagate to the surface of the HPC cylinder. In HP-G-HyFRC, further propagation of the existing cracks is prevented by the bridging fibers. As a

result, the strain energy is dissipated through formation of new cracks, leading to multiple microcrack formation as depicted at time  $t_4$  of **Fig. 3.23 (b)**. The process can be applied to lower strength concrete although time  $t_2$  may be longer due to a higher capacity of the lower strength concrete to accommodate corrosion products as a result of its increased porosity.

#### **3.4.4 Influence of fibers in corrosion propagation stage**

Steel fiber bridging a corrosion-induced crack is shown in **Fig. 3.24 (a)**. For comparison, **Fig. 3.24 (b)** showed a steel fiber which did not bridge any corrosion-induced crack and which did not show any sign of corrosion. Microcracks with no trace of corrosion products emanating from the steel fiber are believed to be caused by drying shrinkage. The arrow in **Fig. 3.24 (a)** points to a crack emanated from the corroded steel rebar. When the crack path met the steel fiber, the crack was deviated and energy was absorbed. The dissipated strain energy was translated into branching of cracks near the tip of the fiber. The stress on the fibers caused debonding of the fibers from concrete and a loose steel fiber-concrete interface was created, leading to a reduced physical protection to the fibers from the concrete against corrosion. As a result, fibers would corrode during both the remaining applied current regime and the NaCl immersion period. The phenomenon is similar to a fiber corrosion under applied current (to be elaborated in **Chapter 5**) and natural corrosion of steel fibers near concrete surface due to fiber exposure to the electrolyte. The latter corrosion is common although the corrosion imposes no adverse effect on the overall durability of structures. Only steel fibers up to a depth of 0.2 mm contributed to spot corrosion observed on concrete surface (Balouch et al., 2010). From the crack branching observation, the beneficial effects of PVA microfibers would be twofold. The pullout process creates microcracks along the steel fiber-concrete interface. Under the presence of PVA fibers and their microcrack arresting capability, the pullout would require more energy and this would enhance the pullout resistance of the steel fibers. This was elaborated in **Chapter 2** of the report. Also, during the corrosion of the disturbed fibers, PVA fibers also help to limit crack-induced corrosion along the steel fibers. This reduced corrosion activity of the steel fibers and maintained the integrity of concrete surrounding the fibers. Hence, the synergistic actions of steel macrofibers and PVA microfibers helped to prolong the structure's life under corrosion.

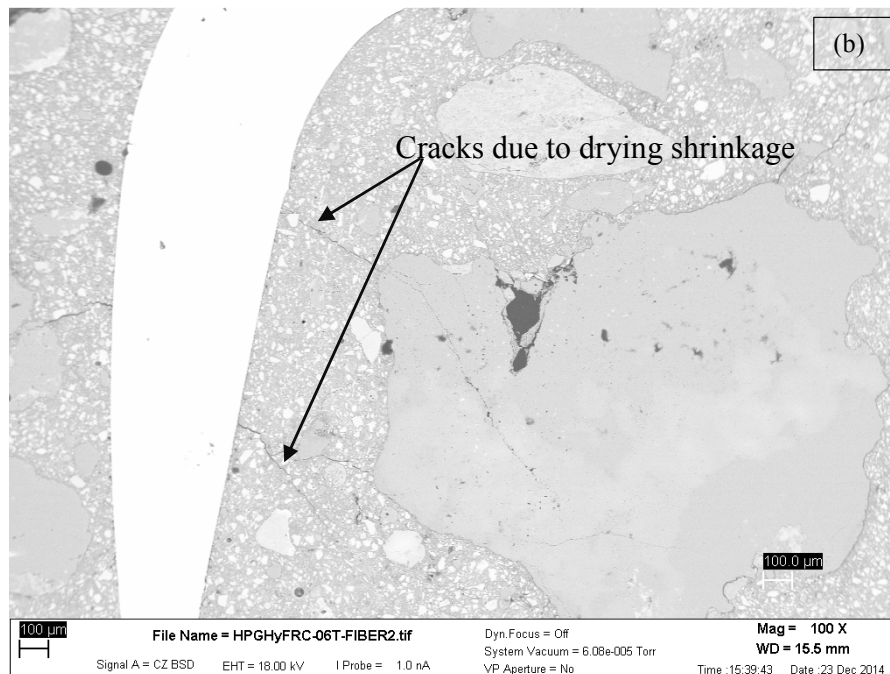
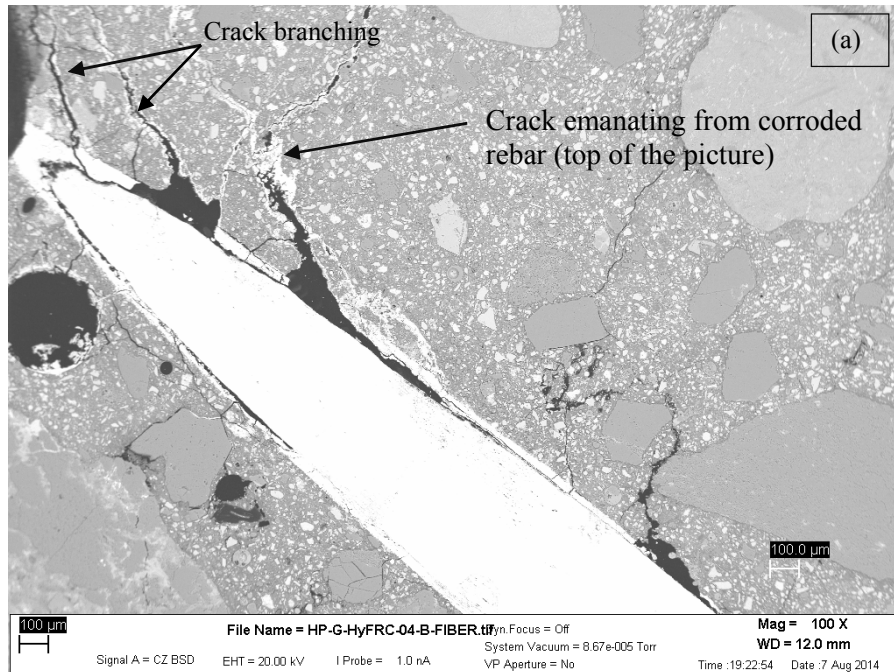


**Figure 3.24: (a) Steel fiber bridging corrosion-induced crack, and (b) steel fiber not bridging corrosion-induced crack**

### 3.4.5 Residual strength after applied current

After electrochemical measurements, the corrosion samples were dried in an oven and subjected to tensile splitting test for rebar retrieval. For consistency, the samples were arranged such that the widest cracks were directed upward. The tensile splitting strengths are summarized in **Fig. 3.25**. It is observed that with either 24 or 48 hours of applied current, the splitting tensile strengths in HPC-

0/60R were reduced by more than 50% as compared to the strength of samples with no applied current. HP-G-HyFRC showed a reduction in strength of only 8% for 24 hours of applied current and 23% for 48 hours of applied current. The bridging action of fibers maintained the integrity of the samples, resulting in high residual strength in HP-G-HyFRC as observed in the results.

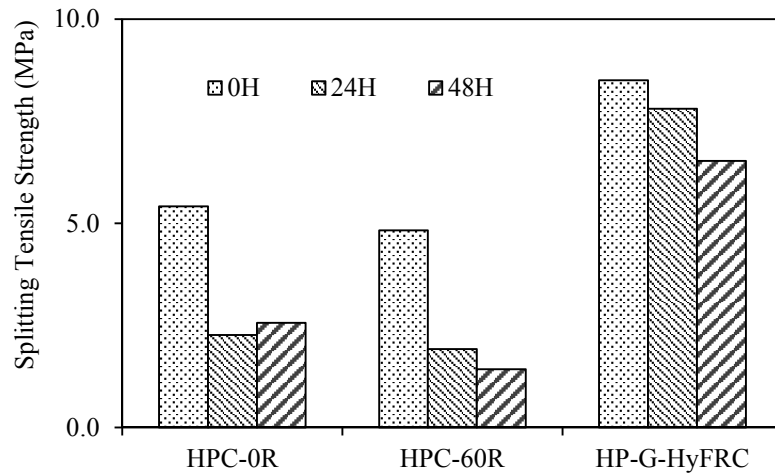


**Figure 3.25: Tensile splitting results of corrosion samples**

### 3.4.5 Cracking and diffusion control of corrosion in NaCl-concentrated solution

It was observed that HPC-0R and HPC-60R experienced wide cracks after the applied current regimes. With this level of damage, it was expected that the corrosion rates would be very high. According to Andrade & Andrade (1996), the maximum average corrosion rate measured in laboratory conditions can go up to  $100 \mu\text{A}/\text{cm}^2$  in cracked concrete submerged in sea water. The observed corrosion rates of HPC-0R and HPC-60R with 24 and 48 hours of applied current were found to be less than 1/10 of the observed maximum value. This is attributed to two factors: (i) cracking characteristic of the dense matrix, and (ii) cathodic control of corrosion reaction due to limited dissolution of oxygen. As shown, wide cracks were observed in HPC-0R and HPC-60R with 24 and 48 hours of applied current. The wide crack opening ensured that the interfacial condition reach an early steady state with the immersion pore solution. With abundant  $\text{Cl}^-$ , the steel-concrete interface can actually form a crevice with low pH environments, causing an increase in corrosion activity (Gonzalez et al., 1990). However, the loose interface after cracking and the resulting neutralization of the acidic pore solution by the immersion solution led to the low corrosion activity in crack HPC-0R and HPC-60R. Interfacial acidification will be further discussed in **Chapter 4**. Also, by using best fit to experimental data to form an equation of state of dissolved oxygen, Sherwood et al. (1992) showed that dissolved oxygen at  $25^\circ\text{C}$  was reduced from  $6.79 \text{ g/L}$  at 3.5% NaCl (typical NaCl concentration of seawater) to  $2.85 \text{ mg/L}$  at 17.5% NaCl (NaCl concentration in the immersion solution). This represents a reduction factor of 2.4. To quantify its effect on corrosion rate, bare bar was immersed in 3.5% and 17.5% NaCl solution and its corrosion rates were measured. It was found that its corrosion rate in 17.5% NaCl solution was about 15% lower than that in 3.5% NaCl solution. The amount of dissolved oxygen in the immersion solution was expected to be even less in view of the presence of other dissolved ions leaching from the concrete samples during the immersion period.



### 3.4.5 Mass loss rates

The gravimetric mass loss ( $m_1$ ) during the applied current between time  $t_0$  and  $t_1$  was estimated by subtracting the theoretical mass loss ( $m_2$ ) after the applied current from the total gravimetric mass loss. The results for the gravimetric mass losses during the applied current regimes only are summarized in **Table 3.4**. As the corrosion rates during the immersion period were relatively small as compared to the applied current intensity magnitude, the mass losses during the applied current were similar to the total gravimetric mass losses. It is also observed that the mass losses seemed to be concentrated during the first 24 hours of the applied current, accounting for 83%, 58% and 63% in HPC-0R, HPC-60R and HP-G-HyFRC, respectively. It is postulated that the thickening and densification of the corrosion product layer between the steel-concrete interface reduced the oxidation rate of iron by the applied current. The nonlinearity of corrosion product growth has been proposed by Liu & Weyers (1998) in modelling time-to-corrosion cracking in chloride-contaminated reinforced concrete structures. It was suggested that the rate of corrosion product growth decreases in proportion to the amount of the products. The mass loss results in this study serve as an experimental proof to the theory. The decreasing rate of corrosion product production has been successfully implemented to model service life of concrete structures subjected to chloride-induced corrosion by many researchers (Balafas & Burgoyne, 2010b; Li et al., 2006; Pantazopoulou & Papoulia, 2001; Vu et al., 2005)

**Table 3.4: Estimated gravimetric mass loss during the applied current period**

|                | Current 1mA/cm <sup>2</sup> | Approximate mass loss during $I_{app}$ |
|----------------|-----------------------------|--|
|                | Hours                       | $\Delta M$ (g)                         |
| HPC-0R-24H     | 24                          | 5.5                                    |
| HPC-0R-48H     | 48                          | 6.7                                    |
| HPC-60R-24H    | 24                          | 3.9                                    |
| HPC-60R-48H    | 48                          | 6.8                                    |
| HP-G-HyFRC-24H | 24                          | 3.1                                    |
| HP-G-HyFRC-48H | 48                          | 5.0                                    |

### 3.4.6 Structural service life under corrosion

In concrete structures, chloride penetration is facilitated through cracks formed by shrinkage and mechanical loading. With this regard, corrosion initiation in HP-G-HyFRC can be delayed with the presence of fibers which help to prevent shrinkage cracking and to distribute cracks induced by mechanical loading. Also, the ability of HP-G-HyFRC to form multiple cracks and to maintain its mechanical properties with the applied current are beneficial in corrosion propagation stage. The structural service life models for HPC with no fiber inclusion and HP-G-HyFRC under chloride-induced corrosion are proposed and shown in **Fig. 3.26**. The models were based on a work by Cady & Weyers (1984) on modelling service life of bridge decks, which was later further elaborated by Weyers (1998). The vertical axis represents level of damage. The dotted horizontal line represents a level of damage that limits the functionality of structures. This may be taken as the time of extensive corrosion cracking and concrete spalling in reinforced concrete structures for which rehabilitation is required. At time  $T_1$ , initial damage resulted from construction defects and cracking caused by loading are induced.  $T_1$  also marks the beginning of ingress of chloride ions

into concrete. Times  $T_2$  and  $T_3$  correspond to corrosion initiation in HPC and HP-G-HyFRC, respectively. Due to more initial damage or cracking, it is proposed that corrosion is initiated earlier in HPC. As corrosion products will have to fill up the porous zone at steel concrete interface before exerting pressure and cracking to the surrounding matrix as proposed by Weyers (1998), further damage was delayed for a period of time after corrosion initiation. When corrosion-induced cracking occurs, the hybrid fibers in HP-G-HyFRC bridge and distribute cracks and as a result the level of damage in the composite increases gradually as compared to a more abrupt increase in damage level in HPC. As a result, it is observed that the service life of HP-G-HyFRC structures is much longer than that of HPC with no fiber reinforcement.

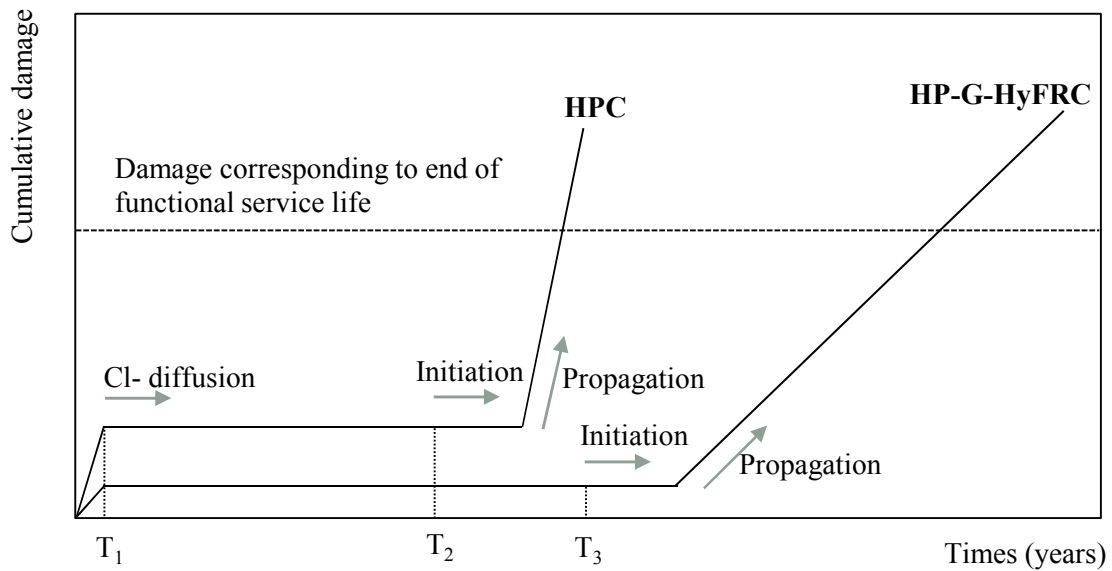


**Figure 3.26: Proposed structural service life models for HPC and HP-G-HyFRC**

### 3.5 Conclusions

From the results and discussion, the following can be concluded from this study:

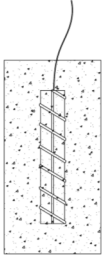
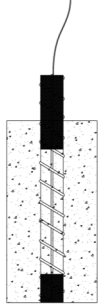
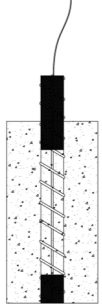
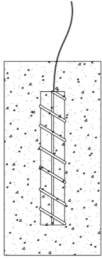
- Without any applied current, corrosion activity of all high performance concrete samples were low and were in an inactive region. This is attributed to the dense concrete and a dense steel-concrete interface which limit movement of ions, moisture and  $O_2$  to participate in corrosion reactions.
- When electrical current was applied to cause corrosion, the corrosion rates for plain HPC with or without supplementary cementitious materials were of similar levels irrespective of the current magnitudes. A similar pattern of macrocracks led to a similar condition at steel-concrete interface, resulting in similar measured corrosion rates.
- The dense steel-concrete interface in HPC led to an early onset of corrosion cracking as compared to lower-strength concrete with a more porous interface and a better ability to accommodate corrosion products.
- Because of the deflection hardening behavior provided by hybrid fibers, HP-G-HyFRC exhibited multiple microcracking under accelerated corrosion test. The distributed cracking

reduced corrosion rates in the composite while at the same time maintained its mechanical properties.

- Adding 4% of NaCl of binder weight into the mixing water effectively destabilized the passivity of steel rebar in concrete and led to a higher gravimetric mass losses as compared to theoretical mass losses under impressed current. This is attributable to an increase in the effectiveness of the applied current resulting from acidification which caused an autocatalytic dissolution of steel.

The superior corrosion resistance during both corrosion initiation and propagation stages for HP-G-HyFRC has been proven in this chapter. This warrants its use for more durable structures. Due to its relatively low permeability and fiber confinement, the effects of supplementary cementitious materials (SCMs) especially slag on corrosion of steel in concrete could not be distinguished in this chapter. The effect of slag on corrosion of steel in concrete is the topic of **Chapter 4**. A higher water-binder (W/B) ratio of 0.54 was used in concrete mixes to be used in **Chapter 4** so that the dominant effect of a dense matrix on corrosion could be eliminated. Also, in sample preparation, no salt was added into the mixing water. This enabled us to explore the influence of slag on the passive film, corrosion initiation and corrosion propagation. The combined effects of slag and fibers were examined in **Chapter 5**. Again, W/B of 0.54 was used. One of the goals was to investigate if fibers have similar benefits on steel rebar corrosion at higher W/B ratios. This will help to ensure a wide application of fibers for durability in structures made of concrete with different W/B ratios. In **Chapter 6**, the influence of interface qualities on corrosion was investigated. Salt was added into the mixing water. This was necessary to ensure a better conformation of the measured mass loss against Faraday's law so that a better comparison of damage for applied current regimes can be made. The results provided a fundamental understanding of the effects of interface quality on corrosion initiation and propagation. This has an implication on corrosion studies in **Chapters 3, 4 and 5**. HPCs with very dense steel-concrete interfaces experience an onset of corrosion cracking earlier than their counterparts with more porous interfaces. This means that the use of fibers in the composite is necessary in guaranteeing a longer service life of structures under corrosion consideration. Crucial parameters and objectives of the chapters on corrosion studies are summarized in **Table 3.5**. Two configurations of corrosion samples were adopted: (i) rebar totally embedded in concrete, and (ii) longer and protruding rebars with sealed ends. The two configurations of the corrosion samples effectively worked the same way, except that those used in this chapter and **Chapter 6** represent a improved constructability.

**Table 3.5: Summary of main parameters in corrosion study**

| Chapter   | W/B  | Hybrid fibers | NaCl mixing water | NaCl immersion solution | Sample configuration  | Objectives  |
|-----------|------|---------------|-------------------|-------------------------|---|---|
| Chapter 3 | 0.25 | Yes           | 4% binder         | 17.5%                   |    | Corrosion resistance of HP-G-HyFRC                        |
| Chapter 4 | 0.54 | No            | 0%                | 3.5%                    |    | Influence of slag on corrosion                            |
| Chapter 5 | 0.54 | Yes           | 0%                | 3.5%                    |   | Combined influence of slag and hybrid fibers on corrosion |
| Chapter 6 | 0.54 | No            | 4%                | 7.5%                    |  | Influence of interface qualities on corrosion             |

# 4 Effects of slag on corrosion of reinforcing bars in concrete under accelerated corrosion test

## Summary

Slag has been used as cement replacement to reduce environmental impact of concrete and construction cost. Slag as cement replacement has also been shown to enhance microstructure and improve durability of concrete with relatively low water-binder (W/B) ratios and with long-term moist curing. However, its effects on corrosion resistance of concrete with relatively high W/B ratios and under a curing condition similar to that generally adopted on construction site are not yet well understood. In this study, corrosion resistance of concrete with W/B of 0.54 and with 7-day moist curing was investigated with accelerated corrosion tests. Three slag replacement levels of 0%, 45% and 60% by mass were used. Pore solutions from pastes of the same W/B ratio and slag replacement levels were extracted and analyzed for their chemical compositions. Microstructure of steel-concrete interfaces were also examined with optical microscopy and scanning electron microscopy (SEM). The results show that over the measurement period of 7 months, replacement of cement by slag up to 60% did not reduce pore solution pH. While slag replacement level of 45% helped to delay corrosion initiation, 60% replacement level led to an early onset of corrosion and higher gravimetric mass loss due to a poorer passivity of steel and a possible enhanced acidification. Despite with more interconnected microcracking, the matrix surrounding the rebar was observed to be denser (less pores) for concrete with slag but this was detrimental to corrosion cracking due to its smaller capacity to accommodate corrosion products. The implication is that for concrete with high W/B ratio and short moist curing regime, high volume replacement of cement by slag can be adverse to the structure's service life under rebar corrosion consideration.

## 4.1 Introduction

For a sustainable growth and development, a paradigm shift in the design approach of civil structural systems is needed. The ultimate goal should be to achieve a life-cycle performance by dealing with every facet of the system's service life: construction, operation, maintenance, repair and rehabilitation, decommissioning and disposal (Mirza, 2006). From construction materials engineering point of view, a greener and higher performance concrete composite is needed. Structures built with more durable concrete will last longer and require less maintenance and repair. Green composite requires less energy to produce and emits less CO<sub>2</sub> to the environment while high performance is often associated with high durability (Mehta & Aitcin, 1990). The greening of construction industry can be achieved through a practice called industrial ecology which refers to recycling the waste products of one industry and using them to substitute the virgin raw materials of another industry (Mehta, Jul 2002).

In plain concrete, cement is the most energy and CO<sub>2</sub>-intensive constituent. As mentioned in the **Chapter 1**, cement industry annually releases approximately 2.4 billion tonnes or 7% of the 34.5 billion-tonne total anthropogenic CO<sub>2</sub> emission. Hence, sustainable development in construction industry requires a substantial reduction in cement consumption. Ground granulated blast furnace slag (GGBS or slag) as an industrial waste material from iron blast furnace has been used to replace cement in order to reduce the environmental impact of concrete and cost of construction. An annual production output of iron slag is approximately between 280 and 335 tonnes (US Department of Interior & US Geological Survey, 2015), meaning that there is a high availability of slag to be used as cement replacement. High level replacement of cement by slag of up to 80% (Siddique & Bennacer, 2012) has been reported; however, studies on its effect on long-term performance of concrete especially with regard to corrosion of reinforcing bar show contradictory results.

Under corrosion consideration, the service life of concrete structure is subdivided into two stages: initiation representing the time for CO<sub>2</sub> and Cl<sup>-</sup> to penetrate towards steel-concrete interface and to trigger corrosion, and propagation defined as the time from the onset of corrosion to the occurrence of damaging cracking (Tuutti, 1982). Research results showed that under moist curing conditions, slag as cement replacement reduced concrete permeability and Cl<sup>-</sup> penetration through pore refinement (Ferreira et al., 2004; Jau & Tsay, 1998; Yeau & Kim, 2005). The enhanced permeability property of concrete reduces the ingress rate of aggressive ions into concrete and helps to prolong the initiation stage. A long-term corrosion study conducted by Maslehuddin et al. (1990) showed that corrosion rates of steel in concrete made with blast-furnace slag and water-cured for 27 days are lower than the rates for concrete made with plain and blended cement. It is noted that the water-binder ratio was 0.45 and up to 60% of cement was replaced by slag. However, curing condition can have a great influence on corrosion resistance of slag concrete. It was shown that slag reduced concrete compressive strength and prolonged exposure to a drying environment increased the pore volume at all pore sizes in concrete (Bouikni et al., 2009). Also, under impressed voltage test, 50% replacement of cement by slag with 28-day air curing led to an early onset of concrete corrosion cracking (Topçu & Boğa, 2010). The cube compressive strength of the mix used in the study was found to be about 34 MPa at 28 days.

Steel in concrete is protected from corrosion by a thin layer of thermodynamically stable iron oxides and oxy-hydroxides formed under high pH-environment of concrete pore solution (Bertonini et al., 2004). It is the breaking-down of the passive film by Cl<sup>-</sup> and CO<sub>2</sub> that causes corrosion at the end of the initiation phase. The replacement of cement by slag leads to a dilution effect and pozzolanic reaction which consumes the available calcium hydroxide Ca(OH)<sub>2</sub> or CH in concrete. As a result, slag as cement replacement may cause two negative effects on corrosion of steel in concrete: a reduced pore solution pH which may hinder the formation of a more stable passive film, and a reduced availability of CH. Analyses of pore solutions extracted from mortars made with different types of slag showed a reduction in total alkalinity with increasing slag replacement levels (Kawamura & Takemoto, 1988). However, it was reported that at 50% slag replacement, pH levels of powdered samples in distilled water were maintained at a level above 12 (Dinakar et al., 2007). It was also observed that there was no significant lowering of pH with respect to mixes with ordinary Portland cement. In measuring the pH, the samples were powdered, sieved and mixed with distilled water at a ratio of 1 to 5. This may explain the relatively low pH values as compared to those reported for concrete pore solutions which are in the range of 12.5-13.2 (Dinakar et al., 2007).

It is observed that most of the studies on corrosion resistance of concrete with high volume slag were conducted for low water-binder ratios and for samples undergoing long-term moist curing. Also, studies on the effects of slag on corrosion propagation stage are still lacking. This is pertinent as the lifespan of reinforced concrete structures subject to corrosion is the sum of the time required for corrosion initiation and propagation. In this study, the effects of high volume slag as cement replacement on corrosion of reinforcing bars in concrete will be investigated with a curing condition generally adopted on construction site. Accelerated corrosion test with an applied current of  $1 \text{ mA/cm}^2$  to cause corrosion cracking to concrete was adopted. A corresponding set of samples without applied current were also prepared to study the effects of slag on corrosion initiation. Microstructural analysis with scanning electron microscopy (SEM) was also used to study the steel-concrete interfaces with and without the induced corrosion. The influence of slag on CH availability, pore solution pH and pore solution chemistry was also studied. The study as a whole provides a fundamental understanding on the effects of slag on corrosion of reinforcing bars in concrete. The results also gives a systematic explanation to some abnormal phenomena observed in the accelerated corrosion tests. First, a review about the effects of slag on chloride ingress, pore solution and electrochemical performance of steel in concrete will be conducted.

## **4.2 Literature review**

### **4.2.1 Chloride permeability**

Resistance to  $\text{Cl}^-$  penetration is one important indicator of corrosion protection of steel by concrete as low  $\text{Cl}^-$  permeability will lengthen the corrosion initiation period. Many studies have shown that the use of slag as cement replacement in concrete helps to reduce  $\text{Cl}^-$  permeability. In concrete mixes with water-binder ratio of 0.42,  $\text{Cl}^-$  permeability was found to be reduced with the curing period or the content of slag by binder weight (Yeau & Kim, 2005). The authors attributed this to denser microstructure of slag specimens. Rapid  $\text{Cl}^-$  penetration test was conducted on concrete integrated with slag by Cheng et al. (2005). It was shown through SEM analysis that slag modified hydration products and pore structure in the hardened cementitious materials, leading to a reduction in the total charge passed. Song et al. (2004) conducted a study on  $\text{Cl}^-$  penetration of concrete integrated with 30, 50 and 70% slag. It was found that  $\text{Cl}^-$  penetration resistance increased with increasing cement replacement levels and with the fineness of slag. In  $\text{CaCl}_2$  solution, 50% slag samples after 7 days of moist curing show a good resistance to  $\text{Cl}^-$  attack (Torii et al., 1995).

Besides the enhanced microstructure of concrete with slag which limits the penetration of  $\text{Cl}^-$  ions, slag in concrete also has a  $\text{Cl}^-$  binding capability (Luo et al., 2003). That means for concretes with the same water or gas permeability, slag concrete would exhibit lower free  $\text{Cl}^-$  in the pore solution. This is critical as it is the amount of free  $\text{Cl}^-$  that contributes to the corrosion of steel in concrete. Implementing pore solution extraction and water evaporation of samples, Luo et al. (2003) showed that binding capability of internal  $\text{Cl}^-$  ( $\text{Cl}^-$  introduced into the mixing water) in both mortars and pastes increased with the presence of slag. An earlier study conducted by Arya et al. (Arya et al., 1990) also showed similar increase in  $\text{Cl}^-$  binding capacity of cement pastes integrated with slag, fly ash and silica fume. For the binding mechanism, it is proposed that the bulk of the  $\text{Cl}^-$  ions in the presence of slag is bound either by adsorption or ion exchange with  $\text{OH}^-$  into the interlayers of  $[\text{Ca}_2\text{Al}(\text{OH})_6 \cdot 2\text{H}_2\text{O}]^+$  of Aluminate Ferrite mono (AFm) structure to form Friedel's salt (Suryavanshi et al., 1996). AFm is a family of hydrated calcium aluminate or Fe(III) phases occurring in hydrated cement paste and contains  $\text{OH}^-$ ,  $\text{SO}_4^{2-}$  and  $\text{CO}_3^{2-}$  as principal anions

(Matschei et al., 2007). Using thermal analysis, it was further demonstrated that much of the improvement in  $\text{Cl}^-$  binding of slag concrete is a result of high aluminate levels in slag leading to higher production of the AFm phase or Friedel's salt (Dhir et al., 1996). In addition to the influence of aluminate content, Byfors et al. (1986) also mentioned that the  $\text{Cl}^-$  binding capability of pastes depends on the original alkalinity of the binder and its fineness.

#### 4.2.2 Pore solution pH and steel passivity

High pH level in concrete pore solution ranging from 12.5 to 13.2 (Dinakar et al., 2007) provides a conducive environment for the formation and maintenance of passive film on steel surface in concrete. The protective mechanism of the passive film is maintained when pH is above 10.5 (Roy et al., 1999). SCMs as cement replacement in concrete may reduce pH level due to dilution effects and pozzolanic reaction. However, it was reported that pH range of pore solutions extracted from pastes made with different types of cement and different replacement levels of cement by supplementary cementitious materials (SCMs) was maintained between 12.4 and 13.5 although the dominant cations (Na and K) were of different concentrations (Andersson et al., 1989). In a separate study as previously mentioned, it was found that 50% of slag replacement had no ill effects on alkalinity reduction in pastes (Dinakar et al., 2007).

However, relying only on pH values to characterize corrosion resistance of steel in concrete can be misleading as pH is insensitive to the change in alkalinity in pore solution. For example, a change in  $\text{OH}^-$  concentrations of 50% from 0.2 to 0.1 M reduces pH from 13.1 to 13.0 only. As these pH levels are greater than 10.5, the passivity of steel is not expected to be adversely affected. However, under contamination of aggressive ions such as  $\text{Cl}^-$ , corrosion initiation is determined by  $\text{Cl}^-/\text{OH}^-$  ratio (Hausmann, 1967) and the samples with pore solution of 13.3 can actually provide better protection of steel against corrosion initiation. Its  $\text{Cl}^-$  threshold is expected to be 2 times of that in samples with pore solution pH of 13.0. A study conducted by Hartt (2003) confirmed that concrete specimens with high alkalinity cement showed prolonged corrosion initiation period and exhibited increased  $\text{Cl}^-$  threshold concentration. This explains that high level of pH should not be solely used as an indication of corrosion resistance of concrete. This consideration is applicable to concrete integrated with slag.

Pore solution analysis of slag cement paste also showed a more negative reduction potential, meaning that the species in the pore solution have a tendency to be reduced (Andersson et al., 1989). Also, the presence of reducing agents such as soluble sulphides ( $\text{S}^-$ ,  $\text{HS}^-$  and  $\text{S}_n^{2-}$ ) consume dissolved oxygen and other oxidized species during hydration which will inhibit passive film formation on steel surface (Macphee, 1993). Electron microscopy of the steel-paste interfaces confirmed that ordinary Portland cement (OPC) paste supports the formation of a more stable layer for passive film. Micrographs at steel-paste interface in **Fig. 4.1** showed a more diffused layer containing corrosion products in paste with 75% slag as cement replacement after 11 months of hydration. The corresponding OPC specimen showed no detectable migration of Fe into the interface, supporting the formation of a more effective passive film.



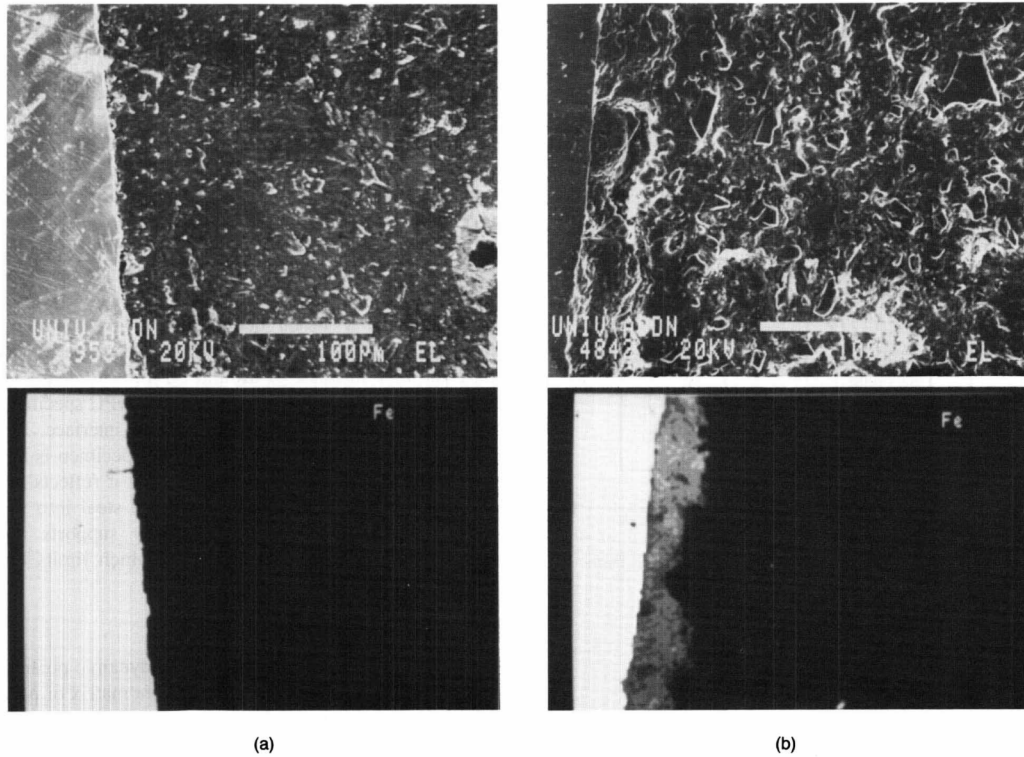


**Figure 4.1: SEM and X-ray map at steel-paste interface: (a) OPC specimen, and (b) slag-OPC specimen (Macphee, 1993)**

### 4.2.3 Corrosion resistance of steel in concrete with slag

The use of slag as cement replacement was shown to increase concrete resistivity at later age due to a combination of filler and pozzolanic effects, which results in pore refinement and increased density (Dinakar et al., 2007). Under normal and sea-water conditions, steel corrosion in concrete samples with slag at 90 days are about 8 to 20 times lower than their corresponding OPCs. This may be attributed to low diffusivity and high resistivity of the concrete. At water-binder ratio of 0.58 and with just 14 days of air-curing before an exposure to simulated marine environment, partially sealed samples with 60% replacement of cement by slag showed the least corrosion rates as compared to other samples with just OPC or smaller replacement levels (Mangat & Molloy, 1991). Similarly, under long term exposure to 5% NaCl solution for 5 years, the corrosion rate of steel in concrete made with slag cement showed lower corrosion rate than other concretes made with OPC and OPC with fly ash (Maslehuddin et al., 1990). In a study by Dehghanian (1999), it was shown that with an exposure to different NaCl solution concentrations, slag replacement of cement at 30% showed the least corrosion rate after 90 days of exposure (**Fig. 4.2**). In all scenarios, it was observed that replacement of cement by slag enhanced concrete performance as compared to 100% OPC concrete. Pal et al. (2002) showed that by maintaining concrete compressive strength, as slag replacement level increases (up to 70% by mass replacement), concrete resistivity also increased while corrosion rates decreased. The enhancement to pore structure may increase the resistivity of concrete by many folds and this helps to offset the possible weakening of passive film at early concrete age. In the same study, accelerated electrolytic corrosion test with constant voltage also showed that the time to initiate corrosion also increases with increasing slag replacement level in concrete. At various ages of curing from 7 to 180 days, it was demonstrated

that concrete with 70% and 53% slag exhibited the highest resistance to chloride penetration and the highest electrical resistivity (Ferreira et al., 2004). Replacement of cement by 40% and 60% slag reduced concrete permeability and  $\text{Cl}^-$  penetration (Cheng et al., 2005). SEM analysis showed that slag modified the hydration products and pore structure in a hardened cementitious material. Also, through electrochemical and mechanical property measurements, it was shown that beams under sustained load exhibited lower corrosion rates when slag was integrated in the binder.

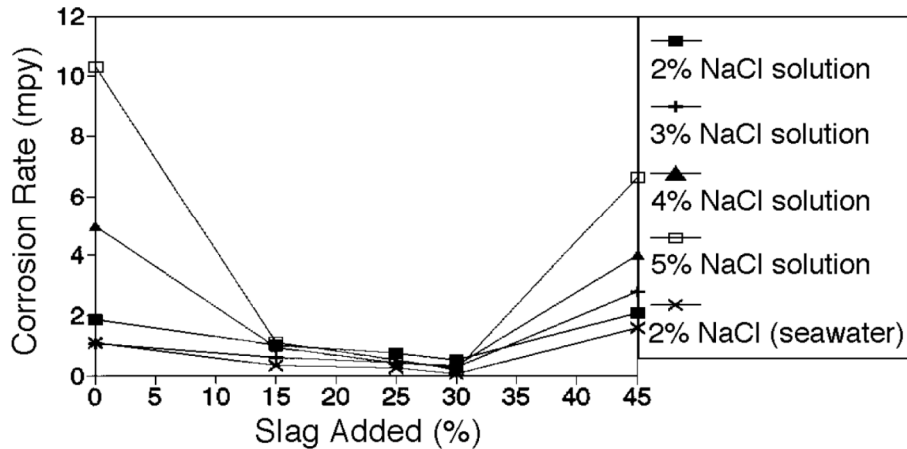


**Figure 4.2: Corrosion rate of steel as a function of percent cement replaced by slag in concrete after 90 days of NaCl solution exposure (Dehghanian, 1999)**

However, the enhanced corrosion performance of concrete with high volume slag was generally observed for concrete with long-term moist curing as in (Maslehuddin et al., 1990; Pal et al., 2002) at relatively low water-binder ratio as in (Ferreira et al., 2004). This is not a reflection of a common practice adopted in construction where water-binder ratios can be very varied and the moist curing duration is generally much shorter (3 to 7 days depending on construction cycles). In other studies (Dinakar et al., 2007; Mangat & Molloy, 1991), the samples were exposed to NaCl environment immediately after moist curing. As such, the migration of  $\text{Cl}^-$  will not be less aggressive as compared to that in unsaturated concrete being exposed to NaCl solution.  $\text{Cl}^-$  ingress into concrete is a complex problem and is controlled by two main mechanisms: diffusion of  $\text{Cl}^-$  and movement of  $\text{Cl}^-$  due to capillary suction of  $\text{Cl}^-$ -contaminated water into concrete (Saetta et al., 1993). The latter process is predominant in dry concrete and may convey a large quantity of ions. Through mathematical models, it was proven that permeable inflow of sea water during the wetting phase of wet/dry cycles caused a far greater ingress of  $\text{Cl}^-$  than by ionic diffusion (Saetta et al., 1993). Dry concrete imbibes salt water by capillary suction until saturation or depletion of salt water reservoir (Hong & Hooton, 1999). When saturated, concrete allows for penetration of  $\text{Cl}^-$  mainly by diffusion only. Using different concrete mixes, Hong (1999) showed that shorter curing times increase the rate of chloride ingress.

Topçu & Boğa (2010) conducted an electrochemical study of concrete made with 0, 25 and 50% slag as cement replacement. A constant voltage of 10 V was applied on corrosion samples embedded with steel rebar. Continuous air and water curing regimes were adopted. It was shown that for 28-day air curing, concrete with 50% slag showed poor corrosion performance as compared to concrete with 0 and 25% slag. Samples with 50% slag showed an earlier jump in corrosion currents, which was associated with the onset of corrosion deterioration. These samples also showed more negative corrosion potentials and higher corrosion rates. Also, water curing was

found to prolong deterioration (cracking) occurrence times. This study stresses the importance of long-term moist curing of concrete integrated with SCMs to ensure their enhanced durability properties. For water-binder ratios of 0.43 and 0.4, Bouikni et al. (2009) proposed that about 7 days of initial water curing is necessary to minimize damage to microstructure that can adversely affect the durability of slag concrete when exposed to dry environment. This study will systematically verify the corrosion performance of concrete with 45 and 60% slag replacement levels under 7-day moist curing.

### 4.3 Materials and methods

#### 4.3.1 Materials

ASTM Type II cement was used as the main binder and slag was used as cement replacement. Their chemical compositions based on X-ray fluorescence (XRF) were given in **Table 2.1** of **Chapter 2**. Aggregates were composed of pea gravel with a maximum size of 10 mm and fine sand with a measured fineness modulus of 3.2. Structural steel reinforcement with a yield strength of 420 MPa was used as the anode. Its chemical compositions was given in **Table 3.1** of **Chapter 3**.

#### 4.3.2 Concrete mix designs

Concrete with water-binder (W/B) ratio of 0.54 was used. Cement was also replaced by slag at 45% and 60% replacement levels by mass. A total of 3 mix designs were used for this study and they are summarized in **Table 4.1**. In all cases, the content of binder and the ratio of coarse to fine aggregates were kept constant. This is different from what is generally adopted in other studies (Bouikni et al., 2009; Pal et al., 2002) where W/B is generally reduced to compensate for strength reduction due to the presence of slag as cement replacement.

**Table 4.1: Concrete mix designs for accelerated corrosion study kg/m<sup>3</sup>**

|                  | <b>C-0S</b> | <b>C-45S</b> | <b>C-60S</b> |
|------------------|-------------|--------------|--------------|
| W/B              | 0.54        | 0.54         | 0.54         |
| Water            | 228.6       | 228.6        | 228.6        |
| Cement           | 425.8       | 234.2        | 170.3        |
| Slag             | -           | 191.6        | 255.5        |
| Fine aggregate   | 853.3       | 836.3        | 833.0        |
| Coarse aggregate | 775.5       | 760.1        | 757.1        |

#### 4.3.3 Specimen preparation and corrosion testing procedure

Cylinders of size 100 x 200 mm embedded with 250 mm long #8 or 25 mm-diameter bars in the center were procured for the accelerated corrosion test. The surface of each bar was sandblasted, and insulated along the lower 31.25 mm and the upper 81.25 mm by Scotchkote electrical coating and heat shrink tube. The protective layers prevented the bar from corroding in these regions and limited the corrosion to within its middle 137.5 mm. The top end of the bar was drilled to accommodate a 6-32 x 3/8 screw for wiring. The steps for bar preparation are shown in **Fig. 4.3**. The specimens were cast and moist-cured for 7 days before an exposure to laboratory air for a minimum of 21 days. Additional cylinders cured under the same regime were also produced to find compressive strengths at 28 and 56 days. Effectively, the samples would work in the same

way as those presented in **Chapter 3** except that the configuration of the latter was simplified for easy procurement.

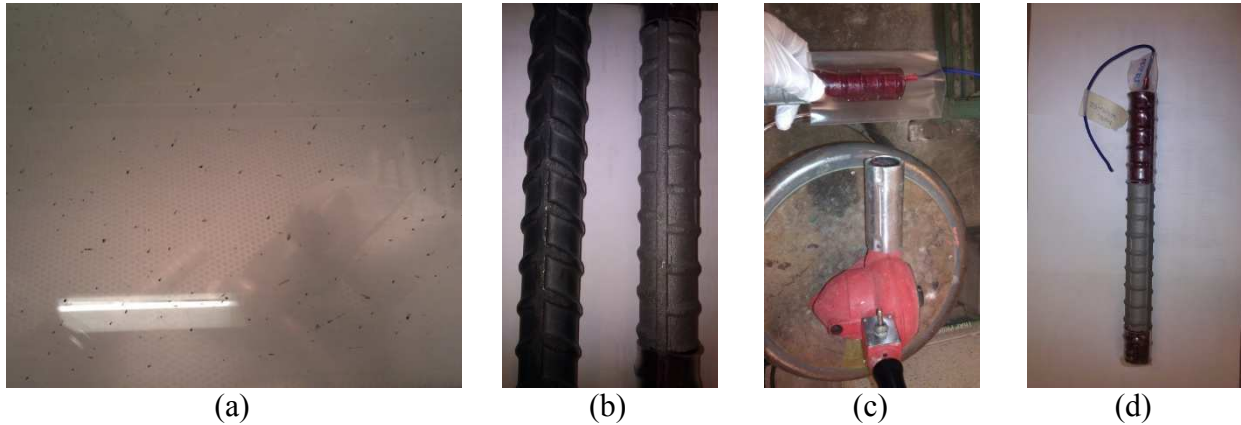


**Figure 4.3: Bar preparation for accelerated corrosion test: (a) sandblasting, (b) bars before and after sand blasting with epoxy coating, (c) heat shrink tubing, and (d) bar with heat shrink tube and wiring ready for casting**

The setup of accelerated corrosion test is shown in **Fig. 4.4**. The test setup is similar to that outlined in **Chapter 3**. However, a number of differences exist. The samples were immersed in a solution with 3.5% NaCl by mass up to a height roughly 12.5 mm from the top surface of the concrete cylinder. After immersing the samples in the NaCl solution for 24 hours, a continuous current of 111.5 mA ( $1 \text{ mA/cm}^2$ ) was applied for either 24 or 48 hours to the accelerated-corrosion samples, after which they were allowed to stabilize in 3.5% NaCl solution. The 48 hours of  $1 \text{ mA/cm}^2$  applied current regime is equivalent to about 55 years of corrosion in real structures with a low corrosion rates of  $0.1 \mu\text{A/cm}^2$  (Andrade & Alonso, 1996). The electrochemical tests consisting of linear polarization and Tafel tests were performed at 1, 3, 7, 14, 28, 56 and 98 days after NaCl soaking for both non-accelerated and accelerated corrosion samples. Linear polarization resistance measurements were conducted by sweeping a potential  $\pm 10 \text{ mV}$  from the corrosion potential at a rate of  $0.1 \text{ mV/s}$ . For Tafel scan measurements, a potential sweep of  $\pm 75 \text{ mV}$  was implemented on the samples. It is noted that during the application of current, the counter electrode was used as reference. That is the reference electrode sensor was connected to the counter electrode and no SCE reference electrode was used.

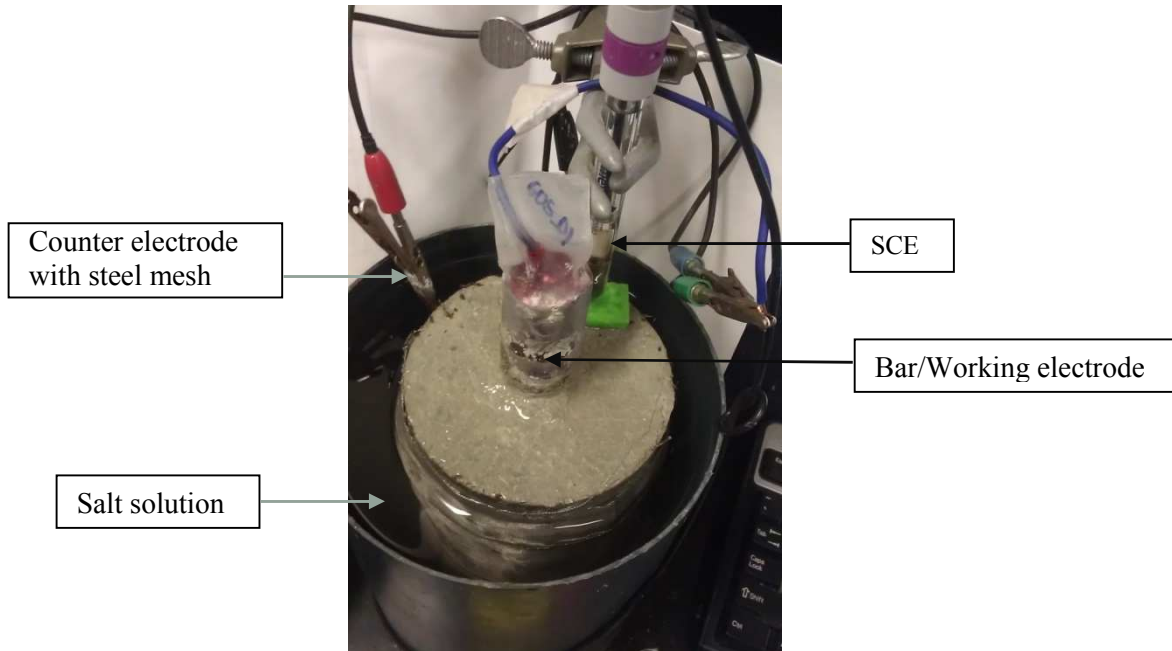


**Figure 4.4: Accelerated corrosion test setup**

For each current regime and mix design, 2 samples were prepared, one for linear polarization and one for Tafel testing. Corrosion rates were found with Eq. 3.2. Corrosion rate intensities ( $i_{corr}$ ) could be found by dividing corrosion rates  $I_{corr}$  with the exposed corrosion surface area of  $111 \text{ cm}^2$ . With 3 different applied current regimes, a total of 6 samples were prepared for each mix. In the sample annotation, C stands for plain concrete; 0S, 45S and 60S for slag replacement levels of 0%, 45% and 60% by mass; and nH for n hours of applied current. For example, C-45S-48H refers to concrete sample with 45% slag as cement replacement and with 48 hours of applied current.

#### 4.3.4 Microscopic analysis

Following the accelerated corrosion, the samples from linear polarization group were sliced in the middle region to obtain disc elements of thickness 21.5 mm. The elements were prepared for optical and SEM microscopic analysis. The procedure was outlined in Chapter 3.

#### 4.3.5 Gravimetric mass loss analysis

The samples from the Tafel test group were dried in oven at  $110 \text{ }^\circ\text{C}$  for 24 hours and were subsequently subjected to splitting tensile test to extract the rebars in the middle. The wiring, heat shrink tube and coating on the rebars were then removed or cleaned off. HCl hexamethylene tetramine solution was used to remove corrosion products so that significant etching of the base metal could be minimized. The process for gravimetric mass loss measurement was detailed in Chapter 3.

#### 4.3.6 Thermal gravimetric analysis (TGA)

For thermal analysis, corresponding pastes with W/B ratio of 0.54 were prepared. The samples were cured in  $24 \text{ }^\circ\text{C}$  fog room at 100% relative humidity (RH) for 28, 56 and 90 days. At each age, the samples were crushed to sizes less than 12.5 mm, dried in oven at  $110 \text{ }^\circ\text{C}$  for 24 hours, pulverized in an aggregate grinder and further ground in a ceramic pestle until more than 90% of

the sample mass passed through ASTM sieve No. 230 (62  $\mu\text{m}$ ). The ground samples were kept in vacuum desiccator to avoid carbonation and re-absorption of moisture until the thermal analysis experiment.

The thermal analysis was conducted with thermo-gravimetry/differential thermal analyzer EXSTAR6000 TG/DTA series with temperature ranging from 20 to 1000  $^{\circ}\text{C}$  at a scanning rate of 10  $^{\circ}\text{C}/\text{min}$ . Nitrogen gas at a flow rate of 100 ml/min was passed through the system. These conditions produced thermogravimetric (TG) curves of percentage weight loss over time. It was assumed that the total CH was proportional to the weight losses induced by dehydration of water from CH and decarbonation of  $\text{CaCO}_3$  during the heat application. Hence, from the TG curves, the weight of CH was derived from decomposition of both CH and  $\text{CaCO}_3$  using a methodology as outlined by Girao (2007). The mass changes are defined by three governing equations as given below.

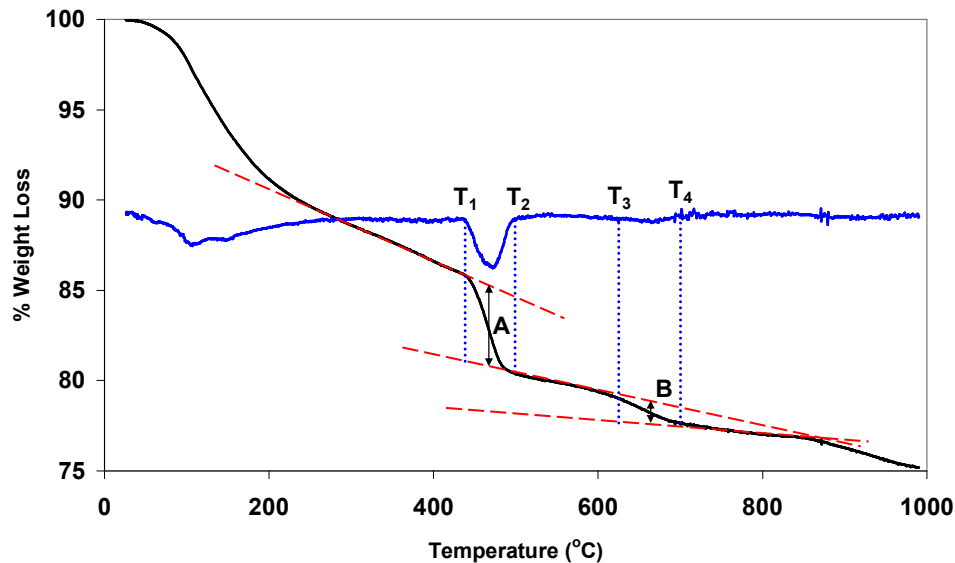
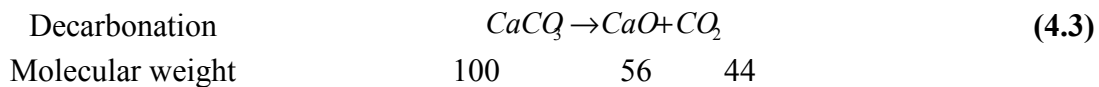
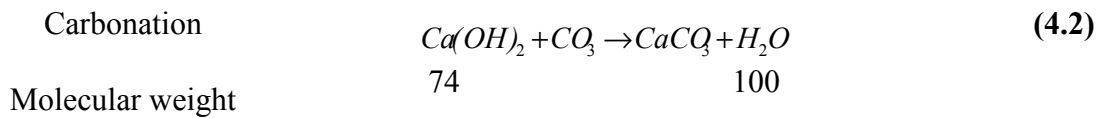
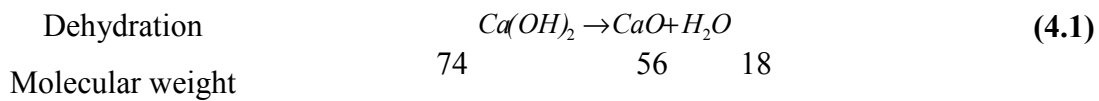


**Figure 4.5: Example illustrating the calculation of A and B in the TG curve (Girao, 2007)**

Applying a mass balance, the total CH can be calculated by  $74/18 \times A + (74/44 \times B)$  where A is the weight loss induced by dehydration of  $\text{H}_2\text{O}$  from CH which takes place between approximately 410-540  $^{\circ}\text{C}$ , and B is the weight loss caused by decarbonation of  $\text{CaCO}_3$  which occurs between 600-780  $^{\circ}\text{C}$ . Both A and B are calculated using TGA curves as depicted in Fig.

4.5. Tangents at the boundary temperatures are drawn and the mid-point differences are the values of A and B.

#### 4.3.7 Pore solution analysis

Pastes prepared for TGA/DTA analysis were also used for pore solution extraction and analysis. The extraction was done with a pore press equipment similar to that described by Barneyback & Diamond (Barneyback Jr & Diamond, 1981) as outlined in **Chapter 3**. ICP analysis was conducted and concentrations of Al, Ca, K, Na, S and Si were found by comparing the peak intensities against the intensities found in standard solutions.

#### 4.3.8 Gas permeability test

Gas permeability test for the three mixes used in the corrosion studies was conducted based on recommendations by Kollek (1989) and the test setup was outlined in **Chapter 2**. A total of two 100 x 200 mm cylinders were produced for each mix. One of the cylinder was cured at 24 °C under 100% RH for 7 days and one for 28 days to study the effect of curing conditions on concrete permeability. At 28 days, the samples were sliced into 50 mm segment and oven dried at 110 °C until a constant weight was achieved. The slices were cooled in vacuum to room temperature for 24 hours before the gas permeability test was conducted. The gas permeability of a proprietary polymer fiber-reinforced mortar (FRM) under a commercial name Elephant Armor-DOT (E) was also studied. Water-dry mortar ratio was 0.25 by mass and the sample was cured for only 5 days in air due to its fast strength gain as claimed by the supplier. Although the air permeability results for the mix were presented in this chapter for comparison purpose, the mix would only be used in a later study of the project.

### 4.4 Results

#### 4.4.1 Mechanical properties of concrete mixes

The compression test results with error bars are given in **Fig. 4.6**. It is observed that compressive strengths for any concrete mix did not change significantly from 28 to 56 days. This means that the strengths stabilized after 7 days of moist curing and 21 days of air curing. As the current was applied after 28 days, the effects of strength gain or microstructure change on corrosion were effectively eliminated within a specific mix. It is also noted that increasing the amount of slag in concrete also reduced concrete compressive strengths. Prolonged air curing period prevented significant pozzolanic reaction from taking place and strength gain. Although compressive strengths of samples without slag were higher, the difference in tensile strengths which was assumed to be proportional to the square root of compressive strengths is expected to be small within the mixes. For example, for concrete mixes with compressive strengths increasing from 35 MPa to 40 MPa or a 14% increase, the tensile strength is expected to increase by just 7%. Hence, strength difference would not have a marked influence on the tensile cracking behavior of the samples under the accelerated corrosion test. This allows for a fair comparison of corrosion propagation behavior of the mixes.

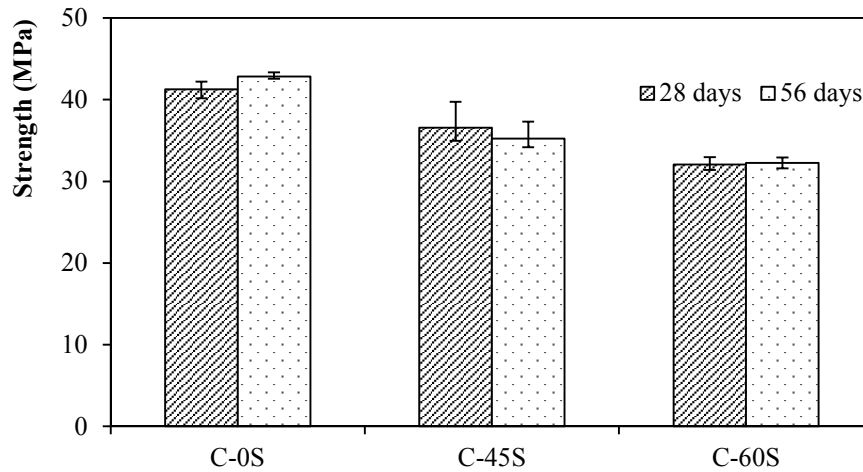


**Figure 4.6: Compressive strengths of concrete at 28 days and 56 days**

#### 4.4.2 Corrosion initiation

The results for corrosion potentials of samples without applied current are given in **Fig. 4.7**. According to ASTM C876-09 (American Society for Testing and Materials (ASTM), 2009), there is a greater than 90 % probability that reinforcing steel bar is corroding in an area at a given time when the half-cell corrosion potentials are more negative than -350 mV against copper-copper sulfate reference electrode (CSE) or -277 mV versus saturated calomel electrode (SCE). It is observed that corrosion potentials for C-45S-0H remained stable at around -200 mV throughout the exposure period. Corrosion potentials for C-0S-0H became more negative than -277 mV after 3 days in 3.5% NaCl solution. On the other hand, corrosion potentials of the C-60S-0H were always more negative than -277 mV during the measurement period. Its corrosion potentials further dropped after 3 days in 3.5% NaCl solution indicating a higher probability of active corrosion. The results showed that 45% of slag as cement replacement seemed to provide a good protection for steel against corrosion initiation. This may be attributed to two complementary effects: (i) increased Cl<sup>-</sup> binding ability of hydration products with the presence of slag, and (ii) pozzolanic reaction of slag and the resulting refinement of concrete pore structure which restricts the ingress of Cl<sup>-</sup> and O<sub>2</sub>. Chloride binding phenomenon was observed by other researchers (Arya et al., 1990; Dhir & Jones, 1999; Luo et al., 2003). The improvement in Cl<sup>-</sup> binding of slag concrete is a result of high aluminate levels in slag, leading to higher production the AFm phase or Friedel's salt (Dhir et al., 1996). However, as slag replacement level was increased to 60%, the available CH to participate in the pozzolanic reaction became limited. Also, slag releases reducing agents in the form of soluble sulphides (S<sup>2-</sup>, HS<sup>-</sup> and S<sub>n</sub><sup>2-</sup>) during hydration (Macphee, 1993). It is postulated that during an early age when passive film was being formed, the agents competitively consumed O<sub>2</sub> and other oxidized species, inhibiting the formation of good quality passive film on steel surface. This was explained in the literature review. These two factors led to the more negative corrosion potentials in samples with 60% slag replacement.



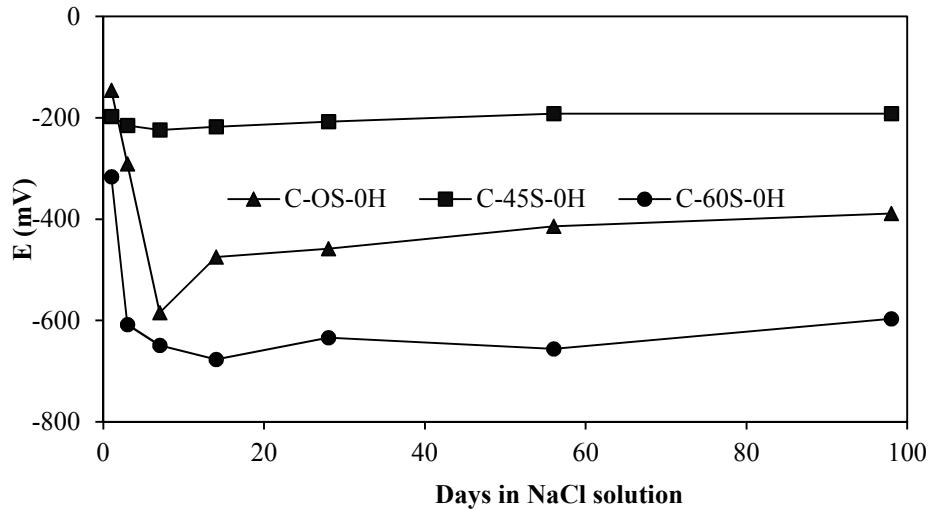


**Figure 4.7: Corrosion potentials for samples without applied current**

The corresponding corrosion rates are given in **Fig. 4.8**. It is observed that corrosion rates for C-45S-0H were always less than the active corrosion limit. Corrosion rates for C-0S-0H were less than  $0.1 \mu\text{A}/\text{cm}^2$  at 1, 3 and 7 days but they increased to a value greater than  $0.1 \mu\text{A}/\text{cm}^2$  in later measurements. Corrosion rates for C-60S-0H were always greater than  $0.1 \mu\text{A}/\text{cm}^2$ . If corrosion rates greater than  $0.1 \mu\text{A}/\text{cm}^2$  are considered as active, the corrosion rate results are consistent with the trend observed in corrosion potential measurements. Other studies have shown that due to limited dissolved  $\text{O}_2$  in pore solution, corrosion potentials can be very negative although the measured corrosion rates are low (Dehghanian, 1999; Kouloumbi et al., 1994). Its effects in high performance concrete was elaborated in **Chapter 3**. In this study, the high permeability of the concrete and the immersion of the cylindrical corrosion samples with 3.5% NaCl solution to a level slightly lower than their top surfaces helped to prevent the problem of high apparent negative potential but low corrosion activity. It is noted that electrolytic resistance of concrete was not measured in this study. The results presented here is part of a wider corrosion study where the influence of PVA and steel fibers on corrosion was also considered. Electrolytic resistance cannot be used as an indication of corrosion resistance of concrete with steel fibers as reinforcement. It was shown that although steel fibers reduced concrete electrolytic resistance by providing shortcuts for electrical current, they actually increased corrosion resistance of concrete through passive confinement effect (Grubb et al., 2007).

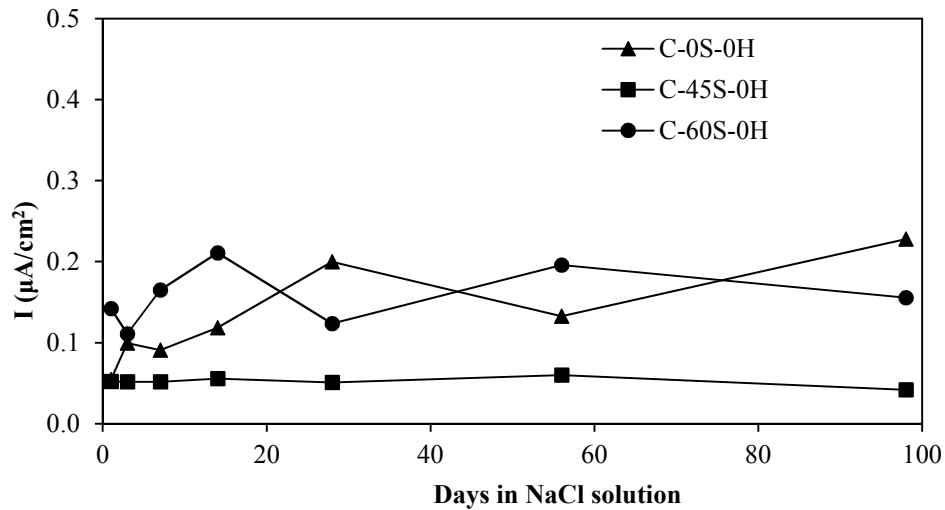
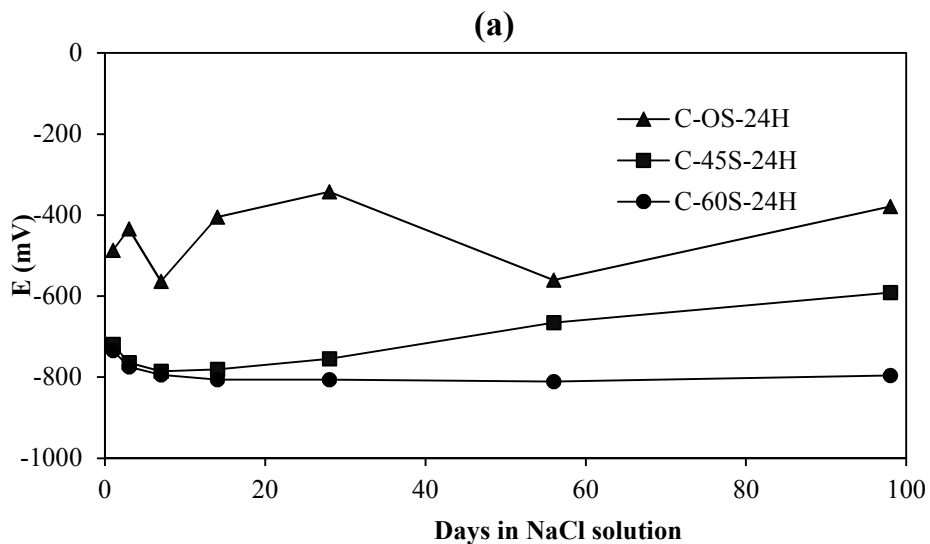
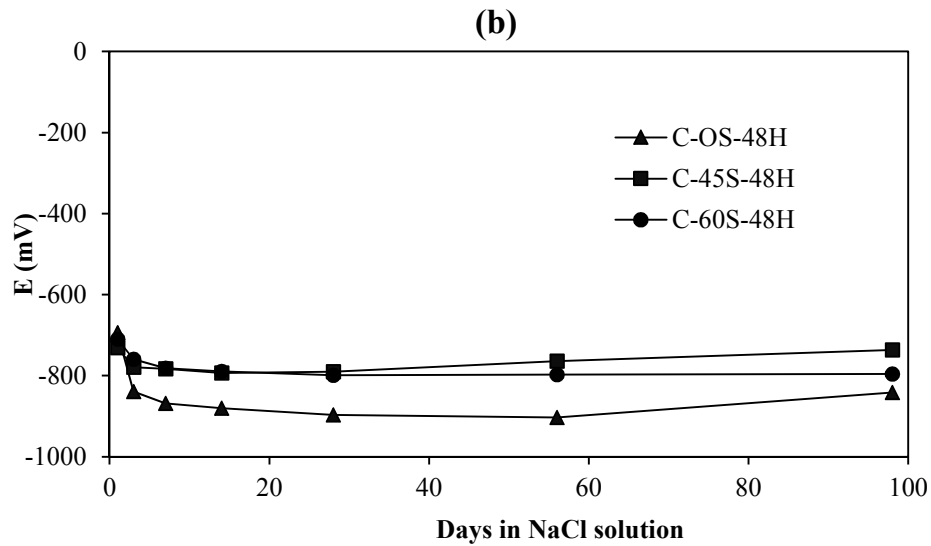


Figure 4.8: Corrosion rates for samples without applied current

#### 4.4.3 Corrosion results with applied current

Corrosion potentials of samples with 24 and 48 hours of applied current are given in **Fig. 4.9**. It is observed that corrosion potential values for all samples were more negative than -277 mV. This indicates that all samples are in an active corrosion region. C-0S-24H had the least negative corrosion potentials as compared to C-45S/60S-24H while C-60S-24H showed the most negative corrosion potentials throughout the measurement period. With 48 hours of applied current, the corrosion potentials of all samples dropped to a value of around -800 mV, representing a possibility of high corrosion activity. Contrary to what was observed with 24 hours of applied current, C-0S-48H exhibited the most negative corrosion potentials. As corrosion potential values indicate only the possibility of corrosion activity, it is worth investigating the corrosion rates to better understand the effects of slag on corrosion performance of concrete after the applied current.





**Figure 4.9: Corrosion potentials for samples with applied current of: (a) 24 hours, and (b) 48 hours**

The corresponding corrosion rates of samples with the two applied current regimes are given in **Fig. 4.10**. Although C-0S-24H was always in an active corrosion region ( $> 0.1 \mu\text{A}/\text{cm}^2$ ), its corrosion intensities were much smaller as compared to the values for C-45S-24H and C-60S-24H. For the 24-hour corrosion regime, the order for corrosion activity is C-0S-24H  $<$  C-45S-24H  $<$  C-60S-24H, a similar trend to corrosion potential results. One possible explanation for the observed low corrosion rates in C-0S-24H is that not all of the applied current was effective in causing corrosion in the sample. It is believed that the passive film of samples with 0% slag was more stable and as a result steel in C-0S was better protected against the applied current. To induce a constant current of  $1 \text{ mA}/\text{cm}^2$ , a variable voltage was applied between the anode and cathode. With high resistance of the rebar to be oxidized under the potential field, part of the electrons reaching the counter electrode may also come from other sources such as water oxidation. This led to less oxidation of the steel rebar, less pressure to the surrounding concrete, less cracking and ultimately smaller observed lower corrosion rates. Water oxidation and its effects on accelerated corrosion will be discussed in the next section. However, when the duration of applied current was increased to 48 hours, visible surface cracks may have occurred and exposed steel to the electrolyte. As a result, corrosion rates for all the samples were in the active corrosion regime and were of similar magnitude.

It is also interesting to observe that corrosion rates for samples with high corrosion activity tended to decrease with time. It is postulated that with a continuous supply of oxygen and moisture, the corrosion products would change phase to form a more stable corrosion products, leading to an enhanced passive protection of the steel surface. It was shown that the morphology of corrosion products in accelerated corrosion became more solidified upon exposure to air (Andrade et al., 2011). Also, with time the immersion NaCl solution will be more concentrated with  $\text{OH}^-$  arising from the dissolution of  $\text{Ca}(\text{OH})_2$ . pH of the immersion solution was measured to be higher than 12 after 3 days of immersion. The high pH solution will be conducive to the reformation of the passive film on the steel surface. This resulted in a decrease in corrosion activity. It is noted that during

the applied current, the steel-concrete interface can become very acidic due to hydrolysis of water by  $\text{Fe}^{2+}$ . Hence, the presence of macrocracks may also allow for acid dilution by the basic electrolyte. This may help to heal the steel surface through reformation of the passive film. Visible surface cracks occurred in the samples after 48 hours of applied current may expose the embedded steel rebars to the electrolyte. This reduced the influence of interfacial densification of corrosion and acidification at the interface, leading to similar corrosion activities of all the samples.

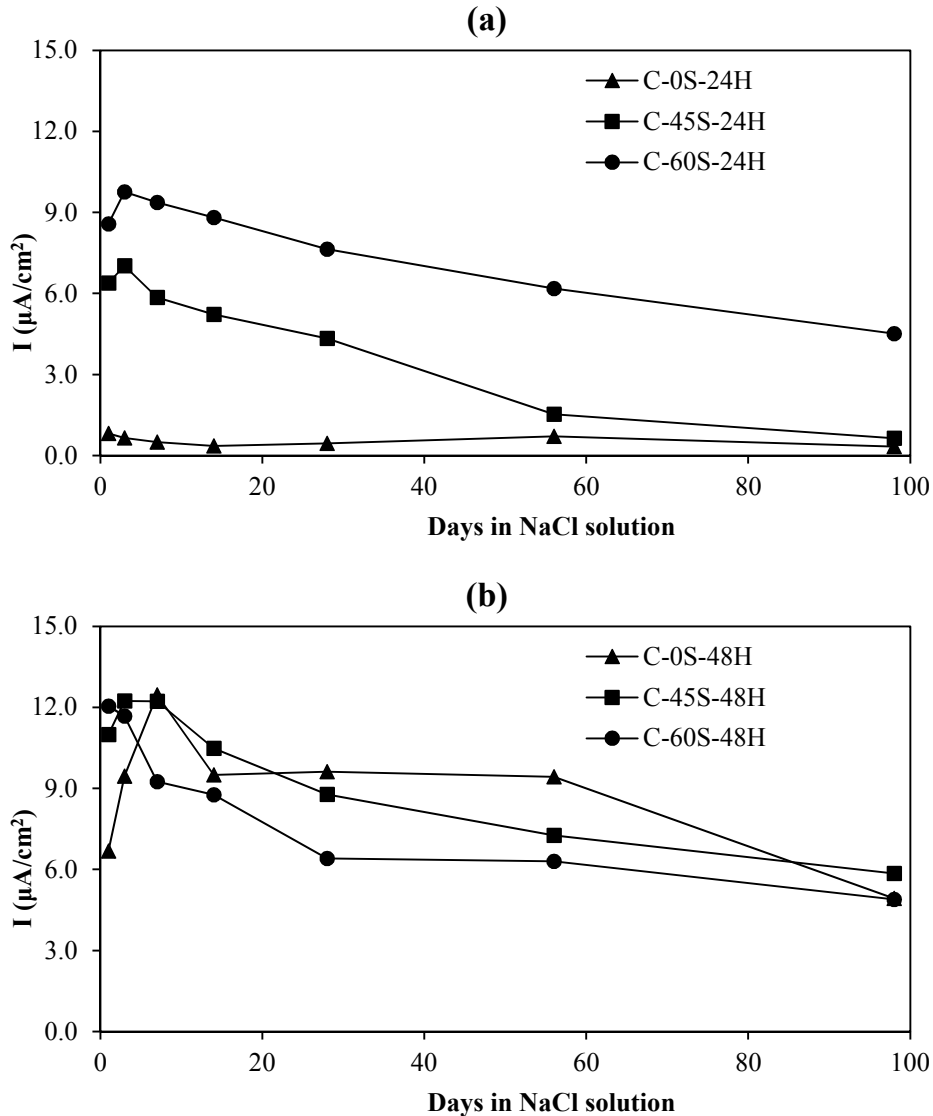


**Figure 4.10: Corrosion rates for samples with applied current of: (a) 24 hours, and (b) 48 hours**

#### 4.4.4 Gravimetric mass loss results

The results for gravimetric mass loss and theoretical mass loss are summarized in **Table 4.2**. The theoretical mass loss is the sum of mass loss during the applied current and during the 90-day period that the samples were left in NaCl solution. The latter was calculated based on time integration of the measured corrosion rates as explained in **Chapter 3**. The gravimetric mass losses

were also normalized to the bar masses of the exposed area. It is observed that the gravimetric mass losses increased with applied current intensity. With 24 and 48 hours of applied current, the gravimetric mass losses was lower as compared to theoretical mass losses. The results confirmed that not all induced current is effective in causing corrosion to the steel anode. It is also noted that the gravimetric mass losses for C-0S and C-45S were lower than those for C-60S. This may be attributed to a poorer protection of steel against corrosion in C-60S, leading to more dissolution of iron under the impressed current. With 24 hours of the applied current, the gravimetric mass loss for C-60S-24H was 1.1 g as compared to 0.3 g for C-0S-24H and 0.4 g for C-45S-24H. The small mass loss in C-0S prevented crack formation and this helped to explain the low corrosion rates observed in C-0S-24H. When the applied current duration was 48 hours, the mass losses for all samples were greater than 2.6 g. This is equivalent to a radius loss of 30.3  $\mu\text{m}$  for the steel substrate, enough to cause cracking to concrete. This contributed to the high corrosion rates observed for all the samples as shown in **Fig. 3.10**.

**Table 4.2: Gravimetric and theoretical mass losses**

|           | Current 1mA/cm <sup>2</sup> | Gravimetric    |       | Theoretical    |
|-----------|-----------------------------|----------------|-------|----------------|
|           | Hours                       | $\Delta M$ (g) | % M   | $\Delta M$ (g) |
| C-0S-0H   | 0                           | 0              | 0.00% | 0.06           |
| C-0S-24H  | 24                          | 0.3            | 0.06% | 2.92           |
| C-0S-48H  | 48                          | 2.6            | 0.48% | 7.90           |
| C-45S-0H  | 0                           | 0              | 0.00% | 0.01           |
| C-45S-24H | 24                          | 0.4            | 0.07% | 3.55           |
| C-45S-48H | 48                          | 2.9            | 0.53% | 7.76           |
| C-60S-0H  | 0                           | 0.2            | 0.04% | 0.05           |
| C-60S-24H | 24                          | 1.1            | 0.20% | 4.61           |
| C-60S-48H | 48                          | 3.4            | 0.62% | 7.38           |

#### 4.4.5 Flatbed digital imaging and optical microscopy

The flatbed scanned images of sections from the corrosion samples are shown in **Fig. 4.11**. Lines for visible cracks were also drawn on the surfaces but were not indicative of crack sizes. For C-0S, it is observed that 24 hours of applied current induced no visible cracks to the sample. On the other hand, C-45/60S samples showed cracks for both 24 and 48 hours of applied current. The crack development is consistent with electrochemical results and gravimetric mass losses in which small corrosion rates and mass loss were observed for C-0S-24H. Also, when cracks occurred, the steel rebar was more exposed to the electrolyte and that increased corrosion rates manifold for C-45S/60S-24H and C-45S/60S-48H as shown in **Fig. 4.10**. It is also observed that in C-0S-48H and C-60S-48H, several non-through cracks were developed. These cracks stopped before reaching the surface due to toughening provided by crack deflection and crack bridging provided by the aggregates (Li & Maalej, 1996). The observation confirmed that cracks were initiated at the steel-concrete interface where hoop tensile stress was the highest.

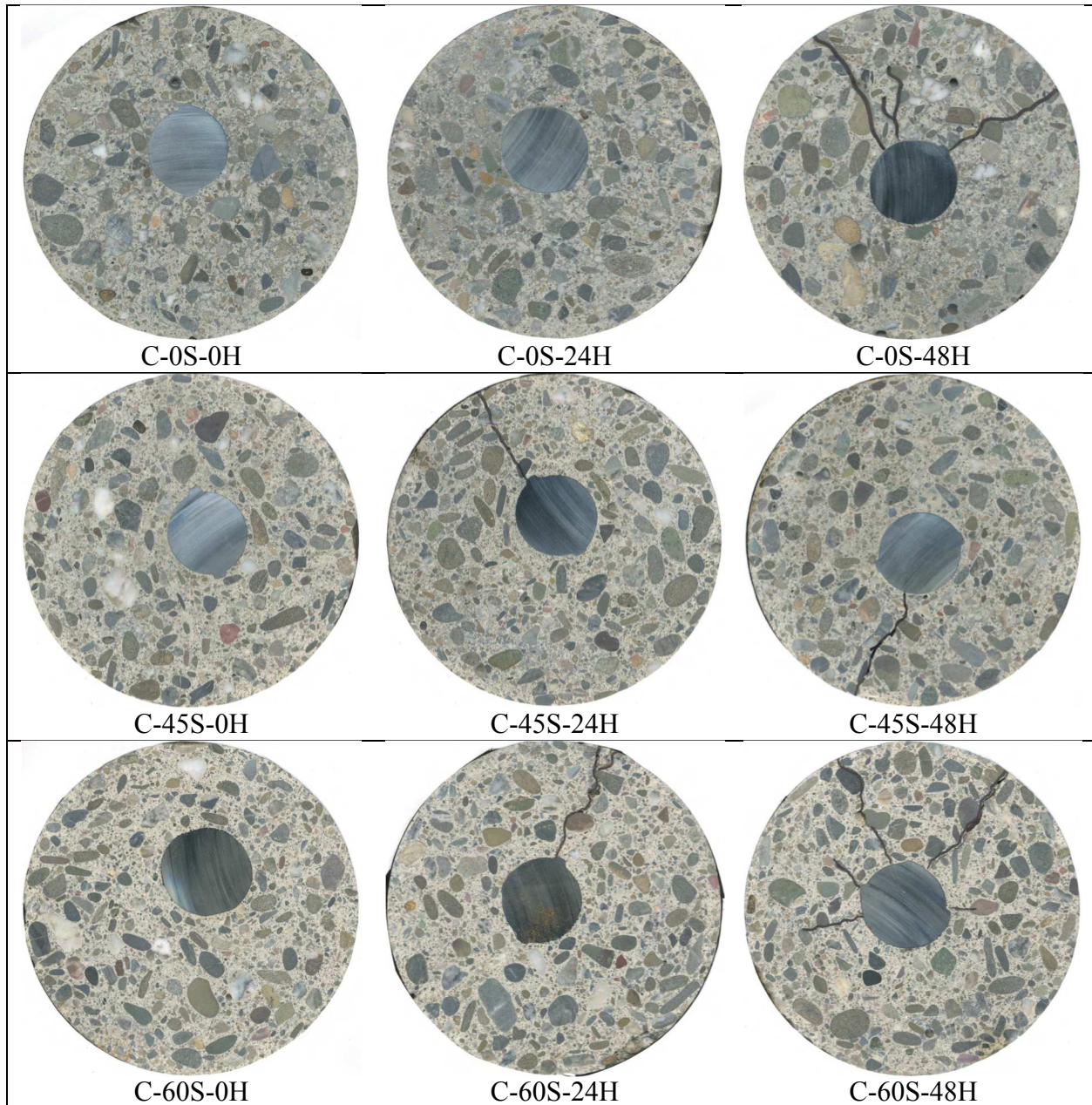


**Figure 4.11: Scanned images of sections from plain concrete corrosion samples**

The optical microscopy results for steel-concrete interfaces for corresponding samples are shown in **Fig. 4.12**. No corrosion products were observed for the samples with no applied current. Also, at the cut sections of samples with applied current, corrosion layer thickness did not seem to correlate well with the gravimetric mass losses as presented in **Table 4.2**. For example, the corrosion thickness for C-45S-24H for the section analyzed was thicker than that for C-45S-48H although the mass loss for C-45S-48H was higher. This may be attributed to the non-uniformity of corrosion on the steel surface. Surface observation of rebars retrieved from tensile splitting tests of corrosion samples confirmed this. **Fig. 4.13** shows that corrosion occurred in patches for selected samples undergoing accelerated corrosion test. This may be attributable to variation in steel-concrete interface quality along the rebar. Research studies showed that poor interface quality



makes steel more susceptible to corrosion (Castel et al., 2003; Söylev & François, 2005; Soylev & François, 2003). With regard to accelerated corrosion, steel at poor interface is more susceptible to being oxidized by the impressed current as it was less protected electrochemically and physically by concrete. With no applied current, it is also observed that rebar in C-60S-0H also showed limited number of corrosion patches on the rebar surface. This may be attributed to a poorer passive film quality in C-60S as discussed and its higher permeability. This led to the higher corrosion rates of the sample as compared to C-0S/45S-0H. Gas permeability results will be given in the next part of this chapter.

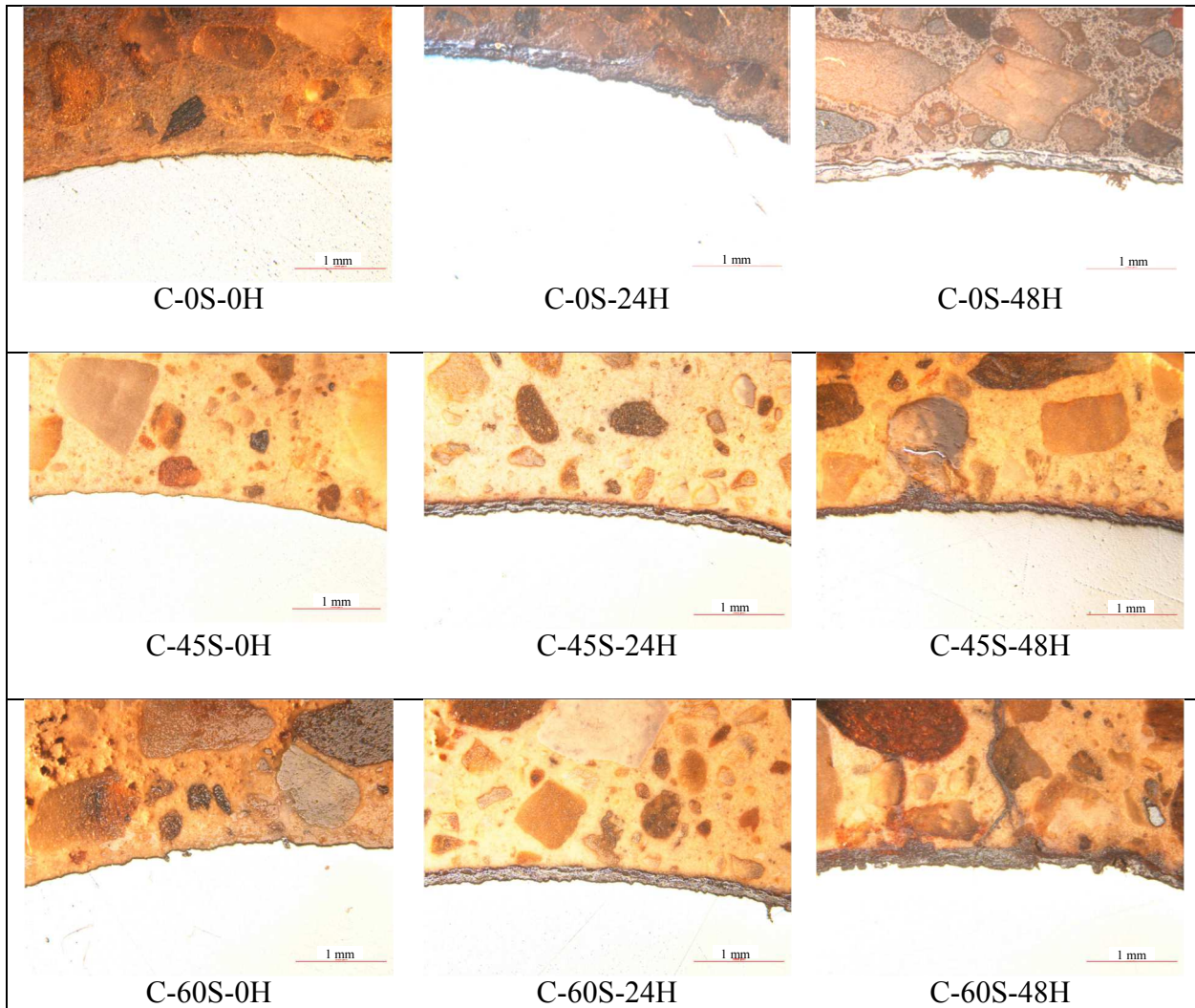


**Figure 4.12: Optical microscopic results for steel-concrete interfaces**

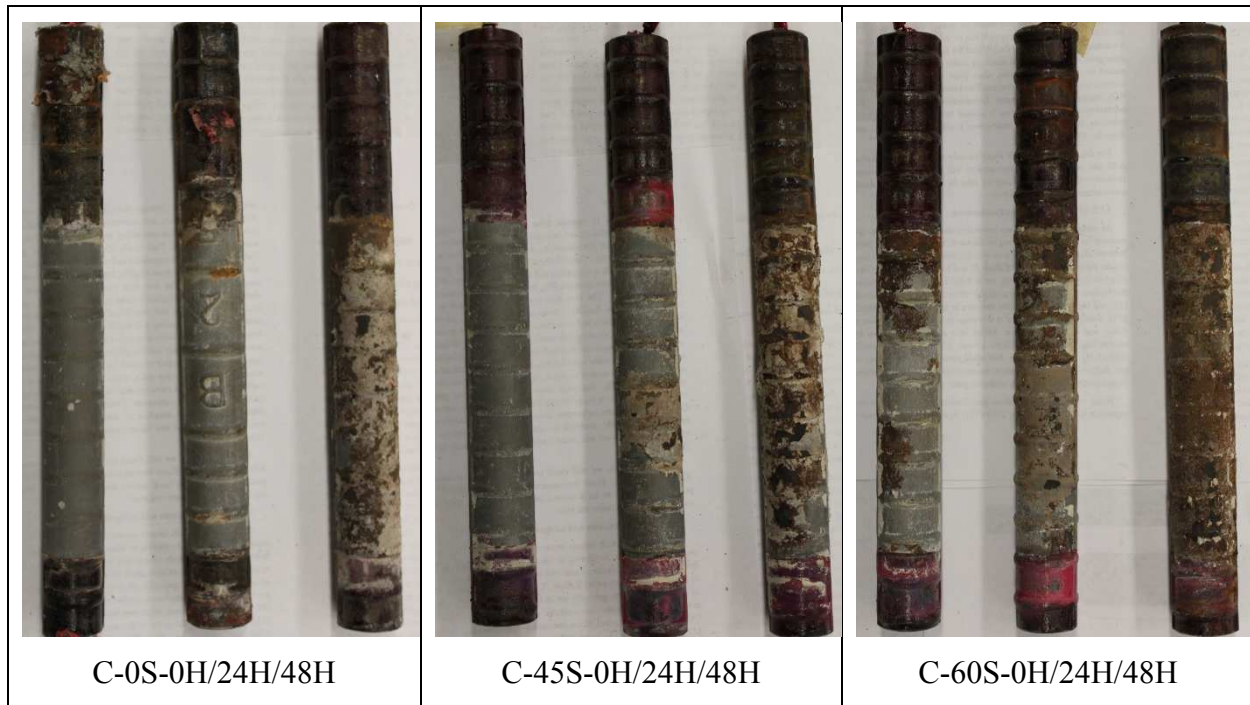


**Figure 4.13: Non-uniformity of corrosion on steel surfaces**

#### **4.4.6 Pore solution analysis results**

Pore solutions were extracted from paste samples which were moist-cured for 28, 56 and 90 days. In the naming convention, P stands for paste with the same W/B ratio of 0.54 as that used for the concrete mixes. The continuous moist curing is necessary to ensure that pore solution could be extracted from the paste samples. Pore solutions from the moist-cured samples are expected to be representative of bulk concrete samples used in the corrosion study. pH results for samples with 0%, 45% and 60% slag replacement levels are given in **Fig. 4.14**. pH values of bleeding water after 10 minutes of casting and of pore solution after 7 months of curing were also provided although their chemical compositions were not analyzed by ICP. It is observed that replacement of cement by slag has no influence on pH values. At all ages, pH values of all samples were around 13 (except for the bleeding water), indicating a conducive environment for passive film formation. However, the stability of the passive film can be adversely affected by reducing agents in concrete pore solution. This will be confirmed by composition analysis results of pore solutions to be provided in the next paragraph.



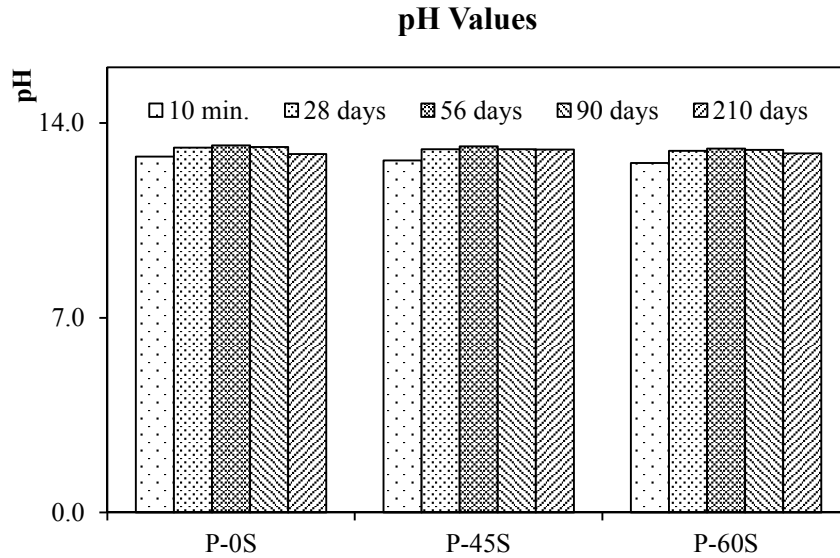


**Figure 4.14: Pore solution pH values**

ICP analysis results for concentrations of Al, Ca, K, Na, S and Si are given in **Fig. 4.15**. It is observed that Al concentrations increased with increasing slag replacement levels. This is attributed to the higher amount of  $Al_2O_3$  in slag. Ca concentration decreased with increasing slag replacement levels due to pozzolanic reaction while Si seemed to increase. The continuing hydration and pozzolanic reaction, however, may bind Si into the C-S-H gels and this led to a reduction in Si concentrations with time for all samples. It is also noted that Ca concentrations were much lower as compared to K or Na. Hence, the dominant parameter influencing the high pH values in pore solutions as given in **Fig. 4.14** was the total alkalinity from K and Na. This explains why high volume replacement of cement by slag did not adversely reduce pH levels of pore solutions. Also, it is observed that Ca concentrations within a specific concrete changed little with time. This may be because the concentrations of Ca were determined by the dissolution limits of CH which are expected to be different for the three mixes due to the presence of various other ions in the pore solutions and different quantities of CH interlocked in the matrix. Also, in general, S concentrations were higher in P-45S/60S than those in P-0S. This is very noticeable at 28 and 90 days. The drop of S concentration in P-60S at 56 days may be attributed to errors in the ICP analysis. At 28 days, P-45S and P-60S have about 2 and 2.6 times, respectively, of S concentrations as much as that observed in P-0S. The higher concentration of S is believed to cause a less stable passive film formation in C-45/60S. It is also noted S concentrations in P-45S and P-60S at 28 and 56 days were lower than those at 90 days by several magnitudes, possibly due to a slow release of S from slag grains (Taylor et al., 2001). The pore solution composition results provide a quantitative evaluation of pore solution chemistry and prove the higher S (probably in the form of  $SO_4^{2-}$ ) concentrations in P-45S and P-60S. As discussed earlier, the presence of the reducing agents in the pore solution was argued to lead to formation of less stable passive film in concrete (Macphee, 1993). Using anodic polarization and electrical impedance spectroscopy (EIS), Ghods et al. (2009) confirmed that the presence of  $SO_4^{2-}$  in concrete pore solutions has a negative effect on the protective properties of the passive films. SEM image showed cracks distributed over the surface of the rebar.

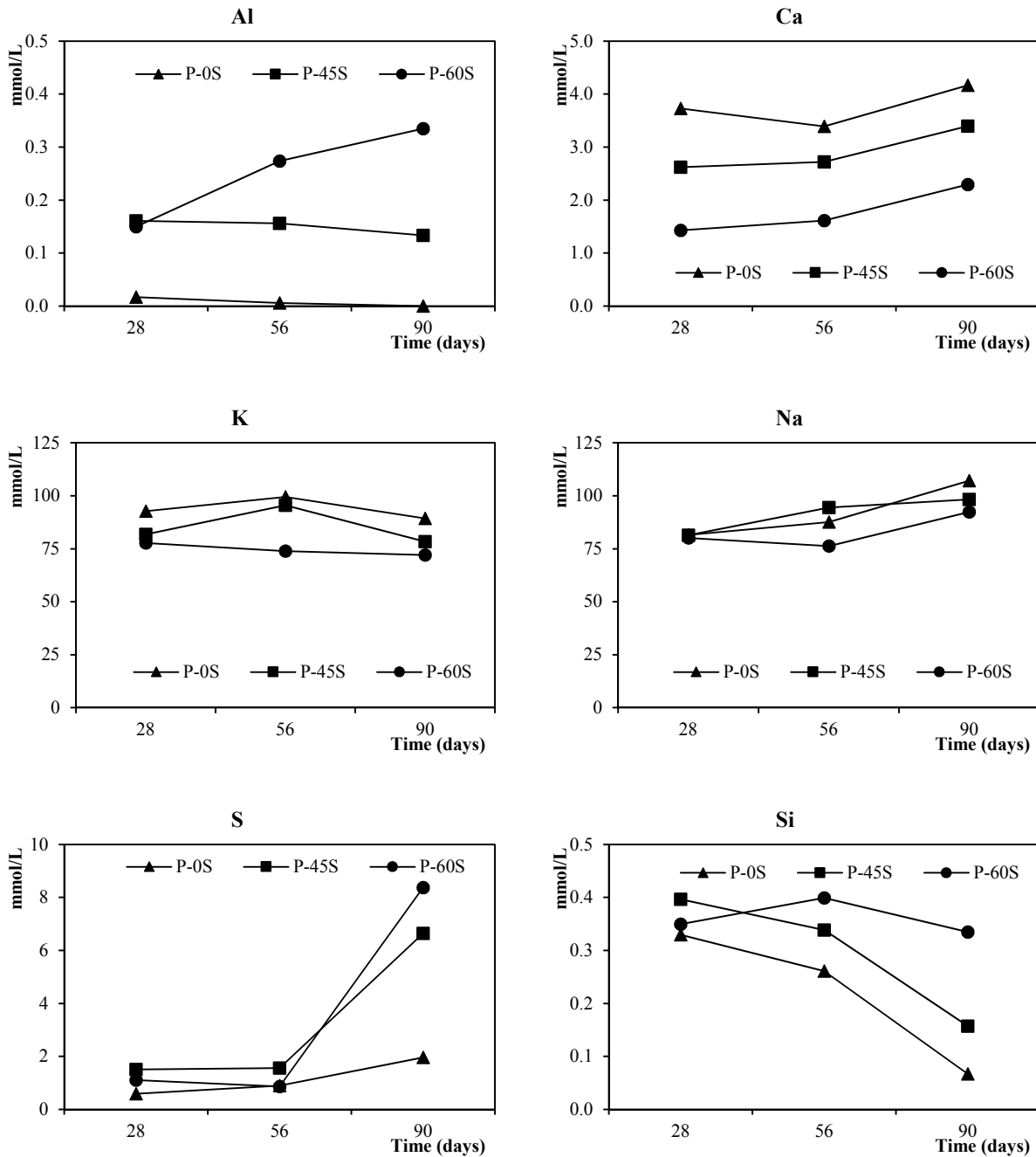
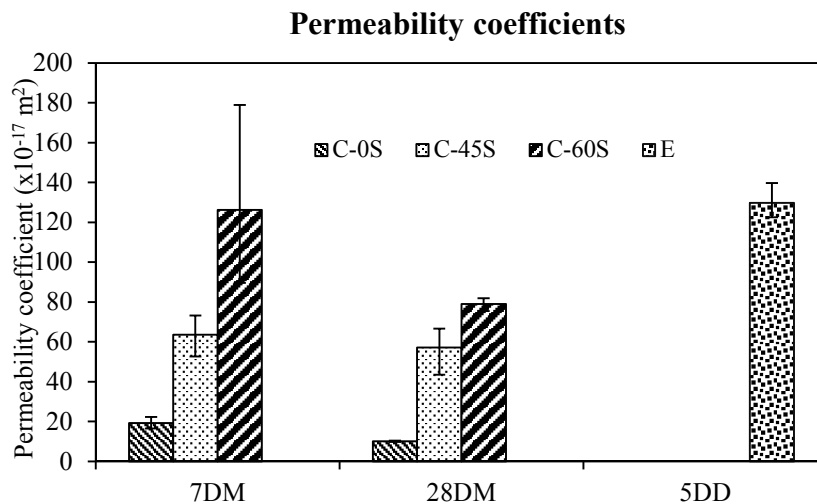


Figure 4.15: Measured concentrations of Al, Ca, K, Na, S and Si in pore solutions

#### 4.4.7 Gas permeability test results

The results for coefficients of gas permeability depicted as bar charts along with error bars are given in Fig. 4.16. In the annotations, 7DM is for 7 days of moist curing with additional 21 days of air curing, 28DM is for 28 days of moist curing and 5DD is for 5 day of air curing. Also, FRM was annotated by letter E in the graph. It is observed that increasing slag replacements levels also made concrete more permeable to gas. C-45S-7DM had a permeability coefficient that was about

3 times higher than that of C-0S-7DM. The less negative corrosion potentials and low corrosion rates of C-45S as shown in the corrosion initiation results may hence be attributed to the Cl<sup>-</sup> binding of the matrix with the presence of slag (Dhir et al., 1996; Luo et al., 2003). The gas permeability coefficient of C-60S-7DM was approximately 2 times that of C-45S-7DM. This may be attributed to drying shrinkage cracking and limited pozzolanic reaction in the mix with increased replacement level. Hence, for C-60S-7DM, the permeability factor of the matrix is postulated to be dominant in controlling its corrosion performance. It is also observed that moist curing improved concrete microstructure and reduce concrete permeability. This is reflected in the reduced coefficients of gas permeability of samples with 28 days of moist curing as compared to those with only 7 days of moist curing. In construction, the longer curing period may be applicable for underground structural components such as foundations which are exposed to moisture in the soil. The proprietary FRM has very high gas permeability and its permeability coefficient was at similar level to that of C-60S-7DM. This may be due to the high volume fraction of synthetic microfibers in the composite, which resulted in poorer consolidation of the matrix. FRM will be used in the study of interface qualities on corrosion to be presented in **Chapter 6**.



**Figure 4.16: Coefficient of gas permeability**

#### 4.4.8 TGA results

The DTA/TGA analysis results for paste with 0%, 45% and 60% slag replacement are given **Fig. 4.17**. It is observed that slag greatly reduced the available CH in the pastes. The reduction intensities increased with increasing slag replacement levels, attributable to the dilution effect and pozzolanic reaction which consumes CH from hydration reactions. Within individual mix designs, the amount of CH changed insignificantly with time. This is consistent with pore solution analysis results where Ca concentrations were found to reduce with increasing slag replacement levels yet change little with time within a certain mix.

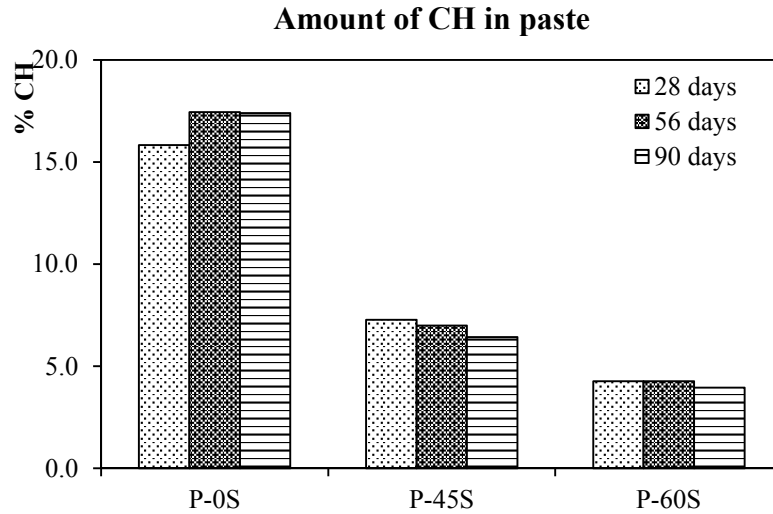


**Figure 4.17: Weight percentage of CH in pastes with and without slag replacement**

## 4.5 Discussion

### 4.5.1 Early corrosion initiation for C-60S

It is intriguing to observe that although pH values for all pastes were around 13, time to initiation of corrosion for C-60S were shorter than that of C-0S/45S. This is based on the more negative corrosion potentials and higher corrosion rates for C-60S-0H at an earlier stage of electrochemical measurements. This is also apparent from the corrosion patches observed on rebar surface in C-60S-0H after 98 days in NaCl solution. The phenomenon may be attributed to three factors: (i) higher permeability of the matrix, (ii) localized shrinkage cracking, and (iii) less stable passive film for C-60S due to higher concentration of S in its pore solution which was already discussed in the pore solution analysis results. The increase in concrete permeability was attributed to two major factors. As slag replacement level increased, smaller fraction of it would undergo pozzolanic reaction due to its dilution effect and the resulting limited availability of CH. Also, air drying after 7-day moist curing reduced the available water required to maintain pozzolanic reaction. Air drying may also cause shrinkage-induced cracking. Autogenous shrinkage may also be a problem with slag concrete. It was shown that autogenous shrinkage increased with the presence of slag in concrete (Lee et al., 2006; Lim & Wee, 2000). The combined action of reduced pozzolanic reaction and cracking due to drying and autogenous shrinkage caused increased pore interconnectivity in C-60S as compared to C-0/45S, leading to higher permeability in the matrix as presented earlier. The elastic modulus results in **Fig. 4.18** also showed consistent results. It is observed that C-60S has a modulus of elasticity 29% lower than that of C-0S and 11% lower than that of C-45S. Elastic modulus further reduced at 56 days for C-45S/60S and that may be attributed to microcracking caused by drying of the samples.

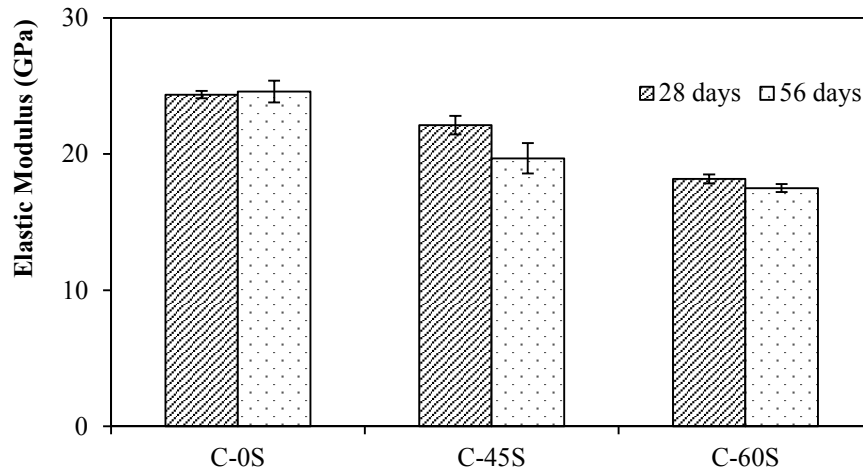


**Figure 4.18: Elastic modulus of concrete at 28 and 56 days**

To verify if high gas permeability also leads to an increase in  $\text{Cl}^-$  penetration, split sections of corrosion samples with no applied current along and transverse to the rebar direction were sprayed with 0.1 N  $\text{AgNO}_3$ . In a region contaminated by  $\text{Cl}^-$ ,  $\text{AgNO}_3$  forms a white precipitate of  $\text{AgCl}$ , while in an area with little  $\text{Cl}^-$ ,  $\text{AgNO}_3$  reacts with  $\text{OH}^-$  ions to form  $\text{AgOH}$  which appears as a brown precipitate on the surface (Otsuki et al., 1993). The color change occurs when water soluble  $\text{Cl}^-$  is greater than 0.15% weight of cement. It is observed in **Fig. 4.19** that with no applied current, there was no significant difference in the  $\text{Cl}^-$  penetration front amongst the samples. This is contradictory to gas permeability test results where it was found that coefficients of gas permeability increased with increasing slag replacement levels. The phenomenon is attributed to  $\text{Cl}^-$  binding ability of slag as discussed in the literature review. In C-45S-0H and C-60S-0H, their high permeability which could facilitate  $\text{Cl}^-$  diffusion was postulated to be offset by an enhanced  $\text{Cl}^-$  binding capacity of the composites with slag as cement replacement. This explains the similar  $\text{Cl}^-$  penetration depths in both the samples and C-0S-0H. The observation infers that gas permeability results should be treated with caution in relation to  $\text{Cl}^-$  penetration and  $\text{Cl}^-$ -induced corrosion resistance of concrete. Hence, the earlier onset of corrosion in concrete samples with 60% slag may be caused by other reasons rather than increased  $\text{Cl}^-$  penetration, in this case localized shrinkage cracking and poorer quality passive film. It is also noted that the transverse surfaces were obtained several months after the cylinder were tensile split and the light color along the surfaces running across the rebars may be attributed to carbonation of concrete.

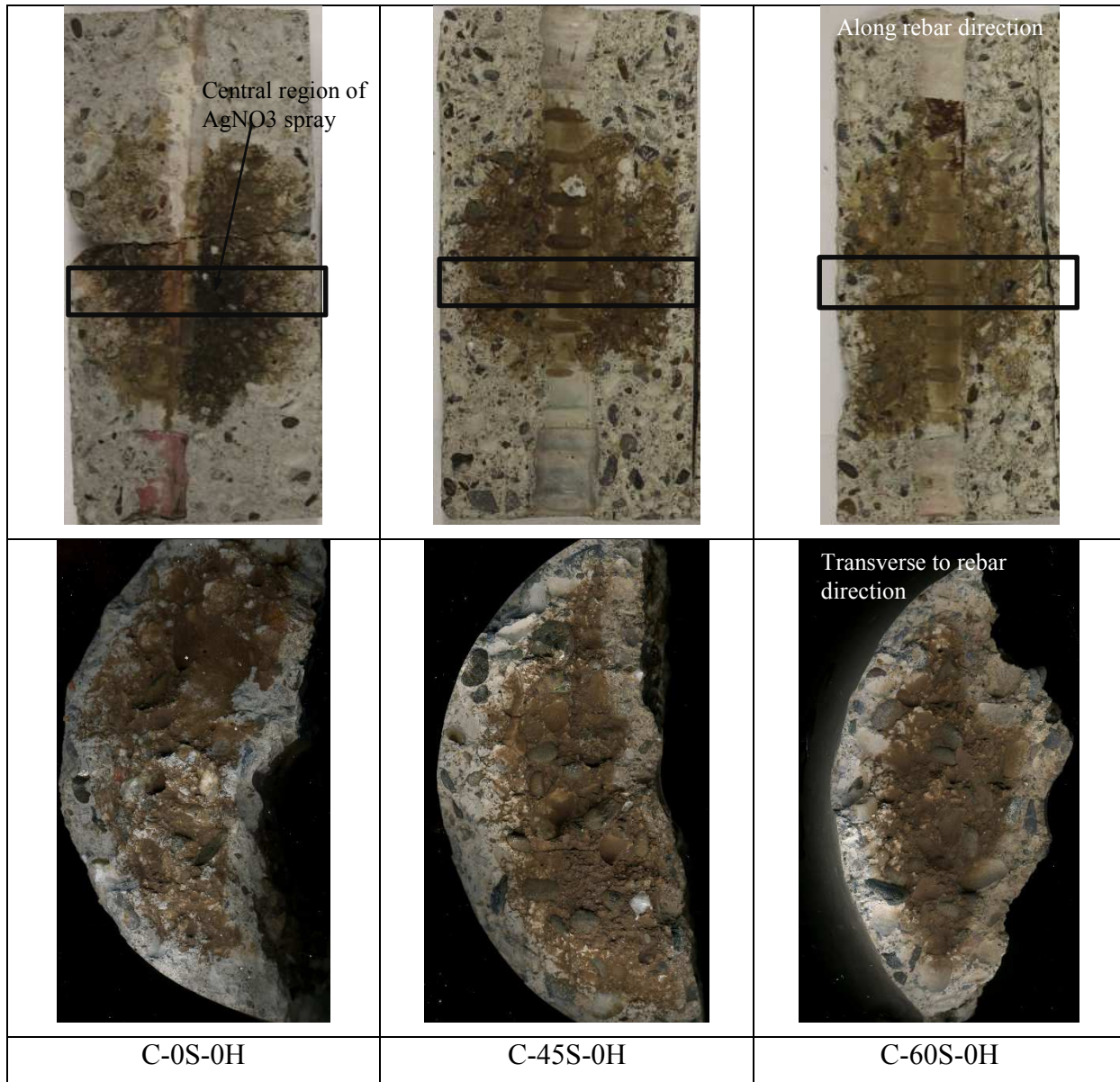


**Figure 4.19: Cl<sup>-</sup> penetration with AgNO<sub>3</sub> spray**

Autogenous and drying shrinkage was more critical in the corrosion samples as compared to that in plain concrete due to the presence of rebar which provided a restraint to concrete. The presence of restraint led to high tensile stress in concrete. If the stress is higher than the composite's tensile strength, cracking occurs. Observation of the surface of C-60S (with 60% slag replacement) after 21 days in air provided in **Fig. 4.20** confirmed localized cracking on the sample surface. No such visible cracks existed on C-0S and C-45S. This is consistent with observations by other researchers who found that high volume replacement of cement by slag increased autogenous shrinkage in concrete due to self-desiccation induced by higher consumption of cementitious materials in hydration (Lee et al., 2006; Lim & Wee, 2000). Also, drying shrinkage of concrete integrated with slag increased with earlier drying time (Tazawa et al., 1989). The shrinkage cracking provides a shortcut for an ingress of Cl<sup>-</sup> to reach the steel surface, leading to an earlier initiation of corrosion in the sample.

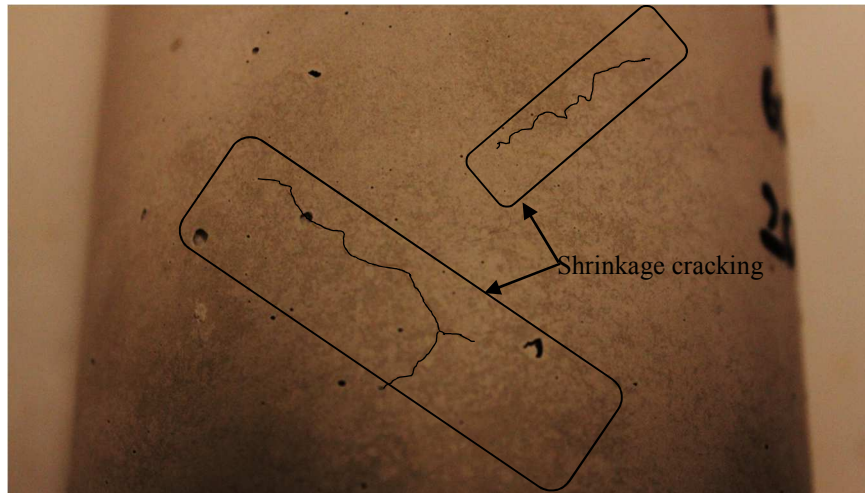


**Figure 4.20: Shrinkage cracking in C-60S before immersion in 3.5% NaCl solution**

With regard to passive film stability, it was proposed that at early age of hydration, passive film in paste with high level of slag replacement was based on Fe(II) rather than Fe(III) owing to the consumption of O<sub>2</sub> by the reducing species from slag (Macphee, 1993). As discussed in the literature review, SEM and X-ray map showed a more diffused passive film in the sample with 75% slag in his study. A less stable film combined with higher permeability with resulting higher Cl<sup>-</sup> concentration led to a less effective protection to steel against corrosion. Pore solution chemical analysis results provided in **Fig. 4.15** confirmed that S concentrations at 28 days were higher in C-60S than that in C-0S. This is believed to contribute to an early onset of corrosion for C-60S. However, in C-45S, a more refinement of microstructure and less drying shrinkage helped to offset the poor passive film quality. As a result, corrosion initiation was delayed to a later age.

#### **4.5.2 Crack initiation**

It is observed that C-45S-24H showed cracking after the applied current regime although C-0S-24H showed no sign of cracking. This may be attributed to: (i) slightly higher mass loss in C-45S-24H, and (ii) a denser steel-concrete interface in C-45S. According to the time-to-cracking model suggested by Weyers (1998), before an internal pressure is created, the free space at steel-concrete interface needs to be filled up. The free space is directly related to the surface area of reinforcement, W/B ratio, degree of hydration and degree of consolidation. BSE micrographs in **Fig. 4.21** show that C-45S and C-60S had a denser matrix surrounding the rebar as compared to that of C-0S. This may be attributed to an improved particle packing in concrete with slag replacements. The smaller number of voids allowed for less corrosion products to fill in the pores and that initiated an early formation of cracking in C-45S-24H as compared to C-0S-24H. From the BSE and EDX element mapping images in **Fig. 4.22**, it is also evident that more corrosion products which can be identified with Fe and O diffused into the surrounding matrix in C-0S-48H. This demonstrates that the more porous yet less interconnected matrix in C-0S allows for an enhanced accommodation of corrosion products. On the other hand, with 48 hours of applied current, C-45S-48H showed less extensive cracking as compared to C-0S-48H. It is unclear if the nature of corrosion products and their volume expansion ratios after concrete cracking were different. EDX elemental analysis (**Fig. 4.22**) showed a higher concentration of oxygen (brighter contrast) within the corrosion products for C-0S. However, further studies in characterizing the properties of corrosion products in different concrete mixes will be needed.



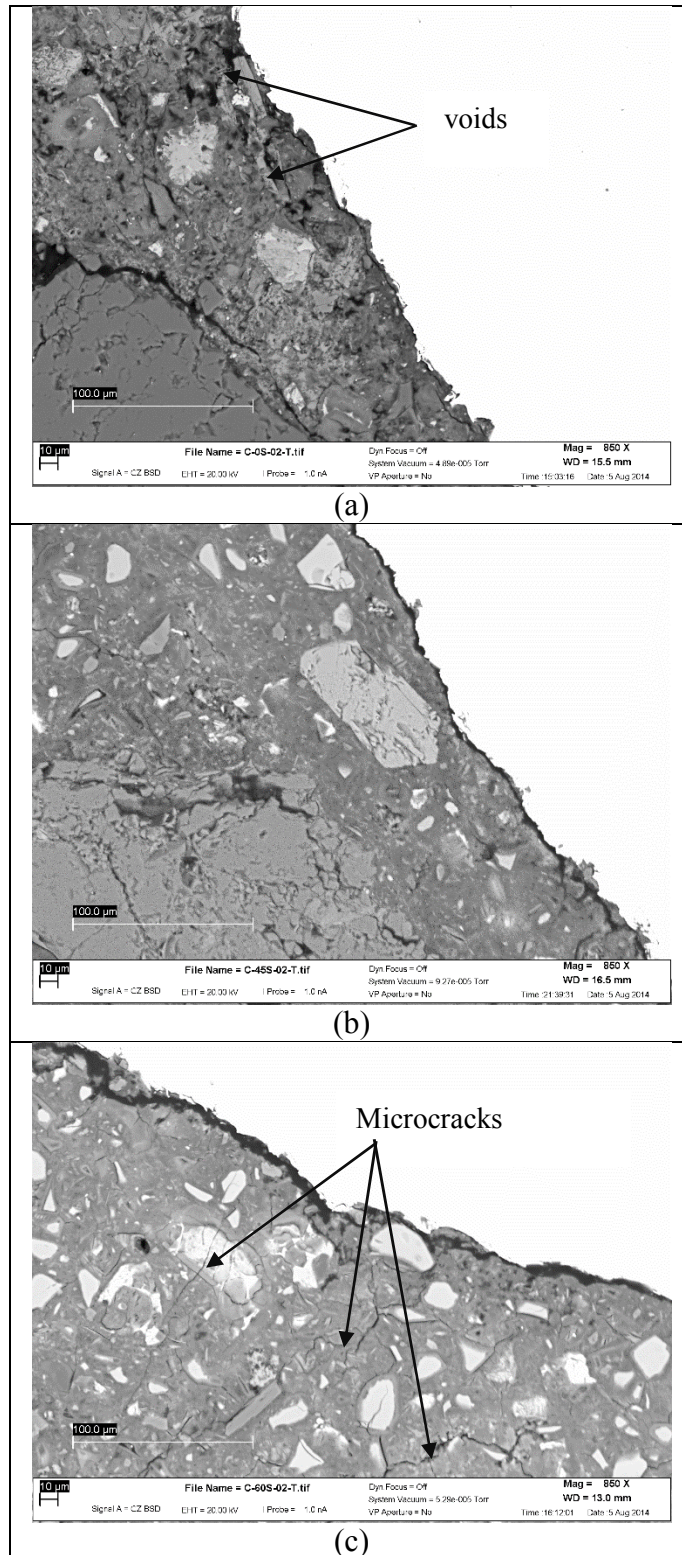


**Figure 4.21: SEM micrographs of interfaces for: (a) C-0S-0H, (b) C-45S-0H, and C-60S-0H**

Although C-60S has a denser matrix at the interface, its permeability, as shown in the gas permeability results, was higher due to shrinkage and a limited pozzolanic reaction, resulting in



the continuity of pores. As shown in **Fig. 4.21**, microcracks were observed in C-60S matrix. The cracks are postulated to be caused by autogenous and drying shrinkage in C-60S. Oven drying cracking was phased out as no such cracking was observed in C-0S and C-45 despite the same drying condition in the sample preparation. This contributed to an early corrosion initiation in C-60S as already discussed. As the pores and drying cracks in C-60S were of microscale, they were less effective in accommodating corrosion products as compared to the larger pores in C-0S. This helps to explain the more extensive cracking in C-60S under the impressed current. The gap between the rebar and the matrix was caused by oven drying of the samples as explained in **Chapter 3**.

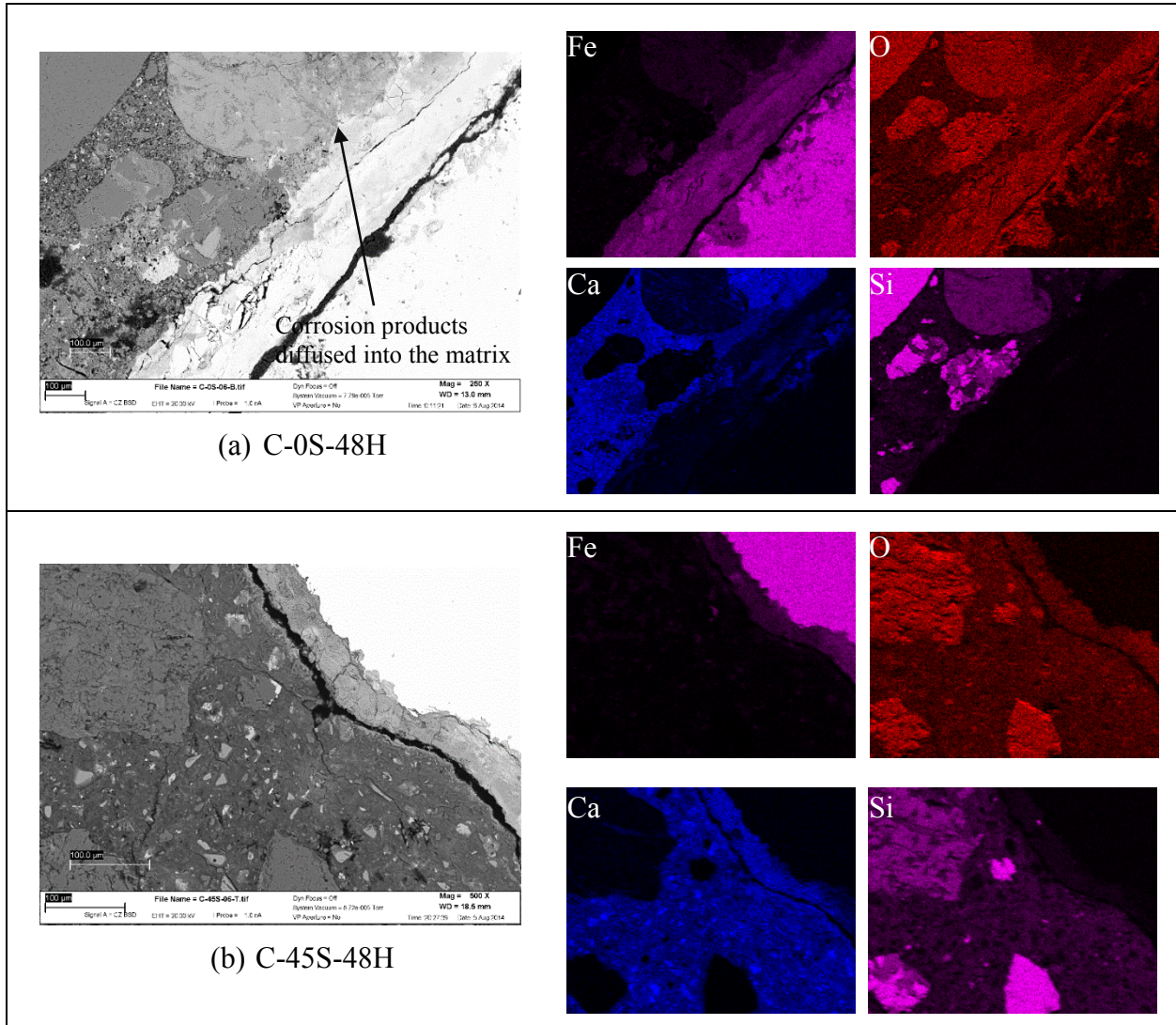
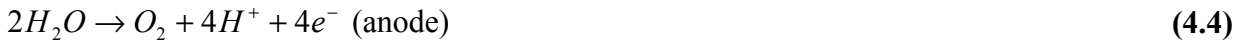


**Figure 4.22: SEM micrographs and corresponding EDX results for Fe, O, Ca and Si at interfaces of: (a) C-0S-48H, and (b) C-45S-48H**

### 4.5.3 Gravimetric mass loss and water oxidation

It is observed from **Table 4.2** that gravimetric mass losses with applied current are always less than the theoretical mass losses. This phenomenon was observed by other researchers (Ballim &

Reid, 2003) and they attributed this to other competing reactions against oxidation of steel. These processes may include water oxidation and migration of other compounds into the paste or concrete pores that might change the corrosion process (Caré & Raharinaivo, 2007). Water oxidation evolves oxygen (O<sub>2</sub>) at anode and hydrogen (H<sub>2</sub>) at cathode. The half reactions at the anode and cathode are given in **Eq. 4.4** and **4.5**, respectively. Water oxidation generally occurs when the cell voltage to maintain constant current is greater than 1.23 V which is the potential difference between hydrogen evolution and oxygen evolution equilibriums in aqueous solution (Poursaee & Hansson, 2009). The uncompensated cell voltages (consisting of IR drop and electrochemical potential) of all samples during the applied current were between 5 V and 10 V, indicating high possibility of water oxidation. It is observed from **Eq. 4.4** that 2 moles of H<sub>2</sub>O contribute 4e<sup>-</sup> to the total charge flow in the circuit. This will offset the net charge flow from the steel anode and lead to smaller observed gravimetric mass loss as compared to theoretical mass loss. During the accelerated corrosion test, small gas bubbles could be seen rising intermittently from the cathode and this is believed to be H<sub>2</sub>.



#### 4.5.4 Gravimetric mass loss and interfacial acidification

Water oxidation helps to explain the lower gravimetric mass losses as compared to the theoretical values when there is no added NaCl in the mixing water. But another interesting phenomenon needs to be elucidated with the results from the accelerated corrosion test. It is noted that with 24 hours and 48 hours of applied current, the mass losses increased with increasing slag replacement levels. Besides the varied qualities of the passive film as a reason, the increase in gravimetric mass losses with increasing slag replacement levels may also be contributed by partial acidification at the interface. As discussed, water oxidation generates H<sup>+</sup> at the anode, leading to a local depression of pH and destabilization of the passive film. As a result, iron ions are created through the impressed current at a fast rate and they react with water to form Fe(OH)<sub>2</sub> and H<sup>+</sup> as depicted in **Eq. 4.6** (Glass et al., 2008). The reaction may also involve Fe<sup>3+</sup> (**Eq. 4.7**) which may be formed either during the applied current or from Fe<sup>2+</sup> through further reduction reaction. As the reactions take place within the interfacial region, it is difficult for H<sup>+</sup> to be neutralized by OH<sup>-</sup> from concrete pore solution and the immersion solution. Cl<sup>-</sup> in the pore solution will act as a charge balancing species to produce HCl, leading to local pH reduction. Early in the process, a reduction in pH will initiate dissolution of CH at the interfacial region to provide a buffering mechanism. With time, the CH at the interface will be deprived and the buffering action will not be sustained, leading to further lowering of pH level. This is prevalent in accelerated corrosion test where corrosion activity is augmented with the applied current. Low pH condition increase dissolution of iron to form Fe<sup>2+</sup> and 2e<sup>-</sup>. The free electrons will react with available H<sup>+</sup> to form hydrogen gas. The dissolution will add on to the steel mass loss induced by the impressed current. Although detailed results are not provided here, the local reduction in pH under accelerated corrosion was confirmed in a complementary study in which interfacial pore solutions during accelerate corrosion were extracted. pH values of the extracted solutions were measured to be less than 2. This phenomenon is more critical for samples with slag as cement replacement. This is due to a general reduction in CH within the paste resulted from dilution and pozzolanic reaction as presented in the TGA/DTA results. Less CH means less buffering action and more dissolution of rebar by the acidic solution at the interface.



It is also noted that pH values of solutions extracted from crevices of different structural steels were found to vary depending on the types of steel and compositions of other ions in the bulk solutions (Turnbull, 1983). For carbon steel in 3.5% NaCl solution, the pH value of the crevice solution was found to go down to only about 6. The much lower pH obtained from the steel-concrete interface observed in this study may be attributed to 2 main possibilities: (i) acceleration of the corrosion process through the impressed current, and (ii) hydrolysis of  $Fe^{3+}$  which may be formed from initial oxidation of the steel substrate or through further reduction of  $Fe^{2+}$  upon exposure to oxygen. The equilibrium constant, which is defined as the ratio of concentrations of products over reactants for a reaction, for  $Fe^{3+}$  is several magnitudes higher than that of  $Fe^{2+}$  (Baes & Mesmer, 1976). This implies that for the same concentration of  $Fe^{2+}$  and  $Fe^{3+}$  participating in a hydrolysis reaction, hydrolysis of  $Fe^{3+}$  would give higher concentration of  $H^+$ , leading to a more aggressive depression of local pH.

#### 4.5.5 Corrosion mass loss rate without added NaCl

It is observed in **Table 4.2** that the mass losses are not proportional to the duration of the applied current. In C-0S, an applied current of 24 hours led to a mass loss of only 0.3 g or 11.5% of that for 48 hours of applied current. This trend also applied to C-45S/60S. This may be attributed to the ineffectiveness of the applied current in oxidizing the anode within the first 24 hours. All rebars were, in the first place, protected by passive films although they may be of different passivity strengths, as discussed. At the start of the applied current test, it would be difficult for the electrons to be removed from the rebars and the electrons reaching the cathode would have to come from other sources such as water oxidation where it was easier to extract electrons from. However, as time progressed, the passive film slowly degraded possibly due to interfacial pH depression resulted from water oxidation. The film may have been destroyed in the second phase and this led to more steel oxidation under the same applied current intensity. The time to degrade the film is believed to be proportional to its stability and C-0S seemed to have to the most stable film.

Due to small corrosion rates after the applied current in the samples used in the study, the additional mass losses during the electrochemical measurement were of a small fraction to the total mass losses. Hence, the gravimetric mass losses during the applied current could be estimated to be the same as the total gravimetric mass losses and the results are summarized in **Table 4.2**. It is observed that the mass losses were concentrated in the second 24 hours of the current regime. This is contradictory to what was observed in the results presented in **Chapter 3** where large proportions of the mass losses occurred in the first 24 hours. The main difference was that no NaCl was added into the mixing water of the corrosion samples used in this chapter. The rebars had to be depassivated first by the applied current and a high cell voltage would be required. This led to more water oxidation reactions and the smaller observed gravimetric mass losses in the first 24 hours of the applied current. In modelling corrosion cracking of reinforced concrete structures, a model with a reduced corrosion activity with time as observed in **Chapter 3** is more applicable as corrosion initiation stage was eliminated with 4% NaCl in the mixing water.

#### 4.6 Conclusions

From the results and discussion, the following can be concluded from this study:

- With 7 days of moist curing, slag as cement replacement of 60% by mass in concrete with W/B = 0.54 led to poor protection of steel rebar against corrosion initiation. This is attributed to shrinkage-induced cracking and a less stable passive film attributed to the presence of reducing agents in the pore solution.
- Nevertheless, slag replacement level of up to 60% does not reduce pore solution pH. This is because Na and K are the dominant contributors to the alkalinity of the pore solutions and the pH values are not sensitive to the variation in the alkalinity.
- Although slag replacement level of 45% slowed down corrosion initiation, the onset of cracking occurred early due to a denser matrix and the steel-concrete interface. The dense interface is believed to cause a higher pressure build-up to the surrounding concrete when corrosion products formed.
- For the same regimes of applied current, increasing slag replacement levels led to more mass losses due to the less stable passive film and steel-concrete acidification. Based on this observation, in real structures, propagation stage as part of the service life may be shortened in reinforced concrete made with high volume slag replacement.
- Results from corrosion potentials were generally consistent with corrosion rates. More negative corrosion potentials coincided with higher measured corrosion rates.
- With no added NaCl in the mixing water, it is not necessary for impressed corrosion test to create a uniform corrosion on steel surface due to varying interface quality and the resulting non-uniform protection provided by concrete to steel.
- The results from the study emphasize that for concrete with high W/B and with moist curing condition generally adopted in construction (less than 7 days of moist curing), high slag replacement levels can be detrimental to concrete resistance against corrosion both in the initiation and propagation stage.

In the next chapter, the combined effects of slag and fiber on steel corrosion in concrete will be presented. In addition, the influence of induced current intensities on corrosion rates and corrosion cracking was also studied. Low current intensities would better represent corrosion activity in real structures but it is unclear if higher or lower induced current would be more detrimental to samples used in laboratory. A smaller applied current means lower cell voltage and less water oxidation, leading to more effective applied current and mass loss of steel. However, with low applied current, corrosion products would be able to more gradually penetrate into the matrix pores and would cause less stress to the surrounding matrix. The studying in the next chapter would help to substantiate the argument on corrosion product penetration. The results would also provide us information on the setup of accelerated corrosion test in the laboratory to better mimic natural corrosion in concrete structures.

# 5 Effects of hybrid fibers and current intensities on corrosion of reinforcing bars in concrete with high-volume slag addition

## Summary

Hybrid fibers of different sizes in concrete are known to improve concrete mechanical properties and crack distribution at relatively low fiber volume fractions as compared to single-size fiber-reinforced concrete. In this study, the combined effects of hybrid fibers and slag on corrosion resistance of concrete was investigated. Water-binder (W/B) ratio of 0.54 and conventional 7-day moist curing were adopted. Fiber hybridization consisted of 1.3% hooked-end steel macro fibers and 0.2% polyvinyl alcohol (PVA) microfibers. Three slag replacement levels of 0%, 45% and 60% by mass were used. Accelerated corrosion test with different current intensities were implemented. Corrosion rates, mass losses and concrete microstructures were investigated. Test results reveal that although hybrid fibers reduced concrete consolidation as reflected in lower elastic modulus results, they do not adversely affect corrosion initiation of steel in concrete. Under accelerated corrosion test to mimic the corrosion propagation stage, hybrid fibers significantly reduced corrosion rates through passive confinement. The effects of hybrid fibers on corrosion behavior of hybrid fiber reinforced concrete (HyFRC) were dominant as compared to the influence of slag. At smaller applied current density, corrosion products were less powdery and tougher to remove, attributable to its more gradual formation and possibly to the phase transformation of corrosion products under continuing availability of oxygen and moisture. Interestingly, under accelerated corrosion test, steel fibers near the specimen surface were found to corrode due to a potential drop between the anode and the cathode although the phenomenon did not affect the total charge flow from the anode.

## 5.1 Introduction

For a more sustainable civil infrastructure development, a greener and higher performance concrete composite is needed. One of the candidates is a concrete composite called hybrid fiber reinforced concrete (HyFRC). In the composite, microfibers such as polyvinyl alcohol (PVA) fibers are used to control microcracks which are inherent in concrete or formed during loading. Macrofibers such as steel fibers are also added to engage the cracks as they grow so that a gradual crack propagation is warranted. The synergy of macro- and microfibers leads to multi-level crack arresting mechanism and an improved composite performance at a relatively lower fiber volume fraction as compared to other high-performance fiber reinforced concrete. It was shown that the use of 0.2% of PVA fibers and 1.3% of steel fibers in concrete allows for a deflection hardening response beyond the yield strain of steel (Blunt & Ostertag, 2009). Deflection hardening is defined as an ability of the composite to carry increasing load after the first crack is formed. The characteristic is beneficial in terms of durability as it coincides with the formation of distributed microcracks which limit the ingress of aggressive ions and moisture into concrete. Also, distributed

microcracks enhance post-crack flexural stiffness and that will improve the structure's serviceability limit state (Ostertag & Blunt, 2008). Application areas of the composite include bridge approach slabs (Ostertag & Blunt, 2007) and seismic resistant bridge columns (Trono et al., 2013).

To reduce environmental impact at materials production stage, it is suggested that cement be replaced by industrial wastes such as slag. However, slag as cement replacement may cause durability problems to concrete. In the previous chapter, under 7-day moist curing, concrete with slag replacement level of 60% showed poor corrosion resistance in both initiation and propagation stage. Corrosion test was conducted on cylindrical samples with #8 rebar in the middle as the anode. Corrosion initiated earlier in the samples with 60% slag as compared to those with 0% and 45% slag replacement level. Also, 60% slag replacement led to more mass losses and higher corrosion rates after the impressed current regimes. This is due to shrinkage-induced cracking, the presence of reducing agents in pore solution and reduction in available CH to provide a buffering action in samples with 60% slag. On the other hand, fibers have been shown to increase corrosion resistance of steel rebar in concrete (Grubb et al., 2007; Jen & Ostertag, 2012). This was attributed to passive confinement provided by the fibers to the expansion caused by corrosion products (Grubb et al., 2007). With hybridization of fibers and the resulting deflection hardening, the level of confinement will be increased. However, it is unclear if the beneficial effects of hybrid fibers are more dominant than the disadvantage of high level slag as cement replacement in concrete. So far, the combined effects of fibers and slag on corrosion of steel reinforcing bar has not yet been investigated.

In this study, the effects of hybrid fibers on corrosion of reinforcing bar in concrete with different slag replacement levels were investigated. Hybridization of 1.3% steel fibers and 0.2% PVA fibers were used in concrete with water-binder (W/B) ratio of 0.54. The volume fractions were shown to provide deflection hardening behavior to the concrete composite (Blunt & Ostertag, 2009). Accelerated corrosion test with a constant applied current to induce corrosion cracking to concrete was adopted. Two current intensities of 1 mA/cm<sup>2</sup> and 0.2 mA/cm<sup>2</sup> were implemented to study their effects on corrosion cracking and mass losses. A corresponding set of samples with no applied current were also prepared to study the effects of slag and fibers on corrosion initiation. Where applicable, results for plain concrete with 1 mA/cm<sup>2</sup> of applied current from **Chapter 4** were also presented again for comparison. Microstructural analysis with scanning electron microscopy (SEM) was also used to study the steel-concrete interfaces with and without accelerated corrosion. The results provided a systematic explanation to some unexpected phenomena observed in the accelerated corrosion tests. The study as a whole also helps to provide a fundamental understanding on the combined effects of slag and fibers on corrosion of reinforcing bars in concrete.

## **5.2 Materials and methods**

### **5.2.1 Materials**

ASTM Type II cement was used as the main binder and slag was used as cement replacement. Their chemical compositions based on X-ray fluorescence (XRF) were given in **Table 2.1** of **Chapter 2**. Aggregates were composed of pea gravel with a maximum size of 10 mm and fine sand with a measured fineness modulus of 3.2. Structural steel reinforcement with a yield strength of 420 MPa was used as the anode. Its chemical compositions was given in **Table 3.1** of **Chapter**



3. The hybrid fiber mixture contained a combination of 30 mm and 60 mm steel macrofibers, and 8 mm PVA microfibers (**Fig. 5.1**). The properties of the fibers including those for the 30 mm steel fiber and PVA fibers which were given in **Chapter 2** are summarized again in **Table 5.1**.



**Figure 5.1: Fibers used in the study: (a) 30 mm and 60 mm hooked-end steel fibers, and (b) PVA microfibers**

**Table 5.1: Fiber properties**

| Fiber designation | Fiber material | Fiber length (mm) | Fiber diameter (mm) | Fiber tensile strength (MPa) | Young modulus (GPa) |
|-------------------|----------------|-------------------|---------------------|------------------------------|---------------------|
| PVA fiber         | PVA            | 8                 | 0.038               | 1600                         | 40                  |
| 30 mm steel fiber | Steel          | 30                | 0.55                | 1350                         | 210                 |
| 60 mm steel fiber | Steel          | 60                | 0.75                | 1050                         | 210                 |

### 5.2.2 Concrete mix designs

Hybrid fiber-reinforced concrete (HyFRC) with water-binder (W/B) ratio of 0.54 and slag replacement levels of 0%, 45% and 60% was used to study the combined effect of fibers and slag on steel corrosion. Steel and PVA fibers were used with volume fractions of 1.3% and 0.2%, respectively. The total volume fraction of steel fibers comprised 0.8% of 60 mm long and 0.5% of 30 mm long steel fibers. The volume fractions were optimized for both fresh concrete and mechanical properties as outlined in a study by Blunt and Ostertag (2009). With the presence of hybrid fibers, the relatively high W/B was necessary to ensure good workability of the composite without the aid of chemical admixtures. To study the effects of current magnitude on corrosion, plain concrete with the same W/B and slag replacement levels were also prepared. All the total 6 mix designs used for this study are summarized in **Table 5.2**. In all cases, the amount of binder and the ratio of coarse to fine aggregates were kept constant. Applied current of 1 mA/cm<sup>2</sup> was implemented for HyFRC and 0.2 mA/cm<sup>2</sup> for the plain concrete.

**Table 5.2: Mix designs for concrete mixes used in accelerated corrosion study (kg/m<sup>3</sup>)**

|                   | HyFRC-0S | HyFRC-45S | HyFRC-60S | C-0S  | C-45S | C-60S |
|-------------------|----------|-----------|-----------|-------|-------|-------|
| W/B               | 0.54     | 0.54      | 0.54      | 0.54  | 0.54  | 0.54  |
| Water             | 228.6    | 228.6     | 228.6     | 228.6 | 228.6 | 228.6 |
| Cement            | 425.8    | 234.2     | 170.3     | 425.8 | 234.2 | 170.3 |
| Slag              | -        | 191.6     | 255.5     | -     | 191.6 | 255.5 |
| Fine aggregate    | 853.3    | 814.4     | 810.9     | 853.3 | 836.3 | 833.0 |
| Coarse aggregate  | 775.5    | 740.2     | 737.0     | 775.5 | 760.1 | 757.1 |
| 60mm Steel fibers | 62.9     | 62.9      | 62.9      | -     | -     | -     |
| 30mm Steel fibers | 39.2     | 39.2      | 39.2      | -     | -     | -     |
| 8mm PVA           | 2.4      | 2.4       | 2.4       | -     | -     | -     |

### 5.2.3 Specimen preparation and corrosion testing procedure

Specimen preparation and corrosion testing follow the procedure outlined in **Chapter 4**. The specimens were cast and moist-cured for 7 days before being exposed to laboratory air for a minimum of 21 days. For HyFRC, additional cylinders cured under the same regime were also produced to find compressive strength at 28 and 56 days. For plain concrete, an applied current regime of 22.3 mA (0.2 mA/cm<sup>2</sup>) was induced for 240 hours. The expected total charge or mass loss is the same as in the case of 111.5 mA (1 mA/cm<sup>2</sup>) applied current of 48 hours. Afterward, the samples were allowed to come to a steady state in 3.5% NaCl solution. The electrochemical tests for HyFRC samples were performed at 1, 3, 7, 14, 28, 56 and 98 days following the applied current. Plain concrete samples with the smaller applied current magnitude were measured up to 14 days only. In the sample annotation, C' stands for plain concrete with 0.2 mA/cm<sup>2</sup> applied current; HyFRC for hybrid fiber-reinforced concrete; 0S, 45S and 60S for slag replacement levels of 0%, 45% and 60% by mass; and nH for n hours of applied current. For example, HyFRC-45S-48H refers to HyFRC sample with 45% slag as cement replacement and with 48 hours of applied current. It is noted that C' was used instead of C to annotate plain concrete samples with 0.2 mA/cm<sup>2</sup> of applied current, to distinguish from samples with higher applied current magnitude as presented in **Chapter 4**.

### 5.2.4 Microscopic analysis

Following the accelerated corrosion, the samples from linear polarization group were sliced in the middle region to obtain disc elements of thickness 21.5 mm. The elements were prepared for optical and SEM microscopic analysis. The procedure was outlined in **Chapter 3**.

### 5.2.5 Gravimetric mass loss analysis

The samples from the Tafel test group were dried in oven at 110 °C for 24 hours and were subsequently subjected to splitting tensile test to extract the rebars in the middle. The wiring, heat shrink tube and coating on the rebars were then removed or cleaned off. HCl hexamethylene tetramine solution was used to remove corrosion products so that significant etching of the base metal could be minimized. The process for gravimetric mass loss measurement was detailed in **Chapter 3**.



## 5.3 Results

### 5.3.1 Mechanical properties

The compression test results are given in **Fig. 5.2**. It is observed that compressive strengths for any of the concrete mixes did not change significantly from 28 to 56 days. This means that the strengths stabilized after 7 days of moist curing and 21 days of air curing. As the current was applied after 28 days, the effects of strength gain on corrosion were not expected to significantly affect corrosion performance of the samples. Also, increasing the amount of slag in concrete also reduced concrete compressive strengths. Moist curing of only 7 days may not have allowed for full pozzolanic reaction. It is noted that the 7-day moist curing regime was to simulate onsite curing condition. Although compressive strengths of samples without slag were higher, the difference in cracking strengths was expected to be small across the mixes due to the presence of fibers. Fiber-matrix interaction determines the post-crack tensile strength in fiber-reinforced concrete. With the same types and volume fractions of fiber reinforcement, the post-crack response would be similar and would not significantly influence the cracking behavior of the samples under the accelerated corrosion test.

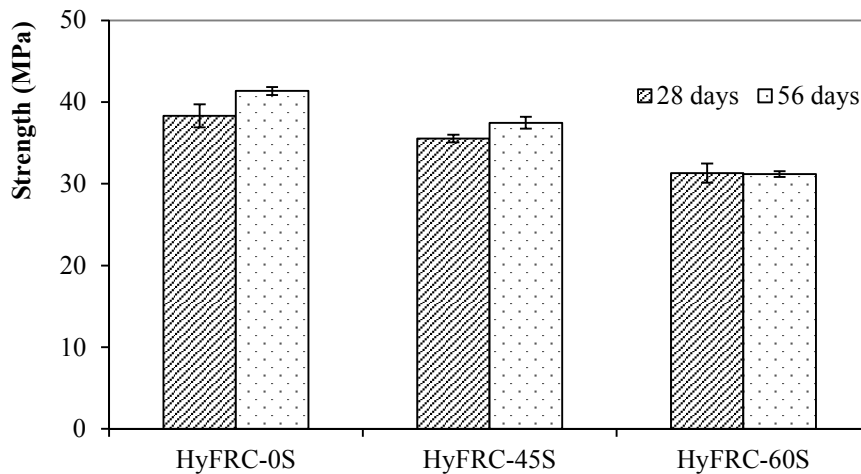


**Figure 5.2: Compressive strengths of HyFRC at 28 days and 56 days**

### 5.3.2 Corrosion initiation in HyFRC

The results for corrosion potentials of samples without applied current are given in **Fig. 5.3**. It is observed that corrosion potentials for HyFRC-0S/45S-0H became more negative than -277 mV at 7 days while those for HyFRC-60S-0H were always more negative than -277 mV throughout the measurement period. As mentioned in the previous chapter, there is a greater than 90 % chance that reinforcing steel bar is corroding in an area at a given time when the half-cell corrosion potentials are more negative than -277 mV versus saturated calomel electrode (SCE). Hence, 45% of slag as cement replacement maintained steel passivity up to 7 days and provided similar corrosion protection to that in samples with 0% slag replacement. The protection of steel against corrosion decreased when slag replacement level was increased to 60%. This may be attributed to the release of reducing agents in the form of soluble sulphides ( $S^{2-}$ ,  $HS^-$  and  $S_n^{2-}$ ) during hydration.

Reducing agents consume  $O_2$  and other oxidized species, inhibiting the formation of a more stable passive film on steel. This was discussed in detail in **Chapter 4**. It is noted that no shrinkage cracking was observed on the surfaces of all HyFRC samples. Hence, the effect of shrinkage on corrosion initiation was eliminated in the study. Unlike the case of plain concrete, only limited pozzolanic reaction and the presence of reducing agents in the pore solutions were the main parameters that determined corrosion initiation characteristics of steel in the HyFRC mixes.

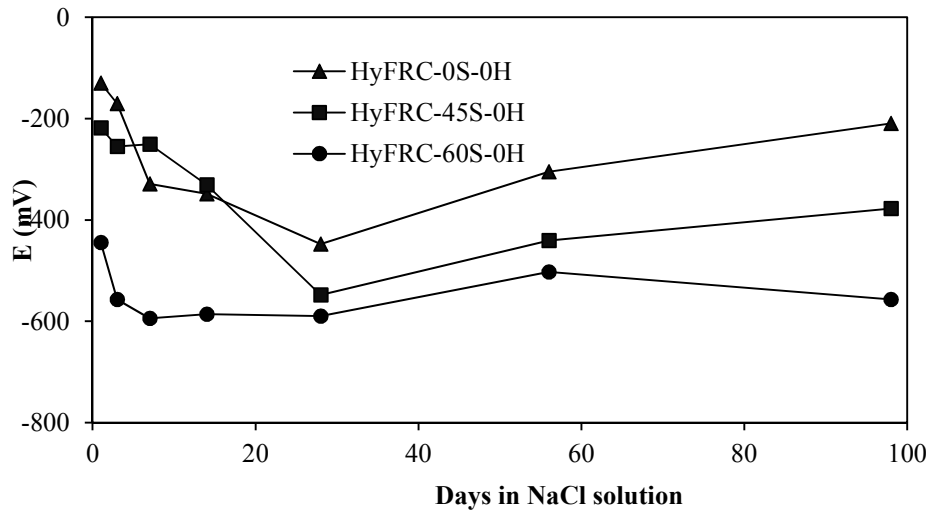


**Figure 5.3: Corrosion potentials for samples without applied current**

Based on corrosion potential results, the time to corrosion initiation for HyFRC seems to be similar to that found for plain concrete as presented in the previous chapter. One exception is for HyFRC-45S where corrosion potential turned more negative than  $-277$  mV after 14 days. The corrosion potential of C-45S as presented in **Chapter 4** were always less negative than  $-277$  mV. The presence of hybrid fibers may reduce concrete consolidation leading to a higher permeability in HyFRC. The presence of fibrillated fibers even at 0.1% volume fraction were shown to increase  $Cl^-$  permeability in concrete (Bayasi & Zeng, 1993; Toutanji et al., 1998). Elastic modulus results were used as a preliminary indicator of concrete consolidation and permeability. That is a reduced elastic modulus with the presence of fibers would indicate a poorer consolidation for the same mix compositions of the matrix. **Fig. 5.4** provides average elastic modulus values for plain concrete and HyFRC at 28 and 56 days. It is observed that HyFRC had lower elastic modulus as compared to plain concrete, probably indicating a poorer consolidation. This argument will be substantiated with microstructural study of HyFRC to be provided in the discussion part of the report.

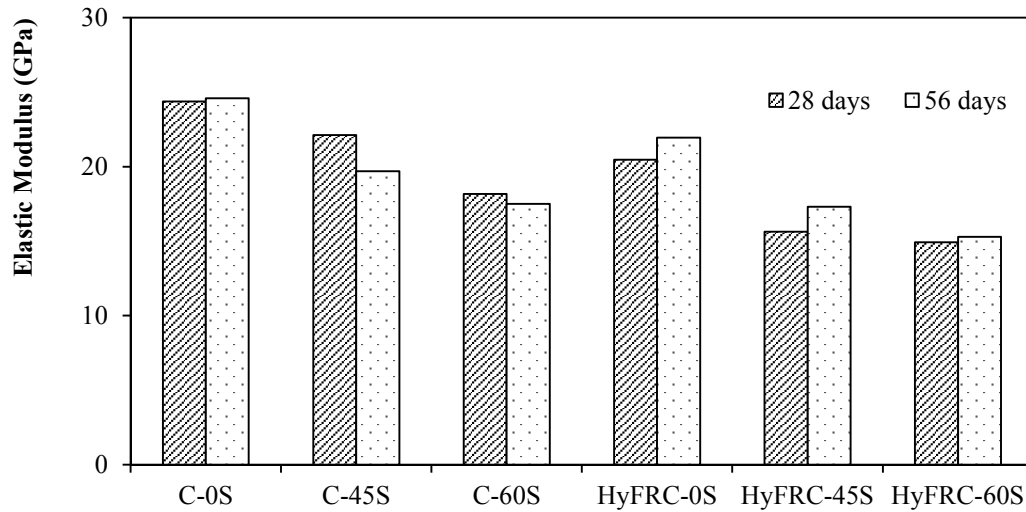


**Figure 5.4: Corrosion potentials for samples without applied current**

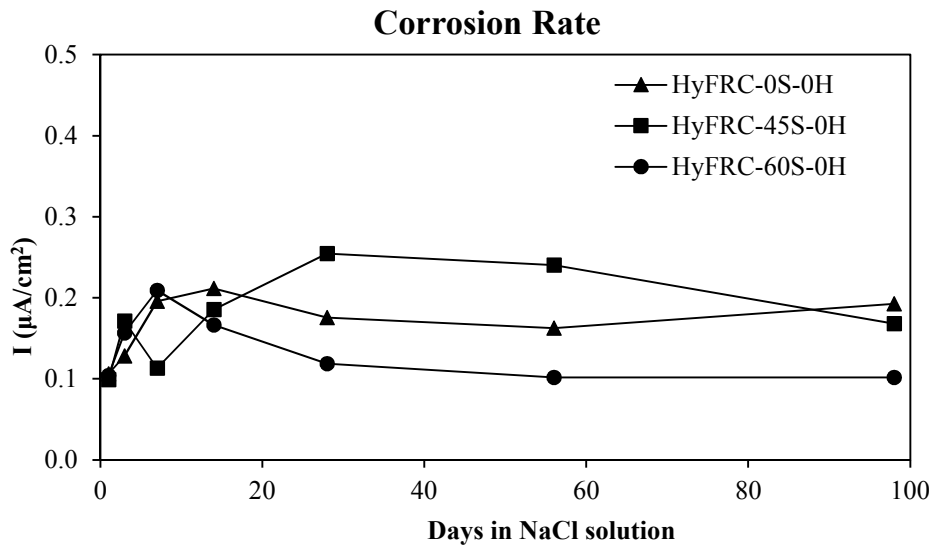


**Figure 5.5: Corrosion rates for samples without applied current**

The corresponding corrosion rates are given in **Fig. 5.5**. In this study, corrosion rates greater than  $0.1 \mu\text{A}/\text{cm}^2$  were taken as active. It is observed that corrosion rates for all samples with no applied current were in an active zone. The corrosion rate values were consistent with corrosion probability as indicated by the corrosion potential results. Corrosion rates for all HyFRC samples (except for HyFRC-45S) were of similar magnitude as compared to the values for plain concrete as presented in **Chapter 4**. However, in real structures where shrinkage and mechanical loading are expected to cause an initial damage, the higher crack resistance and crack distribution ability of HyFRC means that the composite will experience less cracking and as a result a delay in corrosion initiation. For the same loading level to induce cracking, corrosion resistance of cracked hybrid

fiber-reinforced concrete was shown to be superior than that of plain crack concrete (Blunt et al., 2015).

### 5.3.3 Corrosion results for HyFRC with applied current

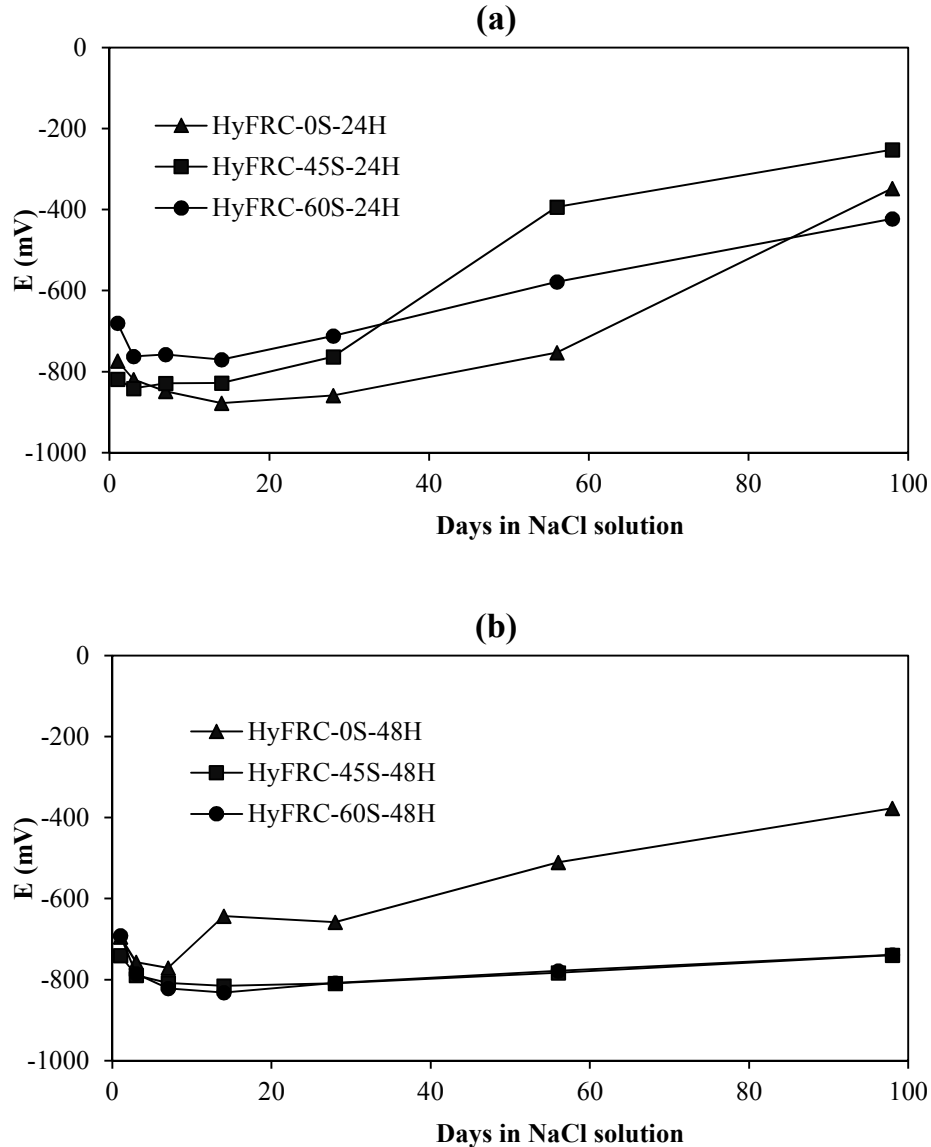


**Figure 5.6: Corrosion potentials for HyFRC samples with applied current of: (a) 24 hours, and (b) 48 hours**

Corrosion potentials of HyFRC samples with 24 and 48 hours of applied current are given in **Fig. 5.6**. It is observed that corrosion potential values were more negative than  $-277$  mV. This indicates that all samples are in an active corrosion region. There is no distinguishable difference in corrosion potentials across all samples with 24 hours of applied current. In **Chapter 4**, 60% slag as cement replacement showed the most negative corrosion potentials. It is possible that the confinement provided by hybrid fibers are dominant over the effects of slag on steel corrosion

under the applied current, leading to an insignificant difference in corrosion activity. With 48 hours of applied current, the corrosion potentials for HyFRC-45/60S-48H dropped to a value around -800 mV, representing a possibility of high corrosion activity. On the other hand, HyFRC-0S-48H showed the least negative corrosion potentials. In all cases, corrosion potentials tended to increase with time, indicating a possible reduction in corrosion activity. This may be attributed to a crack confinement of fibers and partial reformation of the passive film due to an increase in pH of the immersion solution as result of CH leaching. It is noted that pH of the immersion solution was measured to be about 12.0 at 98 days. The more basic immersion solution would also lead o more effective dilution of acidotic solution at the steel-concrete interface. A discussion on interfacial acidification was made in **Chapter 4**. However, corrosion potentials for concrete reinforced with steel fibers could not be used alone to accurately assess the relative corrosion rates (Grubb et al., 2007). It is important to investigate the corrosion rates to better understand the combined effects of slag and fibers on concrete performance against corrosion after the applied current.

The corrosion rates of corresponding samples after the applied current regimes are given in **Fig. 5.7**. For 24 and 48 hours of applied current, corrosion rates of all samples were of similar values except for HyFRC-60S-24H and HyFRC-0S-48H. Corrosion rates for HyFRC-0S-48H were generally smaller than those for HyFRC-45/60S-48H. This may be attributed to a less extensive cracking as a result of a higher porosity of the matrix at steel-concrete interface in HyFRC-0S-48H. Microstructural study of C-0S in the previous chapter confirmed an increase in porosity of the matrix. As corrosion products were formed during impressed current, they were able to fill in the surrounding pores resulting in a densification at steel-concrete interface, causing minimal or no cracking to the surrounding concrete. This was also possible with an enhanced tensile strength of the composite and enhanced confinement action provided by the hybrid fibers. The interfacial densification would limit the movements of ions and oxygen to the anodic sites and that helped to reduce corrosion rates.

The interfacial densification may also explain why corrosion rates for samples with 48 hours of applied current tended to be smaller or of similar magnitude to corrosion rate values in samples with only 24 hours of applied current. If concrete cracked under corrosion-induced pressure, fibers bridging the cracks would provide increasing confinement action due to the deflection hardening behavior of the composite. That resulted in higher level of interfacial densification and a reduced corrosion activity. However, corrosion rates would not be greatly reduced as the wider crack opening would allow for ingress of O<sub>2</sub> and egress of ions from the steel surface.

Also, it is noted that corrosion rates for all samples decreased with time. As discussed, this may be due to dilution of the interfacial acidic environment by the high pH immersion solution and a partial reformation of the passive film on the rebar surface. This may also be attributable to phase transformation of corrosion products under continuous availability of O<sub>2</sub> and moisture, leading to an increase in volume and further interfacial densification. A study conducted by Takaya (2013) showed that corrosion product types were different depending on corrosion test and exposure conditions. It is also noted that corrosion performance of HyFRC-60S-24H/48H was generally enhanced as compared to HyFRC-0S and HyFRC-60S with the same corresponding regimes of applied current. This is contradictory to what was observed in plain concrete without hybrid fibers. It is postulated that HyFRC-60S experienced more mass loss due to its poor quality of the initial passive film. The higher mass loss and more corrosion products mean that HyFRC-60S experienced more densification at steel-concrete interface due to confinement by hybrid fibers, resulting in a subsequent reduction in corrosion activity.

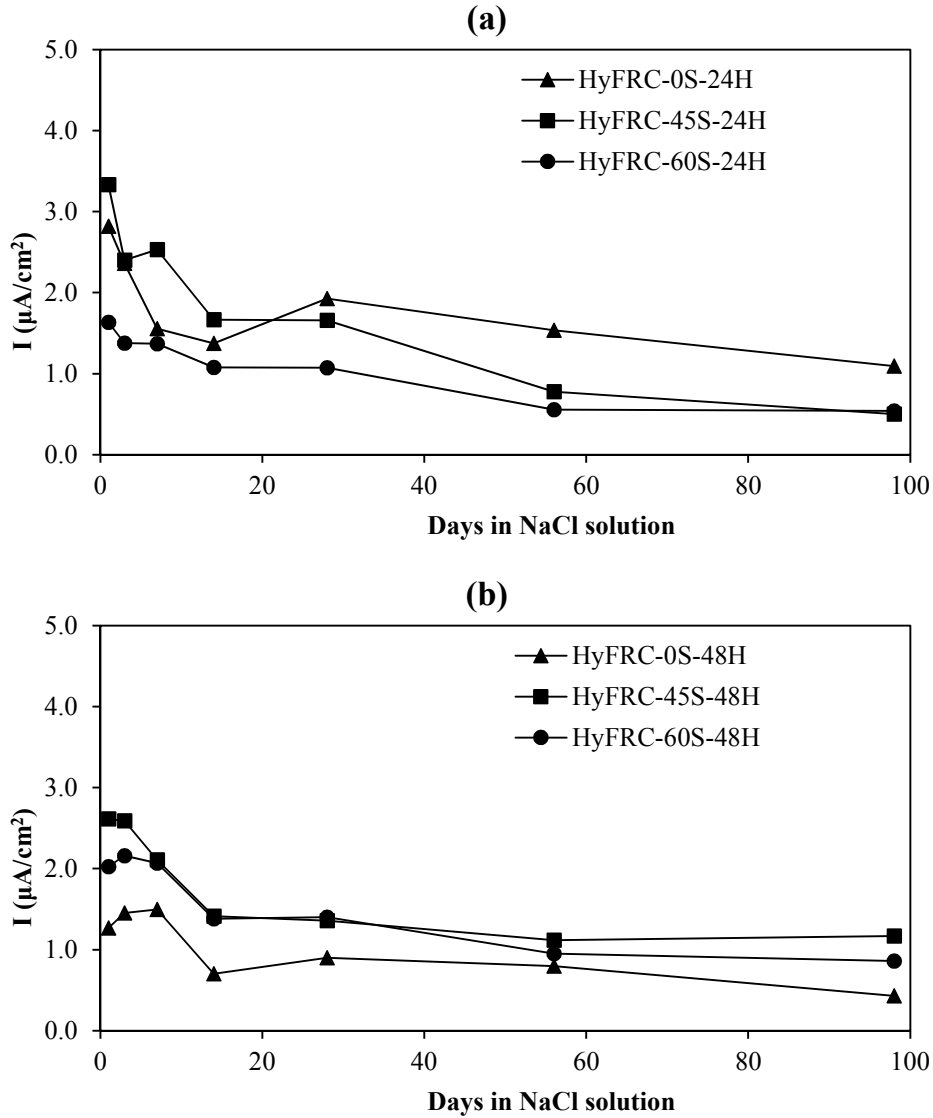


**Figure 5.7: Corrosion rates for HyFRC samples with applied current of: (a) 24 hours, and (b) 48 hours**

### 5.3.4 Corrosion results for plain concrete with slow applied current

Corrosion potentials and corrosion rates for plain concrete samples with slow induced current magnitude of  $0.2 \text{ mA}/\text{cm}^2$  for 240 hours are given in **Figs. 5.8** and **5.9**, respectively. The electrochemical measurements after the applied current regimes were conducted over 14-day period only. Corrosion rates for plain concrete with an applied current magnitude of  $1 \text{ mA}/\text{cm}^2$  for 48 hours from **Chapter 4** are also given in **Fig. 5.9** for comparison. Applied current duration of 24 and 48 hours was chosen so that the expected magnitude of charges is the same for both cases. That is the current application duration had to be increased by the ratio of the applied current intensities, which is 5 for a reduction in current intensity from  $1 \text{ mA}/\text{cm}^2$  to  $0.2 \text{ mA}/\text{cm}^2$ . In the annotations, C is for plain concrete with  $1 \text{ mA}/\text{cm}^2$  of applied current while C' for plain concrete with  $0.2 \text{ mA}/\text{cm}^2$  of applied current. It is observed that corrosion potentials were of values of about

-800 mV, indicating possible high corrosion activity for all C' samples. Corrosion rate results show that C' samples had lower corrosion rates as compared to those in C samples. Increasing current density was shown to increase concrete tensile hoop strain and crack width due to less diffusion of corrosion products at the same percentage of mass loss (El Maaddawy & Soudki, 2003). For a smaller applied current density, corrosion products would be able to more gradually penetrate into the available pores near the interface. This allows for an increase in densification at the steel-concrete interface and a reduction in corrosion rates with slower applied current.

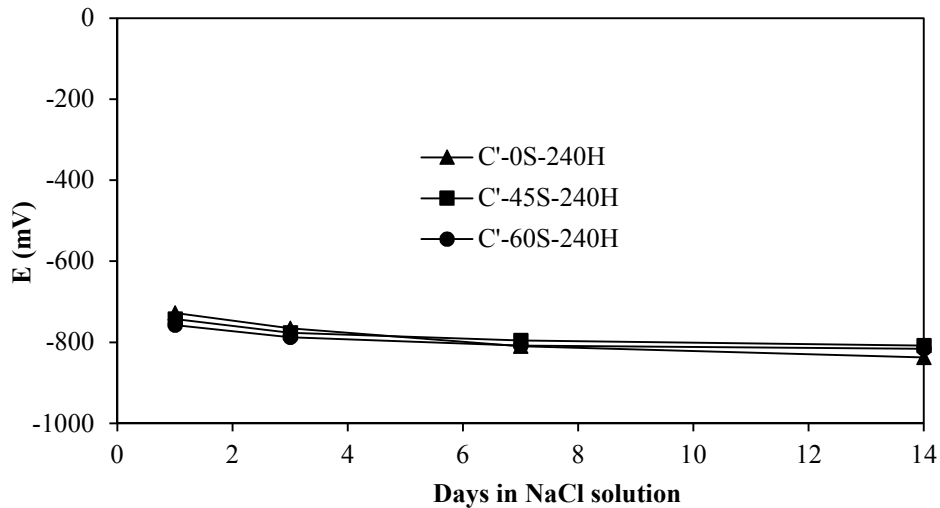


**Figure 5.8: Corrosion potentials for plain concrete samples with 0.2 mA/cm<sup>2</sup> applied current for 240 hours**

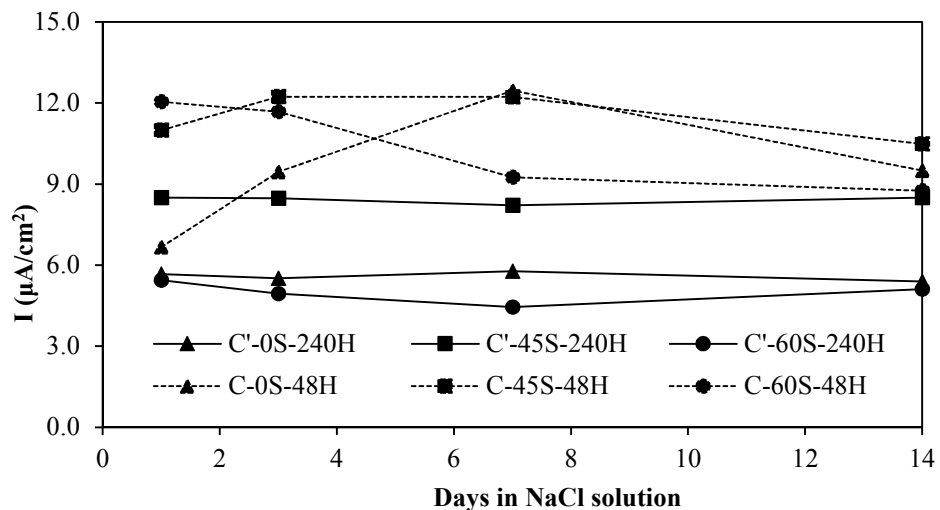


**Figure 5.9: Corrosion rates for plain concrete samples with 0.2 mA/cm<sup>2</sup> applied current for 240 hours and with 1 mA/cm<sup>2</sup> applied current for 48 hours**

Interestingly, it is also observed that C'-45S-240H generally had higher corrosion rates than those for C'-0/60S-240H. One possible explanation is that at low applied current, corrosion products

induced by the applied current may exert higher pressure to the surrounding C'-45S due to its less porous steel-concrete interface. The difference in interface quality was elaborated in the previous chapter where C-0S showed voids near the interface and C-60S exhibited more microcracking possibly arising from autogenous and drying shrinkage. In contrast, concrete with 45% slag replacement showed a denser matrix. The denser matrix of C-45S or C'-45S-240H led to higher corrosion-induced pressure to the matrix for similar levels of induced corrosion, resulting in more cracking and more exposure of the rebar to the corrosion environment. Observation of crack patterns after the applied current regime confirmed that C'-45S-240H had wider corrosion-induced cracking as compared to cracking found in C'-0/60-240H (**Fig. 5.10**). The crack patterns at the bottom surfaces of the samples provide a clearer picture of crack characteristics where C'-45S-240H showed a through wider crack across the sample. The effects of voids and microcracking should be less apparent for 1 mA/cm<sup>2</sup> applied current intensity due to a faster corrosion production rate and a poorer ability of corrosion products to diffuse into the voids of the matrix.



**Figure 5.10: Corrosion-induced cracks for plain concrete with slow applied current**

### 5.3.5 Corrosion rates for HyFRC and plain concrete

The beneficial effects of hybrid fibers can be seen in **Fig. 5.11** which combines corrosion rate results for HyFRC-0S/45S/60S-48H and C'-0S/45S/60S-240H over 14 days of electrochemical measurements. It is observed that the presence of hybrid fibers in concrete helped to significantly reduce corrosion rates. The benefits of steel fibers in controlling corrosion of steel rebar in concrete have been explained in a study by Grubb et al. (Grubb et al., 2007). At anode, steel fibers provide passive confinement of corrosion products which allows for densification at steel-concrete interface and limits further ingress of deleterious compounds to the reactions sites. Also, an improved crack distribution within the surrounding matrix similarly limit access of moisture and O<sub>2</sub> from reaching the surface of rebar. Hybridization of 1.3% steel fibers and 0.2% PVA fibers was shown to provide deflection hardening to concrete (Blunt & Ostertag, 2009) and the behavior is expected to further enhance the confinement effect in HyFRC used in this study. Based on the corrosion rate results, it is also observed that different slag replacement levels have little effects on corrosion performance in HyFRC.



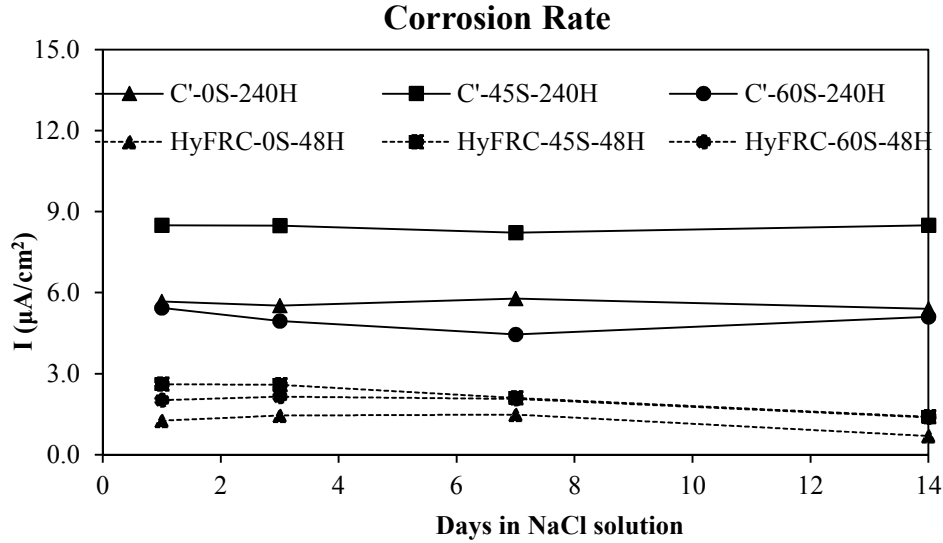


Figure 5.11: Corrosion rates for plain concrete samples with 0.2 mA/cm<sup>2</sup> applied current for 240 hours

### 5.3.6 Gravimetric mass loss results

The results for gravimetric measured mass losses and theoretical mass losses are summarized in **Table 5.3**. The theoretical mass loss is the sum of mass loss during the applied current and during the 90-day period for HyFRC samples and 14 days for C' samples when they were left in NaCl solution. The mass loss was also normalized by the estimated mass of bar section exposed accelerated corrosion. The theoretical mass losses after the applied corrosion regime were based on time integration of the measured corrosion rates. Although corrosion rates for C' samples were measured only for 14 days, the mass loss after the applied current were small relative to the mass loss during the applied current. Hence, despite different immersion periods, a direct mass loss comparison can be made between the two set of samples. Mass losses for C-0S/45S/60S with 48 hours of applied current are also given in **Table 5.3** for comparison.

**Table 5.3: Gravimetric and theoretical mass losses**

|               | Current 1mA/cm <sup>2</sup> | Gravimetric    |       | Theoretical    |
|---------------|-----------------------------|----------------|-------|----------------|
|               | Hours                       | $\Delta M$ (g) | % M   | $\Delta M$ (g) |
| HyFRC-0S-0H   | 0                           | 1              | 0.10% | 0.05           |
| HyFRC-0S-24H  | 24                          | 1.3            | 0.13% | 3.20           |
| HyFRC-0S-48H  | 48                          | 1.3            | 0.13% | 5.77           |
| HyFRC-45S-0H  | 0                           | 0.6            | 0.06% | 0.06           |
| HyFRC-45S-24H | 24                          | 1.5            | 0.15% | 3.10           |
| HyFRC-45S-48H | 48                          | 1.7            | 0.17% | 5.92           |
| HyFRC-60S-0H  | 0                           | 0.9            | 0.09% | 0.03           |
| HyFRC-60S-24H | 24                          | 1.8            | 0.18% | 3.00           |
| HyFRC-60S-48H | 48                          | 2.5            | 0.25% | 5.88           |
| C'-0S-240H    | 240                         | 3.0            | 0.55% | 5.77           |
| C'-45S-240H   | 240                         | 3.0            | 0.55% | 5.88           |
| C'-60S-240H   | 240                         | 4.4            | 0.81% | 5.74           |
| C-0S-48H      | 48                          | 2.6            | 0.48% | 7.90           |
| C-45S-48H     | 48                          | 2.9            | 0.53% | 7.76           |
| C-60S-48H     | 48                          | 3.4            | 0.62% | 7.38           |

It is observed that mass losses of HyFRC samples did not increase proportionately with the applied current duration. With no applied current, the mass losses were 1 g, 0.6g and 0.9 g for HyFRC-0S-0H, HyFRC-45S-0H and HyFRC-60S-0H, respectively. When the applied current regime was 24 hours, the mass losses were increased to 1.3 g, 1.5 g and 1.8 g for HyFRC-0S, HyFRC-45S and HyFRC-60S, respectively. Also, when the induced current period increased from 24 to 48 hours, the mass losses increased by only 0 g, 0.2 g and 0.7 g for the three respective samples. This is contradictory to what was observed in gravimetric mass loss results for plain concrete as shown in **Chapter 4** where the change in mass losses increased with increasing applied current durations. That is more mass loss occurred within the second 24 hours of applied current. In this study, the high mass loss with no applied current may be attributed to steel rebar corrosion as a result of poor consolidation of HyFRC and a reduced concrete electrical resistance with the presence of steel fibers (Grubb et al., 2007). An increase in air voids which is an indication of poor consolidation in HyFRC will be elaborated later with microstructural studies. The increase in porosity and matrix resistance led to an early breakdown of the passive film and the onset of corrosion. Bars retrieved from split cylinders (**Fig. 5.12**) show patches of corrosion on their surfaces even with no induced corrosion. The presence of fibers in concrete compromised concrete consolidation (based on reduced elastic modulus shown earlier) and that led to an early onset of corrosion even without any applied current. This result stresses the importance of good workmanship in producing highly durable concrete structures.

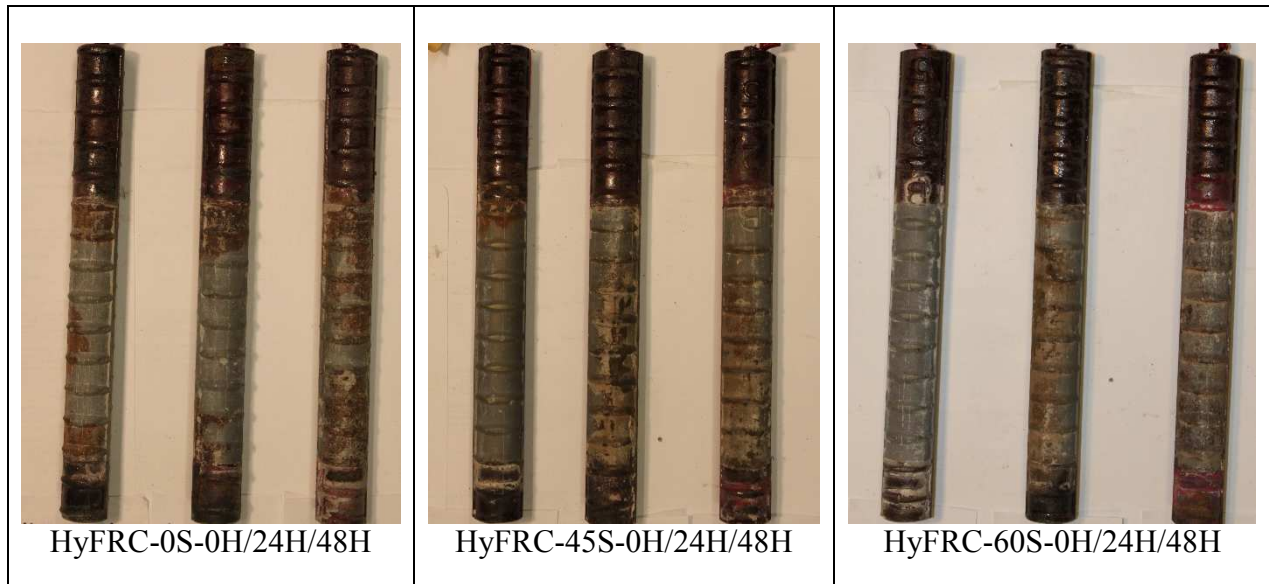


**Figure 5.12: Corrosion on bar surfaces showing patches of corrosion on bars with no applied current**

The small or no increase in mass losses with increasing applied current durations in HyFRC may be attributed to two complementary mechanisms. First, when corrosion products were formed and expanded in volume, a tensile stress would be exerted on the surrounding concrete. Cracking would occur if the tensile strength of HyFRC was exceeded. The fibers would bridge the cracks and this resulted in passive confinement and densification at steel-concrete interface. Second, to generate the desired current density of  $1 \text{ mA/cm}^2$ , the cell voltage between the anode and cathode would have to be increased. This led to water oxidation which offset the total charge drawn from the anode. Water oxidation phenomenon was explained in **Chapter 4**.

The higher cell voltage across the concrete would also oxidize steel fibers located near the sample surface. The fibers at this location are susceptible to corrosion due to a lack of protection from the matrix. The corrosion of fibers is evident in **Fig. 5.13** where surfaces of the HyFRC-45S samples after 98 days in NaCl and immediately after 24 and 48 hours of applied current were shown. It is observed that after 98 days in NaCl, steel fibers showed little sign of corrosion on HyFRC-45S-0H surface. However, after 24 or 48 hours of applied current, black corrosion products from steel fibers were formed at various locations on the sample surfaces. Similar observations applied for HyFRC-0S and HyFRC-60S although they were not shown here. The mechanism of steel fiber corrosion under accelerated corrosion test will be explained in the next part of this chapter. It is also noted that the white deposit seen on the top surface of HyFRC-45S-24H in **Fig. 5.13** is crystallized salt which accumulated on the surface with time after NaCl solution was poured on top of it in preparation for electrochemical measurements.



**Figure 5.13: Fiber corrosion on surfaces of HyFRC-45S**

As compared to plain concrete with  $1 \text{ mA/cm}^2$  of applied current presented in the previous study, C' with  $0.2 \text{ mA/cm}^2$  of applied current generally had slightly higher mass losses, as shown in **Table 5.3**. With smaller applied current, the corresponding cell voltage was expected to be less and that would help reduce water oxidation reactions. If the charge to generate the current come from both steel anode and water oxidation, a smaller cell voltage means less water oxidation but more oxidation of steel anode, leading to higher gravimetric mass losses. Investigation of the cell voltages recorded confirms that the cell voltages (uncompensated for IR drop) to generate  $0.2 \text{ mA/cm}^2$  were lower than those required to generate  $1 \text{ mA/cm}^2$ . For instance, average initial cell voltage for a typical C'-45S was  $1.9 \text{ V}$  as compared to  $10 \text{ V}$  to generate  $1 \text{ mA/cm}^2$  in a typical C-45S. It is also interesting to note the cell voltage increased in proportion to the current intensities. This may be attributed to a similar concrete resistance and rebar polarization resistance in these two samples. The higher mass losses of C' group but smaller corrosion rates as compared to C group also confirm the enhanced interfacial densification at a lower applied current intensity.

Corrosion products formed with slow and high current intensities seem to be different in nature. Observation of corroded bar surfaces for samples with 60% slag replacement level confirmed that less powdery and more rigid corrosion products appeared in C'-60S-240H as shown in **Fig. 5.14**. It is believed that with smaller current, iron ions would have more time to react with available  $\text{OH}^-$  from the cathode and moisture to form corrosion products of a more stable phase. The smaller required cell voltages to generate the  $0.2 \text{ mA/cm}^2$  would also induce less acidification at the interface and that would further enhance the formation of more stable corrosion products.



C'-60S-240H



C-60S-48H

**Figure 5.14: Corrosion product natures for C'-60S-240H and C'-60S-48H**

### **5.3.7 Flatbed digital imaging and optical microscopy**

The flatbed scanned images of sections from HyFRC corrosion samples are shown in **Fig. 5.15**. Lines for visible cracks were also drawn on the surfaces. For HyRC-0S, no visible cracks were observed for different regimes of the induced current. This was because of the enhanced protection from the passive film and the more porous matrix of HyFRC-0S, leading to more densification at steel-concrete interface. At 24 hours of applied current, HyFRC-45S exhibited a fine crack while HyFRC-60S showed no sign of crack. The crack lead to slightly higher corrosion rates in HyFRC-45S-24H than the rates observed in HyFRC-60S-24H, as given in the electrochemical results earlier. With 48 hours of applied current, more extensive cracking occurred in HyFRC-45S-48H and HyFRC-60S-48H, leading to an increase in confinement provided by hybrid fibers. The lower or similar observed corrosion rates of the two samples as compared to HyFRC-45S-24H and HyFRC-60S-24H confirms the confinement and densification of corrosion products by hybrid fibers and the resulting reduction in corrosion activity.



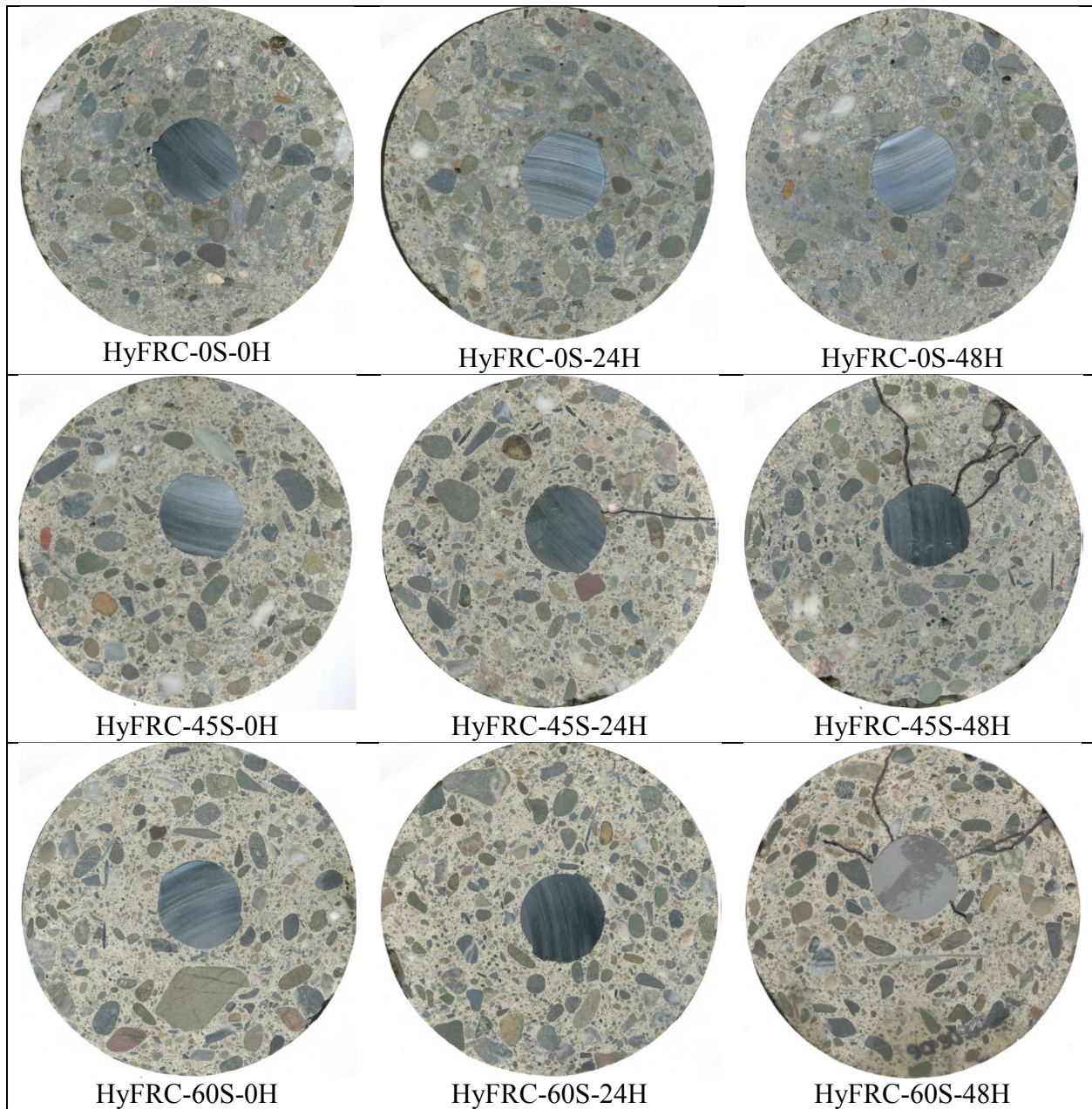


**Figure 5.15: Scanned images of sections for HyFRC corrosion samples**

The optical microscopy results at steel-concrete interfaces for corresponding samples are shown in **Fig. 5.16**. The dark areas around steel-concrete interfaces for samples with no applied current may represent small levels of corrosion. This is consistent with the surface observation of rebars obtained from the splitting tensile tests in which patches of corrosion products were observed. The microscopic results also reveal that with 24 and 48 hours of applied current, corrosion product thickness did not seem to correlate well with the gravimetric mass losses as presented in **Table 5.3**. This may be attributed to the non-uniformity of corrosion on the steel surface as shown in **Fig. 5.12**. It is also observed that a number of cracks were wedge-shaped filled by corrosion products and did not run through to the surface of the samples. The formation of multiple wedge-shaped

cracks and the filling up by corrosion products were attributed to the passive confinement provided by hybrid fibers. This led to the interfacial densification and a reduction in corrosion rates.

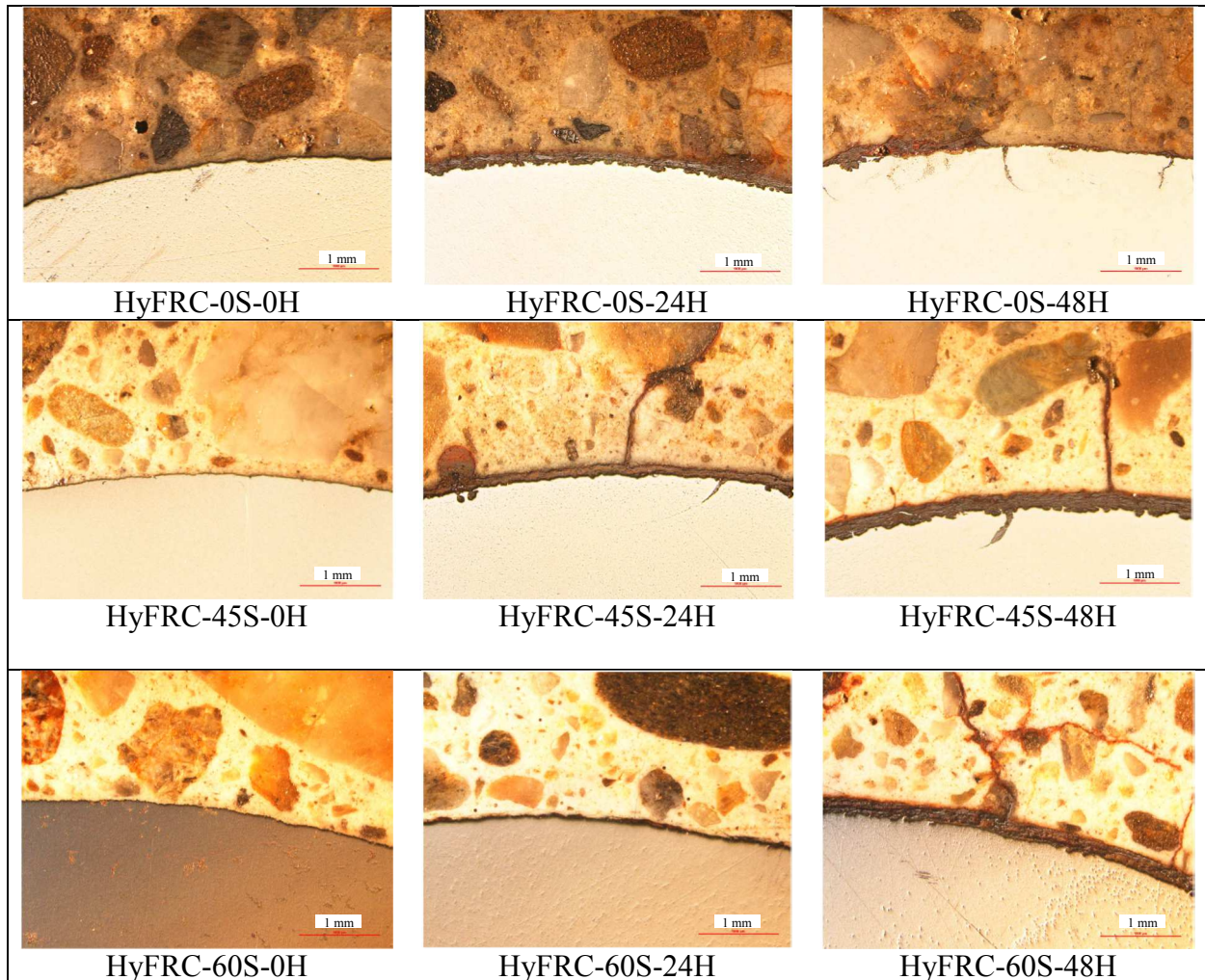


**Figure 5.16: Optical microscopic results for steel-concrete interfaces**

### **5.3.8 Backscattered electron imaging (BSE) & EDX element mapping**

The backscattered electron (BSE) images and corresponding EDX element mapping of HyFRC samples with 48 hours of applied current are shown in **Fig. 5.17**. Corrosion layer can be identified by regions of high concentration of oxygen and Fe. It is evident that in HyFRC-45S/60S-48H, formation of corrosion products exerted enough expansive pressure to cause cracking to concrete. The cracking allowed for corrosion products to move outward to the external surfaces of the corrosion samples. Corrosion stain could be observed on the surfaces of samples with through cracks. It is postulated that corrosion products moved outward as both solids and soluble cations whose solubility was not expected to vary along the crack due to its pH equilibrium with the electrolyte. It is also noted that the boundary of corrosion layer in HyFRC-0S-48H were not well defined as compared to those in HyFRC-45S/60S-48H. Residues of corrosion products can be seen in the matrix pores along the corrosion layer boundaries of HyFRC-0S-48H.



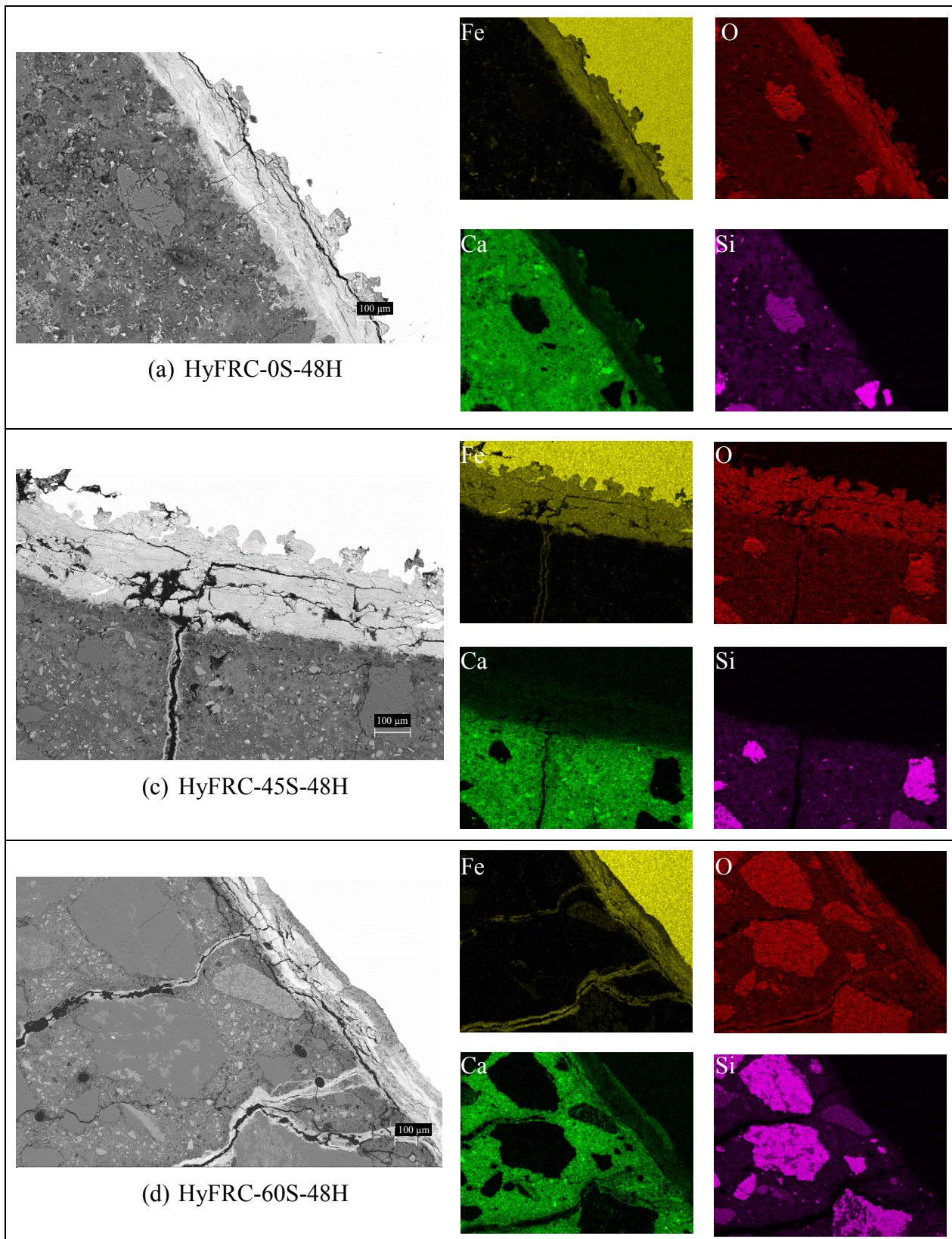




**Figure 5.17: BSE images and corresponding EDX element mapping for: (a) HyFRC-0S-48H, (b) HyFRC-45S-48H, and (c) HyFRC-60S-48H**

EDX element mapping showed a gradation of Fe concentrations near concrete-corrosion layer boundary for HyFRC-0S-48H. The diffusion of the corrosion products into the matrix pores relieved stress and strain on the surrounding matrix. This combined with its high tensile strength under the presence of fibers led to an absence of cracking, higher interfacial densification and less mass loss in HyFRC-0S-48H. Interestingly, Ca was also present in the corrosion layer. It is likely that Ca was dissolved under acidification during the applied current and bound into corrosion products. Using XRD, Takaya et al. (2013) observed  $\text{CaFeClO}_2$  in corrosion layer of steel in concrete under accelerated corrosion test. The densification of corrosion products is evident through a smaller gapping formed within the corrosion layer as compared to what was observed in plain concrete as presented in **Chapter 4**. The small gapping in the corrosion layer may be caused by oven drying of the samples which removed moisture from the corrosion products.

## 5.4 Discussion

### 5.4.1 Passive confinement of fibers on corrosion rates

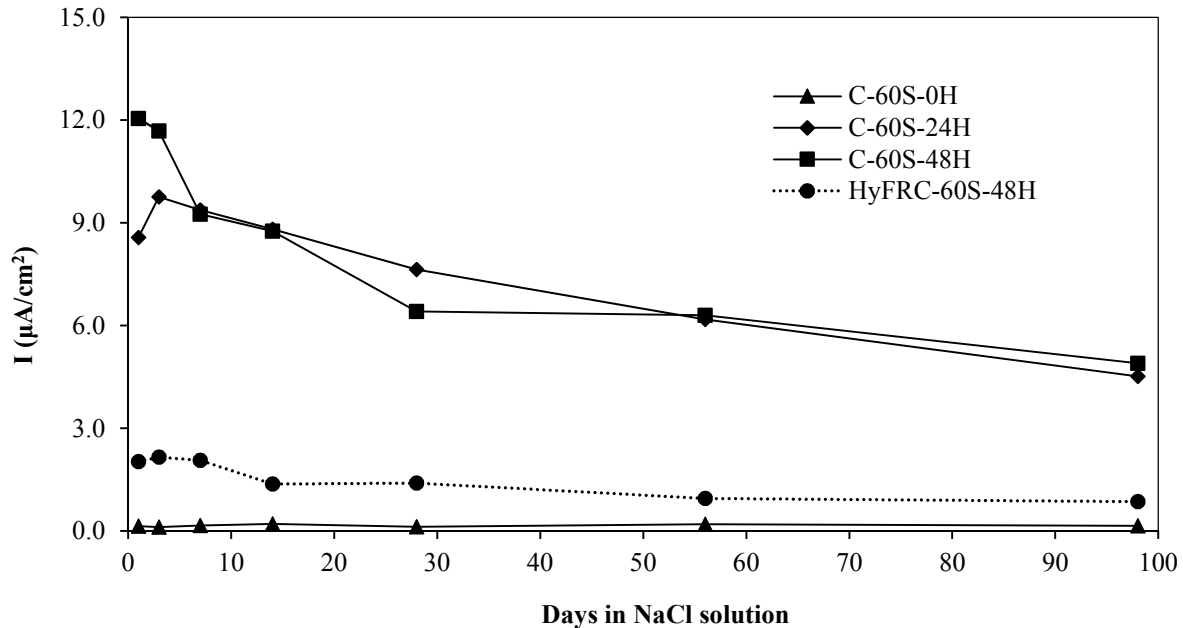


**Figure 5.18: Corrosion rates of HyFRC-60S-48H and C-60H-0/24/48H**

The corrosion rates for HyFRC-60S-48H were plotted against the corrosion rates for C-60S with 0 hour, 24 hours and 48 hours of applied current. The diagram is depicted in **Fig. 5.18**. It is observed that even with 48 hours of applied current and similar or higher mass losses, HyFRC-60S-48H showed much lower corrosion rates (about 5 times smaller) as compared to C-60S with the same corresponding applied current regime. This allows for extension of service life of structures and clearly reveals the beneficial effects of hybrid fibers in concrete composite in limiting corrosion activity during corrosion propagation stage. Nevertheless, due to the applied

current and the resulting crack formation, HyFRC-60S-48H showed higher corrosion rates than C-60S-0H without any applied current.

#### 5.4.2 Corrosion of steel fibers in accelerated corrosion test

It was observed that steel fibers near the surfaces of HyFRC corroded under accelerated corrosion tests. However, it is unclear why steel fibers corroded as the induced current was intended for the anodic rebar. A need to complete an electrical circuit of the corrosion test setup requires current in the form of electrons or ions to flow into the concrete. The current flow follows the path of the least electrical resistance, which means that the current will flow by means of electron transport along the steel fibers because of their higher conductivity than that of concrete, and by means of ion transport within the concrete and the electrolyte. Thus, at the tips of the steel fibers, the current must be converted to and from electron or ions. The conversion requires electrochemical reactions to take place in the regions. Closer to the cathode where steel fibers have to receive  $\text{OH}^-$ , the electrochemical reaction is oxidation of Fe to  $\text{Fe}^{2+}$  to form corrosion products. Further into concrete, the electrons will be involved in reduction reaction to form  $\text{OH}^-$  which will be transported to the rebar. This explains more aggressive corrosion spots and stains on HyFRC samples with an applied current regime.

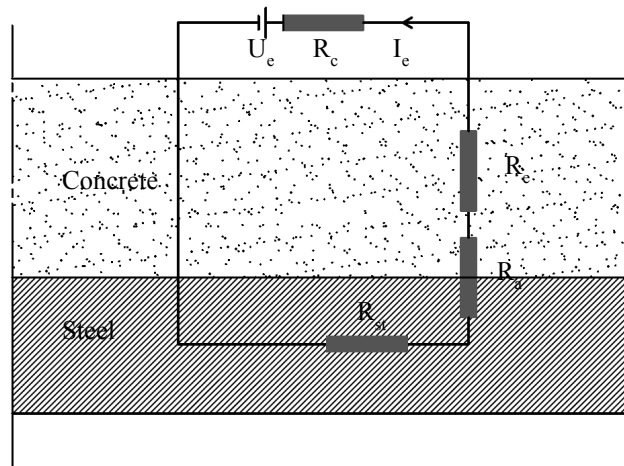


**Figure 5.19: Equivalent electrical half circuit for accelerated corrosion test**

The corrosion of steel fibers under applied current may also be explained through an equivalent electrical half circuit for the accelerated corrosion test setup which is shown in **Fig 5.19**. The equivalent circuit model is similar to the one proposed in **Chapter 3** and consists of cell voltage  $U_e$ , concrete or electrolyte resistance  $R_e$ , steel rebar resistance  $R_{st}$  and cathodic resistance  $R_c$ , anodic polarization resistance  $R_a$ , and electrical current  $I_e$  between the anode and cathode. Note that  $R_c$  is located at the steel mesh outside of the matrix while the cell voltage  $U_e$  is now provided by the external Potentiostat. Also, capacitance and impedance are omitted here in view of the direct current (DC) implemented in the accelerated corrosion test. Under impressed current test, the current  $I_e$  was maintained to a constant value while the cell voltage  $U_e$  was varied to achieve the constant current density. Steel fibers near the sample surface would be oxidized by the potential difference between the anode and the cathode. As electrons are unable to travel through electrolytes which separate steel rebar from steel fibers, it is required to explain how ions flowed between the cathode (stainless steel mesh), the electrolyte and the anode.

**Fig. 5.20** elaborates the mechanism of ion/electron transport and steel fiber corrosion under accelerated corrosion test. The numbering sequentially represents the sequence in the process. When iron of the rebar is oxidized (1), electrons will flow through the circuit wiring and will be deposited on the cathode where a reduction reaction to form  $\text{OH}^-$  takes place (2). The number of moles of  $\text{OH}^-$  should be the same as that of the deposited electrons. To complete the electrical circuit, the negatively charged  $\text{OH}^-$  will be transported to the anode which is positively charged. Due to the difference in charge, a voltage drop more positive toward the anode is created. Combined with less protection from the concrete cover, this makes the steel fiber near the surface susceptible to being oxidized to form  $\text{Fe}^{2+}$ . The iron ions react with part of the  $\text{OH}^-$  from the external cathode to form corrosion products (3). At the same time, a cathodic area is formed on the steel fiber where reduction reactions take place to form new  $\text{OH}^-$  to offset the consumed  $\text{OH}^-$  from the external cathode (4). From the ion compensation, it can be concluded that steel fibers near the sample surface can corrode but their corrosion does not contribute to the net electron flow from the rebar. Also, steel fibers more perpendicular to the anodic rebar will be more susceptible corrosion due to a higher potential drop between both ends of the fibers. Two 30 mm steel fibers, one oriented almost parallel to the rebar and one almost perpendicular, with similar matrix cover at locations closest the sample surface were extracted from HyFRC-0S-48H and their surfaces were digitally scanned. It is confirmed in **Fig. 5.21** that the fiber more perpendicular to the anodic rebar experienced more aggressive corrosion at the tip closer to the concrete surface where it is least protected.

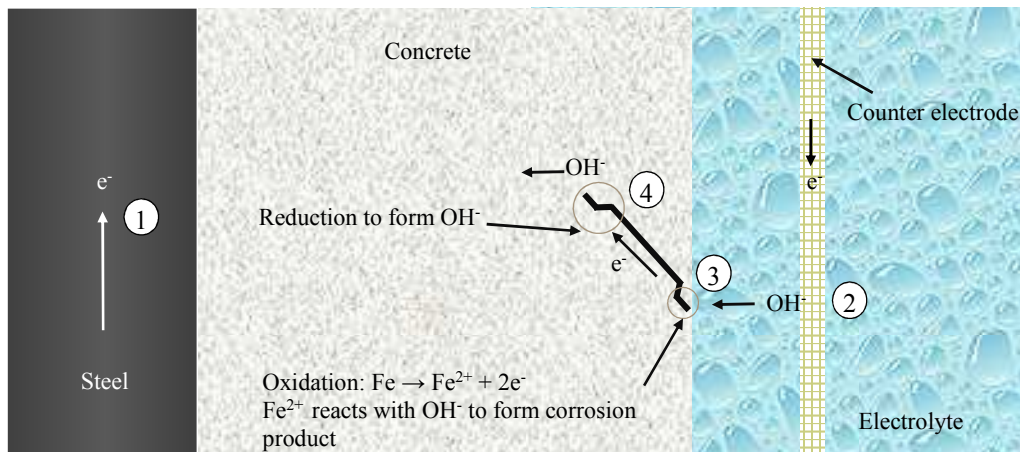


**Figure 5.20: Mechanism of steel fiber corrosion under applied current**

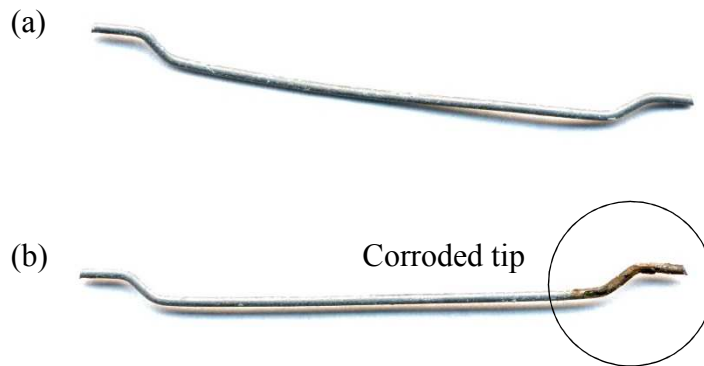


**Figure 5.21: 30 mm steel fiber retrieved from C-0S-48H: (a) fiber more parallel to anodic steel rebar, and (b) fiber more perpendicular to anodic steel rebar**

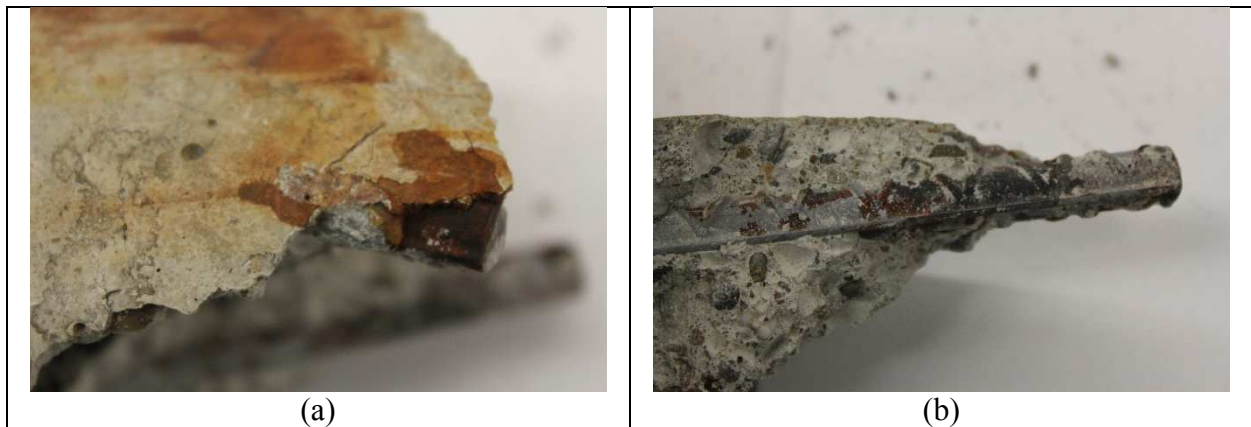


**Figure 5.22: Corrosion of #2 rebar embedded near the surface of the sample: (a) stain on the surface, and (b) extent of corrosion**

To confirm that corrosion of fibers did not contribute to a reduction in electron flow from the anodic rebar and that a voltage difference causes corrosion of steel fibers, a cylindrical corrosion sample was prepared. No. 8 rebar was used as the anode. W/B ratio of 0.54 was used and 3.5% NaCl was added to the mixing water to prevent formation of the passive film. Two #2 rebars were embedded at a depth between 0 mm and 5 mm near the surface. Impressed current intensity of  $1 \text{ mA/cm}^2$  was applied for 48 hours. At the end of the test, corrosion stains were observed on the sample surface. Opening up the sample showed sign of extensive corrosion on both the #2 rebars. The corrosion on the #2 rebars occurred near the sample surface where the rebars were least protected. This is shown in **Fig. 5.22**. The gravimetric mass loss of the main anodic rebar in the middle of the sample was found to be 7.2 g. This is much higher than the mass losses observed in plain concrete and HyFRC samples. This is attributed to the presence of NaCl in the mixing water, which prevented the formation of the passive film on steel. The mass loss value is similar to the mass loss observed in a corrosion sample produced with plain concrete and added NaCl whose results will be given in the next chapter. This study confirmed that a voltage drop between the anode and cathode under accelerated corrosion caused corrosion of steel fibers near the surface but the fiber corrosion did not offset the mass loss of the main anode.

### 5.4.3 Corrosion of fibers with no applied current and its effect on corrosion of anodic rebar

Steel fibers in concrete were found to be more resistant to corrosion than conventional steel rebar. The threshold value for  $\text{Cl}^-/\text{OH}^-$  to initiate corrosion in steel fibers was found to be higher than that for steel rebars (Mangat & Gurusamy, 1988). Due to their smaller sizes, steel fibers are in more intimate contact with lime rich layer in interfacial zone which acts as a reservoir of  $\text{OH}^-$  and helps to maintain steel passivity. The layer also restrict the migration of  $\text{Cl}^-$  to the anodic sites. In addition, the increased corrosion resistance is attributed to the improved uniformity of the structure and surface of steel fibers under cold-formation by drawing (Raupach & Dauberschmidt, 2003). Cathode/anode areas ratio also play a role in determining corrosion susceptibility of steel fibers. In a study conducted by Arya & Vassie (Arya & Vassie, 1995), it was shown that for the same anode area, higher cathode-to-anode area ratios led to higher corrosion density in the anode. The increase may be attributed to galvanic potential between the anode and cathode. In the case of the same size crack bridged by fiber or steel rebar, the cathode/anode ratio of the fiber will be smaller than that in steel rebar due to its generally shorter length, leading to more corrosion resistance of fibers. Nevertheless, it is recognized that during oxygen-controlled corrosion, the corrosion rate limiting factor is the transport of  $\text{O}_2$  to the steel surface. Consequently, differences in anodic polarization behavior due to composition differences and anode-cathode area ratio has little effect on corrosion rate. Therefore, the most likely reasons for the enhanced corrosion resistance of steel fibers are factors influencing the size and number of defects between the steel fibers and the matrix.

However, in bulk concrete, fibers near the surface are susceptible to corrosion due to a lack of physical protection from concrete. Severe corrosion was detected on bright fibers at the surface of the cube in carbonation zone (Lambrechts et al., 2003). Despite this, corrosion did not transgress along the fibers deeper in the bulk concrete. After 7 months of wetting and drying cycles of fiber-reinforced concrete ( $\text{W/B} = 0.78$ ) with salt fog, it was shown that only fibers embedded less than 1 mm in concrete were susceptible to corrosion (Balouch et al., 2010). The results are consistent with what was observed in the accelerated corrosion test. Fibers near the sample surface are ready to give off electrons and corrode under the cell voltage. Beyond this cover, steel fibers were well protected by concrete from corroding. **Fig. 5.23** of a split HyFRC-0S-48H confirmed that only fibers near the surface corroded while fibers deep in the bulk concrete were intact.

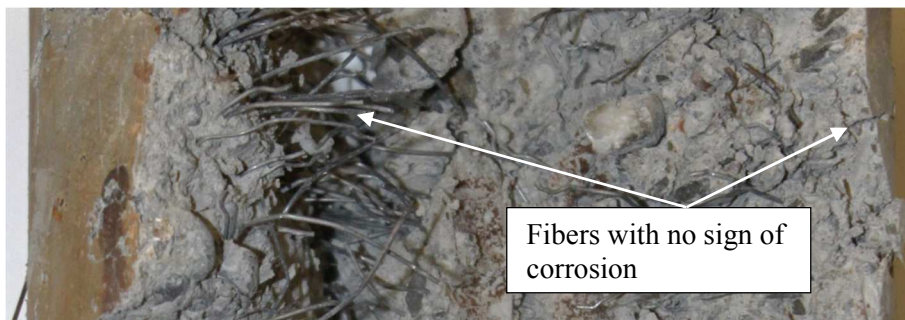


**Figure 5.23: Split HyFRC-0S-48H showing no corrosion of fibers in the bulk concrete**

As mentioned in the previous paragraphs, steel fibers near concrete surface corrode under natural corrosion. As the corrosion is of spot nature, it is not expected to exert any stress to concrete. However, fiber corrosion may consume oxygen and integrate available  $\text{Cl}^-$  into the corrosion products, leading to a depletion of the elements to participate in corrosion of the embedded anodic



steel. Although not experimentally proven, it was argued that the large surface of steel fibers can act as an oxygen sink, leading to a cathodic control in corrosion process of embedded rebar in concrete (Grubb et al., 2007). However, this may not be the case as the reduced concentration of dissolved oxygen would be shortly replenished by dissolution of oxygen from the atmosphere. Also, the binding of Cl<sup>-</sup> by corrosion products of steel fibers, if any, would be insignificant relative to the binding capacity of ordinary Portland cement, in view of their small tendency to corrode and their small volume fractions in concrete used in this studies. Depending on storage solution and concentration of chloride in the solution, chloride uptake of Portland cement paste can be greater than 1% of the cement mass (Tritthart, 1989). The lack of involvement of steel fibers in corrosion mechanism of the anodic rebar is supported by the similar corrosion rates of HyFRC and of plain concrete with no applied current as presented earlier in **Chapter 4**.

#### 5.4.4 Chloride penetration of plain concrete under slow applied current

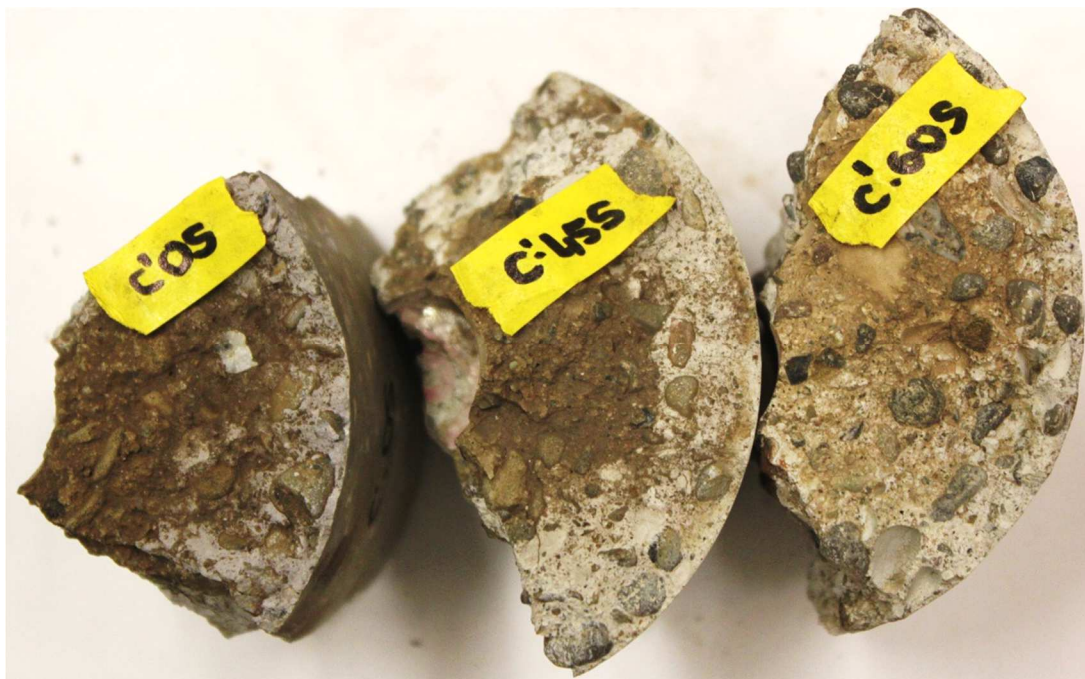


**Figure 5.24: Cl<sup>-</sup> penetration with AgNO<sub>3</sub> spray on concrete samples with slow applied current**

Concrete elements of split samples with low applied current were further cracked in their transverse direction. The exposed surfaces were sprayed with 0.1N AgNO<sub>3</sub> to indicate Cl<sup>-</sup>-contaminated regions where white precipitate will form. The transverse split surfaces were used to eliminate the effect of corrosion-induced cracking parallel to rebar on Cl<sup>-</sup> penetration and AgNO<sub>3</sub> color indication. It is clear from **Fig. 5.24** that C'-60S shows a deeper Cl<sup>-</sup> penetration front (where color transitions from light brown to dark brown) as compared to that in C'-0S and C'-45S. This means that under the applied current, more Cl<sup>-</sup> was able to penetrate into concrete with 60% slag as cement replacement. This seems to be contradictory to the results of Cl<sup>-</sup> penetration depths in plain concrete samples with no applied current as given in **Chapter 4** where it was found that no significant difference in Cl<sup>-</sup> penetration depths amongst the samples. This is because under applied current, Cl<sup>-</sup> would be driven from the electrolyte to the positively-charged anode within the concrete. Hence, permeability would play a more significant role in controlling Cl<sup>-</sup> migration

as binding ability of slag which requires formation of hydration products would not be realized under the relatively short period of the applied current.

#### 5.4.5 Porosity and gravimetric mass losses

Higher magnification at steel-concrete interface shows a wider discoloration of the matrix by corrosion products for HyFRC-0S-48H (**Fig. 5.25**). As mentioned, corrosion products were able to better diffuse into the micropores of HyFRC-0S than those of HyFRC-45S/60S. Hence, for the same duration of applied current, it was expected that the mass loss in HyFRC-0S was higher than the mass losses in HyFRC-45S/60S. However, this is not the case based on gravimetric mass loss results. HyFRC-0S-48H had the least mass loss as compared to HyFRC-45S/60S-48H. It is postulated that more stable passive film in HyFRC-0S, interfacial densification by corrosion products and buffering action of CH contributed to the lower mass losses in the sample. In **Chapter 4**, it was argued that a more stable passive film formed in concrete without slag replacement and that helped to reduce anodic mass loss. In addition, the more porous HyFRC-0S allowed corrosion products to permeate into the micro pores within the interfacial region. As corrosion products were accumulated and densified by the confining fibers, they formed a protective layer around the steel rebar. The layer would make it more difficult to further oxidize the anode, leading more oxidation of water to compensate for the total charge flow in the system to meet the desired  $1 \text{ mA/cm}^2$  applied current. On the other hand, due to a denser interface, cracks formed early in for HyFRC-45S/60S before a protective layer of comparable thickness was created by the collecting corrosion products. Also, a lack of CH in the matrix is postulated to result in an early onset of more aggressive interfacial acidification in HyFRC-45S/60S. Acidification would offset the beneficial effect of fiber confinement and this led to higher observed mass losses in HyFRC-45S/60S.

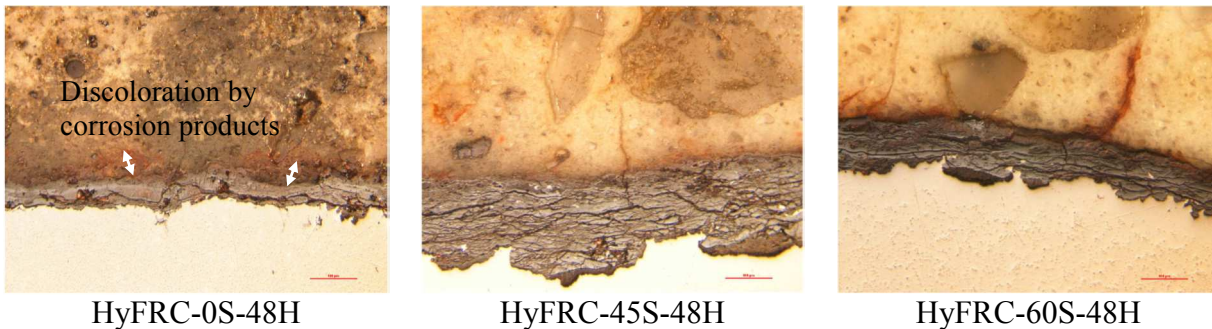


**Figure 5.25: Microscopic pictures of steel-concrete interface**

#### 5.4.6 Hybrid fibers and porosity

Microscopic pictures at steel-concrete interface for C-45S-24H and HyFRC-45S-24H are reproduced in **Fig. 26**. It is observed that more air voids exist in HyFRC matrix as compared to plain concrete without inclusion of hybrid fibers. The increase in porosity explains an earlier corrosion initiation as indicated by corrosion potential measurement in HyFRC as compared to that in plain concrete. Nevertheless, HyFRC and plain concrete samples with no applied current showed similar corrosion rate. The increase in entrapped voids also led to a reduction in elastic modulus as shown earlier in **Fig. 5.4**.

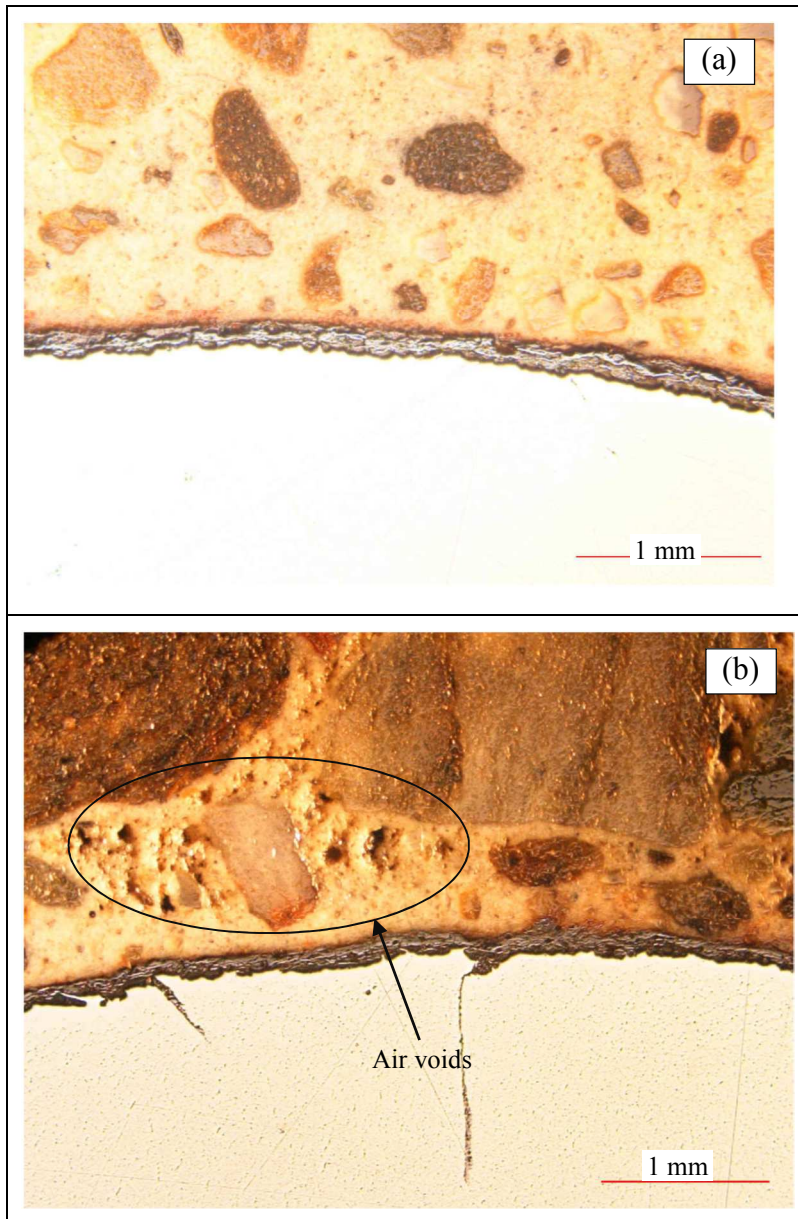


**Figure 5.26: Microscopic pictures at steel-concrete interface of: (a) C-45S-24H, and (b) HyFRC-45S-24H**

## 5.5 Conclusions

From the results and discussion, the following can be concluded from this study:

- Based on corrosion rate measurement, hybrid fibers in concrete do not adversely affect corrosion initiation in concrete despite their poorer consolidation and more porous matrix as compared to plain concrete.
- With 24 and 48 hours of  $1 \text{ mA/cm}^2$  applied current, hybrid fibers in concrete significantly reduced corrosion rates through confinement and densification of corrosion products at steel-concrete interface.



- The effects of hybrid fibers on corrosion were more dominant than the effects of slag on corrosion propagation and corrosion rates. This is reflected in similar corrosion rates for HyFRC-0S, HyFRC-45S and HyFRC-60S for the same applied current regime. However, mass losses increased with increasing slag replacement levels due to the presence of sulfur-based reducing agents in concrete pore solutions and less buffering action from  $\text{Ca(OH)}_2$ .
- Lowering corrosion density increased steel mass loss due to higher effectiveness of the applied current. However, corrosion rates were reduced due to enhanced densification at steel-concrete interface as corrosion products could more gradually permeate into the pores in the interfacial region.
- At a small applied current density, corrosion products were different from that observed under higher applied current level. They were less powdery and tougher to remove with hexamethylene tetramine HCl solution.
- Under accelerated corrosion test, steel fibers near the surface corroded due to lack of physical protection from concrete and due to a high voltage drop induced between the anode and cathode.
- HyFRC with no slag replacement allowed for more corrosion products to diffuse deeper into its more porous microstructure. This seems to be beneficial as it reduced pressure on the matrix and allowed for densification of corrosion products at steel-concrete interface, leading to a reduction in mass losses and corrosion rates under accelerated corrosion test.

The next chapter will present the influence of different steel-concrete interface qualities on corrosion of steel in concrete. This is critical as a more porous interface may initiate corrosion early but may prolong the damage to concrete because of its ability to accommodate more corrosion products. Slowing down of corrosion rates may be achieved too when corrosion products densify and act as a protective layer for steel. The phenomenon has an implication on high strength concrete where the refinement of microstructure will limit the amount of corrosion products that can penetrate into the matrix. As fibers are activated only after cracks are formed, the findings to be presented in the next chapter will provide an information on the relative effectiveness of fibers in high strength and normal strength concrete.

# 6 Influence of interface qualities on corrosion of reinforcing bars in concrete

## Summary

More porous concrete matrix allows for moisture, oxygen and aggressive ions such as chloride to penetrate easily to reach steel-concrete interface, leading to an earlier onset of corrosion. However, the effects of interface qualities on corrosion initiation and propagation have yet not been systematically investigated. In this study, corrosion samples with three different steel-concrete interfaces: direct contact, proprietary fiber-reinforced mortar (FRM) separation, and filter paper separation, were constructed and their corrosion behaviors were examined under accelerated corrosion tests. The results showed that with no applied current, the more porous interface created by the FRM and the filter paper led to a higher corrosion activity. However, an ability to accommodate more corrosion products created by the induced current and the resulting interfacial densification reduced their subsequent corrosion rates. Also, a lower content of CaO in FRM powder was found to cause higher mass losses under accelerated corrosion tests due to a reduced buffering action by Ca(OH)<sub>2</sub> in the matrix. Considering service life of structures where corrosion initiation period is longer than corrosion propagation period, a dense interface is a preliminary requirement for more durable reinforced concrete structures.

## 6.1 Introduction

Corrosion of rebar in concrete starts when activating substances such as Cl<sup>-</sup> and CO<sub>2</sub> reach the steel surface (Tuutti, 1982). The stage is termed corrosion propagation and is characterized by the formation of corrosion products which cause cracking to the matrix and subsequent spalling of concrete due to a higher volume of corrosion products as compared to the original metal. It was shown that only a small amount of corrosion products covering about 20% of the rebar perimeter is enough to cause cracking to concrete (Wong et al., 2010). Factors influencing the propagation stage are concrete moisture content, temperature, pore solution chemical compositions, concrete cover, environmental variations and concrete porosity. Pores around the steel-concrete interface can accommodate corrosion products and delay the onset of cracking. Weyers (1998) suggested a time-to-cracking or propagation model for concrete structure in Cl<sup>-</sup>-laden environment. The model consists of three stages: free expansion, internal pressure build-up, and concrete cracking when the internal pressure exceeds the tensile strength of concrete. In the free expansion stage, an internal pressure cannot be created as the free space at steel-concrete interface is being filled up. The free space is directly related to the surface area of reinforcement, water-binder (W/B) ratio, degree of hydration and degree of consolidation.

Besides the effect on the onset of crack propagation, the interface qualities also influence corrosion initiation. Through corrosion potential measurement, it was shown that a lack of physical adherence to concrete caused an early corrosion initiation (Yonezawa et al., 1988). At a macro-scale, self-consolidating concretes (SCC) with their high consistency and resistance to bleeding possesses a better concrete-steel interface quality and exhibits enhanced corrosion resistance. It

was shown that steel in SCCs were less sensitive to the top bar effect, a phenomenon in which top bars are susceptible to corrosion due to bleeding (Castel et al., 2003). Soylev & François (2003) studied the influence of steel-concrete interface defects on reinforcing steel corrosion in vibrated concrete and SCC of different strengths. Through polarization resistance measurement and corroded surface area quantification, they found that for the same design strength, SCC showed lower corrosion susceptibility due to its consistency and better compaction. Also, concrete with higher strengths showed less corrosion.

Studies on the influence of steel-concrete interface qualities on both corrosion initiation and propagation in concrete are still lacking. Investigation of the effects will be the objective of the research. Interface qualities were varied by wrapping either a thin layer of proprietary polymer fiber-reinforced mortar (FRM) or filter paper with 2.5  $\mu\text{m}$  pore size around steel rebars in concrete. To facilitate corrosion, 4% NaCl by weight of the total binder was added into the mixing water. In corrosion initiation study, corrosion potentials and corrosion rates were measured up to 98 days. In propagation stage study, accelerated corrosion test with a constant 1 mA/cm<sup>2</sup> applied current for 24 and 48 hours to induce different levels of corrosion was implemented. At the end of the electrochemical measurements, the samples were prepared for microstructural analysis with scanning electron microscopy (SEM). The results gave an insight into the effects of interfacial porosity on corrosion initiation and propagation of steel in concrete. A literature review on the effects of steel-concrete interface on corrosion will be provided next.

## **6.2 Literature review**

As corrosion of steel in concrete is initiated on the steel surface, steel-concrete interface (SCI) quality is critical in determining corrosion performance of concrete. A good adhesion of concrete on steel surface provides a good protection of steel against corrosion. This is because the lime-rich layer from cement hydration at the interface prevents a local drop in pH under Cl<sup>-</sup> attack through buffering action against acidification (Page, 1975; Yonezawa et al., 1988). Ca(OH)<sub>2</sub> or CH also acts as a screen to protect steel surface from direct access of oxygen (Page, 1975; Yonezawa et al., 1988). Also, a dense SCI blocks the diffusion of corrosion products which as a result facilitates repassivation (Page, 1975; Yonezawa et al., 1988). As such, defects at steel-concrete interface can have an adverse effect on corrosion performance of steel in concrete. Defects or disturbance to steel-concrete interface may be classified into two categories: (i) inherent defects caused by bleeding, poor concrete consolidation and wall effects, and (ii) load-induced defects. Their effects on corrosion of steel in concrete will be discussed.

### **6.2.1 SCI inherent defects and steel corrosion**

The influence of SCI inherent qualities on corrosion of steel has been extensively studied. It is known that a solution with high pH level induces the formation of passive film on steel surface and this protects steel against corrosion. However, the physical presence of concrete surrounding the rebar also plays a critical role in determining corrosion characteristic of the embedded rebars. Mortar was found to provide a better protection to steel than just the alkaline environment. Also, the critical threshold of chloride content in concrete for steel corrosion cannot be simply determined by Cl<sup>-</sup>/OH<sup>-</sup> ratio but the value also depends on other parameters such as quality of steel-concrete interface. This was verified by a study conducted by Yonezawa et al. (1988). They studied the corrosion behavior of steel in simulated pore solution and in concrete with two different interfacial conditions: (i) good adhesion, and (ii) filter paper separation. It was found that for 0.52

M NaCl concentration in both the mixing water and the simulated pore solution, active corrosion started earlier in the case of steel directly in solution than steel wrapped with filter paper in mortar. Corrosion potentials of the two sets of samples are given in **Fig. 6.1**. There was no indication of repassivation. The results were shown to be in marked contrast to what was achieved for electrodes with good adhesion to concrete in which passivity was maintained throughout the measurement period. SEM analysis showed CH crystals become round-shaped due to partial dissolution to buffer a local drop in pH.

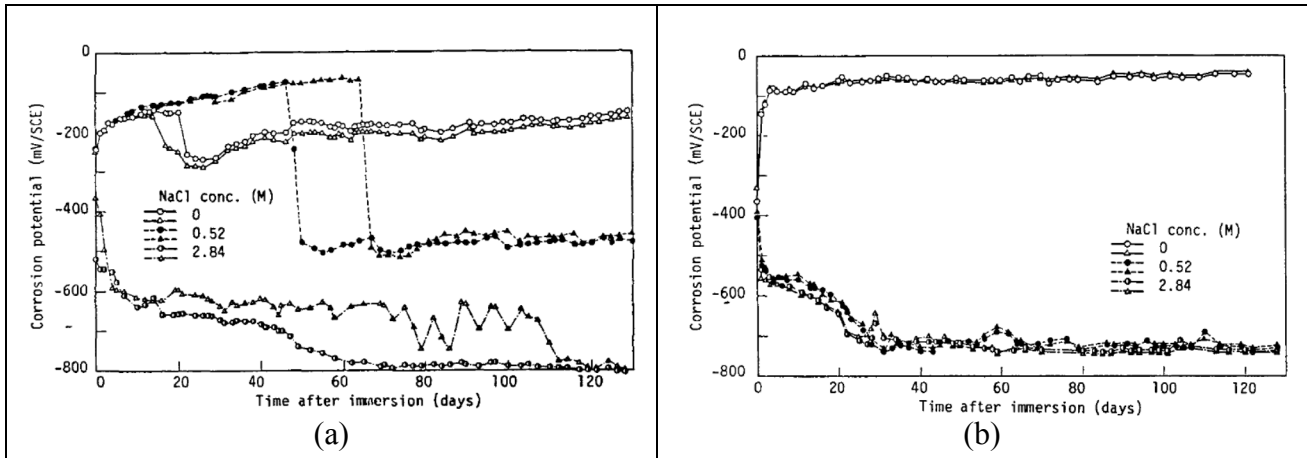


**Figure 6.1: Corrosion potentials: (a) steel wrapped with filter paper in mortar (NaCl in both mixing water and immersion solution), and (b) steel directly immersed in CH solution (Yonezawa et al., 1988)**

Depending on rebar orientation, gaps may form under steel rebars and this may cause different corrosion responses of steel in concrete. Mohammed et al. (1999) studied steel corrosion in concrete subjected to 3.5% NaCl wetting and drying with respect to bar orientation, influence of stirrup on macrocell formation, types of rebars (plain and deformed) in uncracked concrete, and the effect of water-binder ratio (W/B). Microcell corrosion results showed that bottom halves of the top steel experienced significant microcell corrosion. This is attributed to a gap formed between steel and concrete. The gap initiated breakdown of the passive film and this led to the onset of corrosion. The gap was caused by bleeding and as a result top steel was more significantly affected. It is also seen that bottom halves of bottom steel had lower current density. This is because little bleeding took place over the bottom region of concrete element. The finding is depicted in **Fig. 6.2**. Based on a similar reasoning, for the same type of steel, smaller water-cement ratio or higher workability concrete would be expected to lead to reduced corrosion density due to their decrease in porosity. Self-consolidating and non self-consolidating concretes were used to produce different qualities of steel-concrete interface (Soylev & François, 2003). It was shown that at the same strength level, SCC showed higher bond strength and lower corrosion activity due to its stability and consistency. Also, near the column bottom, the concrete was denser and hence total corrosion area was found to be smaller.

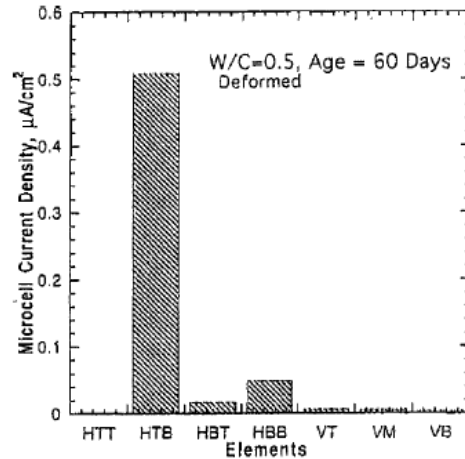


**Figure 6.2: Microcell current density for various steel elements (H for Horizontal, V for Vertical, first T/B that follows for top/bottom bars, and second T/B for top/bottom elements) (Mohammed et al., 1999)**

### 6.2.2 SCI disturbance due to loading and steel corrosion

Corrosion resistance of beams under sustained loading was conducted by Castel et al. (Castel et al., 2003). They found that although Cl<sup>-</sup> concentration at the rebar location reached the threshold value, there was no clear correlation between chloride content and steel corrosion. The discrepancy was attributed to steel-concrete interface quality, which can be classified into three categories: (i) local steel-concrete debonding due to concrete bleeding, (ii) mechanical degradation due to shear bonding failure, and (iii) randomly distributed concrete heterogeneity. Based on this, corrosion process of steel can be better explained. Tensile reinforcement which in their study corresponded to top casting direction was affected by both steel-concrete debonding and by mechanical damage. This explained the extensive corrosion of the tensile rebars. In a separate study conducted by Michel et al. (2013), steel-concrete interfacial damage was used to explain corrosion response of cracked plain concrete and FRC. It was found that in beams with sustained flexural load applied until the extent of interfacial slip was the same, steel rebars in plain concrete and FRC (with 0.5% and 1% fiber volume fractions) showed similar level of corrosion response. This means that disturbance to steel-concrete interface is one of the main parameters that control corrosion performance of steel in concrete.

As mentioned, this study will further investigate the role of interface qualities on corrosion of steel in concrete. Although Yonezawa (1988) already conducted a similar interface study, their focus was on corrosion initiation phase. In this study, the effect of steel-concrete interface on corrosion propagation will also be explored. The results provide pertinent information on how different interface qualities can differently affect corrosion propagation in concrete. This has an implication on normal strength and HPC concrete as their steel-concrete interface qualities are different. The results will also shed light on how loading and disturbance to steel-concrete interface can affect corrosion performance of concrete. For example, it may be possible to infer if hybrid fiber-reinforced concrete whose damage to the interface may be minimized under loading due to its crack control ability provides a better corrosion resistance to steel as compared to plain concrete.

## 6.3 Materials and methods

### 6.3.1 Materials

ASTM Type II cement whose chemical compositions were given in **Table 2.1** of **Chapter 2** was used as the binder in concrete. In addition, proprietary polymer fiber-reinforced mortar (FRM) under a commercial name Elephant Armor-DOT (E) was used as a coating on the steel surface before casting to modify steel-concrete interface. Trimmed and polished rebars were dipped into fresh FRM mortar, leaving a coat of FRM on their surfaces upon lifting. The presence of the synthetic fibers and different chemical compositions of FRM would create an interface different from that of rebars directly embedded in concrete. The initial expectation was that the fibers would provide a local confinement to corrosion products and as a result would reduce corrosion activity. This, however, is not the case based on corrosion and microstructural analysis results to be presented. For chemical composition analysis, the mortar was sieved to pass through 45  $\mu\text{m}$  size to separate fibers and sand particles from the binder powder. The powder was analyzed with X-ray fluorescence for their chemical compositions whose results are summarized in **Table 6.1**. Again, it is noted that  $\text{SO}_3$  could not be accurately quantified in the XRF analysis and was not listed in the table. As compared to cement, the binder in the FRM has a lower content of CaO but higher amount of  $\text{Al}_2\text{O}_3$  which may help to contribute to its early strength development.

**Table 6.1: Compositions of FRM powder**

|                         | FRM Powder (%) |
|-------------------------|----------------|
| $\text{SiO}_2$          | 23.43          |
| $\text{TiO}_2$          | 0.88           |
| $\text{Al}_2\text{O}_3$ | 17.52          |
| FeO                     | 2.77           |
| MnO                     | 0.04           |
| MgO                     | 2.51           |
| CaO                     | 50.69          |
| $\text{Na}_2\text{O}$   | 0.99           |
| $\text{K}_2\text{O}$    | 0.81           |
| $\text{P}_2\text{O}_5$  | 0.36           |
| $\text{SO}_3$           | -              |

### 6.3.2 Concrete mix designs

The concrete mix has a water-binder (W/B) ratio of 0.54. In preparation of the FRM, water was added into the mortar at a ratio of 0.25 by mass. The mix proportions of concrete and FRM are summarized in **Table 6.2**. NaCl of 4% by total binder weight was added into the mixing water. This was to eliminate the problem of ineffectiveness of the applied current as discussed in the previous chapters.

**Table 6.2: Mix designs for accelerated corrosion test (kg/m<sup>3</sup>)**

|                  | <b>C</b> | <b>FRM</b> |
|------------------|----------|------------|
| W/B              | 0.54     | 0.25       |
| Water            | 228.6    | -          |
| Cement           | 425.8    | -          |
| Fine aggregate   | 853.3    | -          |
| Coarse aggregate | 775.5    | -          |

### 6.3.3 Specimen preparation and corrosion testing procedure

Specimen preparation and corrosion testing follow the procedure provided in **Chapter 3** where the anodic rebars were completely embedded in concrete. The specimens were cast and moist cured for 7 days before being exposed to laboratory air for a minimum of 21 days. Three additional cylinders cured under the same regime were also produced to find compressive strength at 28 and 56 days.

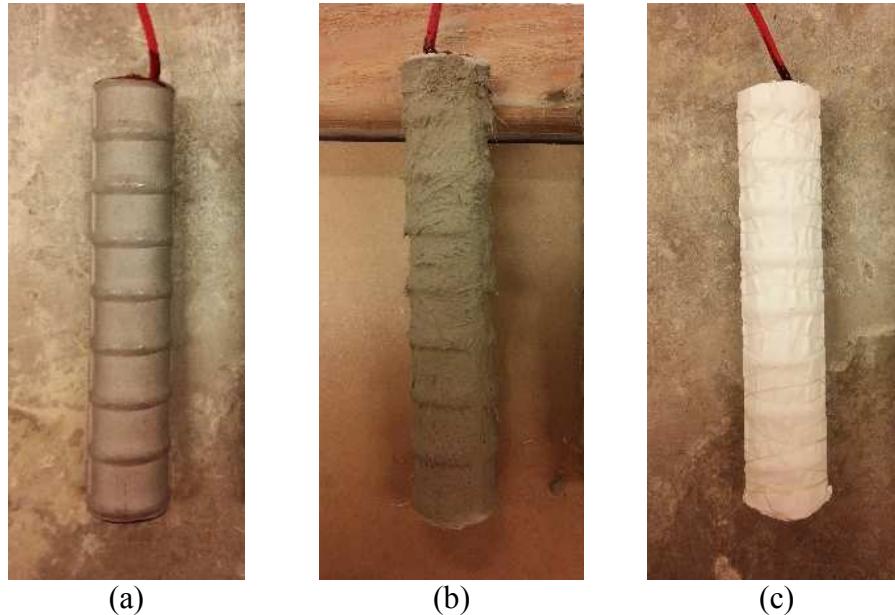


**Figure 6.3: Bars with different interfaces: (a) plain rebar, (b) rebar coated with FRM, and (c) rebar covered with filter paper**

To investigate the effect of interface qualities on crack propagation induced by corrosion, three types of interfaces were implemented for concrete: direct contact, separation with FRM and separation with filter paper. As mentioned, in FRM separation, rebar was dipped into the fresh mortar for several times to create a thin layer of the mortar on the rebar surface. Based on microstructural analysis results to be presented later, the thickness of the coating was approximated at 200  $\mu\text{m}$ . The mortar was then left to dry in air for 1 hour before casting. The intention was to see if a modification to the steel-concrete interface with the FRM composite could enhance the corrosion performance of the rebar. For the filter paper separation, quantitative filter paper with 2.5  $\mu\text{m}$  pore size was wrapped one round around the rebar and fastened by nylon wire. The introduction of filter paper was to imitate a porous and poor interface between steel and concrete.

Bars with different interfaces are shown in **Fig. 6.3**. In the sample annotations, C is for concrete, D is for direct contact with no separation, E is for separation with FRM, F for separation with filter paper, and nH for n hours of applied current. For example, C-D-48H refers to concrete sample with steel in direct contact with the matrix and with 48 hours of applied current.

### **6.3.4 Microscopic analysis**

Following the accelerated corrosion, the samples from linear polarization group were sliced in the middle region to obtain disc elements of thickness 21.5 mm. The elements were prepared for optical and SEM microscopic analysis. The procedure was outlined in **Chapter 3**.

### **6.3.5 Gravimetric mass loss analysis**

Meanwhile, the samples from the Tafel test group were dried in oven at 110 °C for 24 hours and were subsequently subjected to splitting tensile test to extract the rebars in the middle. The wiring, and coating on the rebars were then removed or cleaned off. HCl hexamethylene tetramine solution was used to remove corrosion products so that significant etching of the base metal could be minimized. The process for gravimetric mass loss measurement was detailed in **Chapter 3**.

## **6.4 Results**

### **6.4.1 Mechanical properties**

The compression test results for plain concrete at 28 and 56 days, and FRM at 7 and 56 days are given in **Fig. 6.4**. Only one E sample was tested at 56 days and hence no error bar was provided. FRM is claimed by producer to be an early strength composite which can attain a compressive strength of up to 27.5 MPa within 4 hours of casting and hence the FRM samples were air-cured until testing. The compression test for FRM was conducted at 7 days because of its high early strength development as claimed by the manufacturer. It is observed there was no significant strength change for FRM from 7 to 56 days. At 7 days, FRM had a compressive strength that is 25% less than that of the plain concrete at 28 days with 4% NaCl in the mixing water. Also, the elastic modulus for FRM was found to be only 15.1 GPa at 7 days, 30% lower than 21.6 GPa of the plain concrete at 28 days. This may be attributed to the absence of coarse aggregates and a higher porosity with the presence of microfiber in the FRM. The gas permeability test results which were given in **Chapter 4** confirmed that FRM with 5-day air curing had a gas permeability coefficient about 6 times higher than that for normal strength concrete. Although the gas permeability result was for FRM at a different curing age, with a fast strength gain, FRM was expected to have a permeability that changes insignificantly over time. It is also noted that for plain concrete, there is an insignificant strength change from 28 to 56 days. This is attributed to acceleration action of NaCl which led to an enhanced early-age hydration of concrete. The acceleration action of NaCl is similar to that of the well-known CaCl<sub>2</sub> accelerator (Neville, 1996). A slight reduction in strength at 56 days may be caused by expansive complex salt formation with the presence of NaCl in the mixing water (Berntsson & Chandra, 1982).



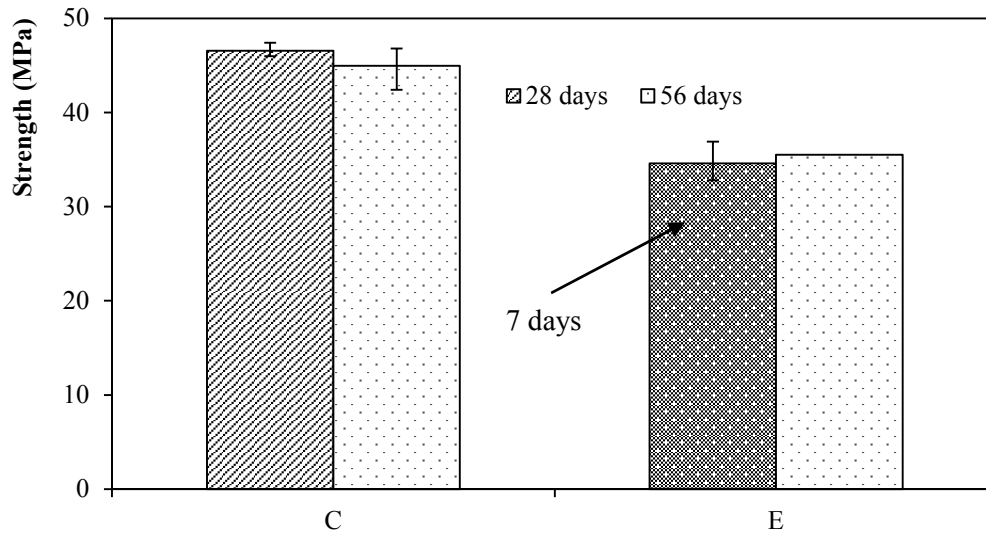


Figure 6.4: Compressive strengths of plain concrete and FRM (E)

### 6.4.2 Corrosion initiation in samples with different interface qualities

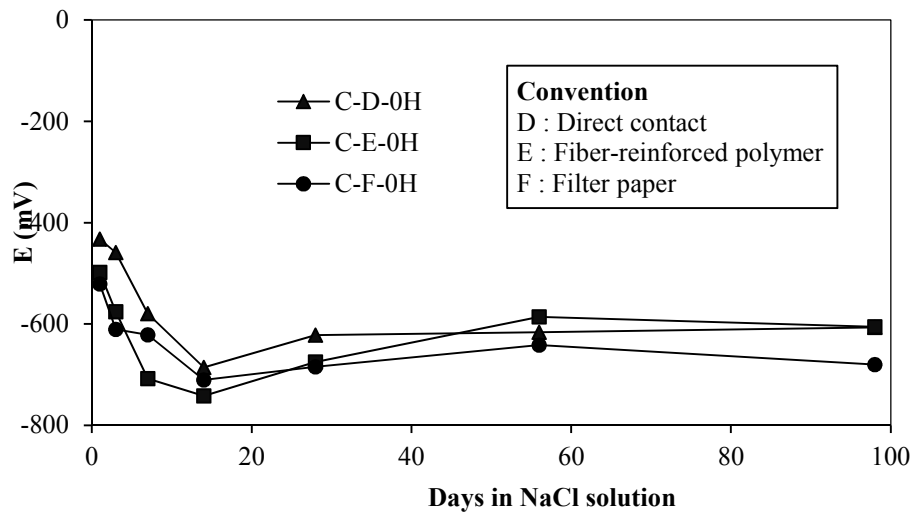
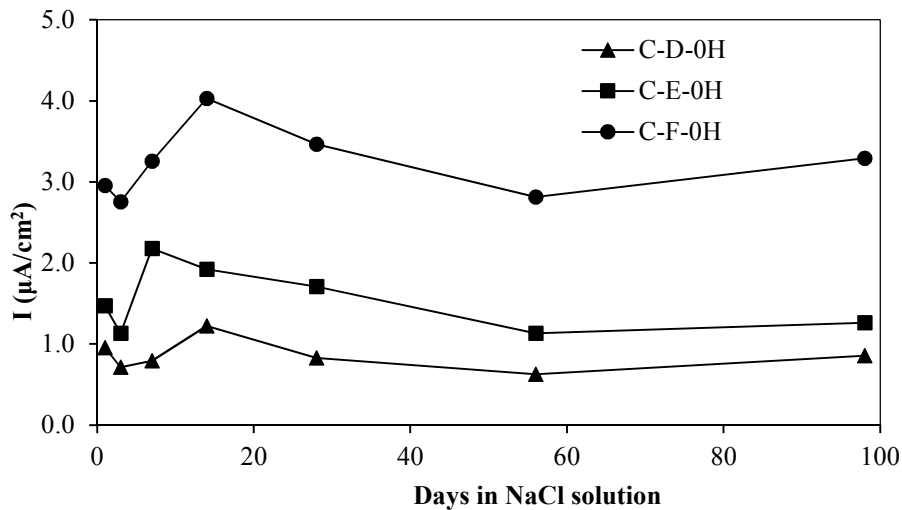


Figure 6.5: Corrosion potentials for samples without applied current

The results for corrosion potentials of samples without applied current are given in Fig. 6.5. It is observed that all samples had corrosion potentials more negative than -277 mV from the first day of measurement. Hence, it is highly probable that all samples experienced an active corrosion. NaCl of 4% by weight of binder is effective in initiating corrosion of steel in concrete. Also, C-D-0H had less negative corrosion potential as compared to C-F-0H at the start of the measurement. This is as expected as the filter paper separated the steel from the matrix and led to a higher availability of oxygen and moisture at the interface to participate in corrosion reactions at early

stages of the electrochemical measurements. In addition, a lack of physical contact and hence a chemical protection provided by CH led to higher corrosion activity. Similarly, the higher porosity of FRM as proven by its higher gas permeability coefficient and lower elastic modulus as compared to plain concrete (as in **Chapter 4**) contributed to the generally more negative corrosion potentials of C-E-0H as compared to C-D-0H.

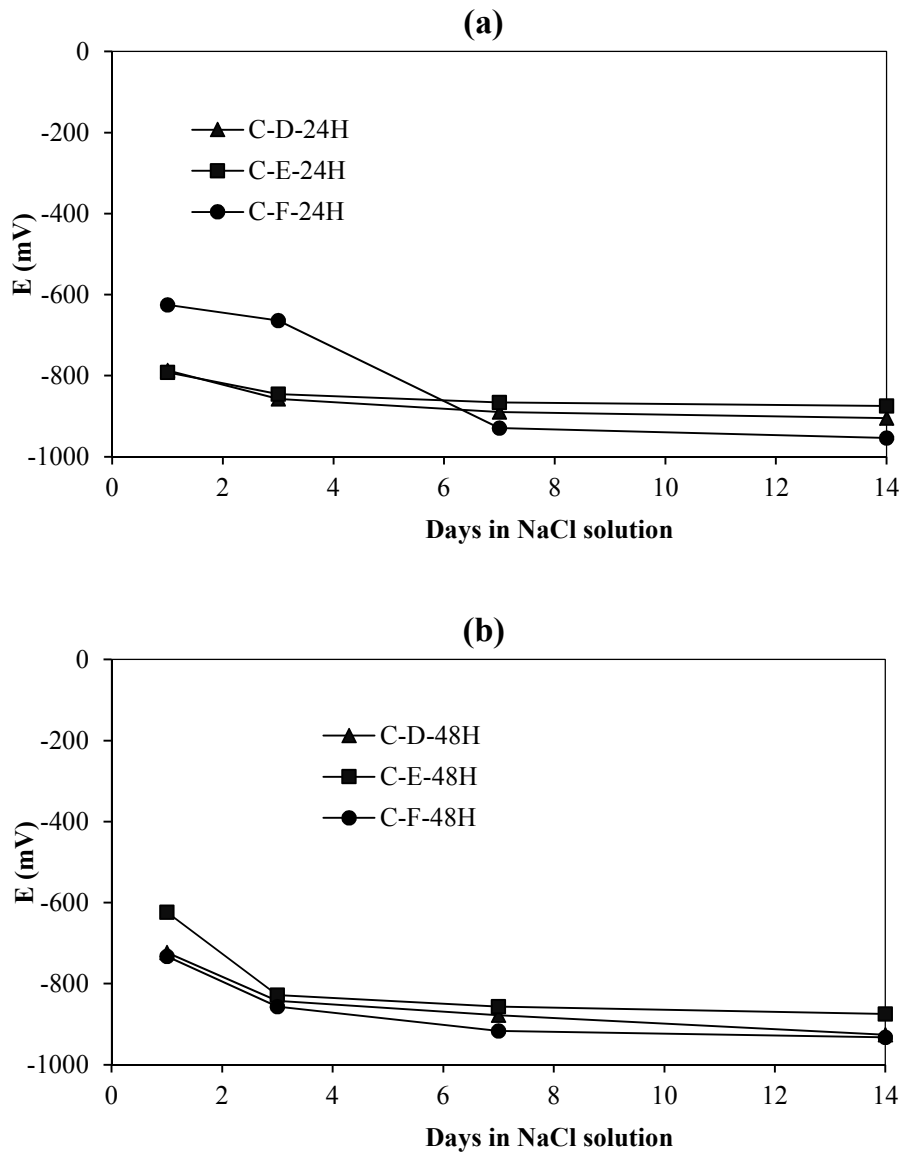
The corresponding corrosion rates are given in **Fig. 6.6**. In this study, corrosion rates greater than  $0.1 \mu\text{m}/\text{cm}^2$  were taken as active. It is observed that corrosion rates for all samples with no applied current were all in the active zone. Consistent with the trend observed in corrosion potential results, corrosion rates for C-D-0H were lower than C-E-0H and C-F-0H at all measurement points. In order of corrosion activity,  $\text{C-D-0H} < \text{C-E-0H} < \text{C-F-0H}$ . As mentioned, it was initially postulated that FRM with synthetic fibers would provide a local confinement to corrosion products and hence would limit corrosion activity. However, the high permeability of the composite was the dominant factor in controlling corrosion of steel and this led to the observed high corrosion activity. It was also observed that the corrosion rates for C-F-0H were approximately 2 times higher than those for C-E-0H. Similar to FRM, the filter paper introduced more voids at steel-concrete interface and that led to higher corrosion activity in C-F-0H. From the results, it is implied that an improved mitigation action against corrosion initiation may be the use of high performance mortar or slurry coating on the rebar although this was not investigated in this study.



**Figure 6.6: Corrosion rates for samples without applied current**

### 6.4.3 Corrosion results for concrete with applied current

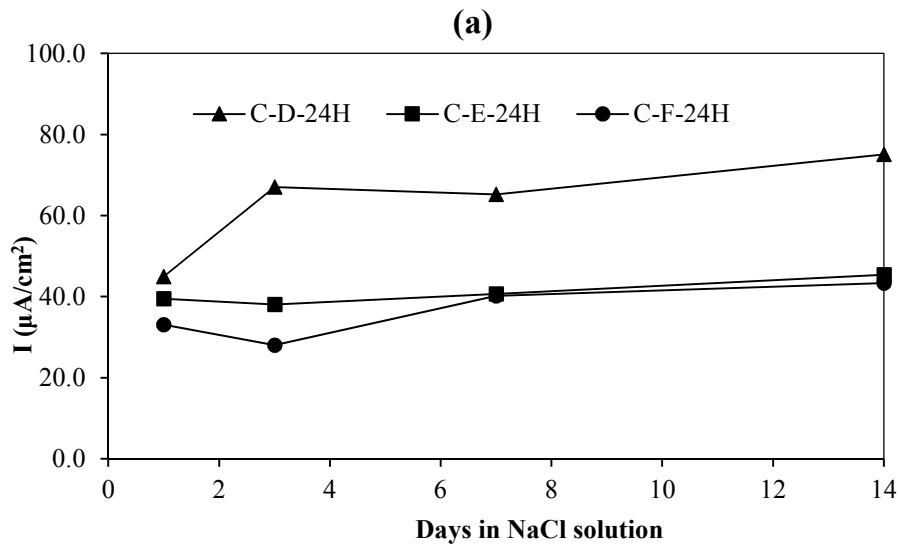
Corrosion potentials of the concrete samples with 24 and 48 hours of applied current are given in **Fig. 6.7**. It is observed that corrosion potential values were more negative than  $-277 \text{ mV}$ . The corrosion potentials ranged between  $-600 \text{ mV}$  and  $-1000 \text{ mV}$ . This indicates that all samples were in an active corrosion region. There is no distinguishable difference in corrosion potentials for the two applied current regimes of 24 hours and 48 hours. Hence, it is important to also investigate the corrosion rates.



**Figure 6.7: Corrosion potentials for samples with applied current of: (a) 24 hours, and (b) 48 hours**

The corrosion rates of corresponding samples after the applied current regimes are given in **Fig. 6.8**. It is interesting to observe that corrosion rates for C-D samples were significantly higher than the corrosion rates for C-E and C-F at both 24 and 48 hours of applied current. This is contradictory to what was observed in the corrosion initiation results where C-E and C-F experienced a higher corrosion activity. The higher corrosion rates of C-D-24H/48H may be attributed to a less resistance to cracking of the samples as compared to C-E and C-F samples. The proprietary FRM mortar and the filter paper led to a higher porosity at the interface. This allowed for corrosion products to be accommodated at the steel-concrete interface without causing much tensile hoop stress to the surrounding concrete. With corrosion products filling up the pores, the interface in turn became more densified. This limited further iron dissolution, oxygen and moisture migration,

leading to the lower observed corrosion rates. With less porosity, C-D would experience more tensile hoop stress and cracking, causing a dilution of the iron ion-concentrated solution at the interface and a higher availability of oxygen and moisture at the steel surface. This helped to maintain a high dissolution and corrosion activity of the steel substrate and as a result led to the observed higher corrosion rates in C-D samples. The results have an implication for fiber-reinforced concrete. If the quantity of fibers added is sufficient to prevent the opening of crack under corrosion stress, corrosion products will be collected and densified at the steel-concrete interface. This as a result reduced corrosion rates and helps to extend service life of structures. A reduction in corrosion rates with the presence of fibers was observed in the previous chapters. It is also noticed that corrosion rates for C-D-24H/48H were much higher than those for C-0S-24H/48H as presented in **Chapter 4**. This is attributed to the addition of NaCl in the mixing water which increased corrosion activity in C-D-24H/48H as a result of increased continuing pitting and interfacial acidification. Interfacial acidification is more critical with the presence of NaCl in the mixing water as  $\text{Cl}^-$  from NaCl is ready to react with  $\text{H}^+$  to form HCl, causing a depression in pH and the dissolution of steel.



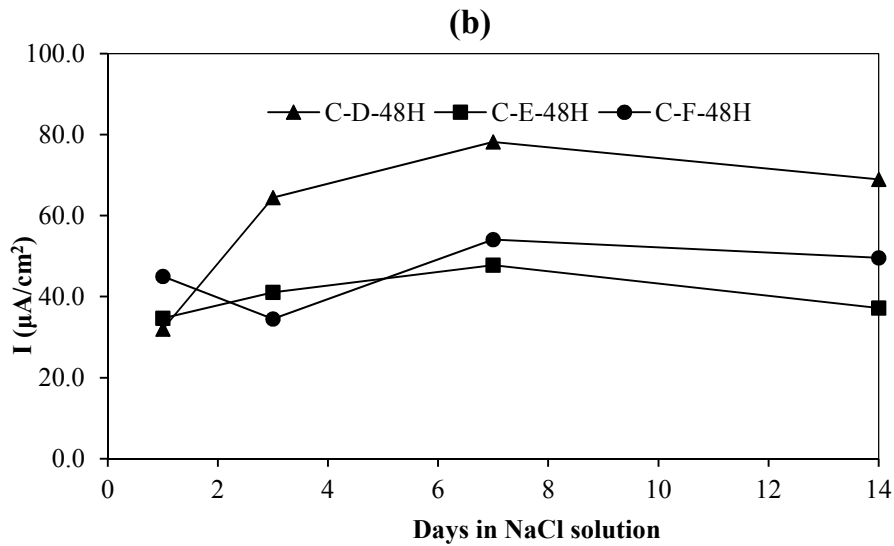


**Figure 6.8: Corrosion rates for plain concrete with 4% NaCl with applied current of: (a) 24 hours, and (b) 48 hours**

The exteriors of the samples were examined after an applied current of 24 and 48 hours. The side and bottom faces of each sample with different applied currents are given in **Fig. 6.9**. It was observed that more extensive cracking occurred for plain concrete samples with rebar in direct contact with the matrix (C-D). This caused more corrosion products to ooze out and caused more stains on the side surfaces. It is also observed that with the configuration of the corrosion samples in which the whole length of rebars was embedded in concrete, cracking did not extend through the entire height of the sample. This is attributed to a reduced stress and more confinement provided by concrete at both ends of the samples. Also, in C-F-24H/48H, part of the corrosion products were squeezed out from the tops of the samples along the electrical wiring. As corrosion products were formed and collected within the filter paper, they imbibed water, resulting in an increase in hydrostatic pressure within the interface. The pressure was built up and released by leaching of liquid with dissolved iron ions through a path formed along the weak interface of the wiring and concrete. This explained the minimal cracking along the cylindrical surfaces and the oozing out of corrosion products from the top faces of C-F-24H/48H samples. Corrosion stain on the top surface of C-F-48H is shown in **Fig. 6.10**. The phenomenon is crucial as it allowed for extraction of the pore solution to prove the acidification that occurs at the steel-concrete interface during accelerated corrosion test. The detail study will not, however, be presented in this report.



**Figure 6.9: Cracking on surfaces of samples with different regimes of applied current**

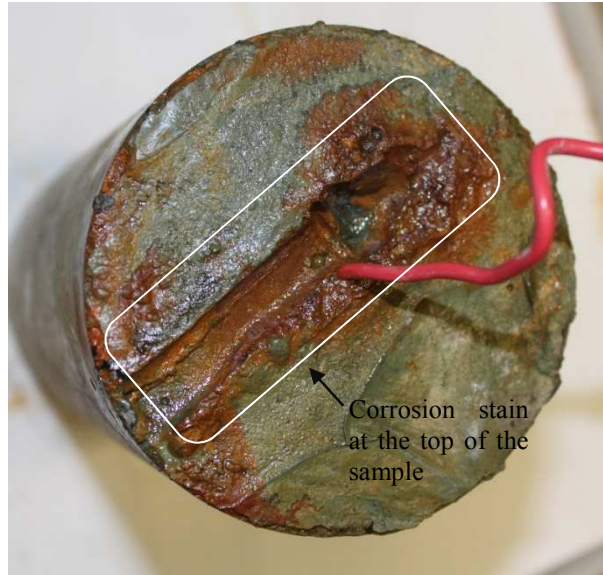


**Figure 6.10: Corrosion stain at C-F-48H top surface where corrosion products leached out**

#### 6.4.4 Gravimetric mass loss results

The results for gravimetric mass losses and theoretical mass losses are summarized in **Table 6.3**. The theoretical mass loss is the sum of mass loss during the applied current and during the 90-day (when no current was applied) or 14-day period (when 24 and 48 hours of current was applied) of electrochemical measurements. The mass losses were also normalized by the corresponding uncorroded bar masses. The theoretical mass losses after the applied corrosion regime was based on time integration of the measured corrosion rates which were presented earlier.

**Table 6.3: Gravimetric and theoretical mass losses**

|         | Current $1\text{mA}/\text{cm}^2$ | Gravimetric    |       | Theoretical    |
|---------|----------------------------------|----------------|-------|----------------|
|         | Hours                            | $\Delta M$ (g) | % M   | $\Delta M$ (g) |
| C-D-0H  | 0                                | 1.5            | 0.28% | 0.22           |
| C-D-24H | 24                               | 6.8            | 1.27% | 5.31           |
| C-D-48H | 48                               | 8              | 1.49% | 8.13           |
| C-E-0H  | 0                                | 1.1            | 0.20% | 0.39           |
| C-E-24H | 24                               | 5.5            | 1.02% | 4.37           |
| C-E-48H | 48                               | 9.7            | 1.81% | 7.18           |
| C-F-0H  | 0                                | 2.7            | 0.50% | 0.87           |
| C-F-24H | 24                               | 7.2            | 1.33% | 4.23           |
| C-F-48H | 48                               | 7.5            | 1.39% | 7.39           |

It is observed that for samples without any applied current, the gravimetric mass losses were always greater than the theoretical mass losses. It is possible that some of the base metal got etched out during the rebar cleaning process. However, consistent with the corrosion rate results, the mass loss for C-F-0H was greater than that for C-D-0H. On the other hand, the mass loss for C-E-0H was less than that of C-D-0H although the corrosion rates for C-E-0H were higher. The small discrepancy may be attributed to more etching of base metal during the cleaning for C-E-0H. The bar retrieved from C-D-0H had to be immersed in the cleaning solution longer to remove all

corrosion products, possibly due to different morphology of corrosion products formed within the samples. Also, when the current duration was increased from 24 to 48 hours, it is observed that the gravimetric mass losses did not increase proportionally with the theoretical mass losses. For example, in C-E samples, the theoretical mass loss was found to increase by 2.82 g while the gravimetric mass loss increased by only 1.2 g. This means that more mass losses tended to occur within the first 24 hours of the applied current. Corrosion products may have been collected at the steel-concrete interface. The densified corrosion products acted as highly impermeable layer that helped to limit the effectiveness of the applied current. Only part of the induced current would hence be effective in dissolving the anodic steel rebar. A typical graph for cell voltage against time for C-E up to 80000 seconds is given in **Fig. 6.11** and showed that the both IR compensated and IR uncompensated cell voltage with respect to the counter electrode steadily increased with time. To maintain the  $1 \text{ mA/cm}^2$  induced current, the voltage values compensated for IR were generally greater than 1.23 V, the level required for water oxidation to occur (Poursaei & Hansson, 2009). This confirms that other mechanisms such as oxidation of water were activated to offset the reduced dissolution of iron and electron contribution from the anodic steel reinforcing bar.

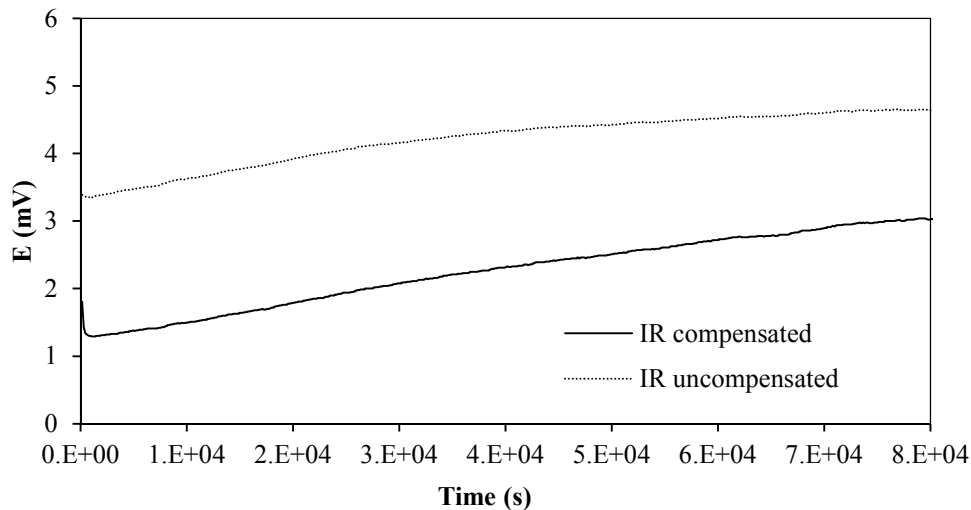


**Figure 6.11: Cell voltage with time for C-E samples**

Bars retrieved from split cylinders before cleaning off corrosion products are shown in **Fig.6.12**. Patches of corrosion products were observed on the surfaces of C-D-0H and C-E-0H while an almost uniform corrosion was found in C-F-0H. This is consistent with the electrochemical results where corrosion rates for C-F-0H were the highest as compared to corrosion rates in C-D-0H and C-E-0H. Also, corrosion products on C-E-0H seemed to be more powdery as compared to that in C-D-0H, possibly attributed to the different compositions of the matrix at steel-concrete interface. Removal of corrosion products on C-E-0H was easier. Uniform corrosion was observed in all other samples with 24 and 48 hours of applied current. This is different from samples with no added NaCl in the mixing water where limited corrosion was observed with 24 hours of applied current. The presence of salt in the mixing water destabilized the passive film on steel. As a result, the applied current was effective in causing corrosion throughout the rebar surface.





**Figure 6.12: Corrosion on bar surfaces showing patches of corrosion on C-D-0H/C-E-0H and uniform corrosion for all other samples**

#### **6.4.5 Flatbed digital imaging and optical microscopy**

The flatbed scanned images of sections of the corrosion samples are shown in **Fig. 6.13**. Marks for visible cracks were also drawn on the surfaces. At 24 and 48 hours, more extensive cracks were observed for C-D samples as compared to C-E and C-F samples. While C-E samples showed less extensive cracking as compared to C-D samples, C-F samples exhibited no visible cracking. From this, it can be concluded that the FRM and the filter paper allowed for corrosion products to be collected within pores of the FRM mortar or the filter paper, causing less extensive or no cracking to the surrounding matrix. The corrosion products filled up the pores and densified at the interface, creating a barrier to moisture, oxygen and ion movement. This led to lower mass losses and corrosion rates for C-E-24H/48H and C-F-24H/48H. It is noted that for the case of C-F-24H/48H, the absence of cracking may also be attributed to the oozing out of corrosion products at the top surfaces of the samples as already discussed in the previous section.

The optical microscopy results at steel-concrete interfaces for corresponding samples are shown in **Fig. 6.14**. The dark areas near the steel-concrete interfaces represents corrosion products or filter paper interspersed with corrosion products. It is observed that there were more corrosion products formed at the interface of C-F-0H as compared to C-D-0H and C-E-0H. With 24 hours of applied current, corrosion products filled up the pores at the interface inducing little or no cracking to the surrounding matrix. With 48 hours of applied current, more extensive cracking occurred for C-D-48H. Parts of the cracks were filled with corrosion products although cracks were observed to be empty further away from the interface. This is attributed to the dissolution of corrosion products into the immersion solution when the crack widths became wider toward the sample surface. In contrast, only small cracks were observed for C-E-48H while no cracks were observed for C-F-48H. As mentioned, the absence of extensive cracks in the two samples led to a densification at the steel-concrete interface and the subsequent reduction in corrosion rates.

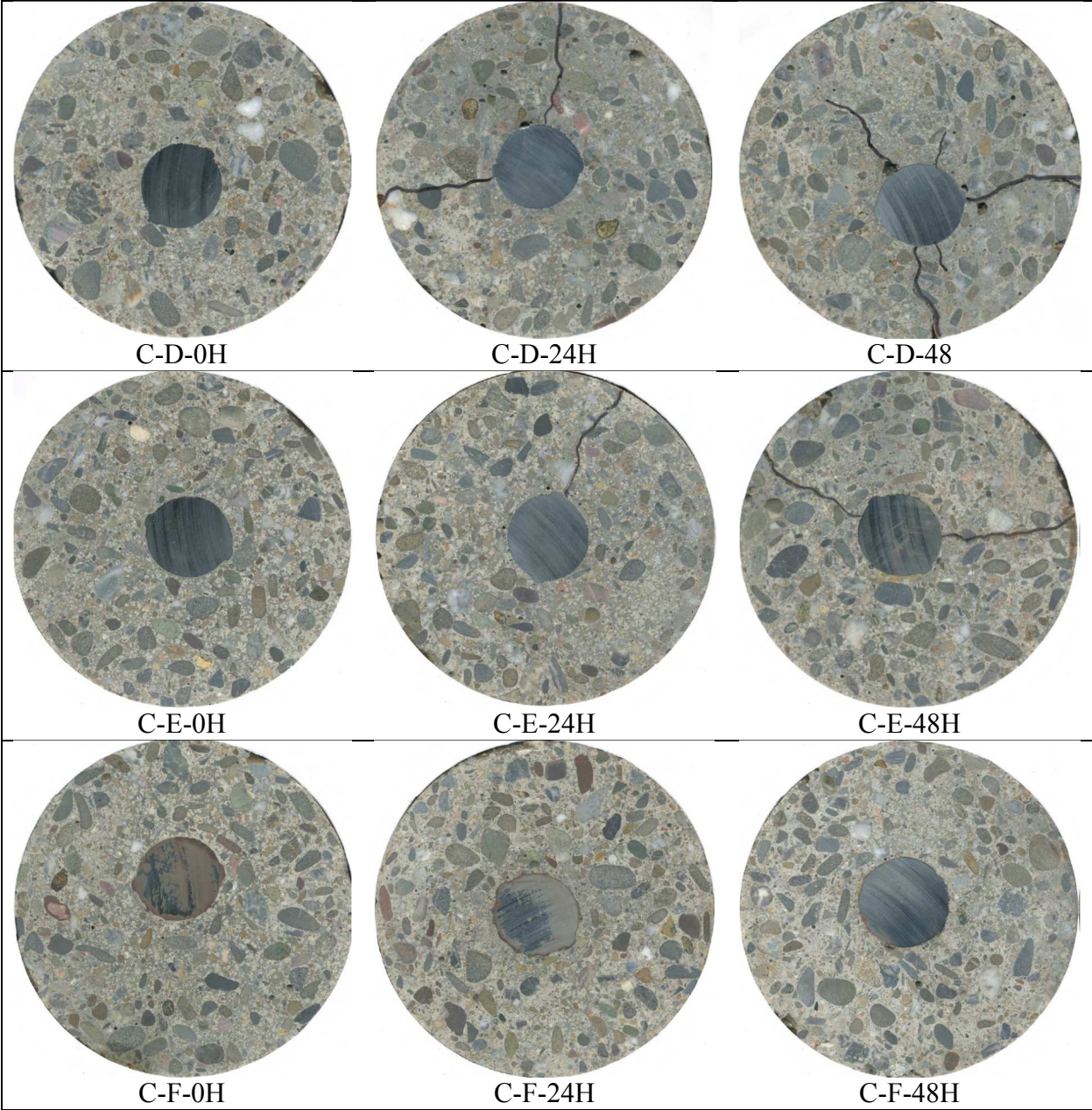


**Figure 6.13: Scanned images of sections for corrosion samples with different interfaces**



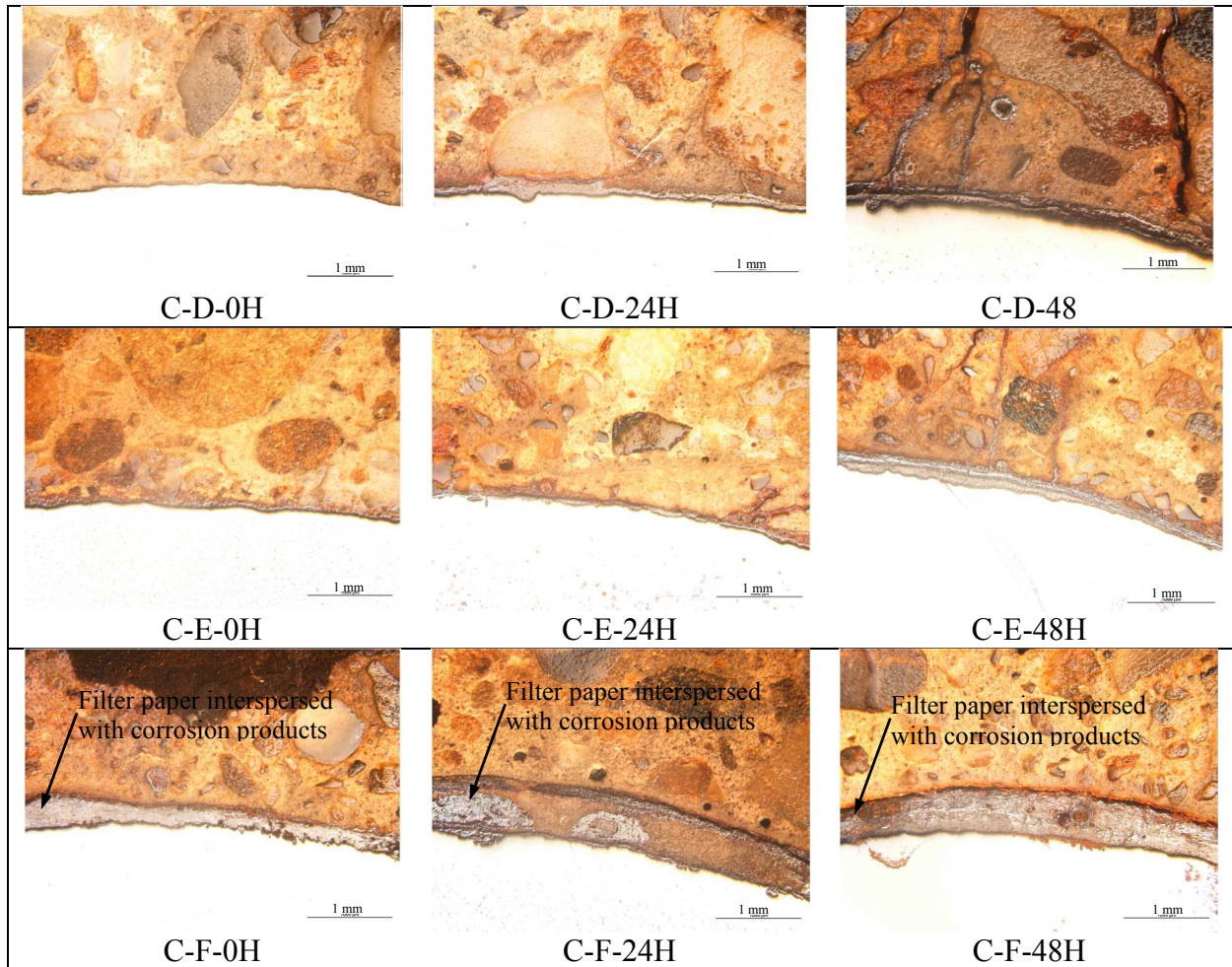
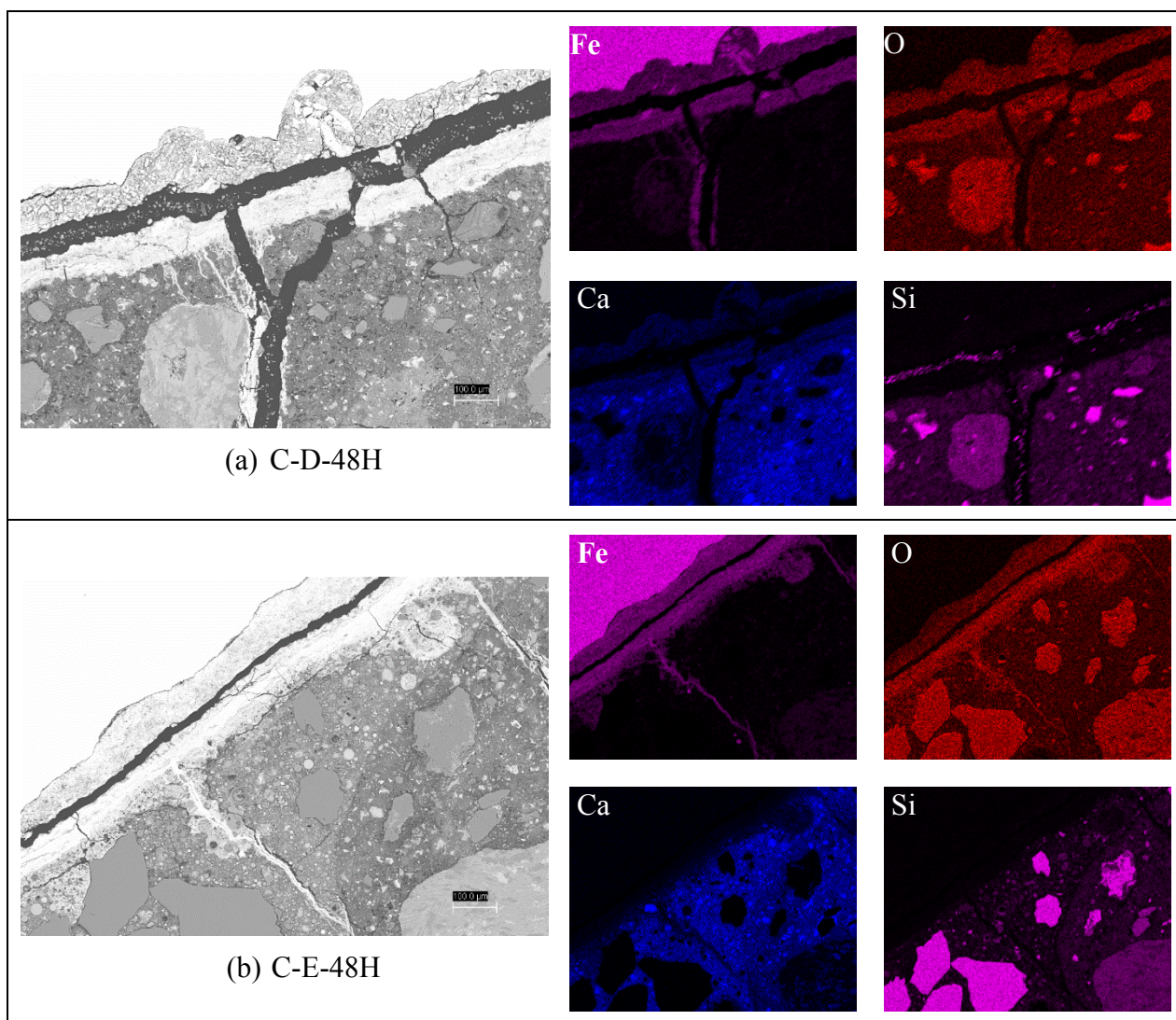


**Figure 6.14: Optical microscopic results at steel-concrete interfaces with different corrosion regimes**

#### 6.4.6 Backscattered electron imaging (BSE) & EDX element mapping

It has been argued that the less extensive cracking in C-E-24H/48H is attributed to the higher porosity of the FRM and hence the ability of the interface to accommodate corrosion products without causing extensive stress to the surrounding concrete. The backscattered electron (BSE) images and corresponding EDX element mapping of all corrosion samples with 48 hours of applied current are shown in **Fig 6.15**. It is observed that there is a clearer boundary between the corrosion products and the matrix in C-D-48H as compared to C-E-48H. In C-E-48H, corrosion products penetrated into the pores or air voids within the FRM coating. Also, corrosion layer in C-E-48H showed smaller gapping after drying and the first rim of corrosion products attached to the steel surface exhibited less concentration of oxygen as compared to that in C-D-48H. This is inferred from the less brightness in the corrosion rim for oxygen element mapping. The smaller gapping and less O<sub>2</sub> concentration in the corrosion layer of C-E-48H were attributed to the filling of corrosion products within the pores of the FRM layer and the resulting interfacial densification. Within corrosion layers, there were no remnants of Ca for C-E-48H. The lower content of CaO in the binder of FRM is believed to result in low CH at the interface, which caused less buffering action and higher corrosion susceptibility of steel in the concrete. This may be another reason that

C-E-0H experienced higher corrosion activity and mass loss as compared to C-D-0H. Under a similar mechanism, corrosion products filled up the pores created by the filter paper and caused no cracking in C-F-48H.





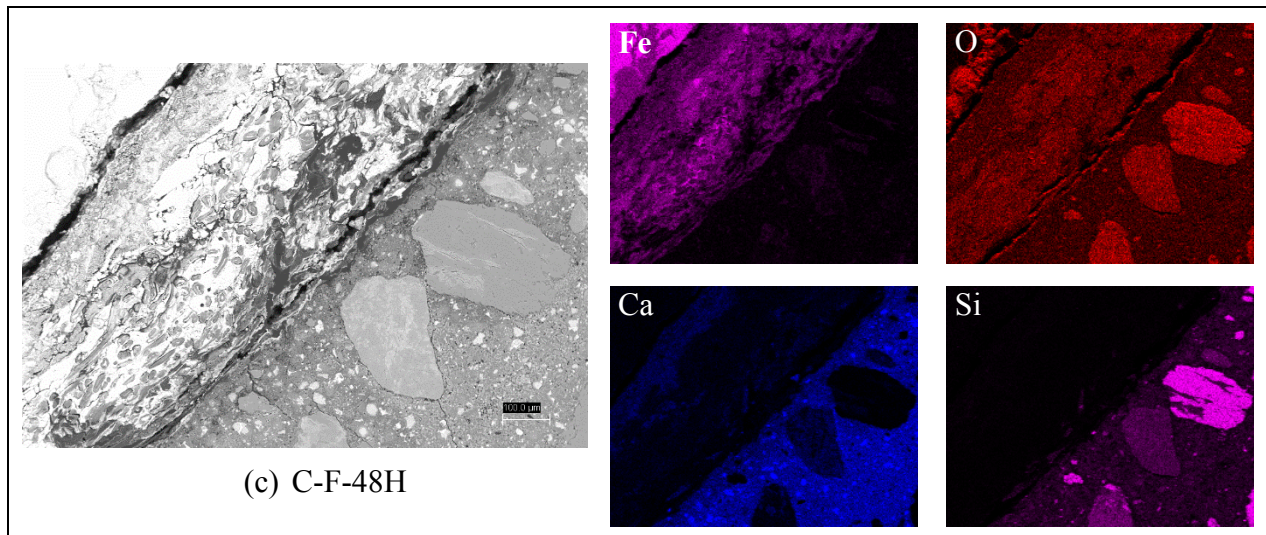


**Figure 6.15: BSE images and corresponding EDX element mapping for: (a) C-D-48H, (b) C-E-48H, and (c) C-F-48H**

## 6.5 Discussion

### 6.5.1 Corrosion of reinforcement in FRM

It is interesting to see if rebars in FRM show similar confinement and reduction in corrosion rates as compared to rebars with and without FRM coating in concrete. Samples with steel embedded in FRM free of NaCl were also subjected to 48 hours of applied current to study the corrosion of steel rebar in the mortar. Electrochemical measurements up to 98 days, gravimetric mass loss and SEM were conducted for the sample. The mass loss was found to be 8.6 g. This is slightly lower than the mass loss of 9.7 g found in C-E-48H, despite the fact that C-E-48H was left in the immersion for a shorter period of time (14 days) after the applied current regime. The absence of NaCl in the mixing water yet the presence of confinement provided by the FRM mortar may reduce the effectiveness of the applied current in FRM samples. The corrosion rates of the FRM sample annotated as E-48H, C-E-48H (up to 14 days only) and C-0S-48H (with no NaCl in the mixing water) from **Chapter 4** are given in **Fig. 6.16** for comparison. It is observed that the corrosion rates of E-48H sample were lower than those in C-E-48H during early electrochemical measurements but higher at later times. The lower early corrosion rates are attributed to confinement provided by fibers in FRM. The higher corrosion rates at later ages may be caused by poorer repassivation of the steel rebar and more extensive cracking of E-48H sample. Chemical analysis results of FRM powder as given in **Table 6.1** showed lower concentration of CaO as compared to that in cement. The smaller content of CaO would reduce the buffering capability of the matrix under acidification induced by accelerated corrosion, unlike C-E-48H sample where only a thin layer of FRM was applied over the steel surface. If the interfacial pore solution was of low pH, partial repassivation would not occur and the corrosion rates would increase when confinement by the polymer fibers relaxed with time.

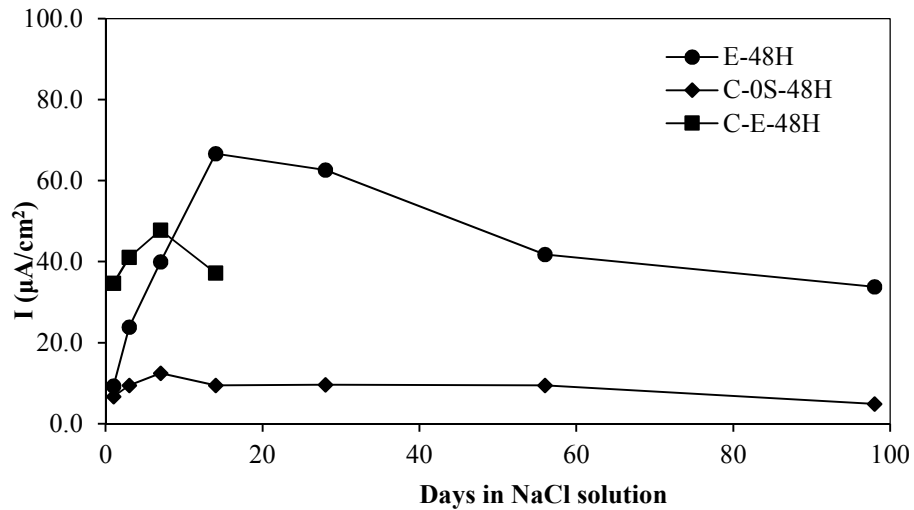


**Figure 6.16: Corrosion rates of rebar in FRM and plain concrete with 48 hours of applied current**

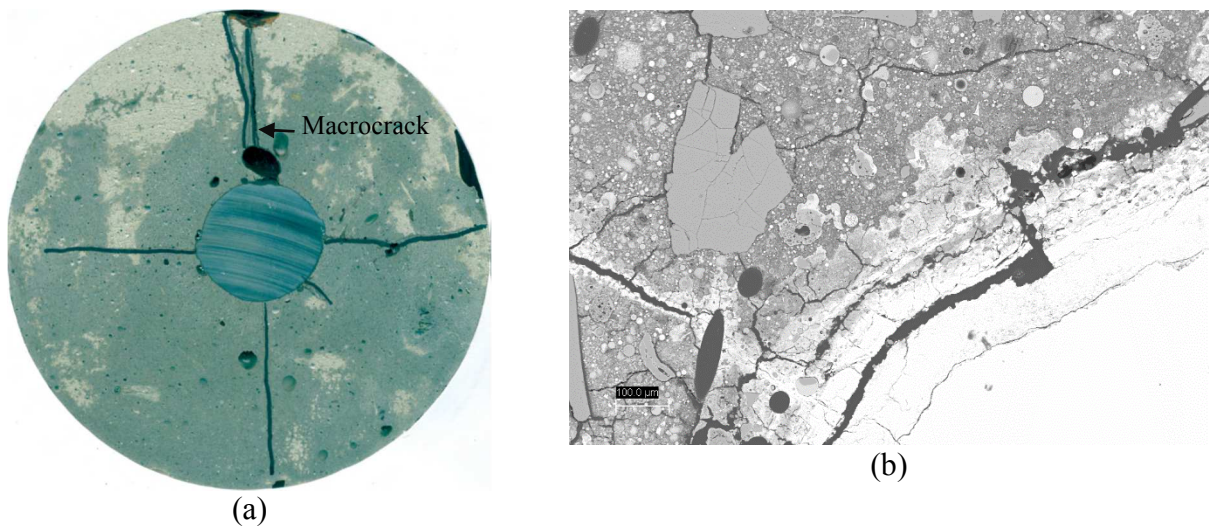


**Figure 6.17: (a) Crack pattern on a cut section of FRM sample, and (b) BSE micrograph showing crack and penetration of corrosion products into the matrix**

The more extensive cracking of E-48H sample as compared to C-E-48H was confirmed in **Fig. 6.17** where scanned surface of E-48H section and BSE image at the interfacial region are shown. The corrosion layer of E-48H appeared thicker and was attributed to the high porosity of the matrix. One of the cracks observed on the cut section was of macro-size. The use of only microfibers in E-48H means that the fibers are not effective in bridging such level of cracking. As a result, confinement by the matrix decreased with time. This led to loosening of the interface and leaching of corrosion products. A wider ridging in the corrosion layer after drying infers that corrosion layer in E-48H was less dense as compared to that in C-E-48H. This further reduced confinement yet increased more access of oxygen and moisture to the steel substrate, causing an increase in corrosion activity with time. The finding highlights the superior property of hybrid fibers in controlling corrosion cracking.

With a smaller mass loss as compared to C-E-48H, the more extensive cracking in E-48H was intriguing. It was postulated that this was caused by the formation of corrosion products of higher volume in the E sample. The higher permeability of E as compared to the surrounding matrix in C-E-48H means that iron ions formed during accelerated corrosion would be able to more freely react with  $\text{OH}^-$  from the cathode, to imbibe more moisture and as a result to expand more. The difference in corrosion mechanism for E (or FRM) and C-E with just FRM coating on the rebar is elaborated in **Fig. 6.18**. It is observed that due to its higher permeability, E sample allows for more  $\text{OH}^-$  generated at the cathode, moisture and  $\text{O}_2$  are able to reach the surface of the anodic steel. On the other hand, the less permeable concrete surrounding the rebar in C-E sample restricts the movement. The denser surrounding matrix may also better maintain the acidic condition at the interface of C-E sample, leading to its high initial corrosion rates. On a similar reasoning, the high mass loss, more expansive corrosion products and a lack of CH to provide buffering mechanism and to contribute to rebar passivation helps to explain the higher corrosion rates of E as compared to C-OS-48H (plain concrete).

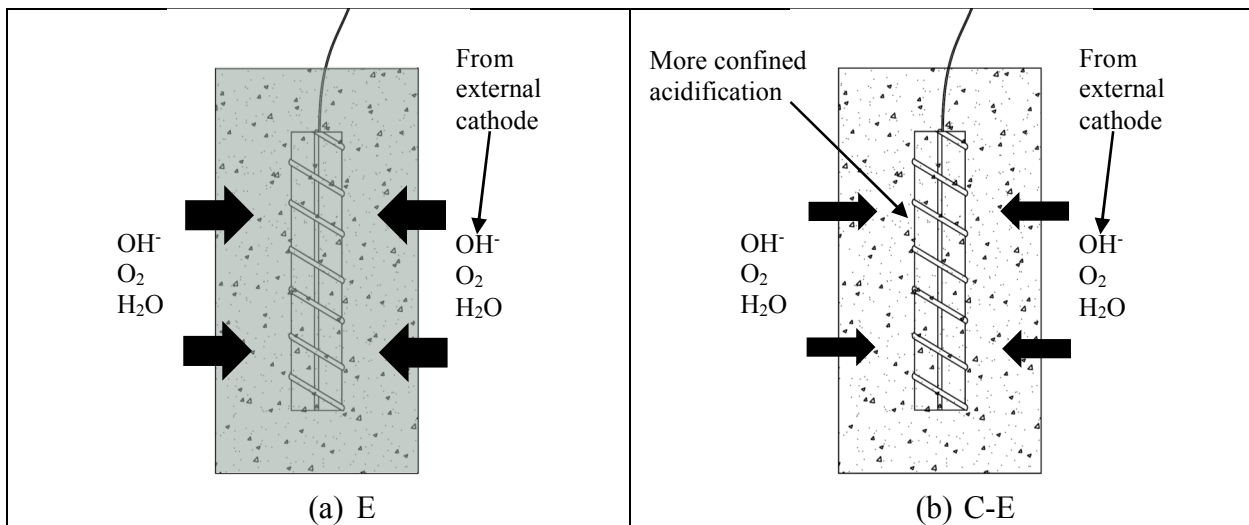


**Figure 6.18: Difference in accelerated corrosion mechanism in: (a) E sample and (b) C-E sample**

It was shown that because of its high tensile strain capacity and microcracking behaviors, engineered cementitious composite (ECC) reinforced with microfiber, similar to the FRM used in this study, significantly prolonged the corrosion propagation period while at the same time enhanced the ability to maintain the load capacity of the corroded beams (Sahmaran et al., 2008). It is unclear if the poor corrosion performance of FRM is attributed to low strain capacity and hence an absence of the multiple cracking behavior. Flexural tensile test results on 75 x 75 x 225 mm beams showed deflection hardening response for FRM as shown in **Fig. 6.19**. Tensile surfaces of the beams after testing shown in **Fig. 6.20** exhibit multiple crack distribution, although very limited. Together with a deflection hardening response as seen in the flexural test results, it is inferred the FRM has a good strain capacity and ductility. Hence, as compared to conventional concrete, the poor performance of FRM can only be attributed to a poor buffering action due to a limited amount of CaO in the binder and its high permeability which was confirmed in the results for permeability coefficients as shown in **Chapter 3** of the report. FRM had a gas permeability coefficient that was about 6 times higher than that for conventional concrete.



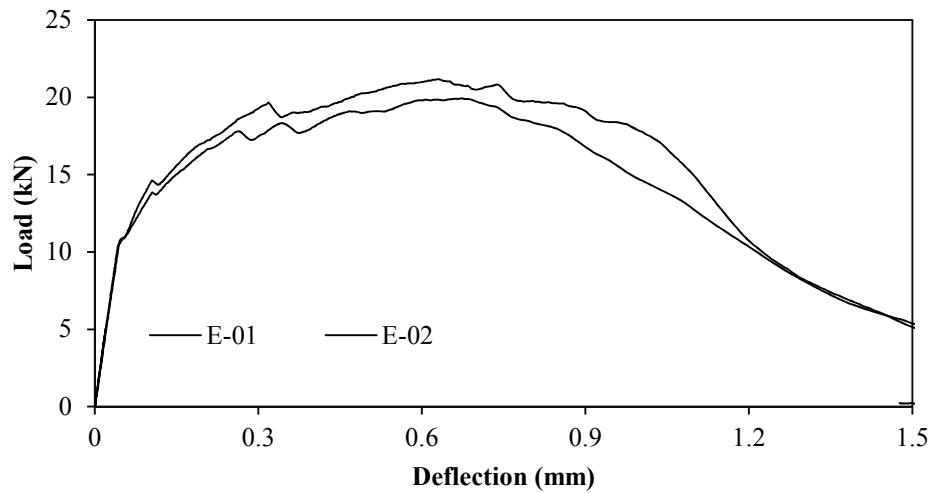


**Figure 6.19: Flexural responses of FRM at 56 days**

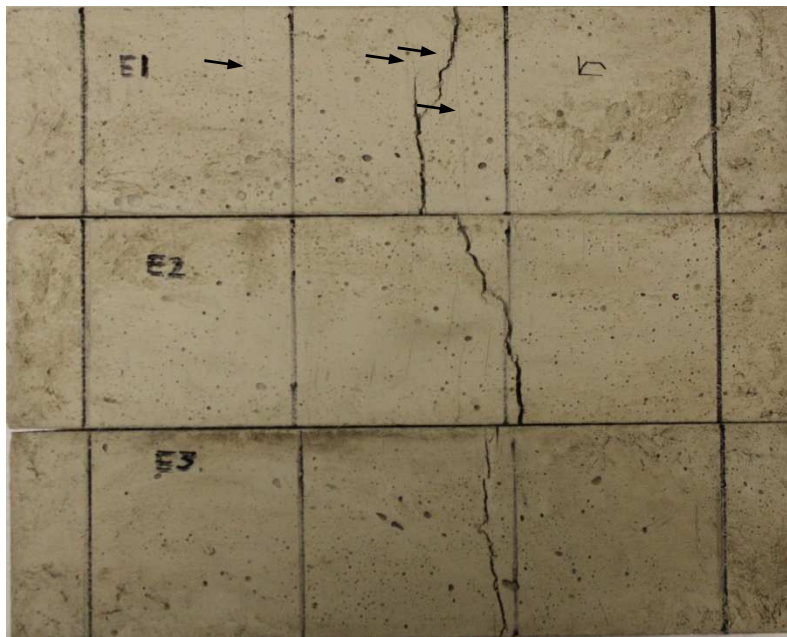


**Figure 6.20: Crack distribution of flexural FRM samples**

### **6.5.2 Influence of steel-concrete interface on corrosion**

The study showed that good steel-concrete quality interface is critical in limiting corrosion initiation. With 4% NaCl in the mixing water, it is expected that the passivity of steel in concrete was no longer stable and got destroyed. However, with no applied current, corrosion rates for steel in direct contact with concrete were found to be lower as compared to those found in the samples with interfaces modified by the porous mortar and filter paper. A dense interface restricts the access of oxygen, moisture, and migration of ions in and out of the anodic area. In addition, CH in intimate

contact with steel surface provides a buffering action against acidification and a sudden drop in pH value of concrete pore solution at the interface, leading to a slower dissolution of steel.

During corrosion propagation, as corrosion products accumulate with increasing duration of the applied current, tensile stress is induced on the surrounding concrete. For the same amount of corrosion products, the denser interface will experience a higher stress and as result is susceptible to more cracking damage. The more porous interface, on the other hand, is able to accommodate more corrosion products. This leads to an interfacial densification and a reduced corrosion activity, provided the surrounding matrix is able to withstand the corrosion-induced pressure and cracking. With respect to service life of reinforced concrete structures subjected to corrosion, a dense interface prolongs corrosion initiation stage but reduces corrosion propagation. In view that time from corrosion initiation to cracking (3 to 7 years as suggested by Weyers (1998)) is much shorter relative to the total service life the structure for plain concrete, a dense interface and dense surrounding matrix is predominant to structures' high durability and long service life in plain concrete. For deflection hardening fiber-reinforced concrete such as HyFRC, the propagation period will be considerably extended due to the formation of multiple cracks and less reduction in mechanical properties of the composite as proven in the previous chapters. With similar corrosion initiation performance as compared to plain concrete, HyFRC is expected to prolong the structural service life under corrosion consideration.

### **6.5.3 Gravimetric and theoretical mass losses**

A plot of theoretical mass losses against gravimetric mass losses for the set of samples presented in this study and other samples whose results were shown in the previous chapters is shown in **Fig. 6.21**. Two sets of data points were given: samples without NaCl in the mixing water and with 4% NaCl of binder weight in the mixing water. It is observed that at small theoretical mass losses (generally associated with no induced current to cause corrosion), the gravimetric mass losses were of several magnitudes higher than the theoretical mass losses. This is attributed to the etching of the base metal during the cleaning process. At higher mass losses, the gravimetric mass losses were usually lower than the theoretical mass losses for samples with no NaCl in the mixing water. This is caused by a reduced efficiency of the applied current in causing dissolution of steel. With no NaCl, steel is initially protected by the passive film. To generate an induced current of  $1 \text{ mA/cm}^2$ , the cell voltage will have to be high, leading to water oxidation and contribution to the net charge flowing into the circuit. However, the use of a valency of 2 in the Faraday's law may actually contribute to an overestimate of the theoretical mass losses in view that corrosion products may contain compounds with higher valency irons such as  $\text{Fe}(\text{OH})_3$  which is known to be one of the major corrosion products of steel in concrete.

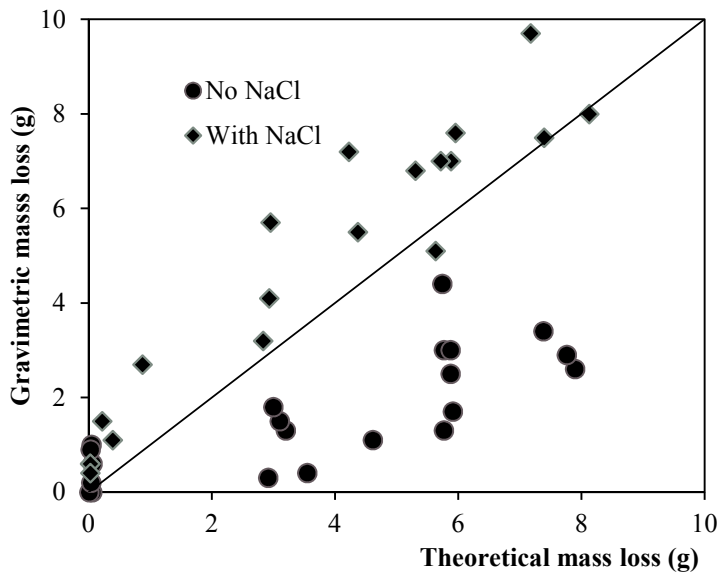


**Figure 6.21: Theoretical against gravimetric mass losses**

On the other hand, with NaCl in the mixing water, passive film may be destabilized at the start of the induced current. With little protection, it is easier to oxidize the anodic steel rebar. Also, an acidic environment at steel-concrete interface, supported by the abundant  $\text{Cl}^-$  in concrete, will also depress the local pH and will further induce dissolution the rebar, leading to a high corrosion activity and a higher value of gravimetric mass losses. Acidification at steel-concrete interface was discussed in **Chapter 4** of the report. Also, during the applied current regime, the corrosion rate  $i_{corr}$  was pushed from its value at the corrosion potential ( $E_{corr}$ ) to  $i_{oxid}$  which is the sum of  $i'_{corr}$  and  $i_{applied}$ , as illustrated in **Fig. 6.22**. In the annotations,  $i'_{corr}$  is the corrosion rate at a corrosion potential corresponding to a new cathodic curve under a new interfacial environment resulted from the impressed current, and  $i_{applied}$  is the applied current density ( $1 \text{ mA/cm}^2$ ). In Faraday's Law, the current magnitude used was  $i_{applied}$  and the  $i'_{corr}$  was not taken into account. As observed in the measured corrosion rates after the induced current period, the  $i'_{corr}$  could be significant especially under acidic condition and when concrete cracked. The unaccountability of  $i'_{corr}$  may contribute partly to an underestimation of the theoretical mass losses, leading to gravimetric mass losses that are higher than the theoretical mass losses.

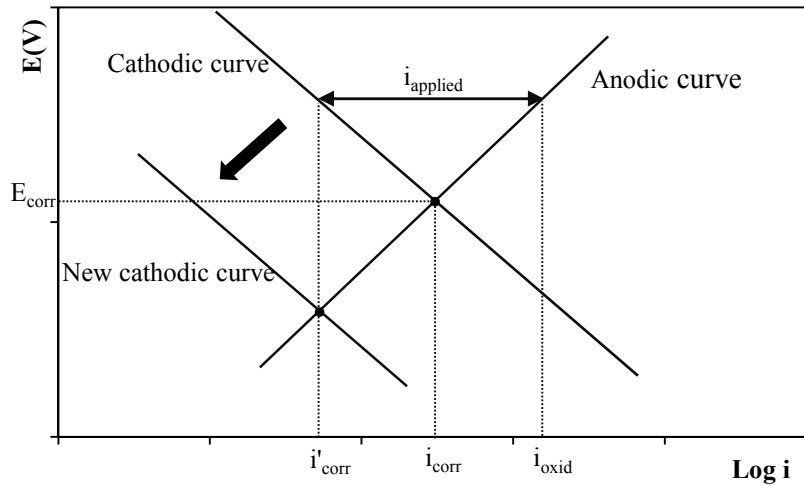


**Figure 6.22: Corrosion equilibrium under accelerated corrosion test**

### 6.5.4 Potential problems with accelerated corrosion test

Poursae & Hansson (2009) discussed the potential pitfalls with applied anodic current to accelerate corrosion tests. The problems include different chemical compositions of corrosion products as compared to natural corrosion, a more uniform corrosion over the whole surface of rebars as compared to discrete localized areas in natural corrosion, acidic condition at the interface and oxidation of water. These phenomena were observed in the current study as discussed above. A few additional abnormal phenomena were also observed for accelerated corrosion test with slag concrete. First, increasing slag replacement increased the amount of sulfate in the pore solution and reduced the available CH in paste, which may compromise the stability of the passive film and the buffering capacity of the matrix. This affected corrosion initiation and mass losses due to impressed current as discussed. Second, gravimetric mass losses were not consistent with theoretical mass loss due to water oxidation which leads to lower measured gravimetric mass losses and hence would offset a tendency to increase mass loss caused by interfacial acidification. In addition, the breaking down or migration of compounds in concrete could change the corrosion process. For instance, Ca was observed in corrosion layers of normal strength concrete. The modification of corrosion products could alter the physical and electrical properties of the corrosion layers, leading to a change in the dynamic of the accelerated corrosion test. Also, an unaccountability of internal equilibrium corrosion activity as depicted in **Fig. 6.22** during the applied current may lead to an underestimate of the anticipated induced mass losses.

To elaborate, the cell voltage drops between the anode and cathode to generate the  $1 \text{ mA/cm}^2$  induced current is shown in **Fig. 6.23**. The total cell voltage consists of a voltage drop between steel and concrete  $\Phi_{\text{Interface}}$ , a voltage drop across concrete  $\Phi_{\text{IR}}$ , and a voltage drop between concrete and the anode  $\Phi_{\text{Concrete-Cathode}}$ .  $\Phi_{\text{Interface}}$  is the driving voltage that caused corrosion of steel under the accelerated corrosion and is the total voltage drop between the anodic steel, passive film and electrolyte in the concrete. At the start of the applied current, the oxidization of steel under the cell voltage in samples with no added NaCl is postulated to contribute to a thickening of the existing passive film. If the film is of the same quality, a thicker film will lead to a higher  $\Phi_{\text{Interface}}$ . Although results are not provided here, this is evident from an increase in initial cell voltage in samples with

no added NaCl in the mixing water. A higher voltage drop will cause an oxidation of water, contributing to a net electron flow in the circuit and a reduction in the effectiveness of the applied current. With time under the presence of  $\text{Cl}^-$ , the film becomes less effective and breaks down from pitting under the induced current. Then,  $\Phi_{\text{Interface}}$  reduces in value and the anodic steel undergoes more active corrosion. Of another note, the voltage drop across concrete  $\Phi_{\text{IR}}$  increases with increasing resistance of concrete. Hence, lower W/B should increase  $\Phi_{\text{IR}}$  while addition of NaCl in the mix increases concrete conductivity and reduces  $\Phi_{\text{IR}}$ . Higher  $\Phi_{\text{IR}}$  may lead to migration of ions within the concrete and the breaking down of chemical compounds in concrete such as traces of metals. From the illustration, it is also observed that the voltage drop between concrete and the external cathode  $\Phi_{\text{IR}} + \Phi_{\text{Concrete-Cathode}}$  may also cause oxidation of compounds near concrete interface. This is critical for concrete reinforced with steel fibers in which the unprotected fibers near the interface can be readily oxidized. This was discussed in **Chapter 5**.

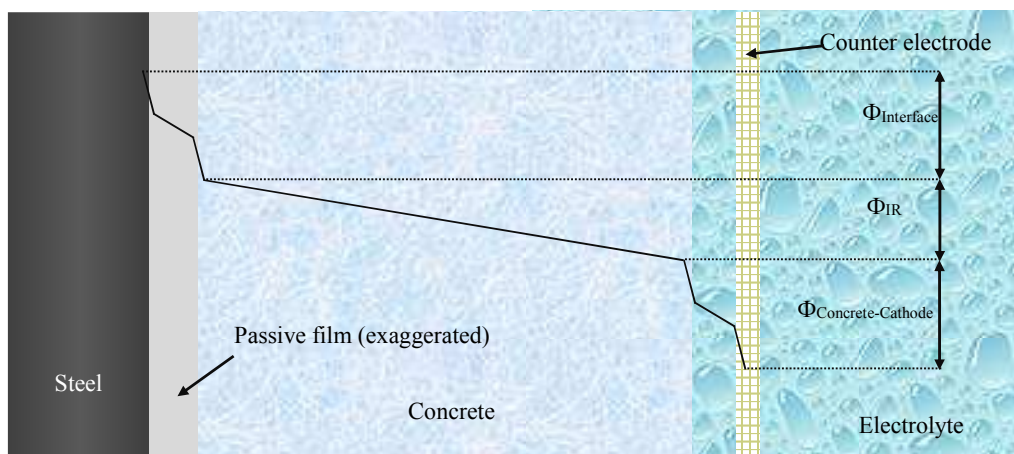


**Figure 6.23: Total cell voltage drops between the anode and cathode**

Despite the issues, the accelerated corrosion test and other tests performed in this study give us a better understanding of corrosion mechanisms and corrosion resistance of concrete with slag as cement replacement, fibers as discontinuous reinforcement and different interfacial conditions.

## 6.6 Conclusions

From the results and the discussions, the following can be concluded from this study:

- Adding 4% of NaCl by mass of the total binder into the mixing water effectively destabilized the passivity of steel rebar in concrete and increased the effectiveness of the applied current in which the gravimetric mass losses were found to be generally higher than the theoretical mass losses.
- Without any applied current, corrosion activity of the samples with more porous interfaces were higher as the higher porosity allowed for higher access of oxygen, moisture and migration of ions.
- When current was applied to cause corrosion, the corrosion rates were found to be in the order of C-F < C-E < C-D. This is attributable to a densification of corrosion products at the porous interfaces and a subsequent reduction in iron dissolution. Although working under a different mechanism, HyFRC with fibers providing confinement to corrosion

products would extend service life of structures and as a result reduce corrosion rates in the corrosion propagation stage. Under mechanical loading, HyFRC with its excellent crack resistance will also help to prolong corrosion initiation period (Blunt et al., 2015).

- In view that corrosion propagation stage is shorter relative to the service life of structures, a dense interface and a dense surrounding matrix is required to ensure a more durable structure.
- The gravimetric mass losses when NaCl is added into the mixing water tend to be higher than the theoretical mass losses. On the other hand, with no NaCl added, the gravimetric mass losses are less.

To summarize the finding from corrosion studies, it was observed in the previous chapters that HPC showed more corrosion cracking damage as compared to its HP-G-HyFRC counterpart. High volume slag in concrete caused an early onset of corrosion activity and cracking. Also, based on corrosion rates, HyFRC with W/B of 0.54 showed similar performance in corrosion initiation stage as compared to plain concrete but helped to delay corrosion propagation. In this chapter, it is shown that a denser interface led to reduced corrosion activity during corrosion initiation stage but caused more extensive damage for similar level of corrosion. This implies that well-consolidated HPC would help to prolong the corrosion initiation period of steel in concrete due to its dense microstructure and that the presence of fibers is necessary to extend the service life of structures during corrosion propagation stage. The findings further substantiate the results found in **Chapter 3**. This means that for an extended service life under corrosion consideration, a concrete composite with good workability, high strength and deflection hardening behavior similar to HP-G-HyFRC is a perfect candidate as it helps to prolong both the corrosion initiation and propagation stages. This confirms the legitimacy of HP-G-HyFRC for use in infrastructure systems for durability and extended service life. The next chapter will present an innovative application of HP-G-HyFRC for energy efficiency in buildings. Together with corrosion studies, this will complete our discussion on the sustainability performance of the composite.

# 7 Innovative double skin façade (DSF) with HP-G-HyFRC for sustainable and energy efficient buildings in the tropics

## Summary

Buildings are an integral part of our daily life. However, the building sector also presents a burden to the society. Globally, it accounts for about 40% of total primary energy use, most of which is spent on heating and cooling. In this study, a sustainable building envelope is proposed through an innovative double-skin façade (DSF) system constructed with a new concrete composite called high performance green hybrid fiber-reinforced concrete (HP-G-HyFRC). Flexural tests conducted on the proposed DSF system revealed that the DSF system, despite a 25% reduction in concrete usage, has a higher structural capacity and ductility as compared to a typical solid façade system generally adopted for public housing in Singapore. The thin application of HP-G-HyFRC in DSF is necessary to ensure deflection hardening behavior of the system. Energy modelling and life cycle assessment (LCA) of the two façade systems revealed that as compared to the existing solid façade system, the DSF system reduces the operational energy and CO<sub>2</sub> emission of buildings during their service life. Although the DSF system has a higher embodied energy and material cost, they can be recovered within the first few years of operation. From the results, it is imperative that LCA should be used in assessing the sustainability of new materials and systems.

**Keywords:** Double skin façade (DSF), HP-G-HyFRC, life cycle assessment, sustainability

## 7.1 Introduction

Buildings are an integral part of the broader civil infrastructure that ensures our welfare, livelihood, safety and security. However, the sector also represents a burden to the society. Buildings of today face a number of sustainability challenges from their inception to the end of their service life. Concrete the most widely used construction material has relatively high embodied energy due to the energy intensiveness of cement which is used as its main binder. Cement has an average carbon intensity of 900 kgCO<sub>2</sub>/tonne (Mahasenana et al., 2003). With an annual global production of blended and unblended cement of 3.6 billion tonnes in 2011 (van Oss, 2013) and an assumed clinker factor of 75%, cement industry accounts for about 7% of the total anthropogenic CO<sub>2</sub> emission estimated to be about 34.5 billion tonnes (Olivier et al., 2013). During their operational phase, buildings also consume a large amount of energy. According to the US Department of Energy report published in 2012, residential and commercial buildings in the US account for about 40% of total primary energy consumption (US Department of Energy, 2012a), of which 38% is spent on heating and cooling (US Department of Energy, 2012b). Other developed countries such as those in Asia experience similar problems. Buildings in Singapore account for more than 50% of its total electricity generated (Energy Market Authority, 2012). With continuing growth in population, increasing demand for building services and comfort levels and a rise in time spent



inside buildings, an upward trend in energy demand for buildings will continue in the future (Pérez-Lombard et al., 2008). In addition, the building sector is also responsible for 30% of global annual greenhouse gas emissions (UNEP Sustainable Buildings & Climate Initiative, 2009). In 2011, 40% of total carbon emissions in the US came from the building sector as compared to 33% in 1980 (US Department of Energy, 2012c).

Due to deterioration, buildings also need frequent repair and rehabilitation to maintain their aesthetic, functional and structural capabilities. This further contributes to operational cost and CO<sub>2</sub> emission. Maintenance can represent between 4% and 15% of the total emission for new office buildings during their service life (Junnila et al., 2006). The most significant emissions come from paints, steel, and insulation, each producing more than 20% of the total maintenance stage emission. In addition, natural hazards such as windstorms and earthquakes may cause unexpected damage to buildings. Wind-related disasters are the most costly natural disaster in the US (Grayson et al., 2013). The bulk of the loss during a typical windstorm is attributed to impact damage caused by wind-borne debris to the building envelopes. Hence, to reduce maintenance and to expand the concept of sustainability, both structural and non-structural components of buildings should also be designed to withstand various hazards. To the end of the building's life, these building components should be recycled for reuse. This will help to reduce annual construction and demolition waste which is estimated to be about 1 billion (Mehta, 2002). This represents about 5% of the total sand and rock used in global concrete production.

From a concrete materials engineering point of view, a more holistic approach is needed to provide a solution that encapsulates the overarching problem of embodied energy, operational energy, and recurring embodied energy resulted from maintenance (Cole & Kernan, 1996) or from rehabilitation due to natural hazard-induced damage. Any solutions would have to be justified and would require a quantification of embodied and operational energy parameters and their associated environmental impacts. To achieve this, life cycle assessment (LCA) which is defined as the compilation and evaluation of the inputs and outputs, and the potential environmental impacts of a product system throughout its life cycle (Guinée, 2002) should be implemented. LCA comprises four main components: (i) goal definition to describe the product, process or the activity, (ii) inventory analysis to identify and quantify energy, water, materials usage and environmental releases, (iii) impact assessment to assess the potential human and ecological effects, and (v) interpretation of the results for decision making (Scientific Applications International Corporation, 2006). Since its inception, LCA has been widely used as a decision tool for products and processes ranging from consumer products (Andersson et al., 1998; Finnveden & Ekvall, 1998) to infrastructure (Horvath & Hendrickson, 1998; Keoleian et al., 2005; Lepech & Li, 2006; Zhang et al., 2008).

By implementing LCA, this part of the study would address the issue of high life cycle energy in buildings from a new angle by utilizing the superior fresh and hardened properties of the newly developed concrete composite called high performance green hybrid fiber-reinforced concrete (HP-G-HyFRC) as presented in **Chapter 2**. The goal was to demonstrate how a high performance concrete composite can be used in buildings to enhance their sustainability. A design priority of reducing heating or cooling loads as recommended by McGregor et al. (2013) for zero-energy buildings was adopted. To achieve this, an innovative double skin façade (DSF) system is proposed to be used in place of a conventional solid façade system. DSF system consists of 30 mm air gap in between 45 mm HP-G-HyFRC skins connected by glass fiber reinforced polymer (GFRP) ribs to reduce thermal bridging. To improve constructability, no main reinforcing bar is used in the

system. Mechanical testing and life cycle assessment (LCA) were conducted to study the system's feasibility to replace a conventional reinforced concrete solid façade system of the same thickness. LCA was limited to embodied energy and operational energy while cost assessment was limited to materials cost and operational cost only. Operational energy was found with energy modelling of a typical functional unit set in Singapore's climate. This study exemplifies an integration of concrete materials engineering, structural engineering, green building design and life cycle consideration in order to find a more sustainable solution for the construction industry.

## 7.2 Double skin façade (DSF) system

### 7.2.1 The façade system

When concrete is used in building envelope, its thermal resistance or R-value can be increased by increasing the envelope thickness. However, increasing element thickness also increases materials usage and weight to the supporting structure. For enhanced thermal properties, insulation materials such as foams can be embedded in concrete. Air with its low thermal conductivity can also be used in place of foams. It was shown that insulation material thickness, insulation cost, heating cost can all be reduced by integrating air gap into an insulating building envelope of brick and plaster (Kurt, 2011).

The approach of using air gap to enhance insulating properties of building envelope leads to a façade system called double skin façade (DSF). DSF is defined as a traditional single façade doubled inside or outside by a second layer of façade which is termed skin (Loncour et al., 2004). With an additional layer, DSF reduces heat load that can be transferred into the building interiors. The heat reduction will also lower design capacity of and demand on heating ventilation and air-conditioning (HVAC) system (McGregor et al., 2013).

The development and mechanical properties of high performance green hybrid fiber-reinforced concrete (HP-G-HyFRC) were outlined in **Chapter 2**. With high strength and crack resistance, the composite has a great potential in building application for energy efficiency. In this study, it is proposed that the composite be used in double skin façade (DSF) in place of a solid reinforced concrete façade system that is generally adopted in public housing of Singapore. Singapore was adopted in the study because of the availability of data, design guidelines and its typical tropical climate. The tropical climate serves as a conservative assessment of the benefits of the proposed DSF system due to its relatively low temperature variation from the generally-accepted comfort temperature level of about 24 °C. The current solid façade system (SW) has a thickness of 120 mm. It is constructed with normal strength concrete and reinforced with 7 mm rebar in both directions of 25 mm clear cover. The proposed DSF consists of two 45 mm skins encapsulating 30 mm air gap, giving it the same thickness as that of the solid façade. For enhanced thermal resistance, the air gap can also be filled with insulating materials such as expanded polystyrene (EP). The two skins were constructed with HP-G-HyFRC and were connected by glass fiber-reinforced polymer (GFRP) rods. GFRP was used as a connector to reduce thermal bridging and to prevent corrosion problems that generally occur to exposed steel rebars. The side and cross-section configurations of the two façade systems are shown in **Fig. 7.1**. The elements shown have a length of 600 mm and a width of 200 mm. The width of the element was taken as 200 mm as it is the spacing of longitudinal reinforcing bars in the SW system. Hook provided at both ends of the rebar in the SW system was to ensure its full development length in the tensile face. The GFRP segments were arranged in a 45-degree truss system with a clear cover of 15 mm to ensure a

composite action of the two skins. This gave the truss half panel length of 90 mm. Due to the element length adopted, the length of the end truss half panels was reduced to 75 mm. The two façade elements were used in flexural tests for load-response comparison.

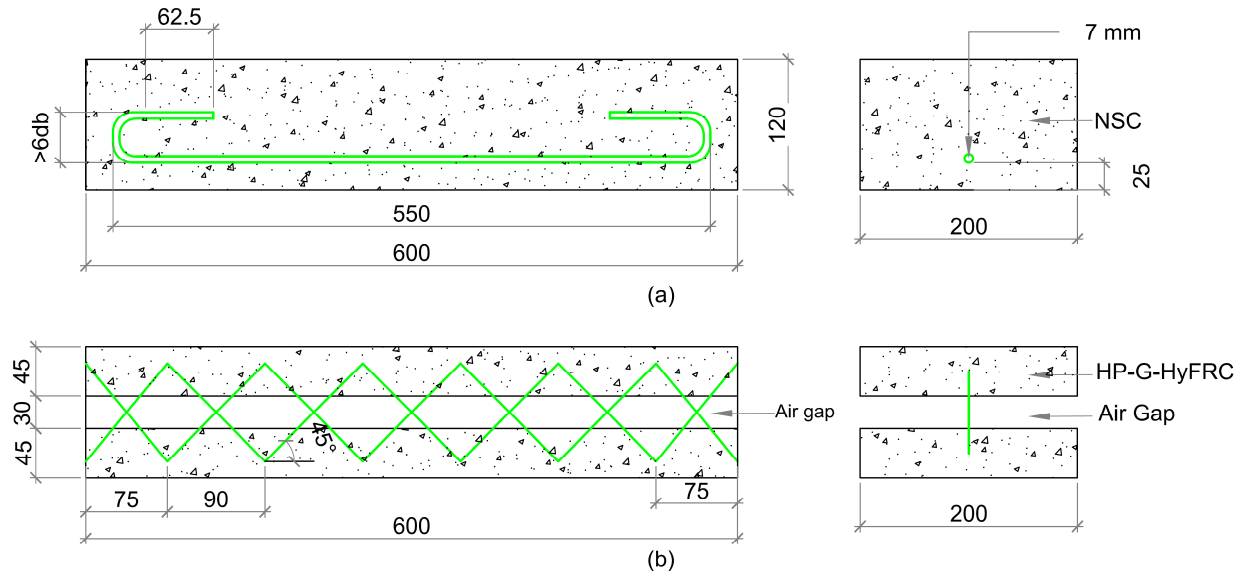


**Figure 7.1: Side and cross-section views of: (a) SW, and (b) DSF with HP-G-HyFRC skins**

### 7.2.2 Heat transfer

The mechanism that a DSF works to insulate a building is similar to that for a cavity wall or double glazed window except that most of incident heat is absorbed by the external skin instead of direct transmission as depicted in **Fig. 7.2**. The absorbed heat is then radiated and conducted toward the inner surface, leading to convection within the air gap and heat absorption by the interior skin. The inner skin then transfer heat to the interior through convection. Re-radiation of heat to the interior and back to the external skin direction also occurs. It is observed that by having an air gap and the second skin, additional heat transfer resistances are provided by convection in the air gap, heat absorption and re-radiation action of the interior skin. If the air cavity can be cooled possibly by a mechanical system, the heat transfer through convection will be less. As the skins are cooler, the amount of re-radiation from them will be also be reduced. It is well known that radiation is proportional the body temperature to the power of 4. However, conduction within the external concrete skin will be increased due to a higher temperature gradient between the external surface and the internal cooled surface. This means that high energy will be needed to cool the air gap. In this study, only static condition is considered.

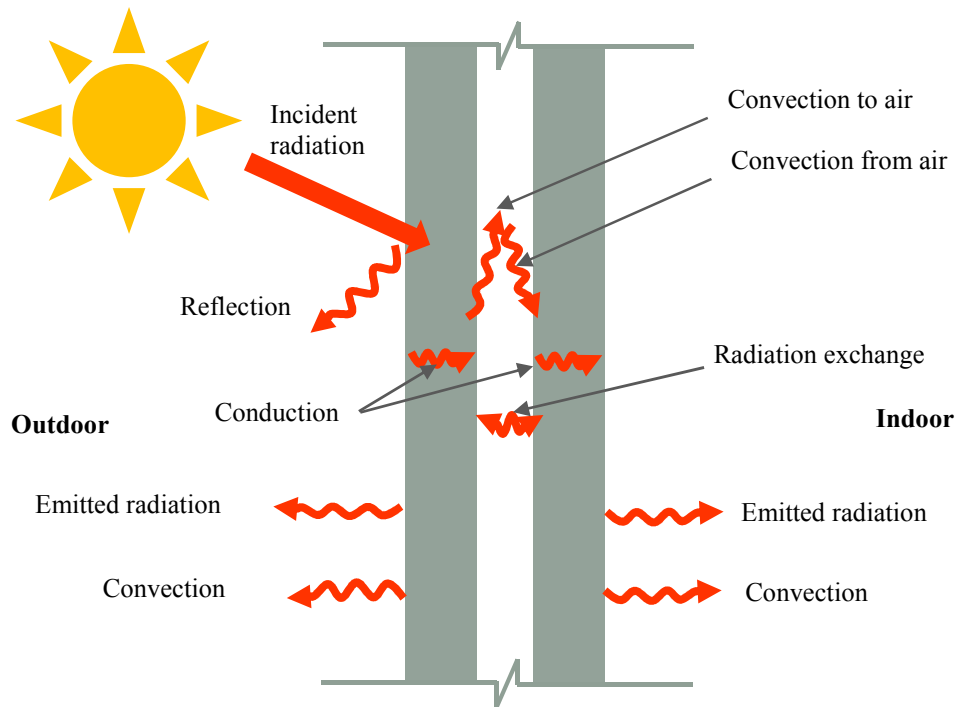


**Figure 7.2: Radiation heat transfer in concrete DSF**

### 7.2.3 Benefits

Besides the enhanced thermal resistance as discussed, the materials and configuration of DSF provide other benefits. HP-G-HyFRC used for the skins has high crack resistance to ensure distributed crack formation under loading and to prevent air leakage into and out of the building. HP-G-HyFRC was also shown to have high early strength of about 30 MPa after 3 days of moist curing. This allows for precast production feasibility of the elements. All of these benefits come with a 25% reduction in weight. Also, the damage resistance of the composites means that it is possible to reuse the façade elements for similar projects when the old buildings need to be demolished when their functionality is deemed obsolete. Lastly, it may be possible to run utilities in the gap between the two skins to save space in the building interiors.

### 7.2.4 Construction

The construction procedure of DSF in the laboratory is given in **Fig. 7.3**. In step 1, GFRP rod was cut to segments of 115 mm and arranged to form a diagonal truss system. Individual elements were held in place by a temporary horizontal rebar. Spacers made of steel rod were tied to both ends of the connector system to obtain 15 mm clear cover to the GFRP. The geometry and arrangement of the connector was to ensure a composite action of the two skins of the DSF. In step 2, the GFRP skeleton was placed into the mold and the casting of the first skin was conducted in step 3. The concrete was allowed to set overnight, after which the temporary tying rod was removed. In step 4, the first skin was demolded. After a new layer of concrete was poured into the mold, the first half of the DSF was inverted and sunk into the new fresh layer of concrete to form the complete DSF. This 2-casting procedure is believed to be applicable for factory production too. Commercially available spray foam may be used later on to fill the gap to improve the thermal resistance of the system.

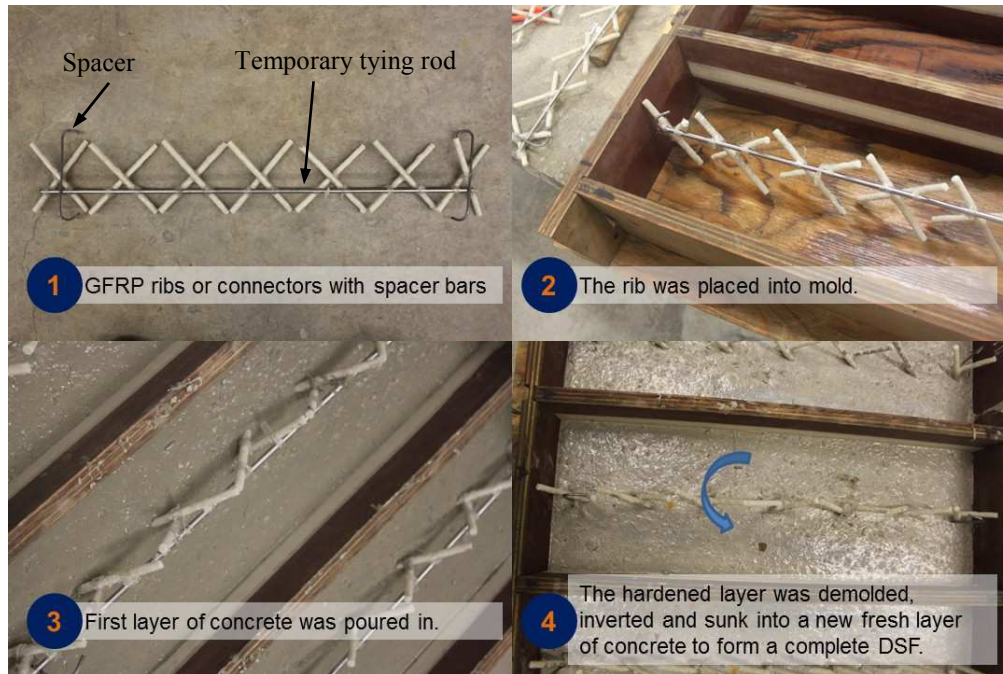


**Figure 7.3: Casting procedure for DSF**

## 7.3 Materials, methods and modelling

### 7.3.1 Concrete composites and reinforcement

Normal-strength concrete (NSC) with water-cement ratio of 0.54 was used to procure the solid façade system. A newly-developed concrete composite called HP-G-HyFRC was used to produce the skins of the DSF system. As detailed in **Chapter 2**, the composite has a water-binder ratio of 0.25. The total binder comprises 40% cement, 45% slag and 15% fly ash by mass. It also contains 1.5% of 30 mm hooked-end steel fibers and 0.15% of 8 mm PVA fibers as discontinuous reinforcement. Hybridization of fibers at the volume fractions allows for deflection hardening characteristic, which is defined as the ability of the composite to carry increasing load after the formation of the first crack. The behavior coincides with the formation of multiple microcracks before the peak load is reached. With the use of superplastizer (SP) and viscosity modifying agent (VMA), HP-G-HyFRC also exhibits high workability. No SP or VMA were used for NSC. The mix designs of the two composites are given in **Table 7.1**. The physical and mechanical properties of the 7 mm reinforcing bar and glass fiber reinforced polymer (GFRP) rods are also summarized in **Table 7.2**.

**Table 7.1: Concrete mix design (kg/m<sup>3</sup>)**

|  | NSC  | HP-G-HyFRC |
|--|------|------------|
| W/CM   | 0.54 | 0.25       |
| Water  | 229  | 163        |
| Cement                                       | 426  | 285        |
| Slag   | -    | 320        |
| Fly ash                                      | -    | 107        |
| Fine aggregate (FA)                          | 853  | 867        |
| Coarse aggregate (CA)                        | 776  | 504        |
| 30mm steel fibers                            | -    | 117        |
| 8mm PVA                                      | -    | 2          |
| Superplasticizer (SP) <sup>†</sup>           | -    | 10.5       |
| Viscosity modifying agent (VMA) <sup>†</sup> | -    | 6.5        |
| Slump flow diameter (mm)                     | -    | 565        |
| Slump height (mm)                            | -    | 44.5       |

<sup>†</sup> L/m<sup>3</sup>

**Table 7.2: Rebar properties**

| Rebar Designation | Rebar Material                 | Diameter (mm) | Tensile Strength (MPa) | Young Modulus (GPa) |
|-------------------|--------------------------------|---------------|------------------------|---------------------|
| 12L14 Rod-6MM     | Carbon steel                   | 7             | 449 (f <sub>y</sub> )  | 200                 |
| GFRP              | Glass fiber reinforced polymer | 6.25          | 896 (f <sub>u</sub> )  | 46                  |

### 7.3.2 Flexural test setup

The flexural capacities of the solid façade and DSF elements were obtained and compared through testing as suggested in ASTM 1609 (2010b) using load control testing machine with a servo-control closed-loop system. The flexural test apparatus consisted of a four-point bending jig with pin and roller-type supports. The sample clear span was set to 450 mm. Mid-span deflections were measured with two linear variable displacement transducers (LVDT) and the average deflection values were used in the load-deflection curves. For DSF elements, the LVDTs were attached to their upper skin. The experimental setup is shown in **Fig. 7.4**.

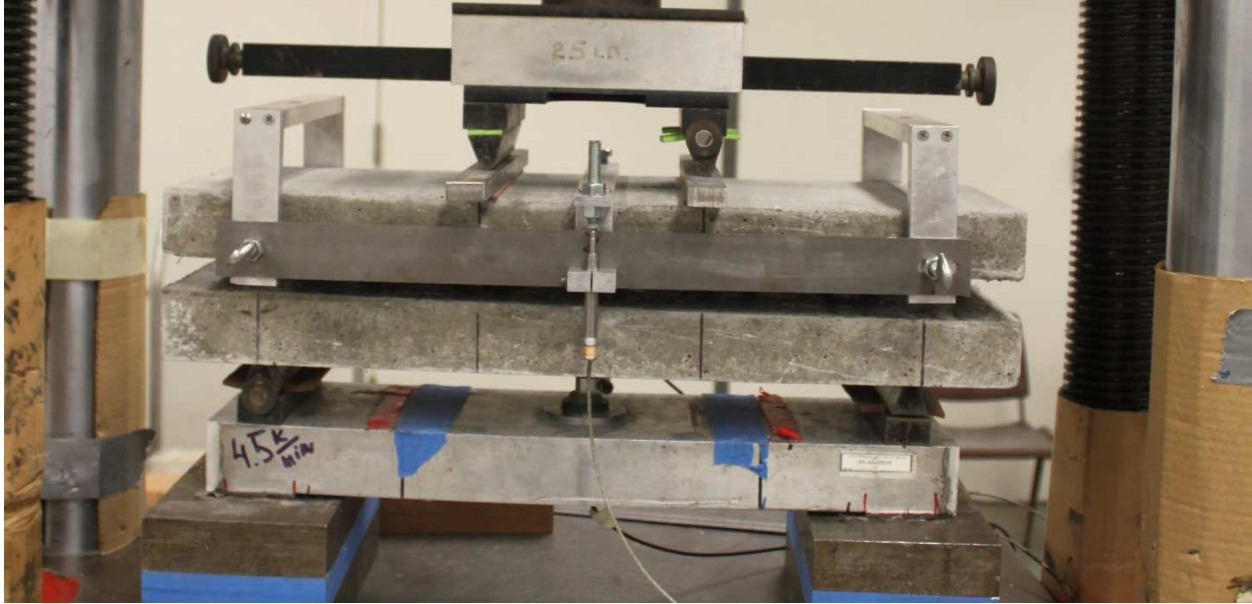


**Figure 7.4: Flexural test set up for DSF element**

### **7.3.3 Functional unit**

A typical bedroom of an apartment in a medium-rise building was chosen as the functional unit to study the operational energy requirements due to cooling with either of the façade systems. The unit has 2.8 m height, 4 m width and 4 m depth. Window area was assumed to cover 30% of the total façade area and to have a dimension of 2 x 1.68 m. This is within the range of average window to wall ratio (WWR) between 20% and 51% as commonly adopted in residential buildings in Singapore (Chua & Chou, 2010). The 30% WWR also represents maximum possible Green Mark points for landed properties in Singapore (Building and Construction Authority (BCA), 2010). The BCA Green Mark scheme rates buildings according to their energy efficiency, water efficiency, environmental protection, indoor air quality and other green and innovative features. The plan view of the room is given in **Fig. 7.5**. The window was assumed to have an overhang of 0.3 m. This value was taken from architectural guide drawings by the Housing & Development Board (HDB) of Singapore (2009). Aluminium frame of 57.2 mm was adopted to account for both window sill and sash. The façade was assumed to face east to obtain a medium exposure to solar radiation and solar heat gain. This ensures an average estimate of the energy saving provided by the DSF system. It was assumed that there was no net energy flow from the other 5 sides of the unit.



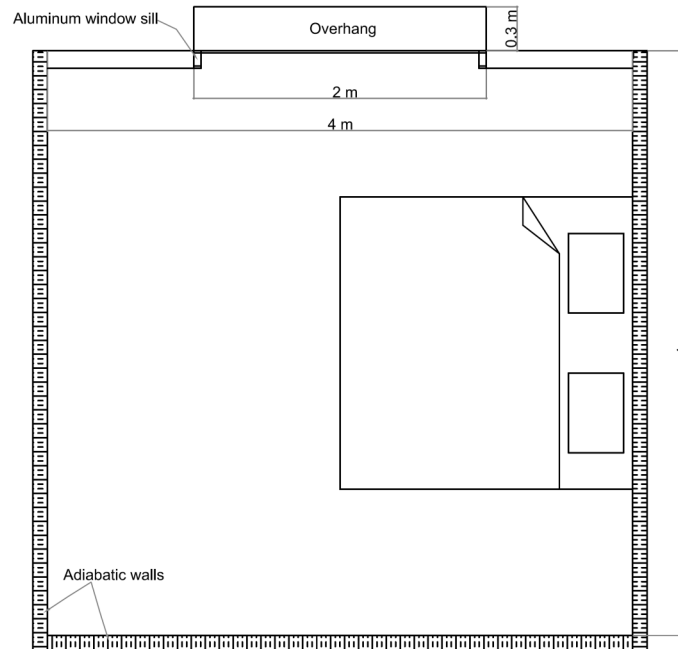


**Figure 7.5: Plan view of functional unit**

### 7.3.4 Embodied energy of concrete constituents

In inventory evaluation, process analysis, economic input-output (IO) analysis or hybrid technique may be used (Treloar, 1997). While process analysis involves the measurement of all direct and indirect energy requirements of the main process and its associated inputs within a truncated boundary, IO analysis maps out energy intensity or impacts between sectors of economy through output prices and a tariff or impact matrix. Although IO analysis has some limitations including price and technology changes (Bullard et al., 1978), all transaction activities within a country are generally recorded in the national IO table, meaning that IO-based inventory analysis is relatively fast and efficient (Suh & Huppes, 2005). Nevertheless, it does not provide accurate and detailed process information as compared to the data-intensive and time-consuming process-based analysis. Hybrid technique aims to answer the problem by combining data from IO and process analyses (Bullard et al., 1978). For instance, IO-derived total energy intensities may be applied to input materials typical of IO sectors to reduce time requirement and possible errors that may arise if implemented with process analysis. Despite their unique benefits and limitations, the three methods have made their way into building-related LCA. A prescriptive process-based method to estimate total energy use of buildings during manufacturing, transportation, construction, occupation and demolition was outlined by Adalberth (1997). A similar methodology has been adopted by various researchers to guide their decision-making on building systems and design strategies (Chen et al., 2001; Monahan & Powell, 2011; Scheuer et al., 2003; Thormark, 2002; Yohanis & Norton, 2002). Other researchers have also successfully implemented IO and hybrid techniques to study environmental impacts of buildings (Bilec, 2007; Chang et al., 2010; Fay et al., 2000; Kneifel, 2010; Ochoa et al., 2002; Sharrard et al., 2008; Suzuki & Oka, 1998; Treloar et al., 2001).

It was shown that the IO and process analyses for LCA give comparable results provided that the process models are proportional in nature (Hendrickson et al., 1998). Also, with deficiency of IO-

based LCA methods as mentioned, in this study, the environmental impacts of concrete production were calculated with a process-based GreenConcrete LCA tool developed by researchers in the CEE department at University of California, Berkeley (<http://greenconcrete.berkeley.edu>). The tool accounts for supply-chain environmental impacts of each process in the production of concrete and its materials. For example, the transportation section in concrete production calculates not only tailpipe emissions during transporting materials to concrete plant but also life-cycle phases of vehicles, infrastructure, and fuels. Analysis of environmental impacts - fuel use and CO<sub>2</sub> emission - are analyzed for all concrete constituent including cement, aggregates, chemical admixtures, and supplementary cementitious materials (SMCs) such as fly ash and granulated blast furnace slag (GBFS) and chemical admixtures.

The processes and technologies adopted for cement production are summarized in **Table 7.3**. The electricity mix for materials processing was based on the sources of the concrete constituents. Sand is assumed to come from Vietnam, gravel from Malaysia, and cement, slag and fly ash from China. The assumed contribution of energy sources for electricity generation of individual countries is given in **Table 7.4**. For transportation input, either Truck Class 8b or Water (Inland barge) was used as modes of transportation and the adopted travelled distances were given in **Table 7.5**. In some cases, GreenConcrete Tool provides only CO<sub>2eq</sub> for transportation. To find corresponding energy for land and water transportation, conversion factors of 15.0 MJ/kg CO<sub>2eq</sub> and 13.2MJ/kg CO<sub>2eq</sub>, respectively, were used. The values were based on mean energy and emission results of different modes of freight transportation in a study conducted by Nealer et al. (Nealer et al., 2012). Fuel for cement pyroprocessing was assumed to come from 100% coal (Lei et al., 2011).

**Table 7.3: Technologies adopted in processes of cement production**

| <b>Cement Production Phases</b>           | <b>Product of each Phase</b>           | <b>Technology</b>                             |
|---|--|---|
| Raw materials prehomogenization           | Raw Meal                               | Dry process raw storing, non-preblending      |
| Raw materials grinding                    | Ground Meal                            | Dry raw grinding, ball mill                   |
| Raw meal blending/<br>Homogenization      | Blended Meal                           | Raw meal homogenization, blending and storage |
| Pyroprocessing                            | Clinker                                | Preheat/precalciner kiln                      |
| Clinker cooling                           | Cooled Clinker                         | Reciprocating grate cooler (modern)           |
| Finish Milling/Grinding/Blending<br>w/ PC | Blended/Traditional<br>Portland Cement | Ball mill                                     |

**Table 7.4: Average contributions of energy source (%) by countries**

|                                       | Singapore<br>(Energy Market<br>Authority,<br>2012) | China<br>(EIA, 2014a) | Malaysia<br>(EIA, 2014b) | Vietnam<br>(EVN, 2013) |
|---------------------------------------|--|-----------------------|--------------------------|------------------------|
| Bituminous Coal                       | -  | 66                    | 41                       | 19                     |
| Natural Gas                           | 78   | 3                     | 46                       | 29                     |
| Residual (Heavy) Oil                  | -  | -                     | -                        | -                      |
| Distillate (Diesel or Light) fuel oil | 18.4   | 2                     | 5                        | 2                      |
| Petroleum Coke                        | -  | -                     | -                        | -                      |
| Nuclear (Uranium)                     | -  | 1                     | -                        | -                      |
| Hydro                                 | -  | 22                    | 7                        | 50                     |
| Biomass                               | 3.6  | 1                     | -                        | -                      |
| Geothermal                            | -  | -                     | -                        | -                      |
| Solar                                 | -  | 0.2                   | 0.5                      | -                      |
| Wind                                  | -  | 5                     | 0.5                      | -                      |

**Table 7.5: Transportation inputs**

|  | Distance<br>Travelled (km) | Mode of transportation      |
|--|----------------------------|-----------------------------|
| Cement Raw Materials to Cement Plant               | 1                          | Truck Class 8b (Model 2005) |
| Gypsum to Cement Plant                             | 200                        | Truck Class 8b (Model 2005) |
| Cement to Concrete Plant                           | 2650                       | Water (Inland barge)        |
| Fine Aggregates to Concrete Plant                  | 1000                       | Water (Inland barge)        |
| Coarse Aggregates to Concrete Plant                | 300                        | Water (Inland barge)        |
| Fly Ash to Concrete Plant                          | 2650                       | Water (Inland barge)        |
| Granulated Blast Furnace Slag to<br>Concrete Plant | 2650                       | Water (Inland barge)        |

### 7.3.5 Embodied energy of rebars, fibers and EP

The environmental impacts of reinforcing steel bars, steel fibers and PVA fibers were found through independent literature review. Life cycle inventories (LCI) for both steel fibers and rebar were obtained from data provided by the Steel Recycling Institute (Crawford, 2013). LCI is an accounting of resources, water, energy and emissions to and from nature for a product system. Rebar was assumed to be rolled on a hot rolling mill. Steel fibers were associated with wire rods whose section can be achieved through cold forming (drawing) of rolled steel products. Trimming of fibers and hook forming at fiber ends were assumed to contribute negligibly to overall energy consumption and CO<sub>2</sub> emission of the whole process and they were ignored in the calculation. The total recycling rate of 70% was assumed for both steel rebar and steel fibers.

The production process of PVA involves polymerization of poly vinyl acetate (PVAc) and the subsequent hydrolysis of PVAc to form PVA (Hallensleben, 2000). A similar type of fiber polypropylene (PP) is produced through polymerization of propylene either through liquid pool or gas phase polymerization (Plastic Europe, 2008). Due to a lack of data, LCI for PP was used for PVA using the results published in a report by Plastics Europe (Plastic Europe, 2008). In the report, information on the production fuel energy and resources was derived from data provided by *International Energy Agency*. Data for other ancillary operations and transportation were obtained from manufacturers, operators or publicly available LCI database. LCI for expanded polystyrene

(EP) was based on Inventory of Carbon and Energy (ICE) developed by Sustainable Energy Research Team at University of Bath (Jones & Hammond, 2011). EP was assumed to have a density of 30 kg/m<sup>3</sup>. Also, it is noted that environmental impact for transportation of the final products to construction sites was ignored in this study due to their insignificant contribution of the overall embodied energy of the products.

### 7.3.6 Operational energy modelling

COMFEN Version 5 (COMFEN5), a computer-based analytical tool developed by Lawrence Berkeley National Laboratory with EnergyPlus as the analytical engine (Mitchell et al., 2012), was used to evaluate energy consumption and CO<sub>2</sub> emissions required to maintain the room to a comfort temperature of 24 °C throughout the year. The adopted comfort temperature is within the prescriptive comfort temperature range between 22.3 °C and 24.7 °C as suggested by de Gear & Brager (1998). COMFEN5 is a user interface that synthesizes user's inputs such as climate data, physical makeup of the room, occupancy schedule and setpoint temperature. The data are then fed to EnergyPlus which in turn gives users the total energy and CO<sub>2</sub> emission required to keep the room to the setpoint temperature. Electricity intensity for CO<sub>2</sub> emission of 500 gCO<sub>2</sub>/kWh was adopted for Singapore (International Energy Agency, 2012). Occupancy level which controls the number of people in the space was set to the default values for a typical residential building and is summarized in **Table 7.6**. A maximum of 1 person was assumed to occupy the room at a certain time. Five analysis scenarios with different combinations of façade, glazing and insulation types (**Fig. 7.6**) were adopted for this study. Annotations used in the scenarios are SW for solid wall or façade, DSF for double skin façade, SG for single glazing, DG for double glazing, and EP for expanded polystyrene. The properties of glazing were varied to study their relative influence and importance on energy consumption and CO<sub>2</sub> emission relative to the wall system. In the modelling, a focus was on cooling energy only and hence no equipment load was applied.

**Table 7.6: Occupancy level for COMFEN analysis in residential buildings**

| <b>Time</b> | <b>Occupancy level (All days)</b> |
|-------------|-----------------------------------|
| 24:00-7:00  | 1                                 |
| 7:00-8:00   | 0.85                              |
| 8:00-9:00   | 0.39                              |
| 8:00-16:00  | 0.25                              |
| 16:00-17:00 | 0.3                               |
| 17:00-18:00 | 0.52                              |
| 18:00-21:00 | 0.87                              |
| 21:00-24:00 | 1                                 |

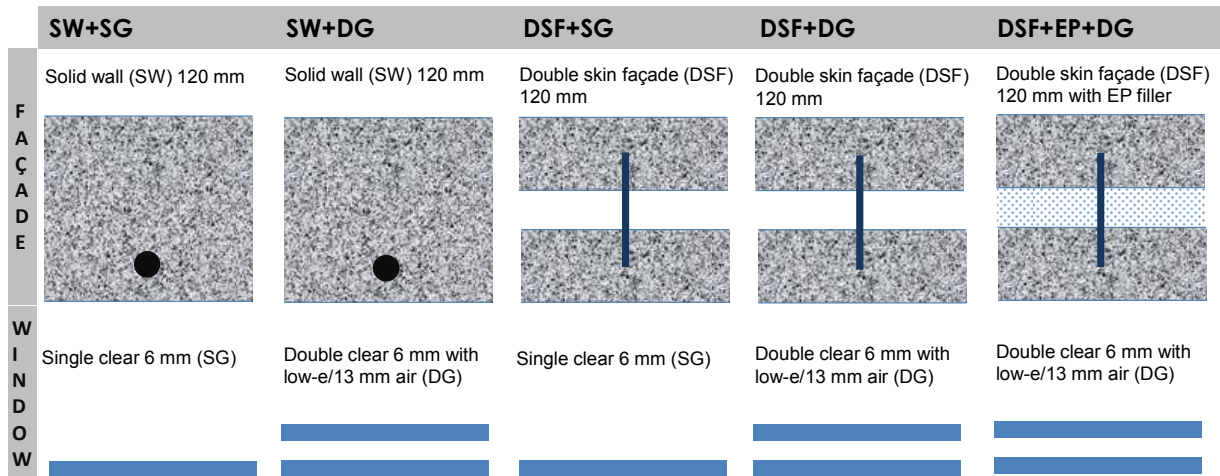


**Figure 7.6: Analysis scenarios for energy modelling**

The weather file for Singapore was obtained from [eere.energy.gov](http://eere.energy.gov). Only one weather file is available for Singapore and was chosen for this study. Analysis of the weather file showed that the weather station was located near Changi International Airport. As Singapore is a small country, the weather station is representative of its general weather pattern. Average and high/low monthly dry-bulb temperatures are depicted in **Fig. 7.7**. Singapore climate is classified as tropical rainforest climate with no true distinct seasons. The climate is characterized by a uniform temperature and high humidity. The average diurnal temperature ranges between 21.6 °C and 33.5 °C. The average annual temperature is about 27.5 °C. At high relative humidity (RH) of about 80%, it is expected that mechanical cooling will be required at the temperature level for thermal comfort of building occupants.

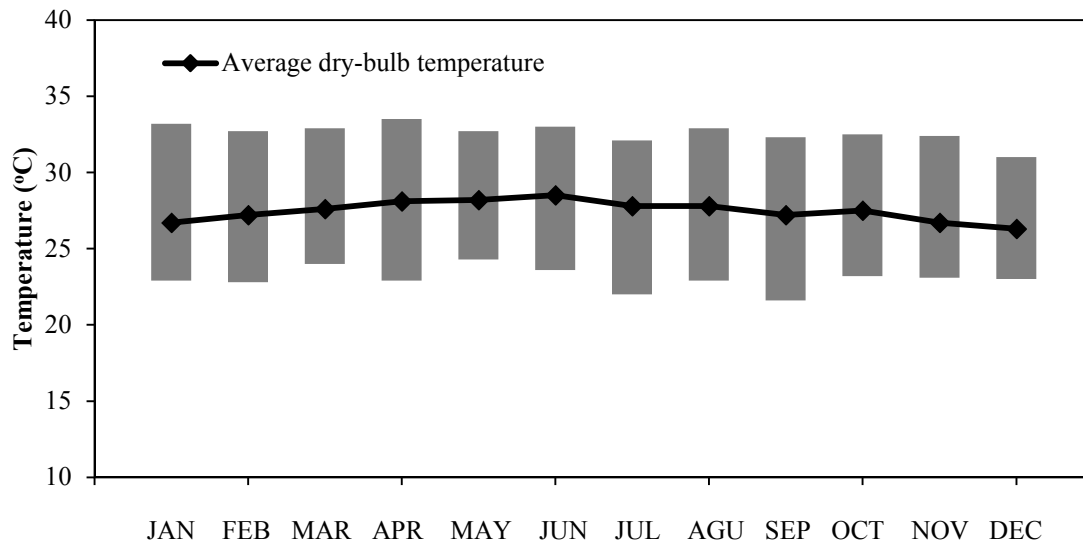


**Figure 7.7: Annual temperatures**

## 7.4 Results

### 7.4.1 Mechanical properties of façade systems

The compression strengths of 28-day moist-cured 100 x 200 mm cylinders were found to be 45 MPa for plain concrete and 84 MPa for HP-G-HyFRC. The flexural response of the solid and DSF façade elements are given in **Fig. 7.8**. The specimens were loaded up to a displacement of  $L/150$  or 3 mm. It is observed that after the matrix cracked, the load carrying capacity of the solid façade suddenly dropped due to its under-reinforcement. This drop also marked the formation of a dominant macrocrack at the bottom face of the system. On the other hand, load carrying capacity of DSF elements gradually increased upon the first crack which was initiated at the end of the elastic branch of the load-deflection curves. Their ultimate loads and ductility were higher than the values for the solid façades. The enhanced structural capacity of DSF is critical during transportation and installation. This ensures that the DSF can be readily used in place of the solid façade system. Also, the system may be used as structural components to take both vertical and horizontal loads in low-rise buildings. The toughness ratio for DSF over SW up to the  $L/150$  displacement (3 mm) was found to be 2. This means that DSF has a higher energy absorption capacity as compared to the solid façade system and this behavior is beneficial for buildings in regions prone to windstorms and impact loadings.

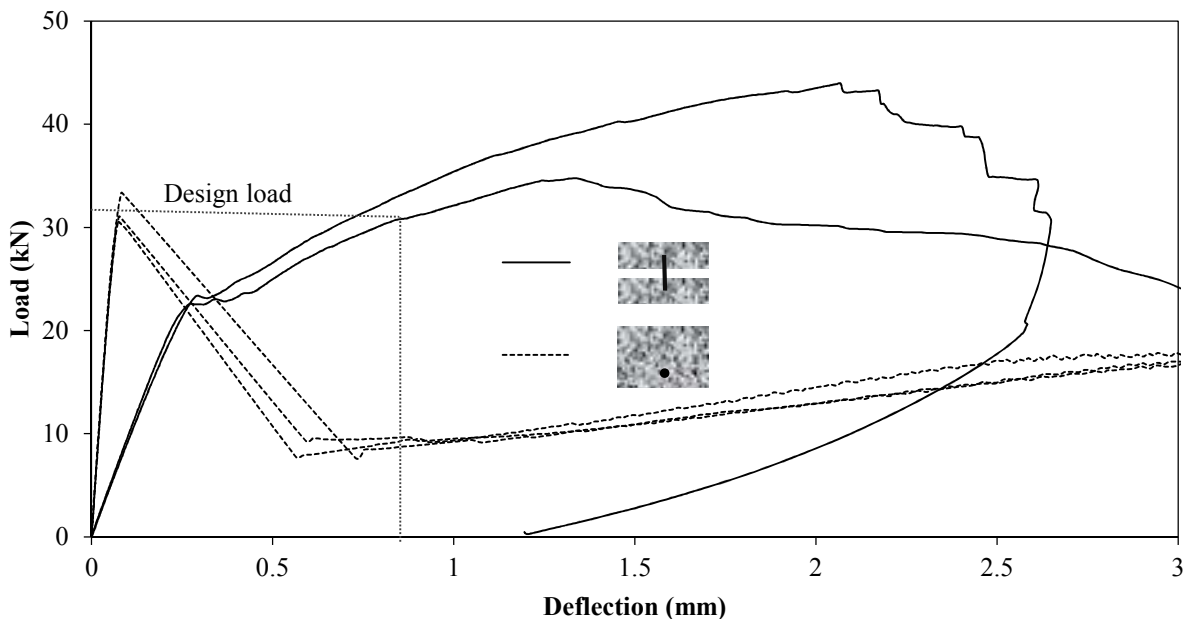


**Figure 7.8: Flexural test results for solid façade, and HP-G-HyFRC DSF**

It is observed that DSF failed by either tensile failure of concrete or crushing of GFRP as depicted in **Fig. 7.9** which explains the variability of the flexural responses of the DSF elements as given in **Fig. 7.8**. DSF elements that failed prior to reaching the 3 mm limit were caused by crushing of the GFRP connector. Due to its brittle failure mode, the crushing of the GFRP connector led to a lower ultimate deformation. Also, no pull out failure of GFRP bar was observed in all DSF elements. This is attributable to the coating of GFRP with sand and epoxy, resulting in an improved

mechanical bond between the matrix and the GFRP interface. Generally, multiple discrete microcracks were observed over the tensile face of the DSF system (Fig. 7.10). Besides enhancement to the flexural response, the formation of discrete microcracks is beneficial for insulation as they limit air leakage between the interior and exterior of the building.

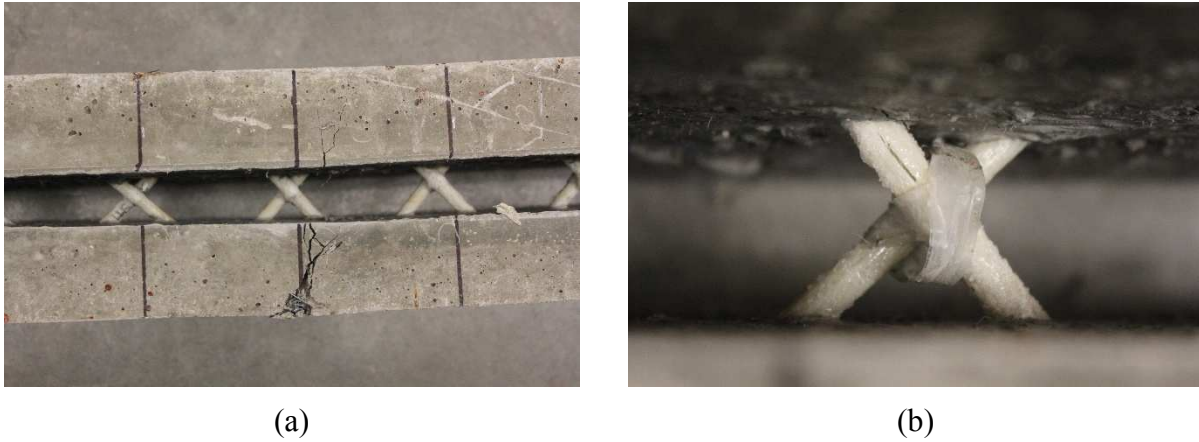


**Figure 7.9: Failure modes of DSF: (a) GHP-G-HyFRC tensile failure, and (b) crushing of GFRP bar**

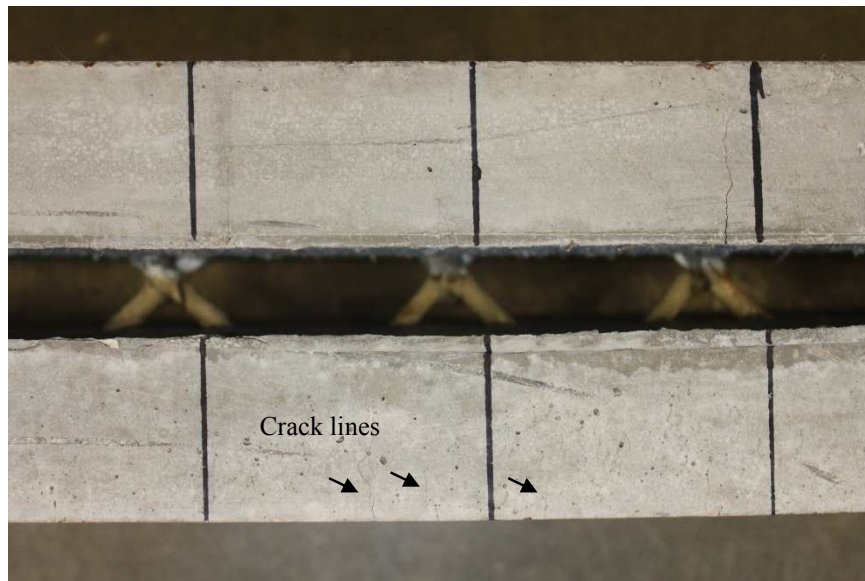


**Figure 7.10: Multiple cracks on the bottom face of DSF**

The deformation at maximum load of DSF elements were several times higher than those of the solid façade. It was concerned that the larger deformation may cause damage to elements that are mounted onto the DSF such as window panels. A preliminary assessment was conducted by comparing the deformation at design load to the deformation limit as prescribed by ACI 318 building code (ACI Committee, 2005). The design load was taken as the ultimate load of the solid wall elements. For floor construction supporting or attached to nonstructural elements likely to be damaged by large deflections, that part of the total deflection occurring after attachment of nonstructural elements shall not exceed the clear span divided by a factor of 480, which is equivalent to 0.94 mm for a clear span of 450 mm. The criteria, although conservative for walls,



were applied to the façade systems. At a design load of 32 kN, the corresponding deformation was found to be 0.85 mm. This is less than the allowable limit and hence it can be concluded that DSF will not cause damage to non-structural attachment in the short term. As the EP filler has negligible structural strength, the results observed here can also be conservatively applied to the case of DSF with EP as a filler material.

#### 7.4.2 Embodied energy of concrete constituents and concrete mixes

**Table 7.7** summarizes the results for embodied energy and CO<sub>2eq</sub> (calculated over 100 years) for concrete constituents per 1000 kg and the two concrete mixes per cubic meter. Due to a derivation from waste materials and the resulting fewer number of production processes, slag and fly ash were found to have lower embodied energy and to produce less CO<sub>2eq</sub> as compared to cement. Energy and CO<sub>2eq</sub> for water, SP and VMA were negligible and were set to zero. Energy and CO<sub>2eq</sub> for GFRP were taken to be the same as the value applied for PVA fibers. As compared to steel fibers, PVA fibers showed much higher embodied energy. This is attributed to a high feedstock energy of PVA fibers. Feedstock energy represents the embedded energy of hydrocarbon chains used to make the polymer products. However, as carbons are locked in the final products, carbon emission for PVA fibers was not remarkably higher than the value for steel fibers. EP had the highest energy and CO<sub>2</sub> intensities per 1000 kg although its contribution to the overall embodied energy and CO<sub>2</sub> of the DSF systems are expected to be relatively small due to its low density (30 kg/m<sup>3</sup>) and relatively low volume required for the DSF system.

The results for concrete mixes showed that HP-G-HyFRC is more energy and CO<sub>2eq</sub> intensive to produce per cubic meter as compared to NSC mix. It is also noted that in HP-G-HyFRC, the most energy and CO<sub>2</sub>-intensive constituents per unit volume were cement and fiber reinforcement. Hence, an efficient use of the composite requires using less of the composite for the same purpose. DSF system in place of the solid wall system where the material volume is reduced by 25% is an example. It is also interesting to note that an increase in CO<sub>2eq</sub> of HP-G-HyFRC is not proportional to the increase in energy as compared to that in NSC. This is attributed to the relatively clean energy used in the production of steel and PVA fibers.

**Table 7.7: Embodied energy and carbon emission of concrete constituents, rebar, EP (per 1000 kg), and concrete mixes (per m<sup>3</sup>)**

| Items             | Energy (MJ) | CO <sub>2eq</sub> (kg) |
|-------------------|-------------|------------------------|
| Cement            | 5084        | 1045                   |
| Slag              | 1825        | 126                    |
| Fly ash           | 1075        | 71                     |
| Fine Aggregates   | 265         | 20                     |
| Coarse Aggregates | 125         | 20                     |
| Water/SP/VMA      | 0           | 0                      |
| Rebar             | 16395       | 1241                   |
| Steel fibers      | 18032       | 1520                   |
| PVA fibers/GFRP   | 73370       | 2000                   |
| EP                | 88600       | 3290                   |
| NSC mix           | 2487        | 468                    |
| HP-G-HyFRC mix    | 4689        | 549                    |

**Table 7.8** gives materials quantities, embodied energies and CO<sub>2eq</sub> emissions required to produce the 3 wall systems implemented in this study. It is observed that although the concrete volume for DSF was 25% less than that used in SW, its embodied energy was about 38% greater. The higher embodied energy is attributed to the higher amount of binder and the presence of fibers in HP-G-HyFRC used in the DSF. For 1 m<sup>3</sup> of concrete mix, HP-G-HyFRC contains 712 kg of binder, higher than 426 kg used in NSC. Also, as shown in **Table 7.7**, fibers as discontinuous reinforcement in HP-G-HyFRC are energy-intensive to produce as compared to other constituents of concrete. They were found to be about 3.5 times more energy intensive as compared to cement. Nevertheless, CO<sub>2eq</sub> of DSF is about 16% less than that in SW. This is attributed to the smaller amount of materials used in DSF and the lower CO<sub>2</sub> intensities of slag and fly ash which were used as cement replacement in HP-G-HyFRC. As compared to DSF with air gap, DSF with EP as a filler material increased the embodied energy by 16% and embodied CO<sub>2eq</sub> by 6%.

**Table 7.8: Materials, embodied energy and carbon emission for SW, DSF, and DSF+EP**

| Items  | SW   | DSF  | DSF+EP |
|--|------|------|--------|
| Concrete (m <sup>3</sup> )                         | 0.94 | 0.71 | 0.71   |
| Steel rebar (kg)                                   | 23.5 | -    | -      |
| GFRP rebar (kg)                                    | -    | 6.1  | 6.1    |
| EP (kg)  | -    | -    | 7.06   |
| Energy (MJ)  | 2726 | 3758 | 4383   |
| CO <sub>2eq</sub> (kg)                             | 470  | 395  | 418    |
| Energy/floor area (MJ/m <sup>2</sup> )             | 170  | 235  | 274    |
| CO <sub>2eq</sub> /floor area (kg/m <sup>2</sup> ) | 29.4 | 24.7 | 26.2   |

### 7.4.3 Operational energy modeling results

The heat transfer coefficients (U-factors) for wall components as calculated from a glazing analysis tool integrated in COMFEN5 are reported in **Table 7.9**. By introducing the air gap, the U-factor was reduced by almost half. Similarly, by changing SG to DG, the U-factor for the glazing systems was reduced by 53%. It is also observed that the U-factor for the SG is higher than that for the solid façade (SW). This means that windows provides less resistance to heat inflow into the building. On the other hand, DG has a similar U-factor to that of DSF. From the results, it is expected that both wall and window systems with enhanced thermal properties are critical to the heat transfer and energy performance of the building. In the case of DSF, using EP as an insulation layer greatly reduced the heat transfer of the system. The U-factor was reduced by almost 3 times in the DSF+EP as compared to that in DSF.

**Table 7.9: U-factors for wall components (w/m<sup>2</sup>k)**

| SW   | DSF  | DSF+EP | SG   | DG   |
|------|------|--------|------|------|
| 4.73 | 2.66 | 0.97   | 5.82 | 2.69 |

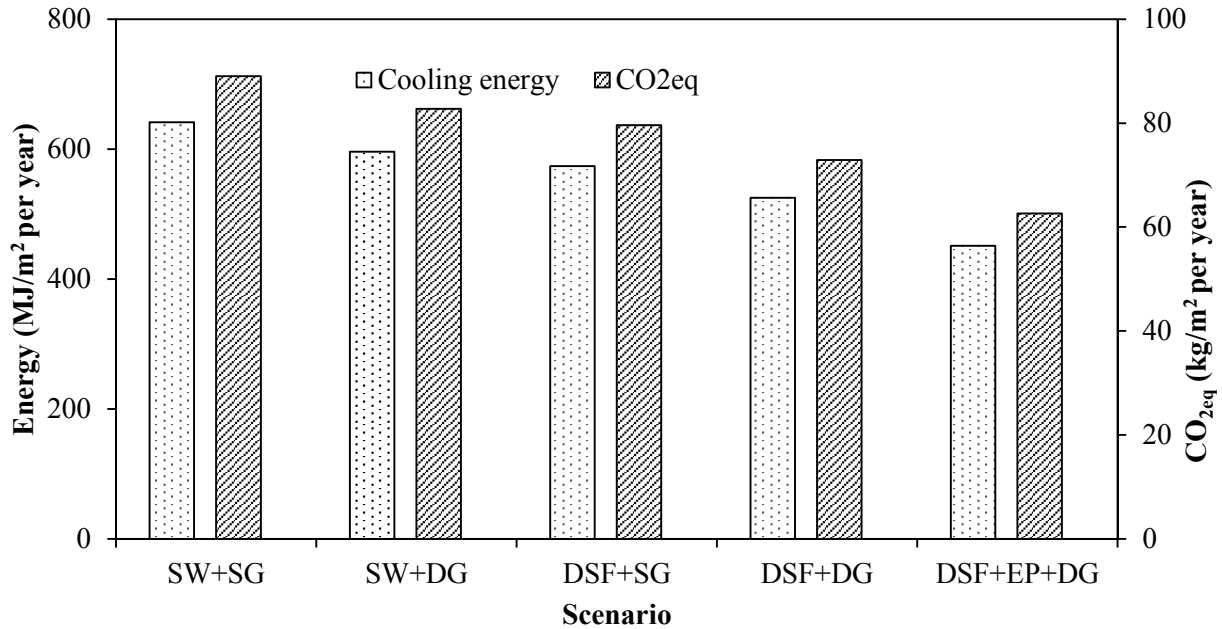


**Figure 7.11: Energy and CO<sub>2</sub> emission for different scenarios**

Operational energy and CO<sub>2</sub>eq results from COMFEN5 modelling for the 5 scenarios are given in **Fig. 7.11**. The values were normalized by the total floor area. The cooling energy consumption of 600 MJ/m<sup>2</sup> per year is in the range for typical cooling energy applicable to residential buildings in developed nations (Ürge-Vorsatz et al., 2015). It is also observed that there was a reduction in energy consumption of 7% by changing SG to DG (maintaining SW) and 10.6% by changing SW to DSF (maintaining SG). The results show that increasing thermal resistance of either the glazing or the wall system was effective in reducing energy consumption. Also, improving thermal resistance of wall was more effective due to a relatively low window-wall ratio (WWR) of 0.3 as adopted in the functional unit. A combined use of DSF and DG helped to save energy by 18% from the base case (SW+SG). The saving is equivalent to the sum of energy savings from individually improving thermal resistance of wall and glazing. Filling the air gap in DSF with EP further reduced the operational energy. From DSF+DG to DSF+EP+DG, the energy was further reduced by 14%. A similar trend was also observed for CO<sub>2</sub> emission. It is noted that lighting and equipment load were disregarded in this analysis. This allows for a comparison of cooling load only and hence a more meaningful comparison of the effectiveness of the façade systems.

#### 7.4.4 Life cycle cost analysis

For life cycle cost analysis, unit costs of concrete constituents, rebars and EP were obtained from various trade websites and email communications with suppliers and are listed in **Table 7.10**. It is observed that as compared to conventional concrete, HP-G-HyFRC has a number of high-cost constituents including steel fibers, PVA fibers, SP and VMA. With these, the cost per cubic meter of HP-G-HyFRC was calculated to be \$433 as compared to just \$70.8 for NSC. With high materials costs, the price for the DSF of the adopted functional unit was calculated to be \$425 as compared to \$93 for the conventional solid façade. This makes DSF about 4.5 times more expensive than the

SW system in terms of materials cost. It is noted that the same types of glazing, window frame and overhang were assumed for the two façade systems and their costs were not included in this calculation.

**Table 7.10: Unit costs of concrete constituents**

| Compositions            | Unit cost (\$/tonne) |
|-------------------------|----------------------|
| Water                   | 2.4                  |
| Cement                  | 122.3                |
| Slag                    | 50                   |
| Fly ash                 | 75                   |
| Fine aggregates         | 8.57                 |
| Coarse aggregates       | 14                   |
| 30 mm steel macrofibers | 2334.8               |
| 8 mm PVA microfibers    | 14537.4              |
| SP                      | 3434.2               |
| VMA                     | 3434.2               |
| Steel rebar             | 1124.3               |
| GFRP rebar              | 19568.3              |
| EP <sup>†</sup>         | 165                  |
| NSC <sup>†</sup>        | 70.8                 |
| HP-G-HyFRC <sup>†</sup> | 433                  |

<sup>†</sup> Per m<sup>3</sup>

Life cycle cost analysis was limited to materials costs required to make the concrete façades of the functional unit. Labor, transportation and installation costs were not considered although it is expected that DSF has an advantage over SW in these aspects because of the high workability of HP-G-HyFRC and a lower weight of the system. **Table 7.11** gives the summary of CO<sub>2</sub>, energy and cost analysis for three scenarios: SW+DG, DSF+DG and DSF+EP+DG. The three scenarios were selected because they contain higher performance window (DG) and this allows for a clearer discussion on the effect of wall types on operational energy performance of the building. Based on operational energy results, the SW+DG scenario annually consumes 1138 MJ or 316 kWh less energy than that consumed by SW. With an electricity rate of \$0.20/kWh (Singapore Power, 2013), the annual savings will be \$63.2. As mentioned, the total materials costs for the façade faces (excluding window casement and glazing) were \$93 for SW and \$425 for DSF. Hence, the additional cost of DSF can be recovered within first 6 years of operation. Also, it is observed that the additional embodied energy of 1048 MJ required in making DSF could be recovered by the second year of operation.

**Table 7.11: Comparative results of functional unit with different wall types**

|   | SW+DG | DSF+DG | DSF+EP+DG |
|---|-------|--------|-----------|
| Total embodied energy (MJ)              | 2726  | 3758   | 4383      |
| Total embodied CO <sub>2</sub> (kg)     | 469.9 | 395.2  | 418.4     |
| Annual operational Energy (MJ)          | 9538  | 8400   | 7220      |
| Annual operational CO <sub>2</sub> (Kg) | 1324  | 1166   | 1002      |
| Total cost (\$)                         | 93    | 425    | 464       |

The higher thermal resistance of EP reduced the U-factors of the DSF by almost 3 times and cut the annual operational energy in DSF+EP+DG by 14% or 1180 MJ (**Table 7.11**) as compared to DSF+DG. This means that the additional embodied energy arising from EP filler can be recovered within the first year of operation. The annual energy saving can be translated to a saving of \$65.5 per month, leading to a full recovery of the additional cost of EP within the first year of operation. In comparison to SW+DG, the additional cost of DSF+EP+DG can be recovered within the first 4 years of operation, shorter than the 6-year period for DSF+DG. Hence, with respect to materials cost, adding a layer of insulating materials in place of the air gap provides a much better economic benefit than just having the air gap in between the two skins of the DSF system.

#### **7.4.5 Uncertainties in data**

The life cycle assessment that has been conducted represents a number of uncertainties. The travelled distances for cement raw materials, aggregates and other constituents of concrete were arbitrarily selected based on the most likely import sources to Singapore. Also, life cycle inventories for steel, PVA fibers, steel rebar and EP were based on studies in Europe. The production processes and different energy sources for production may further increase the level of uncertainty. In addition, the production process of PP fibers is slightly different from PVA and as such the PP life cycle inventory (LCI) results might not be representative of those for PVA fibers. Assumptions used in COMFEN5 modelling can deviate from the real case scenario. For instance, COMFEN5 currently does not allow for modification in operational schedule of the HVAC system. In our analysis it was assumed that the air-conditioner was on for 24 hours a day. Also, efficiency loss due to air leakage cannot be captured with COMFEN5. However, with a consistent modelling setting, it is expected that the errors from the energy modelling would be of similar level for all analysis cases. For a worst case scenario where the operational energy saving is reduced by half, the return on investment period will also be doubled to 12 years for DSF+DG. This level of payback period is still acceptable considering the environmental benefits of the system.

### **7.5 Discussion**

#### **7.5.1 Environmental impact of DSF system**

The implementation of DSF in buildings can bring about great environmental benefits. In addition to an ability to reduce operational energy, the DSF system constructed with HP-G-HyFRC would also incorporate waste materials including fly ash and slag that would otherwise end up in landfills and would pollute the interconnected ecological system. Life cycle assessment in this study was limited to only energy and CO<sub>2</sub> emission. However, other environmental burdens such as toxic chemical emissions and hazard wastes (Horvath & Hendrickson, 1998) were not quantified. Integration of industrial wastes slag and fly ash into concrete as cement replacement would be an advantage in this regard. Also, the LCA is based on a cradle-to-gate approach which does not evaluate the environmental impacts in regards to strength, crack resistance and durability. By considering durability, we are including the service life aspects to the LCA. Ideally, embodied, operational energy and CO<sub>2</sub> emission should be normalized to the DSF's expected life span. In this way, we would capture not only materials production impacts but also service life impacts based on design criteria. The crack resistance of HP-G-HyFRC will help to ensure a high durability and extended service life of the DSF system. The distributed crack formation under loading will also prevent air leakage into and out of the building. The presence of hybrid fibers which provide

HP-G-HyFRC its superior performance infers that poorer quality slag and fly ash can be used as cement replacement, expanding the usability of the waste materials in concrete.

### **7.5.2 Accuracy of COMFEN5**

COMFEN5 uses EnergyPlus engine and graphic user interface to allow users to explore the effects of input variables on energy consumption (Selkowitz et al., 2012). The tool focuses on a room rather a complete building design to facilitate easy comparison of the effects of the variables on energy consumption and CO<sub>2</sub> emission. As a result, COMFEN5 allows for only packaged single zone HVAC system from which air mixing, conditioning and fan system is supplied to one zone only. This simple system, however, is applicable to the scenarios adopted for the study. Although no calibration or comparison against real data has been made for COMFEN5, the EnergyPlus engine has been recognized to provide accurate space temperature prediction which is crucial for HVAC system and plant sizing (Crawley et al., 2008). Hence, it is postulated that COMFEN5 is sufficient for the comparative analysis implemented in this study.

### **7.5.3 Durability of GFRP**

Long-term behavior of DSF with GFRP connectors will have to be further studied. GFRP is a composite material composes of millions of fibers held together by resin. Deterioration of either fibers or resin governs the durability of GFRP (Uomoto, 2003). Deterioration mechanisms may be caused by fatigue, alkali and acidic reaction, ultraviolet ray, freeze and thaw. The tensile capacity of glass fiber-reinforced polymer (GFRP) bars embedded in concrete were shown to be reduced with time due to chemical reactions with concrete pore solution (Trejo et al., 2011). It was reported that for small-size GFRP rebar, the residual capacity could fall below the design capacity after about 22 years. This has an adverse implication on the connector elements and their long-term performance would have to be studied before the system can be implemented in buildings. On a side note, deterioration by ultra-violet ray will not be a problem as the GFRP connector is housed between the two opaque HP-G-HyFRC skins.

### **7.5.4 Constructability of DSF**

Two-casting procedure was adopted for the construction of the DSF system. Although the high workability of the concrete composite made the placement easy, one of the difficulties with the construction method was the preparation and the arrangement of the GFRP connectors. The connectors were made of a single GFRP rod which was cut into segments of the desired length. The segments were then arranged to form a 45-degree diagonal truss system. This system with alignment closely following the load path in flexural façade elements is more effective in load transfer as compared to a vertical truss system.

However, the arrangement of the diagonal truss system is tedious, time consuming and uneconomical for factory production. Einea et al. (1991) discussed various types of shear connectors for precast concrete wall panels. These connectors may resist shear in one or two perpendicular directions. One-way shear connectors can be further classified into concentrated and continuous connectors. The latter runs the full length of the panel and generally comes in as a truss or expanded perforated plate. One type of the truss system is continuous bent bar which is very similar to the shear connector system adopted in this study. Fiber reinforced plastic (FRP) bent bar connector that is both structurally and thermally efficient was proposed in a study by Salmon et al. (Salmon et al., 1997). The system provides continuous insulation without thermal bridges.

Proprietary bent bars made of GFRP have been known to exist in the market. The use of the continuous bent system will improve the constructability of the DSF system while at the same time maintain its insulation properties and structural integrity similar to the function provided by the segmented GFRP connectors.

The EP insulation layer may be installed by attaching it along with the shear connector and placed in the middle of the mold for vertical casting. This method, however, will require more labor in preparing and installing the EP layer. Another option is to produce the hollow DSF first through the two-casting method as presented earlier. The airgap can then be filled with commercially available spray foam after demolding. The selection of option will depend on comparative cost and available technologies.

### 7.5.5 Size effects

The size effect on mechanical properties of concrete was first systematically reported by Bazant (Bazant, 1984). Using smeared crack theory, it was shown that strength in brittle materials is reduced with an increase in element size. The size effects on ultra-high performance fiber-reinforced concrete have been reported by many researchers (Bazant, 1984; Nguyen et al., 2013; Nguyen et al., 2014). In this study, flexural tests on HP-G-HyFRC flexural elements with clear span 450 mm and three thicknesses of 60 mm, 70 mm and 120 mm, were conducted. The flexural responses are given in **Fig. 7.12**. It is observed that as the thickness increased, the smooth deflection hardening behavior also started to disappear. There was a sudden big drop in load level after the first crack was formed for the 120 mm flexural elements, representing the onset of dominant macrocrack. In contrast, the drop was less apparent or non-existent for the 60 mm and 70 mm flexural elements. The results confirm the benefits of using thin HP-G-HyFRC skins in DSF to ensure that the superior mechanical performance of the composite, especially with regard to deflection hardening, still can be realized.

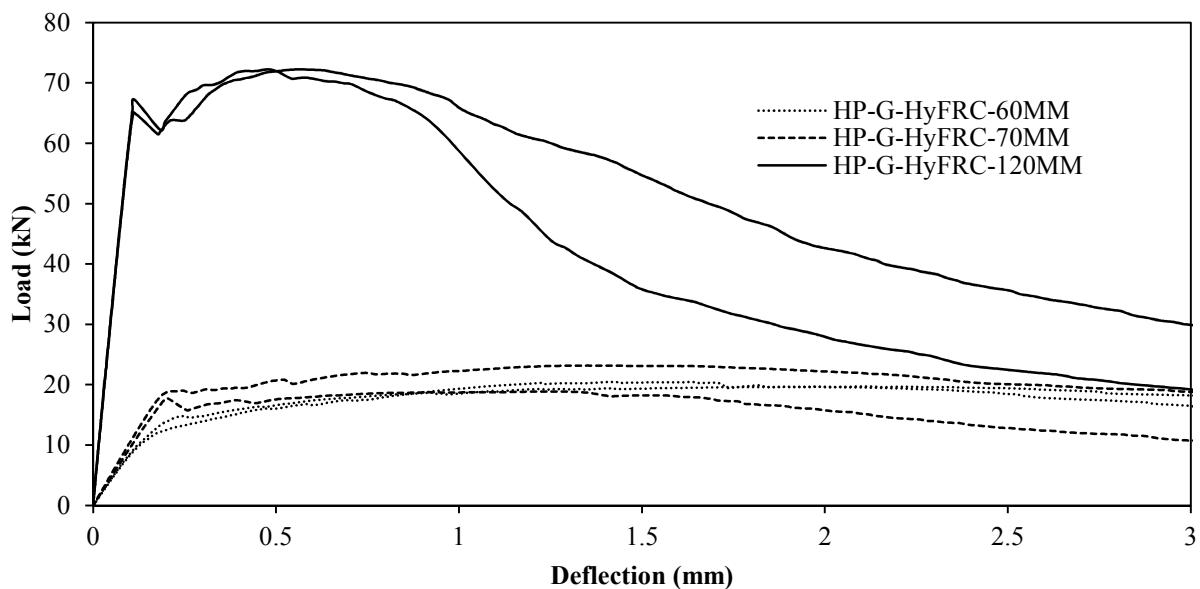


**Figure 7.12: Size effects of flexural responses of HP-G-HyFRC elements**



## 7.6 Conclusions

From the results and discussion provided in this study, it can be concluded that HP-G-HyFRC enhanced the ultimate capacity and toughness of DSF as compared to that found normal strength concrete SW of the same thickness. This was despite a 25% reduction in concrete usage and 25% reduction in weight of the DSF system. Based on size effect study, the thin thickness of DSF skins was actually beneficial to ensure deflection hardening response of the system under flexural load. As compared to conventional solid façade, HP-G-HyFRC DSF was found to be more energy intensive and more costly to construct. However, this innovative application has a huge potential in both saving operational energy and reducing CO<sub>2</sub> emission over the life time of the building. With just air as an insulation medium, the additional cost can be recovered within the first 6 years of operation. Filling the air cavity with expanded polystyrene was shown to further reduce the operational energy and return period of investment. This study stresses the importance of considering life cycle assessment as a method for designing resilient and sustainable civil systems.

# 8 Concluding remarks

## 8.1 Summary

This study arises from a need to make concrete structures more sustainable. Sustainability from concrete materials engineering viewpoint refers to high performance (high workability and superior mechanical performance), high durability and versatility for various applications targeted at reducing operational and maintenance energy. Only limited types of concrete composites can fulfill all these requirements. The study focuses on a new concrete composite called high performance green hybrid fiber-reinforced concrete composite (HP-G-HyFRC) which exhibits high strength and deflection hardening for enhanced durability. A radical approach was adopted in the design consideration of the composite and was based on life cycle framework applicable to concrete structures. This is an extension beyond the performance-based design methodology where the focus is generally on mechanical properties of concrete. The life cycle-based approach also encompasses the environmental impacts and costs during the entire lifespan of structures.

Different stages of a structure's life cycle including materials acquisition, design, construction, operation, maintenance and end of life were considered in the composite development process and application. To reduce cost and environmental impact at materials acquisition stage, cement was replaced by slag and fly ash up to 60% by mass. For easy placement, enhanced performance and reliability, the composite was designed to have high workability, high strength and deflection hardening behavior. To meet the deflection hardening performance criterion, polyvinyl alcohol (PVA) micro- and steel macrofibers were used as discontinuous reinforcement in the composite to provide multi-level crack arresting mechanism. Superplasticizer and viscosity modifying admixtures were also added in the mixing water to improve workability. The final composite has slump flow diameter greater than 500 mm, 28-day strength greater than 70 MPa, and deflection hardening behavior with multiple crack distribution at a relatively low combined fiber volume fraction of 1.65%. These benefits come with another unique feature that sand and gravels commonly used for conventional concrete were directly applied in the composite without any special processing.

The composite was targeted for application in both infrastructure and buildings. For infrastructure, maintenance and disruption to traffic is a major concern as this leads to loss of time in traffic jam and diversion, which as a result causes more gas consumption and more CO<sub>2</sub> emission. Highly durable concrete is a building block for a longer lasting infrastructure. In view of this, the durability of HP-G-HyFRC was investigated. Accelerated corrosion test with impressed current was adopted to study the composite's corrosion performance at the propagation stage. Samples with no applied current were also used in the study to investigate their corrosion initiation performance. Corrosion activity was measured with electrochemical measurement methods. It was found that with no applied current, high performance concrete (HPC) with and without hybrid fibers show similarly low corrosion rates in an inactive corrosion region. However, with an induced current, HPC was susceptible to cracking and that increased corrosion rates considerably. Hybrid fibers in HP-G-HyFRC, on the other hand, controlled the propagation of cracks and reduced the corrosion activity. The fundamental studies on the effects of slag, fibers and interface qualities on corrosion using similar methods revealed that slag at 60% replacement of cement could be detrimental to corrosion

resistance of steel in concrete although inclusion of hybrid fibers helped to mitigate the disadvantage. The results showed that hybrid fibers should be used in concrete with high strength or high-volume supplementary cementitious materials to prolong the corrosion propagation stage of structures.

As operational energy constitutes a huge proportion of energy consumption and CO<sub>2</sub> emission during the service life of buildings, the use of HP-G-HyFRC focuses on reducing the operation energy in buildings. An innovative double skin façade (DSF) with skins made HP-G-HyFRC and with GFRP rebar as connectors to prevent thermal bridging was proposed. The mechanical properties and sustainability performance of the system were assessed and compared with a conventional solid façade system generally adopted in public housing in Singapore. Life cycle assessment (LCA) applied to a typical functional unit was adopted in the sustainability study. Embodied energy of the systems were found with Green Concrete Tools developed by researchers at UC Berkeley while the operational energy was obtained with an energy modelling tool called COMFEN5 with EnergyPlus as its analytical engine. The results revealed that although the DSF has higher embodied energy and more costly to produce, the additional energy and cost can be recovered within the first few years of operation. Replacing air with insulation materials such as expanded polystyrene (EP) even further shortened the return period to investment. The results stress the importance of using LCA in assessing sustainability of new civil systems.

## 8.2 Concluding statements

The aim of the study has been to develop a new type of high performance fiber reinforced concrete and to demonstrate that the composite can be used for infrastructure and buildings for enhanced sustainability and cost saving. The study was divided into composite development, durability assessment and application. As mentioned, durability study is critical in ensuring the superiority of the composite for its application in infrastructure field.

**Chapter 2** on the development of HP-G-HyFRC demonstrated that theoretical analysis could be used to limit the number of trials in determining the critical fiber volume fractions for deflection hardening behavior in the composite. As compared to conventional self-consolidating concrete (SCC), fine aggregate over coarse aggregate ratio had to be increased in fiber-reinforced concrete (FRC) to improved workability. Addition of SCMs in concrete especially fly ash helped to improve the composite's workability. Although the physical properties (size and shape distribution) of the fly ash were not quantified, its ability to enhance fresh concrete workability was attributed to conducive fineness, size distribution and spherical shape of fly ash particles (Peris Mora et al., 1993). The spherical shape of fly ash particles is known to provide ball-bearing action to other concrete constituents although this benefit can be reduced if fly ash becomes finer (Chindaprasirt et al., 2004). PVA microfibers controlled propagation of microcracks inherent in concrete or formed during loading. They also toughened the matrix and ensured a gradual pullout of steel fibers. The synergy of PVA micro- and steel macrofibers led to a smooth deflection hardening behavior and distributed microcracking of the composite under flexure up to peak load at a relatively low fiber volume fractions of 1.5% hooked-end steel fibers and 0.15% PVA fibers. Even at 60% combined replacement of cement by slag and fly ash, the composite exhibits high 28-day compressive strength greater than 70 MPa. All these benefits come with the use of conventional sand and gravels as aggregates.

**Chapter 3** serves to evaluate corrosion performance of HP-G-HyFRC. The results showed that more extensive cracking occurred in HPC with no fibers. The crack widths ranged between 1.1

and 2 mm, several times greater than those observed in normal strength concrete with the same current regimes. After the macrocracks were formed in HPC samples, the corrosion rates seems to be independent of corrosion regimes and crack widths. This may be attributed to a similar loosening of the steel-concrete interface from the propagation of corrosion-induced cracking. On the other hand, hybrid fibers in HP-G-HyFRC helped to reduce corrosion rates by half, attributable to crack control action and passive confinement provided by the fibers. Mechanical properties of HP-G-HyFRC samples were also maintained after the applied current. It was also observed that the gravimetric mass losses were greater than the theoretical mass losses when 4% NaCl was added into the mixing water. The presence of NaCl destabilized steel passivity and increased the efficiency of the applied current through dissolution of the steel anode as a result of interfacial acidification.

Studies in **Chapters 4, 5 and 6** were conducted to provide a fundamental understanding of steel corrosion in concrete with high volume slag replacements, hybrid fibers and different interface qualities, and mechanisms involved in accelerated corrosion test. **Chapter 4** focuses on the corrosion performance of concrete with high-volume slag replacements level. The samples were cured for 7 days to imitate common on-site curing practice. Due to shrinkage-induced cracking and poor quality passive film, samples with 60% slag replacement showed an early corrosion initiation and higher mass losses induced by the impressed current. Although the matrix of concrete with 60% slag contained interconnected micro pores, it was observed to be generally denser possibly attributed to improved particle packing with the presence of slag. This led to a poor ability of the matrix to accommodate corrosion products at the interface and hence the concrete experienced an early onset of cracking. Under the same regime of applied current, samples made of slag concrete also experienced higher mass losses. This is attributed to a less stable passive film and less buffering action from the limited amount of  $\text{Ca}(\text{OH})_2$  under acidification. In **Chapter 5** where the combined effects of slag and hybrid fibers on corrosion was studied, it was concluded that based on corrosion rate measurement, hybrid fibers in concrete did not adversely affect corrosion initiation of steel in concrete despite its higher porosity. However, under propagation stage achieved by the induced current, hybrid fibers in concrete significantly reduced corrosion rates through confinement and densification of corrosion products at steel-concrete interface. **Chapter 6** moved on to study the influence of interface qualities on corrosion initiation and propagation. Higher porosity at the steel-concrete interface initiated an early corrosion. However, the porous interface could accommodate more corrosion products. This led to a smaller pressure buildup from the corrosion products and less damage to the surrounding concrete. As a result, smaller corrosion rates were observed in the samples with more porous interfaces under accelerated corrosion. The results has an implication for high strength concrete whose dense interface could cause an early and more extensive cracking with the same amount of corrosion products as compared to normal strength and more porous concrete. With regard to HP-G-HyFRC, the presence of hybrid fibers are necessary to maintain its integrity and to reduce corrosion rates for enhanced service life under corrosion consideration.

The study ended with a proposed application of HP-G-HyFRC in an innovative double skin façade (DSF) system in place of a conventional solid façade system generally adopted in Singapore. It was found that although the DSF was more energy intensive to produce and more costly to construct, it allowed for a full recovery of the additional embodied energy within the first two years of operation and cost recovery within the first 6 years of operation. The overall study shows a life-cycle consideration adopted from materials design, durability check and application to ensure more sustainable infrastructure and buildings for our society. This is a shift from conventional

sustainability studies of concrete composites where the focus is generally on their embodied energy.

### **8.3 Limitations of the current study**

Despite the many promising results achieved from the study, a number of limitations exist. First, although the procedure as outlined in ASTM G1-03 (American Society for Testing and Materials (ASTM), 2011) to clean the corroded rebar was closely followed, the etching of the base metal is believed to lead to higher gravimetric mass losses than anticipated. This, however, was applicable to all samples and hence comparison of corrosion results and trend in gravimetric mass losses are still valid. Another limitation is that samples were of different ages (between 28 and 56 days old) before the samples were subjected to the induced current regimes. Drying or continuing hydration may change the matrix microstructure and steel-concrete interface. Improved microstructure limits ingress of oxygen, moisture and  $\text{Cl}^-$  into the concrete. This leads to an improved protection of steel against corrosion and the less effectiveness of the applied current in dissolving steel. However, strength and elastic modulus results showed that there was little change in the values within the timeframe that the first and the last samples were exposed to the induced current. Hence, age difference of the samples was not expected to significantly influence their corrosion performance. Another limitation is that the nature of corrosion products under accelerated corrosion are known to be different from those observed under natural corrosion. As such, a direct link between the performances of the composite to site performance should be treated with caution.

Regarding LCA, the use of a typical fictional unit in the modelling is unrealistic. Whole building modelling should be implemented to study the interaction of different building sections and the overall building with the environment. A control to the mechanical cooling system to match the activity schedule and the room function should also be applied. However, limitations of the tool make this unfeasible. Despite the short comings, comparison between the analysis scenarios could still be made in view of the same analytical engine and consistent model setups adopted in the study. Another point worth noting is that construction, transportation and installation costs were not considered in life cycle cost analysis. However, to include them in the calculation is challenging in view of the novelty of the DSF system and its new construction method.

### **8.4 Recommendations for future studies**

One area of interest is the implementation of the newly developed HP-G-HyFRC in large scale structural applications. For economy, its structural benefits including high strength and deflection hardening behavior should be maximized. However, it was shown in **Chapter 7** that due to size effects, thick HP-G-HyFRC members may not exhibit the desired deflection hardening property. Hence, one possible application area is to use only thin HP-G-HyFRC elements in structures such as jackets for structural members. Besides providing protection to the reinforcing bars, the jackets may be able to distribute cracks over a large region, resulting in increased ductility and higher resistance to seismic loading. In rocking columns with partial debonding of reinforcement for earthquake resistance, the use of lower strength HyFRC as the column's shell exhibited minimal damage or low residual displacement at the design ground motion levels (Trono, 2014). HP-G-HyFRC in place of HyFRC in the system may provide better damage resistance to the compression regions. HP-G-HyFRC will also add the benefits of enhanced durability and precast feasibility because of its early strength gain.

It has been discussed that corrosion products are different in accelerated corrosion test and natural corrosion. Also, pore solution pH, moisture, oxygen and even ion states all influence the physical properties of the corrosion products. In natural corrosion where there is more time for moisture and oxygen to react with the dissolved iron ions, it is expected that for the same amount of dissolved base metal, the volume of the final corrosion products are much higher. Hence, it is imperative for the corrosion products be characterized to determine their chemical compositions, volume expansion ratios and mechanical properties. The information will be useful in improving corrosion damage models for reinforced concrete structures. Raman micro-spectroscopy, X-ray diffraction and energy dispersive spectroscopy were used to identify and study the morphology of dehydrated corrosion products (Marcotte, 2001; Neff et al., 2011; Thibeau et al., 1978). A relationship between crystalline structure of corrosion products and their volume expansion ratios was developed (Marcotte, 2001; Suda et al., 1993; Zhao et al., 2011). However, the hydrophilic nature of corrosion products (Andrade et al., 2011) would mean varied expansive capabilities under different exposure conditions. A better understanding of this would enable a better assessment of corrosion-induced distress on reinforced concrete structures. In application to accelerated corrosion test, corrosion product types can be associated with different applied current intensities. Correlation between volume expansion and pressure induced by corrosion products in accelerated and natural corrosion could be then formed. From here, a more realistic concrete damage level can be predetermined and induced in accelerated corrosion test. A successful outcome of the proposed study will be beneficial for more realistic laboratory studies on corrosion propagation. It was also argued that the strength of passive film in concrete can influence the onset of corrosion and that the quality of the film varied with pore solution compositions in concrete. This has an implication when supplementary cementitious materials are used as cement replacement. Hence, to better understand the phenomenon, the film's atomic structure which has a direct effect on its electrochemical and electrical properties should be characterized. Some analysis methods such as electron energy loss spectroscopy (Gunay et al., 2013), Auger electron spectroscopy (AES) and X-ray photoelectron spectroscopy (XPS) (Montemor et al., 1998) have been successfully used to study the behavior and properties of the passive film in concrete. The techniques may be applied to steel embedded in concrete of different binder compositions.

One of the beneficial effects of fibers in concrete is their confinement capability which leads to multiple cracking and the subsequent reduction in corrosion rates. However, fibers are activated only when cracks occur. That means their benefits are realized only during the propagation stage. With the propagation stage that represents a small fraction of the overall service life of conventional reinforced concrete structures (Weyers, 1998), it is imperative that future studies should look into quantifying the initiation and propagation durations related to corrosion of reinforcing bars in HP-G-HyFRC. This allows for a quantitative assessment of the benefits of fibers based on service life consideration. An empirical model for crack initiation and propagation can be used to achieve this. Models that account for concrete porosity at the steel-concrete interface, concrete cover, concrete quality and steel mass loss have been proposed (El Maaddawy & Soudki, 2007; Vu et al., 2005; Weyers et al., 1993). For HP-G-HyFRC, the models should also account for crack distribution and the reduced corrosion activity due to the confinement of fibers. The crack distribution in effect prolongs the service life of structures if crack width limit and structural integrity are parameters used in service life definition.

The mass loss measurement of the corroded rebars using HCl solution with hexamethylene tetramine seemed to remove part of the base metal and may overestimate the gravimetric mass losses. The error will be especially magnified at true small mass loss values. It is interesting to see

if 3D reconstruction of the rebar before and after the corrosion can be implemented for mass loss estimation. The reconstruction allows for uncorroded rebar volume comparison and the difference in volumes can be translated as the mass loss. Algorithms can be implemented so that the shielding can be provided by the intact steel layer only. Using X-ray irradiation apparatus, it was shown that it is possible to nondestructively quantify the extent of corrosion of rebar in concrete (Koyasu et al., 2014). It is expected a similar technique can be used to accurately measure the extent of corrosion of un-embedded corroded rebars for more accurate and fast mass loss measurement.

It was found that the FRM coating on steel rebar slowed down corrosion activity considerably during propagation stage due to the densification of accumulated corrosion products at steel-concrete interface. The concept of thickening the passive film through introduction of uniform porous layer on steel surfaces may be utilized to control corrosion rate and subsequent damage to concrete structures under corrosion consideration. One approach may be to use a coated reinforcing bar in high performance concrete (HPC). The HPC cover is expected to slow down corrosion initiation due to dense microstructure. When corrosion is initiated, the porous layer would collect corrosion products and densify the interface without causing pressure to the surrounding matrix. During propagation, the dense HPC would also limit the ingress of O<sub>2</sub> and moisture to reach the steel surface and that would further limit the corrosion activity. Service life modelling of both the corrosion initiation and corrosion propagation will be needed to prove the concept. However, the concept may not be applicable to real structures as they are subjected to mechanical loading and cracking,

Lastly, in operational energy modelling, only a functional unit was implemented in this study. Whole building energy simulation will allow for a more realistic indication of building performance through interaction with the exterior environment and among different compartments within the building. Various commercial tools with different capabilities and sophistications are available for this purpose. A comparison of features of major building simulation programs was conducted by Crawley et al. (Crawley et al., 2008). A total of 14 categories were used as the comparison basis and included general modeling features, zone loads, building envelope and daylighting, infiltration, ventilation and multizone airflow, renewable energy systems, electrical systems and equipment, HVAC systems, HVAC equipment, environmental emissions, economic evaluation, climate data availability, results reporting, validation, user interface, links to other programs, and availability. Based on the list, it is observed that COMFEN5 used in the study represented a great level of simplification and an improved simulation should at least contains most or all of the 14 features for more realistic results. Also, it was mentioned in **Chapter 7** that the environment within the DSF cavity can be manipulated such as ventilation of the cavity for a reduction in energy consumption and enhancement to comfort. Computer modelling may be implemented to assess the feasibility. However, due to the small introduced air gap, conventional heat transfer tools may be deemed unpractical. Simulation programs with computational fluid dynamic (CFD) can be a candidate for this purpose.



# References

- Abbas, A., Carcasses, M., & Ollivier, J. (2000). The importance of gas permeability in addition to the compressive strength of concrete. *Magazine of Concrete Research*, 52(1), 1-6.
- ACI Committee 224. (1997). Cracking of concrete members in direct tension *ACI 224.2R-92*: ACI Committee 224.
- ACI Committee 363. (1997). State-of-the-art report on high-strength concrete *ACI 363R-92*: ACI Committee 363.
- ACI Committee 544. (2010). Report on the physical properties and durability of fiber-reinforced concrete *ACI 544.5R-10*: ACI Committee 544.
- ACI Committee. (2005). *Building code requirements for structural concrete (ACI 318-05) and commentary (ACI 318R-05)*.
- Adalberth, K. (1997). Energy use during the life cycle of buildings: a method. *Building and Environment*, 32(4), 317-320. doi: [http://dx.doi.org/10.1016/S0360-1323\(96\)00068-6](http://dx.doi.org/10.1016/S0360-1323(96)00068-6)
- Alonso, C., Andrade, C., Rodriguez, J., & Diez, J. M. (1998). Factors controlling cracking of concrete affected by reinforcement corrosion. *Materials and Structures*, 31(7), 435-441. doi: 10.1007/BF02480466
- America Society of Civil Engineers (ASCE). (2013). Report card for America's infrastructure
- America Society of Civil Engineers (ASCE). (March, 2009). Report card for America's infrastructure.
- American Society for Testing and Materials (ASTM). (2009). ASTM C876-09: Standard test method for corrosion potentials of uncoated reinforcing steel in concrete.
- American Society for Testing and Materials (ASTM). (2010a). ASTM C469/469M-10: Standard test method for static modulus of elasticity and Poisson's ratio of concrete in compression I.
- American Society for Testing and Materials (ASTM). (2010b). ASTM C1609/1609M-10: Standard test method for flexural performance of fiber-reinforced concrete (using beam with third-point loading)
- American Society for Testing and Materials (ASTM). (2010c). ASTM C1611/C1611M-09b: Standard test method for slump flow of self-consolidating concrete.
- American Society for Testing and Materials (ASTM). (2010d). ASTM G102-89: Standard practice for calculation of corrosion rates and related information from electrochemical measurements.
- American Society for Testing and Materials (ASTM). (2011). ASTM G1-03: Standard practice for preparing, cleaning, and evaluating corrosion test specimens.
- Andersson, K., Allard, B., Bengtsson, M., & Magnusson, B. (1989). Chemical composition of cement pore solutions. *Cement and Concrete Research*, 19(3), 327-332. doi: [http://dx.doi.org/10.1016/0008-8846\(89\)90022-7](http://dx.doi.org/10.1016/0008-8846(89)90022-7)
- Andersson, K., Ohlsson, T., & Olsson, P. (1998). Screening life cycle assessment (LCA) of tomato ketchup: a case study. *Journal of Cleaner Production*, 6(3-4), 277-288. doi: [http://dx.doi.org/10.1016/S0959-6526\(98\)00027-4](http://dx.doi.org/10.1016/S0959-6526(98)00027-4)
- Andrade, C., & Alonso, C. (1996). Corrosion rate monitoring in the laboratory and on-site. *Construction and Building Materials*, 10(5), 315-328. doi: [http://dx.doi.org/10.1016/0950-0618\(95\)00044-5](http://dx.doi.org/10.1016/0950-0618(95)00044-5)

- Andrade, C., Tavares, F., Toro, L., & Fullea, J. (2011). Observations on the morphology of oxide formation due to reinforcement corrosion *Modelling of Corroding Concrete Structures* (pp. 179-193): Springer.
- Angst, U., Elsener, B., Larsen, C. K., & Vennesland, Ø. (2009). Critical chloride content in reinforced concrete — A review. *Cement and Concrete Research*, 39(12), 1122-1138. doi: <http://dx.doi.org/10.1016/j.cemconres.2009.08.006>
- Arya, C., Buenfeld, N. R., & Newman, J. B. (1990). Factors influencing chloride-binding in concrete. *Cement and Concrete Research*, 20(2), 291-300. doi: [http://dx.doi.org/10.1016/0008-8846\(90\)90083-A](http://dx.doi.org/10.1016/0008-8846(90)90083-A)
- Arya, C., & Vassie, P. R. W. (1995). Influence of cathode-to-anode area ratio and separation distance on galvanic corrosion currents of steel in concrete containing chlorides. *Cement and Concrete Research*, 25(5), 989-998. doi: [http://dx.doi.org/10.1016/0008-8846\(95\)00094-S](http://dx.doi.org/10.1016/0008-8846(95)00094-S)
- Baes, C. F., & Mesmer, R. E. (1976). *Hydrolysis of cations*: Wiley.
- Balafas, I., & Burgoyne, C. J. (2010a). Environmental effects on cover cracking due to corrosion. *Cement and Concrete Research*, 40(9), 1429-1440. doi: <http://dx.doi.org/10.1016/j.cemconres.2010.05.003>
- Balafas, I., & Burgoyne, C. J. (2010b). Modeling the structural effects of rust in concrete cover. *Journal of Engineering Mechanics*, 137(3), 175-185.
- Ballim, Y., & Reid, J. C. (2003). Reinforcement corrosion and the deflection of RC beams—an experimental critique of current test methods. *Cement and Concrete Composites*, 25(6), 625-632. doi: [http://dx.doi.org/10.1016/S0958-9465\(02\)00076-8](http://dx.doi.org/10.1016/S0958-9465(02)00076-8)
- Balouch, S. U., Forth, J. P., & Granju, J. L. (2010). Surface corrosion of steel fibre reinforced concrete. *Cement and Concrete Research*, 40(3), 410-414. doi: <http://dx.doi.org/10.1016/j.cemconres.2009.10.001>
- Banthia, N., & Sappakittipakorn, M. (2007). Toughness enhancement in steel fiber reinforced concrete through fiber hybridization. *Cement and Concrete Research*, 37(9), 1366-1372. doi: <http://dx.doi.org/10.1016/j.cemconres.2007.05.005>
- Banthia, N., & Trottier, J.-F. (1994). Concrete reinforced with deformed steel fibers, part I: bond-slip mechanisms. *ACI Materials Journal*, 91(5).
- Barneyback Jr, R. S., & Diamond, S. (1981). Expression and analysis of pore fluids from hardened cement pastes and mortars. *Cement and Concrete Research*, 11(2), 279-285. doi: [http://dx.doi.org/10.1016/0008-8846\(81\)90069-7](http://dx.doi.org/10.1016/0008-8846(81)90069-7)
- Bayasi, Z., & Zeng, J. (1993). Properties of polypropylene fiber reinforced concrete. *ACI Materials Journal*, 90(6).
- Bazant, Z. P. (1984). Size effect in blunt fracture: concrete, rock, metal. *Journal of Engineering Mechanics*, 110(4), 518-535.
- Bentur, A., Mindess, S., & Diamond, S. (1985). Pull-out processes in steel fibre reinforced cement. *International Journal of Cement Composites and Lightweight Concrete*, 7(1), 29-37.
- Berntsson, L., & Chandra, S. (1982). Damage of concrete sleepers by calcium chloride. *Cement and Concrete Research*, 12(1), 87-92. doi: [http://dx.doi.org/10.1016/0008-8846\(82\)90102-8](http://dx.doi.org/10.1016/0008-8846(82)90102-8)
- Bertonini, L., Elsener, B., Pedferri, P., & Polder, R. (2004). *Corrosion of steel in concrete*: Wiley-VCH.

- Bilec, M. M. (2007). *A hybrid life cycle assessment model for construction processes*. University of Pittsburgh.
- Bisschop, J., & van Mier, J. (1999). Quantification of shrinkage micro-cracking in young mortar with fluorescence light microscopy and ESEM. *HERON-ENGLISH EDITION*-, 44(4), 245-256.
- Blunt, J., Jen, G., & Ostertag, C. P. (2015). Enhancing corrosion resistance of reinforced concrete structures with hybrid fiber reinforced concrete. *Corrosion Science*, 92(0), 182-191. doi: <http://dx.doi.org/10.1016/j.corsci.2014.12.003>
- Blunt, J. D., & Ostertag, C. P. (2009). Deflection hardening and workability of hybrid fiber composites. *ACI Materials Journal*, 106(3).
- Boel, V., Audenaert, K., De Schutter, G., Heirman, G., Vandewalle, L., Desmet, B., & Vantomme, J. (2007). Transport properties of self compacting concrete with limestone filler or fly ash. *Materials and Structures*, 40(5), 507-516.
- Bouikni, A., Swamy, R. N., & Bali, A. (2009). Durability properties of concrete containing 50% and 65% slag. *Construction and Building Materials*, 23(8), 2836-2845.
- Breitenbücher. (1998). Developments and applications of high-performance concrete. *Materials and Structures*, 31(3), 209-215. doi: 10.1007/BF02480402
- Browne, R. D. (1980). Mechanisms of corrosion of steel in concrete in relation to design, inspection, and repair of offshore and coastal structures. *ACI Special Publication*, 65.
- Building and Construction Authority (BCA). (2010). BCA greenmark for landed houses. Singapore
- Bullard, C. W., Penner, P. S., & Pilati, D. A. (1978). Net energy analysis: Handbook for combining process and input-output analysis. *Resources and Energy*, 1(3), 267-313. doi: [http://dx.doi.org/10.1016/0165-0572\(78\)90008-7](http://dx.doi.org/10.1016/0165-0572(78)90008-7)
- Byfors, K., Hansson, C. M., & Tritthart, J. (1986). Pore solution expression as a method to determine the influence of mineral additives on chloride binding. *Cement and Concrete Research*, 16(5), 760-770. doi: [http://dx.doi.org/10.1016/0008-8846\(86\)90050-5](http://dx.doi.org/10.1016/0008-8846(86)90050-5)
- Cady, P. D., & Weyers, R. E. (1984). Deterioration rates of concrete bridge decks. *Journal of Transportation Engineering*, 110(1), 34-44.
- Caré, S., & Raharinaivo, A. (2007). Influence of impressed current on the initiation of damage in reinforced mortar due to corrosion of embedded steel. *Cement and Concrete Research*, 37(12), 1598-1612. doi: <http://dx.doi.org/10.1016/j.cemconres.2007.08.022>
- Castel, A., Vidal, T., Francois, R., & Arliguie, G. (2003). Influence of steel - concrete interface quality on reinforcement corrosion induced by chlorides. *Magazine of Concrete Research*, 55(2), 151-159. doi: 10.1680/macr.55.2.151.37568
- Celik, K., Jackson, M. D., Mancio, M., Meral, C., Emwas, A. H., Mehta, P. K., & Monteiro, P. J. M. (2014). High-volume natural volcanic pozzolan and limestone powder as partial replacements for portland cement in self-compacting and sustainable concrete. *Cement and Concrete Composites*, 45(0), 136-147. doi: <http://dx.doi.org/10.1016/j.cemconcomp.2013.09.003>
- Chang, Y., Ries, R. J., & Wang, Y. (2010). The embodied energy and environmental emissions of construction projects in China: An economic input-output LCA model. *Energy Policy*, 38(11), 6597-6603. doi: <http://dx.doi.org/10.1016/j.enpol.2010.06.030>
- Chen, P.-W., & Chung, D. (1996). Low-drying-shrinkage concrete containing carbon fibers. *Composites Part B: Engineering*, 27(3), 269-274.

- Chen, T. Y., Burnett, J., & Chau, C. K. (2001). Analysis of embodied energy use in the residential building of Hong Kong. *Energy*, 26(4), 323-340. doi: [http://dx.doi.org/10.1016/S0360-5442\(01\)00006-8](http://dx.doi.org/10.1016/S0360-5442(01)00006-8)
- Cheng, A., Huang, R., Wu, J.-K., & Chen, C.-H. (2005). Influence of GGBS on durability and corrosion behavior of reinforced concrete. *Materials Chemistry and Physics*, 93(2-3), 404-411. doi: <http://dx.doi.org/10.1016/j.matchemphys.2005.03.043>
- Chindaprasirt, P., Homwuttiwong, S., & Sirivivatnanon, V. (2004). Influence of fly ash fineness on strength, drying shrinkage and sulfate resistance of blended cement mortar. *Cement and Concrete Research*, 34(7), 1087-1092. doi: <http://dx.doi.org/10.1016/j.cemconres.2003.11.021>
- Chindaprasirt, P., Jaturapitakkul, C., & Sinsiri, T. (2005). Effect of fly ash fineness on compressive strength and pore size of blended cement paste. *Cement and Concrete Composites*, 27(4), 425-428.
- Chua, K. J., & Chou, S. K. (2010). Energy performance of residential buildings in Singapore. *Energy*, 35(2), 667-678. doi: <http://dx.doi.org/10.1016/j.energy.2009.10.039>
- Cole, R. J., & Kernan, P. C. (1996). Life-cycle energy use in office buildings. *Building and Environment*, 31(4), 307-317. doi: [http://dx.doi.org/10.1016/0360-1323\(96\)00017-0](http://dx.doi.org/10.1016/0360-1323(96)00017-0)
- Crawford, G. L. (2013). LCI data for steel products: wire rod and rebar Steel Recycling Institute.
- Crawley, D. B., Hand, J. W., Kummert, M., & Griffith, B. T. (2008). Contrasting the capabilities of building energy performance simulation programs. *Building and Environment*, 43(4), 661-673.
- de Dear, R., & Brager, G. S. (1998). Developing an adaptive model of thermal comfort and preference. *Center for the Built Environment*.
- De Schutter, G., Bartos, P. J. M., Domone, P., & Gibbs, J. (2008). *Self-compacting concrete*: CRC Press.
- Dehghanian, C. (1999). Corrosion behavior of steel in concrete made with slag-blended cement. *Corrosion*, 55(3), 291-296.
- Dhir, R. K., El-Mohr, M. A. K., & Dyer, T. D. (1996). Chloride binding in GGBS concrete. *Cement and Concrete Research*, 26(12), 1767-1773. doi: [http://dx.doi.org/10.1016/S0008-8846\(96\)00180-9](http://dx.doi.org/10.1016/S0008-8846(96)00180-9)
- Dhir, R. K., El-Mohr, M. A. K., & Dyer, T. D. (1997). Developing chloride resisting concrete using PFA. *Cement and Concrete Research*, 27(11), 1633-1639. doi: [http://dx.doi.org/10.1016/S0008-8846\(97\)00146-4](http://dx.doi.org/10.1016/S0008-8846(97)00146-4)
- Dhir, R. K., & Jones, M. R. (1999). Development of chloride-resisting concrete using fly ash. *Fuel*, 78(2), 137-142. doi: [http://dx.doi.org/10.1016/S0016-2361\(98\)00149-5](http://dx.doi.org/10.1016/S0016-2361(98)00149-5)
- Dhonde, H. B., Mo, Y., Hsu, T. T., & Vogel, J. (2007). Fresh and hardened properties of self-consolidating fiber-reinforced concrete. *ACI Materials Journal*, 104(5).
- Dinakar, P., Babu, K. G., & Santhanam, M. (2007). Corrosion behaviour of blended cements in low and medium strength concretes. *Cement and Concrete Composites*, 29(2), 136-145. doi: <http://dx.doi.org/10.1016/j.cemconcomp.2006.10.005>
- EIA. (2014a). China *US Energy Information Administration*. Retrieved Feb. 10, 2015, from <http://www.eia.gov/countries/cab.cfm?fips=CH>
- EIA. (2014b). Malaysia. *US Energy Information Administration*. Retrieved Feb. 10, 2015, from <http://www.eia.gov/countries/cab.cfm?fips=MY>
- Einea, A., Salmon, D. C., Fogarasi, G. J., Culp, T. D., & Tadros, M. K. (1991). State-of-the-art of precast concrete sandwich panels. *PCI journal*, 36(6), 78-98.

- Einsfeld, R. A., & Velasco, M. S. L. (2006). Fracture parameters for high-performance concrete. *Cement and Concrete Research*, 36(3), 576-583. doi: <http://dx.doi.org/10.1016/j.cemconres.2005.09.004>
- El Maaddawy, T., & Soudki, K. (2003). Effectiveness of impressed current technique to simulate corrosion of steel reinforcement in concrete. *Journal of Materials in Civil Engineering*, 15(1), 41-47. doi: doi:10.1061/(ASCE)0899-1561(2003)15:1(41)
- El Maaddawy, T., & Soudki, K. (2007). A model for prediction of time from corrosion initiation to corrosion cracking. *Cement and Concrete Composites*, 29(3), 168-175. doi: <http://dx.doi.org/10.1016/j.cemconcomp.2006.11.004>
- Elsener, B. (2002). Macrocell corrosion of steel in concrete – implications for corrosion monitoring. *Cement and Concrete Composites*, 24(1), 65-72. doi: [http://dx.doi.org/10.1016/S0958-9465\(01\)00027-0](http://dx.doi.org/10.1016/S0958-9465(01)00027-0)
- Energy Market Authority. (2012). Singapore energy statistics 2012. Singapore
- EVN. (2013). Vietnam electricity and power development of vietnam *Vietnam Electricity* Retrieved Feb. 10, 2015, from <http://intpow.com/?id=1940&download=1>
- Fay, R., Treloar, G., & Iyer-Raniga, U. (2000). Life-cycle energy analysis of buildings: a case study. *Building Research & Information*, 28(1), 31-41. doi: 10.1080/096132100369073
- Ferreira, R. M., Liu, G., Nilsson, L., & Gjorv, O. E. (2004). *Blast-furnace slag cements for concrete durability in marine environment*. Paper presented at the 4th International Conference on Concrete under Severe Conditions: Environment and Loading, Seoul, Korea.
- Finnveden, G., & Ekvall, T. (1998). Life-cycle assessment as a decision-support tool—the case of recycling versus incineration of paper. *Resources, Conservation and Recycling*, 24(3–4), 235-256. doi: [http://dx.doi.org/10.1016/S0921-3449\(98\)00039-1](http://dx.doi.org/10.1016/S0921-3449(98)00039-1)
- Gamry Instruments. (2011). Series G Potentiostat/Galvanostat/ZRA Operator's Manual
- Gettu, R., Bazant, Z. P., & Karr, M. E. (1990). Fracture properties and brittleness of high-strength concrete. *ACI Materials Journal*, 87(6).
- Ghods, P., Isgor, O. B., McRae, G., & Miller, T. (2009). The effect of concrete pore solution composition on the quality of passive oxide films on black steel reinforcement. *Cement and Concrete Composites*, 31(1), 2-11. doi: <http://dx.doi.org/10.1016/j.cemconcomp.2008.10.003>
- Girao, A. V. O. M. d. S. (2007). *The nanostructure and degradation of C-S-H in Portland and blended cements*. (PhD), The University of Leeds, Leeds.
- Glass, G., Roberts, A., & Davison, N. (2008). Hybrid corrosion protection of chloride-contaminated concrete. *Proceedings of the ICE-Construction Materials*, 161(4), 163-172.
- Gonzalez, J., Molina, A., Otero, E., & Lopez, W. (1990). On the mechanism of steel corrosion in concrete: the role of oxygen diffusion. *Magazine of Concrete Research*, 42(150), 23-27.
- Grayson, J. M., Pang, W., & Schiff, S. (2013). Building envelope failure assessment framework for residential communities subjected to hurricanes. *Engineering Structures*, 51(0), 245-258. doi: <http://dx.doi.org/10.1016/j.engstruct.2013.01.027>
- Grubb, J. A., Blunt, J., Ostertag, C. P., & Devine, T. M. (2007). Effect of steel microfibers on corrosion of steel reinforcing bars. *Cement and Concrete Research*, 37(7), 1115-1126.
- Grzybowski, M., & Shah, S. P. (1990). Shrinkage cracking of fiber reinforced concrete. *ACI Materials Journal*, 87(2).
- Guinée, J. B. (2002). Handbook on life cycle assessment operational guide to the ISO standards. *The International Journal of Life Cycle Assessment*, 7(5), 311-313.

- Gunay, H. B., Ghods, P., Isgor, O. B., Carpenter, G. J. C., & Wu, X. (2013). Characterization of atomic structure of oxide films on carbon steel in simulated concrete pore solutions using EELS. *Applied Surface Science*, 274(0), 195-202. doi: <http://dx.doi.org/10.1016/j.apsusc.2013.03.014>
- Hallensleben, M. L. (2000). Polyvinyl Compounds, Others *Ullmann's Encyclopedia of Industrial Chemistry*: Wiley-VCH, Weinheim.
- Hartt, W., Kim, K., Jingak, N., & Li, L. (2003). *Effect of cement alkalinity upon time-to-corrosion of reinforcing steel in concrete undergoing chloride exposure*. Paper presented at the Corrosion 2003.
- Hausmann, D. A. (1967). Steel corrosion in concrete-How does it occur? *Materials Protection* (pp. 19-23).
- Hearn, N. (1999). Effect of shrinkage and load-induced cracking on water permeability of concrete. *ACI Materials Journal*, 96(2).
- Hendrickson, C., Horvath, A., Joshi, S., & Lave, L. (1998). Peer reviewed: Economic input-output models for environmental life-cycle assessment. *Environmental Science & Technology*, 32(7), 184A-191A. doi: 10.1021/es983471i
- Hladky, K., Callow, L., & Dawson, J. (1980). Corrosion rates from impedance measurements: an introduction. *British Corrosion Journal*, 15(1), 20-25.
- Hong, K., & Hooton, R. D. (1999). Effects of cyclic chloride exposure on penetration of concrete cover. *Cement and Concrete Research*, 29(9), 1379-1386. doi: [http://dx.doi.org/10.1016/S0008-8846\(99\)00073-3](http://dx.doi.org/10.1016/S0008-8846(99)00073-3)
- Horvath, A., & Hendrickson, C. (1998). Comparison of environmental implications of asphalt and steel-reinforced concrete pavements. *Transportation Research Record: Journal of the Transportation Research Board*, 1626(-1), 105-113.
- Housing & Development Board (HDB). (2009). Guide drawings for window and precast concrete cladding Singapore
- Hsu, T. T. (1963). *Mathematical analysis of shrinkage stresses in a model of hardened concrete*. Paper presented at the ACI Journal Proceedings.
- Hsu, T. T., Slate, F. O., Sturman, G. M., & Winter, G. (1963). *Microcracking of plain concrete and the shape of the stress-strain curve*. Paper presented at the ACI Journal Proceedings.
- Hughes, B. P., & Fattuhi, N. I. (1976). The workability of steel-fibre-reinforced concrete. *Magazine of Concrete Research*, 28, 157-161.
- International Energy Agency. (2012). CO<sub>2</sub> emissions from fuel combustion highlights Paris International Energy Agency.
- Jau, W. C., & Tsay, D. S. (1998). A study of the basic engineering properties of slag cement concrete and its resistance to seawater corrosion. *Cement and Concrete Research*, 28(10), 1363-1371.
- Jen, G., & Ostertag, C. P. (2012). Resistance to corrosion induced cracking in self consolidating hybrid fiber reinforced concrete. In G. Parra-Montesinos, H. Reinhardt & A. E. Naaman (Eds.), *High Performance Fiber Reinforced Cement Composites 6* (Vol. 2, pp. 163-170): Springer Netherlands.
- Jones, C., & Hammond, G. (2011). Inventory of carbon & energy (ICE) Version 2.0 International Energy Agency: University of Bath, UK.
- Junnila, S., Horvath, A., & Guggemos, A. (2006). Life-cycle assessment of office buildings in Europe and the United States. *Journal of infrastructure systems*, 12(1), 10-17. doi: 10.1061/(ASCE)1076-0342(2006)12:1(10)

- Kawamura, M., & Takemoto, K. (1988). Correlation between pore solution composition and alkali silica expansion in mortars containing various fly ashes and blastfurnace slags. *International Journal of Cement Composites and Lightweight Concrete*, 10(4), 215-223. doi: [http://dx.doi.org/10.1016/0262-5075\(88\)90051-6](http://dx.doi.org/10.1016/0262-5075(88)90051-6)
- Kayali, O., & Sharfuddin Ahmed, M. (2012). Assessment of high volume replacement fly ash concrete - Concept of performance index. *Construction and Building Materials*, <http://dx.doi.org/10.1016/j.conbuildmat.2012.05.009>.
- Keis, N., & Komissarov, A. (1963). Cerium in structural and stainless steels and cast iron. *Metal Science and Heat Treatment*, 5(8), 439-443.
- Keoleian, G., Kendall, A., Dettling, J., Smith, V., Chandler, R., Lepech, M., & Li, V. C. (2005, May 8-11). *Life-cycle cost model for evaluating the sustainability of bridge decks*. Paper presented at the Proceedings of the Fourth International Workshop on Life-Cycle Cost Analysis and Design of Civil Infrastructures Systems, Cocoa Beach, Florida.
- Khayat, K. (1999). Workability, testing, and performance of self-consolidating concrete. *ACI Materials Journal*, 96, 346-353.
- Kim, J.-H., & Robertson, R. E. (1998). Effects of polyvinyl alcohol on aggregate-paste bond strength and the interfacial transition zone. *Advanced Cement Based Materials*, 8(2), 66-76. doi: [http://dx.doi.org/10.1016/S1065-7355\(98\)00009-1](http://dx.doi.org/10.1016/S1065-7355(98)00009-1)
- Kneifel, J. (2010). Life-cycle carbon and cost analysis of energy efficiency measures in new commercial buildings. *Energy and Buildings*, 42(3), 333-340. doi: <http://dx.doi.org/10.1016/j.enbuild.2009.09.011>
- Kollek, J. J. (1989). The determination of the permeability of concrete to oxygen by the Cembureau method—a recommendation. *Materials and Structures*, 22(3), 225-230. doi: 10.1007/BF02472192
- Kouloumbi, N., Batis, G., & Malami, C. (1994). The anticorrosive effect of fly ash, slag and a Greek pozzolan in reinforced concrete. *Cement and Concrete Composites*, 16(4), 253-260.
- Koyasu, K., Kitsutaka, Y., & Matsuzawa, K. (2014). *Evaluation of the degradation for reinforced concrete structures using digital X-rays pictures-three dimensional observation on the corrosion of reinforcing bar in concrete* Paper presented at the The 6th International Conference of Asian Concrete Federation, Seoul, Korea
- Kurt, H. (2011). The usage of air gap in the composite wall for energy saving and air pollution. *Environmental Progress & Sustainable Energy*, 30(3), 450-458. doi: 10.1002/ep.10486
- Lambert, P., Page, C. L., & Vassie, P. R. W. (1991). Investigations of reinforcement corrosion. 2. Electrochemical monitoring of steel in chloride-contaminated concrete. *Materials and Structures*, 24(5), 351-358. doi: 10.1007/BF02472068
- Lambrechts, A., Nemegeer, D., Vanbrabant, J., & Stang, H. (2003). Durability of steel fibre reinforced concrete. *ACI Special Publication*, 212.
- Langley, W. S., Carette, G. G., & Malhotra, V. (1989). Structural concrete incorporating high volumes of ASTM class fly ash. *ACI Materials Journal*, 86(5).
- Laranjeira, F., Grünwald, S., Walraven, J., Blom, C., Molins, C., & Aguado, A. (2011). Characterization of the orientation profile of steel fiber reinforced concrete. *Materials and Structures*, 44(6), 1093-1111. doi: 10.1617/s11527-010-9686-5
- Lawler, J. S., Zampini, D., & Shah, S. P. (2002). Permeability of cracked hybrid fiber-reinforced mortar under load. *ACI Materials Journal*, 99(4).



- Lee, K. M., Lee, H. K., Lee, S. H., & Kim, G. Y. (2006). Autogenous shrinkage of concrete containing granulated blast-furnace slag. *Cement and Concrete Research*, 36(7), 1279-1285. doi: <http://dx.doi.org/10.1016/j.cemconres.2006.01.005>
- Leemann, A., Münch, B., Gasser, P., & Holzer, L. (2006). Influence of compaction on the interfacial transition zone and the permeability of concrete. *Cement and Concrete Research*, 36(8), 1425-1433. doi: <http://dx.doi.org/10.1016/j.cemconres.2006.02.010>
- Lei, Y., Zhang, Q., Nielsen, C., & He, K. (2011). An inventory of primary air pollutants and CO<sub>2</sub> emissions from cement production in China, 1990–2020. *Atmospheric Environment*, 45(1), 147-154. doi: <http://dx.doi.org/10.1016/j.atmosenv.2010.09.034>
- Lepech, M., & Li, V. C. (2006). Sustainable infrastructure engineering: integrating material and structural design with life cycle analysis. *Advances in Cement and Concrete X: Sustainability*, 10, 55-60.
- Li, C.-Q., Melchers, R. E., & Zheng, J.-J. (2006). Analytical model for corrosion-induced crack width in reinforced concrete structures. *ACI structural journal*, 103(4).
- Li, V. C., & Maalej, M. (1996). Toughening in cement based composites. Part I: Cement, mortar, and concrete. *Cement and Concrete Composites*, 18(4), 223-237. doi: [http://dx.doi.org/10.1016/0958-9465\(95\)00028-3](http://dx.doi.org/10.1016/0958-9465(95)00028-3)
- Li, V. C., Wang, S., & Wu, C. (2001). Tensile strain-hardening behavior of polyvinyl alcohol engineered cementitious composite (PVA-ECC). *ACI Materials Journal*, 98(6).
- Li, V. C., Wang, Y., & Backer, S. (1990). Effect of inclining angle, bundling and surface treatment on synthetic fibre pull-out from a cement matrix. *Composites*, 21(2), 132-140.
- Li, V. C., Wu, C., Wang, S., Ogawa, A., & Saito, T. (2002). Interface tailoring for strain-hardening polyvinyl alcohol-engineered cementitious composite (PVA-ECC). *ACI Materials Journal*, 99(5).
- Liao, W. C., Chao, S. H., Park, S. Y., & Naaman, A. E. (2007). Self-consolidating high Performance fiber reinforced concrete: SCHPFRC. *High-Performance Fiber-Reinforced Cement Composites: HPRCC*, 5, 293-302.
- Lim, S., & Wee, T. (2000). Autogenous shrinkage of ground-granulated blast-furnace slag concrete. *ACI Materials Journal*, 97(5).
- Liu, Y., & Weyers, R. E. (1998). Modeling the time-to-corrosion cracking in chloride contaminated reinforced concrete structures. *ACI Materials Journal*, 95(6).
- Loncour, X., Deneyer, A., Blasco, M., Flamant, G., & Wouters, P. (2004). Ventilated double facades. *Belgian Building Research Institute Department of Building Physics, Indoor Climate & Building Services*.
- Luo, R., Cai, Y., Wang, C., & Huang, X. (2003). Study of chloride binding and diffusion in GGBS concrete. *Cement and Concrete Research*, 33(1), 1-7. doi: [http://dx.doi.org/10.1016/S0008-8846\(02\)00712-3](http://dx.doi.org/10.1016/S0008-8846(02)00712-3)
- Macphee, D. E. C., H. T. . (1993). Theoretical description of impact of blast furnace slag (BFS) on steel passivation in concrete. *Magazine of Concrete Research*, 45(162), 63-69.
- Mahasanan, N., Smith, S., & Humphreys, K. (2003). The cement industry and global climate change: current and potential future cement industry CO<sub>2</sub> emissions. In J. Gale & Y. Kaya (Eds.), *Greenhouse Gas Control Technologies - 6th International Conference* (pp. 995-1000). Oxford: Pergamon.
- Manera, M., Vennesland, Ø., & Bertolini, L. (2008). Chloride threshold for rebar corrosion in concrete with addition of silica fume. *Corrosion Science*, 50(2), 554-560. doi: <http://dx.doi.org/10.1016/j.corsci.2007.07.007>

- Mangat, P. S., & Gurusamy, K. (1988). Corrosion resistance of steel fibres in concrete under marine exposure. *Cement and Concrete Research*, 18(1), 44-54. doi: [http://dx.doi.org/10.1016/0008-8846\(88\)90120-2](http://dx.doi.org/10.1016/0008-8846(88)90120-2)
- Mangat, P. S., & Molloy, B. T. (1991). Influence of PFA, slag and microsilica on chloride induced corrosion of reinforcement in concrete. *Cement and Concrete Research*, 21(5), 819-834.
- Marcotte, T. D. (2001). Characterization of chloride-induced corrosion products that form in steel-reinforced cementitious.
- Markovich, I., Van Mier, J., & Walraven, J. (2001). Single fiber pullout from hybrid fiber reinforced concrete. *Heron*, 46(3), 191-200.
- Maslehuddin, M., Al-Mana, A. I., Saricimen, H., & Shamim, M. (1990). Corrosion of reinforcing steel in concrete containing slag or pozzolans. *Cement, concrete and aggregates*, 12(1), 24-31.
- Matschei, T., Lothenbach, B., & Glasser, F. P. (2007). The AFm phase in Portland cement. *Cement and Concrete Research*, 37(2), 118-130. doi: <http://dx.doi.org/10.1016/j.cemconres.2006.10.010>
- McGregor, A., Roberts, C., & Cousins, F. (2013). *Two degrees: the built environment and our changing climate*: Routledge.
- Mehta, K. P., & Aitcin, P. C. C. (1990). Principles underlying production of high-performance concrete. *Cement, concrete and aggregates*, 12(2), 70-78.
- Mehta, P. (Jul 2002). Greening of the concrete industry for sustainable development *Concrete International*, 23-28.
- Mehta, P., & Monteiro, P. J. M. (2006). *Concrete: Microstructure, Properties, and Materials* (3rd ed.): McGraw-Hill Professional.
- Mehta, P. K. (2002). Greening of the concrete industry for sustainable development. *Concrete International*.
- Michel, A., Solgaard, A. O. S., Pease, B. J., Geiker, M. R., Stang, H., & Olesen, J. F. (2013). Experimental investigation of the relation between damage at the concrete-steel interface and initiation of reinforcement corrosion in plain and fibre reinforced concrete. *Corrosion Science*, 77(0), 308-321. doi: <http://dx.doi.org/10.1016/j.corsci.2013.08.019>
- Mirza, S. (2006). Durability and sustainability of infrastructure — a state-of-the-art report. *Canadian Journal of Civil Engineering*, 33(6), 639-649. doi: 10.1139/106-049
- Misawa, T., Hashimoto, K., & Shimodaira, S. (1974). The mechanism of formation of iron oxide and oxyhydroxides in aqueous solutions at room temperature. *Corrosion Science*, 14(2), 131-149. doi: [http://dx.doi.org/10.1016/S0010-938X\(74\)80051-X](http://dx.doi.org/10.1016/S0010-938X(74)80051-X)
- Mitchell, R., Yazdanian, M., Zelany, K., & Curcija, C. (2012). *COMFEN 4.1, Lawrence Berkeley National Laboratory*.
- Mohammed, T. U., Otsuki, N., & Hisada, M. (1999). Corrosion of steel bars with respect to orientation in concrete. *ACI Materials Journal*, 96(2).
- Monahan, J., & Powell, J. C. (2011). An embodied carbon and energy analysis of modern methods of construction in housing: A case study using a lifecycle assessment framework. *Energy and Buildings*, 43(1), 179-188. doi: <http://dx.doi.org/10.1016/j.enbuild.2010.09.005>
- Montemor, M. F., Simões, A. M. P., & Ferreira, M. G. S. (1998). Analytical characterization of the passive film formed on steel in solutions simulating the concrete interstitial electrolyte. *Corrosion*, 54(5), 347-353. doi: 10.5006/1.3284861

- Naaman, A. E. (2003). Strain hardening and deflection hardening fiber reinforced cement composites. *High Performance Fiber Reinforced Cement Composites 4 (HPFRCC 4)*, 95-113.
- Naaman, A. E. (2007). *High performance fiber reinforced cement composites: classification and applications*. Paper presented at the Proceedings of Cement Based Materials and Civil Infrastructure International Workshop, Karachi, Pakistan.
- Naaman, A. E., & Najm, H. (1991). Bond-slip mechanisms of steel fibers in concrete. *ACI Materials Journal*, 88(2).
- National Ready Mixed Concrete Association (NRMCA). (2004). CIP 37-Self consolidating concrete (SCC). 900 Spring Street, Silver Spring
- Nealer, R., Matthews, H. S., & Hendrickson, C. (2012). Assessing the energy and greenhouse gas emissions mitigation effectiveness of potential US modal freight policies. *Transportation Research Part A: Policy and Practice*, 46(3), 588-601. doi: <http://dx.doi.org/10.1016/j.tra.2011.11.010>
- Neff, D., Harnisch, J., Beck, M., L'Hostis, V., Goebbels, J., & Meinel, D. (2011). Morphology of corrosion products of steel in concrete under macro-cell and self-corrosion conditions. *Materials and Corrosion*, 62(9), 861-871. doi: 10.1002/maco.201005861
- Neville, A. M. (1996). *Properties of concrete* John Wiley & Sons.
- Nguyen, D. L., Kim, D. J., Ryu, G. S., & Koh, K. T. (2013). Size effect on flexural behavior of ultra-high-performance hybrid fiber-reinforced concrete. *Composites Part B: Engineering*, 45(1), 1104-1116. doi: <http://dx.doi.org/10.1016/j.compositesb.2012.07.012>
- Nguyen, D. L., Ryu, G. S., Koh, K. T., & Kim, D. J. (2014). Size and geometry dependent tensile behavior of ultra-high-performance fiber-reinforced concrete. *Composites Part B: Engineering*, 58(0), 279-292. doi: <http://dx.doi.org/10.1016/j.compositesb.2013.10.072>
- NORDTEST NT BUILD 492. (1999). Concrete, mortar and cement-based repair materials: chloride migration coefficient from non-steady-state migration experiments. Nordtest, Finland.
- Ochoa, L., Hendrickson, C., & Matthews, H. (2002). Economic Input-output life-cycle assessment of U.S. residential buildings. *Journal of infrastructure systems*, 8(4), 132-138. doi: 10.1061/(ASCE)1076-0342(2002)8:4(132)
- Okada, K., & Miyagawa, T. (1980). Chloride corrosion of reinforcing steel in cracked concrete. *In: Performance of concrete in marine environment*.
- Okamura, H., & Ouchi, M. (2003). Self-compacting concrete. *Journal of Advanced Concrete Technology*, 1(1), 5-15.
- Olivier, J. G. J., Janssens-Maenhout, G., Muntean, M., & Peters, J. A. H. W. (2013). Trends in global CO<sub>2</sub> emissions PPBL Netherlands Environmental Assessment Agency.
- Ostertag, C. P., & Blunt, E. J. (2007). *Hybrid fiber reinforced concrete for use in bridge approach slabs*. Paper presented at the CBM-CI International Workshop.
- Ostertag, C. P., & Blunt, J. (2008). Use of fiber reinforced concrete in bridge approach slabs CA09-0632: Caltrans-Division of Research & Innovation
- Ostertag, C. P., Yi, C., & Monteiro, P. J. (2007). Effect of confinement on properties and characteristics of alkali-silica reaction gel. *ACI Materials Journal*, 104(3).
- Otieno, M., Alexander, M., & Beushausen, H.-D. (2010). Corrosion in cracked and uncracked concrete—influence of crack width, concrete quality and crack reopening. *Magazine of Concrete Research*, 62(6), 393-404.

- Otsuki, N., Nagataki, S., & Nakashita, K. (1993). Evaluation of the AgNO<sub>3</sub> solution spray method for measurement of chloride penetration into hardened cementitious matrix materials. *Construction and Building Materials*, 7(4), 195-201. doi: [http://dx.doi.org/10.1016/0950-0618\(93\)90002-T](http://dx.doi.org/10.1016/0950-0618(93)90002-T)
- Page, C. (1975). Mechanism of corrosion protection in reinforced concrete marine structures. *Nature*, 258(11), 514– 515.
- Pal, S., Mukherjee, A., & Pathak, S. (2002). Corrosion behavior of reinforcement in slag concrete. *ACI Materials Journal*, 99(6).
- Pantazopoulou, S., & Papoulia, K. (2001). Modeling cover-cracking due to reinforcement corrosion in RC structures. *Journal of Engineering Mechanics*, 127(4), 342-351.
- Parrott, L. (1991). Factors influencing relative humidity in concrete. *Magazine of Concrete Research*, 43(154), 45-52.
- Pérez-Lombard, L., Ortiz, J., & Pout, C. (2008). A review on buildings energy consumption information. *Energy and Buildings*, 40(3), 394-398. doi: <http://dx.doi.org/10.1016/j.enbuild.2007.03.007>
- Peris Mora, E., Payá, J., & Monzó, J. (1993). Influence of different sized fractions of a fly ash on workability of mortars. *Cement and Concrete Research*, 23(4), 917-924. doi: [http://dx.doi.org/10.1016/0008-8846\(93\)90045-B](http://dx.doi.org/10.1016/0008-8846(93)90045-B)
- Plastic Europe. (2008). Environmental product declarations of the European plastics manufacturers: polypropylene (PP): Association of Plastics Manufacturers.
- Pour-Ghaz, M., Isgor, O. B., & Ghods, P. (2009). Quantitative interpretation of half-cell potential measurements in concrete structures. *Journal of Materials in Civil Engineering*, 21(9), 467-475.
- Poursae, A., & Hansson, C. M. (2009). Potential pitfalls in assessing chloride-induced corrosion of steel in concrete. *Cement and Concrete Research*, 39(5), 391-400. doi: <http://dx.doi.org/10.1016/j.cemconres.2009.01.015>
- Price, W. H. (1951). *Factors influencing concrete strength*. Paper presented at the ACI Journal Proceedings.
- Ramm, W., & Biscopig, M. (1998). Autogenous healing and reinforcement corrosion of water-penetrated separation cracks in reinforced concrete. *Nuclear Engineering and Design*, 179(2), 191-200. doi: [http://dx.doi.org/10.1016/S0029-5493\(97\)00266-5](http://dx.doi.org/10.1016/S0029-5493(97)00266-5)
- Raupach, M. (1996). Chloride-induced macrocell corrosion of steel in concrete—theoretical background and practical consequences. *Construction and Building Materials*, 10(5), 329-338. doi: [http://dx.doi.org/10.1016/0950-0618\(95\)00018-6](http://dx.doi.org/10.1016/0950-0618(95)00018-6)
- Raupach, M., & Dauberschmidt, C. (2003). Critical chloride content for the corrosion of steel fibres in artificial concrete pore solutions. *ACI Special Publication*, 212.
- Refait, P., & Génin, J. M. R. (1993). The oxidation of ferrous hydroxide in chloride-containing aqueous media and pourbaix diagrams of green rust one. *Corrosion Science*, 34(5), 797-819. doi: [http://dx.doi.org/10.1016/0010-938X\(93\)90101-L](http://dx.doi.org/10.1016/0010-938X(93)90101-L)
- Rilem, T. (1999). 116-PCD.: Permeability of concrete as a criterion of its durability. *Mater Struct*, 32(4), 174-179.
- Roy, S. K., Poh, K. B., & Northwood, D. o. (1999). Durability of concrete: accelerated carbonation and weathering studies. *Building and Environment*, 34(5), 597-606. doi: [http://dx.doi.org/10.1016/S0360-1323\(98\)00042-0](http://dx.doi.org/10.1016/S0360-1323(98)00042-0)
- Saetta, A. V., Scotta, R. V., & Vitaliani, R. V. (1993). Analysis of chloride diffusion into partially saturated concrete. *ACI Materials Journal*, 90(5).

- Sagoe-Crentsil, K. K., & Glasser, F. P. (1993). "Green rust", iron solubility and the role of chloride in the corrosion of steel at high pH. *Cement and Concrete Research*, 23(4), 785-791. doi: [http://dx.doi.org/10.1016/0008-8846\(93\)90032-5](http://dx.doi.org/10.1016/0008-8846(93)90032-5)
- Sahmaran, M., Li, V. C., & Andrade, C. (2008). Corrosion resistance performance of steel-reinforced engineered cementitious composite beams. *ACI Materials Journal*, 105(3).
- Sahmaran, M., Yurtseven, A., & Ozgur Yaman, I. (2005). Workability of hybrid fiber reinforced self-compacting concrete. *Building and Environment*, 40(12), 1672-1677. doi: <http://dx.doi.org/10.1016/j.buildenv.2004.12.014>
- Salmon, D. C., Einea, A., Tadros, M. K., & Culp, T. D. (1997). Full scale testing of precast concrete sandwich panels. *ACI structural journal*, 94, 239-247.
- Satish, C. (1997). *Waste materials used in concrete manufacturing*: Noyes Publication.
- Šavija, B., Luković, M., Hosseini, S. A. S., Pacheco, J., & Schlangen, E. (2014). Corrosion induced cover cracking studied by X-ray computed tomography, nanoindentation, and energy dispersive X-ray spectrometry (EDS). *Materials and Structures*, 1-20.
- Scheuer, C., Keolelian, G. A., & Reppe, P. (2003). Life cycle energy and environmental performance of a new university building: modeling challenges and design implications. *Energy and Buildings*, 35(10), 1049-1064. doi: [http://dx.doi.org/10.1016/S0378-7788\(03\)00066-5](http://dx.doi.org/10.1016/S0378-7788(03)00066-5)
- Schiegg, Y., Büchler, M., & Brem, M. (2009). Potential mapping technique for the detection of corrosion in reinforced concrete structures: Investigation of parameters influencing the measurement and determination of the reliability of the method. *Materials and Corrosion*, 60(2), 79-86. doi: 10.1002/maco.200805042
- Schiessl, P., & Raupach, M. (1997). Laboratory studies and calculations on the influence of crack width on chloride-induced corrosion of steel in concrete. *ACI Materials Journal*, 94(1).
- Scientific Applications International Corporation. (2006). *Life-cycle assessment: principles and practice*: National Risk Management Research Laboratory, Office of Research and Development, US Environmental Protection Agency.
- Selkowitz, S., Mitchell, R., McClintock, M., McQuillen, D., McNeil, A., & Yazdanian, M. (2012). *COMFEN 3.0-Evolution of an early design tool for commercial facades and fenestration systems*. Paper presented at the Building Enclosure Sustainability Symposium (BESS) 2011, Pomona, CA, 4/29/11-4/30/11.
- Sharrard, A., Matthews, H., & Ries, R. (2008). Estimating construction project environmental effects using an input-output-based hybrid life-cycle assessment model. *Journal of infrastructure systems*, 14(4), 327-336. doi: 10.1061/(ASCE)1076-0342(2008)14:4(327)
- Sherwood, J., Stagnitti, F., Kokkinn, M., & Williams, W. (1992). A standard table for predicting equilibrium dissolved oxygen concentrations in salt lakes dominated by sodium chloride. *International Journal of Salt Lake Research*, 1(1), 1-6.
- Siddique, R. (2008). *Waste materials and by-products in concrete used in concrete manufacturing* Springer-Verlag Berlin Heidelberg
- Siddique, R., & Bennacer, R. (2012). Use of iron and steel industry by-product (GGBS) in cement paste and mortar. *Resources, Conservation and Recycling*, 69(0), 29-34. doi: <http://dx.doi.org/10.1016/j.resconrec.2012.09.002>
- Singapore Power. (2013). Tariff Rates. Retrieved Dec 6, 2013, from <http://www.singaporepower.com.sg>

- Song, H. W., Kwon, S. J., Lee, S. W., & Byun, K. J. (2004). A study of chloride ion penetration in ground granulated blast furnace slag concrete. *Korea Concrete Institute*, 15(3), 400-408.
- Song, P. S., & Hwang, S. (2004). Mechanical properties of high-strength steel fiber-reinforced concrete. *Construction and Building Materials*, 18(9), 669-673.
- Söylev, T., & François, R. (2005). Corrosion of reinforcement in relation to presence of defects at the interface between steel and concrete. *Journal of Materials in Civil Engineering*, 17(4), 447-455. doi: doi:10.1061/(ASCE)0899-1561(2005)17:4(447)
- Soylev, T. A., & François, R. (2003). Quality of steel-concrete interface and corrosion of reinforcing steel. *Cement and Concrete Research*, 33(9), 1407-1415.
- Stratfull, R. (1957). The corrosion of steel in a reinforced concrete bridge. *Corrosion*, 13(3), 43-48.
- Stratfull, R. F. (1973). *Half-cell potentials and the corrosion of steel in concrete*. Washington District of Columbia: Highway Research Record
- Suda, K., Misra, S., & Motohashi, K. (1993). Corrosion products of reinforcing bars embedded in concrete. *Corrosion Science*, 35(5-8), 1543-1549. doi: [http://dx.doi.org/10.1016/0010-938X\(93\)90382-Q](http://dx.doi.org/10.1016/0010-938X(93)90382-Q)
- Sugiyama, T., Bremner, T. W., & Tsuji, Y. (1996). Determination of chloride diffusion coefficient and gas permeability of concrete and their relationship. *Cement and Concrete Research*, 26(5), 781-790. doi: [http://dx.doi.org/10.1016/S0008-8846\(96\)85015-0](http://dx.doi.org/10.1016/S0008-8846(96)85015-0)
- Suh, S., & Huppel, G. (2005). Methods for life cycle inventory of a product. *Journal of Cleaner Production*, 13(7), 687-697. doi: <http://dx.doi.org/10.1016/j.jclepro.2003.04.001>
- Suryavanshi, A. K., Scantlebury, J. D., & Lyon, S. B. (1996). Mechanism of Friedel's salt formation in cements rich in tri-calcium aluminate. *Cement and Concrete Research*, 26(5), 717-727. doi: [http://dx.doi.org/10.1016/S0008-8846\(96\)85009-5](http://dx.doi.org/10.1016/S0008-8846(96)85009-5)
- Suzuki, M., & Oka, T. (1998). Estimation of life cycle energy consumption and CO2 emission of office buildings in Japan. *Energy and Buildings*, 28(1), 33-41. doi: [http://dx.doi.org/10.1016/S0378-7788\(98\)00010-3](http://dx.doi.org/10.1016/S0378-7788(98)00010-3)
- Swamy, R., & Stavrides, H. (1979). *Influence of fiber reinforcement on restrained shrinkage and cracking*. Paper presented at the ACI Journal proceedings.
- Takaya, S., Nakamura, S., Yamamoto, T., & Miyagawa, T. (2013). Influence of steel corrosion products in concrete on crack opening weight loss of corrosion. *Journal of JSCE, Division E2: Materials and Concrete Structures*, 69(2), 154-165.
- Talbot, C., Pigeon, M., & Marchand, J. (2000). Influence of fly ash and slag on deicer salt scaling resistance of concrete. *ACI Special Publication*, 192.
- Taylor, H. F. W., Famy, C., & Scrivener, K. L. (2001). Delayed ettringite formation. *Cement and Concrete Research*, 31(5), 683-693. doi: [http://dx.doi.org/10.1016/S0008-8846\(01\)00466-5](http://dx.doi.org/10.1016/S0008-8846(01)00466-5)
- Taylor, M. A., & Kuwairi, A. (1978). Effects of ocean salts on the compressive strength of concrete. *Cement and Concrete Research*, 8(4), 491-500. doi: [http://dx.doi.org/10.1016/0008-8846\(78\)90029-7](http://dx.doi.org/10.1016/0008-8846(78)90029-7)
- Tazawa, E., Yonekura, A., & Tanaka, S. (1989). Drying shrinkage and creep of concrete containing granulated blast furnace slag. *ACI Special Publication*, 114.
- The World Bank. (2014). 2014 World Development Indicators

- Theocaris, P. S., & Koufopoulos, T. (1969). Photo-elastic analysis of shrinkage micro cracking in concrete. *Magazine of Concrete Research*, 21, 15-22.  
<http://www.icevirtuallibrary.com/content/article/10.1680/mac.1969.21.66.15>
- Thibeau, R. J., Brown, C. W., & Heidersbach, R. H. (1978). Raman spectra of possible corrosion products of iron. *Applied Spectroscopy*, 32(6), 532-535.
- Thormark, C. (2002). A low energy building in a life cycle—its embodied energy, energy need for operation and recycling potential. *Building and Environment*, 37(4), 429-435. doi: [http://dx.doi.org/10.1016/S0360-1323\(01\)00033-6](http://dx.doi.org/10.1016/S0360-1323(01)00033-6)
- Topçu, İ. B., & Boğa, A. R. (2010). Effect of ground granulate blast-furnace slag on corrosion performance of steel embedded in concrete. *Materials & Design*, 31(7), 3358-3365.
- Torii, K., Sasatani, T., & Kawamura, M. (1995). Effects of fly ash, blast furnace slag, and silica fume on resistance of mortar to calcium chloride attack. *ACI Special Publication*, 153.
- Torrent, R. (1999). Gas permeability of high-performance concrete site and laboratory tests. *ACI Special Publication*, 186.
- Toutanji, H., McNeil, S., & Bayasi, Z. (1998). Chloride permeability and impact resistance of polypropylene-fiber-reinforced silica fume concrete. *Cement and Concrete Research*, 28(7), 961-968. doi: [http://dx.doi.org/10.1016/S0008-8846\(98\)00073-8](http://dx.doi.org/10.1016/S0008-8846(98)00073-8)
- Treadaway, K., Cox, R., & Brown, B. (1989). *Durability of corrosion resisting steels in concrete* Paper presented at the ICE Proceedings.
- Trejo, D., Gardoni, P., & Kim, J. J. (2011). Long-term performance of glass fiber-reinforced polymer reinforcement embedded in concrete. *ACI Materials Journal*, 108(6).
- Treloar, G. J. (1997). Extracting embodied energy paths from input–output tables: Towards an input–output-based hybrid energy analysis method. *Economic Systems Research*, 9(4), 375-391. doi: 10.1080/09535319700000032
- Treloar, G. J., Love, P. E., & Holt, G. D. (2001). Using national input/output data for embodied energy analysis of individual residential buildings. *Construction Management and Economics*, 19(1), 49-61.
- Tritthart, J. (1989). Chloride binding in cement II. The influence of the hydroxide concentration in the pore solution of hardened cement paste on chloride binding. *Cement and Concrete Research*, 19(5), 683-691.
- Trono, W. (2014). *Earthquake resilient bridge columns utilizing damage resistant hybrid fiber reinforced concrete*. (PhD ), University of California, Berkeley Berkeley.
- Trono, W., Jen, G., Ostertag, C. P., & Panagiotou, M. (2013). *Tested and modeled seismic response of a rocking, post-tensioned HyFRC bridge column*. Paper presented at the Proceedings of the Seventh National Seismic Conference on Bridges and Highways: Bridge Resilience for Earthquakes & Other Natural Hazards, Oakland
- Turanli, L., Shomglin, K., Ostertag, C. P., & Monteiro, P. J. M. (2001). Reduction in alkali-silica expansion due to steel microfibers. *Cement and Concrete Research*, 31(5), 825-827.
- Turnbull, A. (1983). The solution composition and electrode potential in pits, crevices and cracks. *Corrosion Science*, 23(8), 833-870.
- Tuutti, K. (1982). Corrosion of steel in concrete. In CBI forskning/research (Ed.).
- UNEP Sustainable Buildings & Climate Initiative. (2009). Buildings and climate change—Summary for decision-makers.
- United Nations. (1987). Our common future, Chapter 2: Towards sustainable development. *UN Documents-Gathering a body of global agreements*. Retrieved Dec 10, 2012, from <http://www.un-documents.net/ocf-02.htm>



- Uomoto, T. (2003). *Durability design of GFRP rods for concrete reinforcement* Paper presented at the FRPRCS-6, Singapore
- Ürge-Vorsatz, D., Cabeza, L. F., Serrano, S., Barreneche, C., & Petrichenko, K. (2015). Heating and cooling energy trends and drivers in buildings. *Renewable and Sustainable Energy Reviews*, 41(0), 85-98. doi: <http://dx.doi.org/10.1016/j.rser.2014.08.039>
- US Department of Energy. (2012a). Building energy data book. Part 1.1 : Buildings sector energy consumption. Retrieved Oct 30, 2014, from <http://buildingsdatabook.eren.doe.gov/TableView.aspx?table=1.1.3>
- US Department of Energy. (2012b). Building energy data book. Part 1.2 : Building sector expenditures Retrieved Feb 09, 2015, from <http://buildingsdatabook.eren.doe.gov/TableView.aspx?table=1.4.1>
- US Department of Energy. (2012c). Building energy data book. Part 1.4 : Environmental data. Retrieved Oct 30, 2014, from <http://buildingsdatabook.eren.doe.gov/TableView.aspx?table=1.4.1>
- US Department of Interior & US Geological Survey. (2015). Mineral commodity summaries 2015
- Valcuende, M., Parra, C., Marco, E., Garrido, A., Martínez, E., & Cánoves, J. (2012). Influence of limestone filler and viscosity-modifying admixture on the porous structure of self-compacting concrete. *Construction and Building Materials*, 28(1), 122-128. doi: <http://dx.doi.org/10.1016/j.conbuildmat.2011.07.029>
- van Oss, H. G. (2013). 2011 Minerals Yearbook. *US Geological Survey*.
- Vu, K., Stewart, M. G., & Mullard, J. (2005). Corrosion-induced cracking: experimental data and predictive models. *ACI structural journal*, 102(5).
- Wafa, F. F., & Ashour, S. A. (1992). Mechanical properties of high-strength fiber reinforced concrete. *ACI Materials*, 89(5), 449-455.
- Walton, P. L., & Majumdar, A. J. (1975). Cement-based composites with mixtures of different types of fibres. *Composites*, 6(5), 209-216. doi: [http://dx.doi.org/10.1016/0010-4361\(75\)90416-4](http://dx.doi.org/10.1016/0010-4361(75)90416-4)
- Weiler, B. G., Christian (1996). Pullout behaviour of fibers in steel fiber reinforced concrete *Otto Graf Journal*.
- Weyers, R. E. (1998). Service life model for concrete structures in chloride laden environments. *ACI Materials Journal*, 95(4).
- Weyers, R. E., Brown, M., Al-Qadi, I. L., & Henry, M. (1993). A rapid method for measuring the acid-soluble chloride content of powdered concrete samples. *Cement, concrete and aggregates*, 15(1).
- Wong, H. S., Zhao, Y. X., Karimi, A. R., Buenfeld, N. R., & Jin, W. L. (2010). On the penetration of corrosion products from reinforcing steel into concrete due to chloride-induced corrosion. *Corrosion Science*, 52(7), 2469-2480. doi: <http://dx.doi.org/10.1016/j.corsci.2010.03.025>
- Yao, W., Li, J., & Wu, K. (2003). Mechanical properties of hybrid fiber-reinforced concrete at low fiber volume fraction. *Cement and Concrete Research*, 33(1), 27-30. doi: [http://dx.doi.org/10.1016/S0008-8846\(02\)00913-4](http://dx.doi.org/10.1016/S0008-8846(02)00913-4)
- Yeau, K. Y., & Kim, E. K. (2005). An experimental study on corrosion resistance of concrete with ground granulate blast-furnace slag. *Cement and Concrete Research*, 35(7), 1391-1399.

- Yi, C., & Ostertag, C. P. (2001). Strengthening and toughening mechanisms in microfiber reinforced cementitious composites. *Journal of Materials Science*, 36(6), 1513-1522.
- Yi, C. K., & Ostertag, C. P. (2005). Mechanical approach in mitigating alkali-silica reaction. *Cement and Concrete Research*, 35(1), 67-75.
- Yohanis, Y. G., & Norton, B. (2002). Life-cycle operational and embodied energy for a generic single-storey office building in the UK. *Energy*, 27(1), 77-92. doi: [http://dx.doi.org/10.1016/S0360-5442\(01\)00061-5](http://dx.doi.org/10.1016/S0360-5442(01)00061-5)
- Yonezawa, T., Ashworth, V., & Procter, R. P. M. (1988). Pore solution composition and chloride effects on the corrosion of steel in concrete. *Corrosion*, 44(7), 489-499. doi: 10.5006/1.3583967
- Zhang, H., Keoleian, G., & Lepech, M. (2008). *An integrated life cycle assessment and life cycle analysis model for pavement overlay systems*. Paper presented at the First International Symposium on Life-Cycle Civil Engineering.
- Zhao, Y., Ren, H., Dai, H., & Jin, W. (2011). Composition and expansion coefficient of rust based on X-ray diffraction and thermal analysis. *Corrosion Science*, 53(5), 1646-1658. doi: <http://dx.doi.org/10.1016/j.corsci.2011.01.007>
- Zhu, W., & Bartos, P. J. (2003). Permeation properties of self-compacting concrete. *Cement and Concrete Research*, 33(6), 921-926.